OPTIMIZED DESIGN OF THERMAL BATTERIES TO ENHANCE PERFORMANCE OF SPACE CONDITIONING SYSTEMS

A Dissertation
Presented to
The Academic Faculty

by

Anne M. Mallow

In Partial Fulfillment
of the Requirements for the Degree
Doctor of Philosophy in the
George W. Woodruff School of Mechanical Engineering

Georgia Institute of Technology
December 2016

OPTIMIZED DESIGN OF THERMAL BATTERIES TO ENHANCE PERFORMANCE OF SPACE CONDITIONING SYSTEMS

Approved by:

Dr. Samuel Graham, Advisor
School of Mechanical Engineering
Georgia Institute of Technology

Dr. Kyriaki Kalaitzidou
School of Mechanical Engineering
Georgia Institute of Technology

Dr. Satish Kumar
School of Mechanical Engineering
Georgia Institute of Technology

Dr. Jason Nadler
School of Materials Science and Engineering
Georgia Institute of Technology

Dr. Omar Abdelaziz
Building Equipment Research Group
Oak Ridge National Laboratory

Date Approved: November 7th, 2016

ACKNOWLEDGEMENTS

I wish to thank my advisor, Dr. Samuel Graham, for his guidance, support, and patience during this PhD journey. I am grateful for collaboration with Dr. Omar Abdelaziz of Oak Ridge National Laboratory, which has facilitated and advanced this research. Additional thanks belong to Dr. Kyriaki Kalaitzidou, Dr. Satish Kumar, and Dr. Jason Nadler for the use of laboratory equipment, guidance on my studies and research, and serving on my dissertation committee.

I would like to thank members of the EMRL group at Georgia Tech for their friendship as well as friends outside of the group including fellows of the Three Amigos plus Stephen. Additionally, I want to acknowledge members of the Building Equipment Research group at Oak Ridge National Laboratory who have been invaluable mentors. Furthermore, I want to recognize my family for their love, patience, and unwavering support.

I am thankful to the NSF IGERT Program, ORNL GO! Program, and the U.S. DOE Building Technologies Office for financial support of this research and my education. Finally, special thanks to ERG Aerospace, Asbury Carbons, and GrafTech, for experimental material and insightful discussions.

TABLE OF CONTENTS

LIST OF TABLES

LIST OF FIGURES

LIST OF SYMBOLS AND ABBREVIATIONS

ABBREVIATIONS

CENG	Compressed Expanded Natural Graphite
DSC	Differential Scanning Calorimetry
DTA	Differential Thermal Analysis
EG	Expanded Graphite
Fo	Fourier number
LHTSS	Latent Heat Thermal Storage System
PCHX	Phase Change Heat Exchanger
PCM	Phase Change Material
PPI	Pores Per Inch
PT37	PureTemp 37
Ra	Rayleigh number
SEM	Scanning Electron Microscope
Ste	Stefan number
TCM	Thermo-Chemical System

SYMBOLS

a_m	Fraction melted
a_{sf}	Specific surface area [mm^2/mm^3]
c_p	Specific heat [J/kg·K]
f	Liquid fraction of the PCM
g	Gravitational acceleration (9.81 m/s^2)
H	Height [m]

h	Enthalpy [J/kg]
h_c	Convective heat transfer coefficient [W/m^2/K]
h_{sf}	Interstitial heat transfer coefficient [W/m^2/K]
k	Thermal conductivity [W/m·K]
L	Latent heat [J/kg, J/g]
m	Mass [g]
p	Pressure [Pa]
Q	Energy [J]
q”	Heat flux [W/cm^2]
T	Temperature [°C, K]
t	Time [s]
v	Velocity of liquid PCM [m/s]
V	Volume [m^3]
X	Interface location [m]
x	Melt distance [m]

GREEK SYMBOLS

α	Thermal diffusivity [m^2/s]
β	Thermal expansion coefficient [1/K]
γ	Relative density
ρ	Density [kg/m^3]
φ	Effective heat storage [J/g/K]
Θ	Dimensionless temperature
μ	Dynamic viscosity [kg/m/s]
ν	Kinematic viscosity [m^2/s]

SUBSCRIPTS

eff	Effective
f	Final; PCM
i	Initial
l	Liquid
o	Reference
s	Solid
av	Average

SUMMARY

The recovery and reuse of waste heat to enhance the overall performance of a thermodynamic system is dependent on effective heat exchangers to absorb or reject thermal energy. Thus, improvements to the heat exchanger design can often be beneficial in the creation of compact or more energy efficient systems. One such advancement is the insertion of an energy storage medium into the heat exchanger to act as a thermal battery. Such technology delays the thermal exchange between the hot and cold fluid streams, allowing the exchange to occur on demand or when more expedient for an energy efficient application. Phase change materials (PCMs) are often used as the storage medium due to their high energy density combined with a nearly isothermal storage process corresponding to the phase-transition temperature. However, their low thermal conductivity significantly limits the rate of thermal charging and discharging. As such, increasing the thermal performance of PCMs is crucial to the widespread adoption of thermal energy storage technologies.

This dissertation studies the design of an advanced heat exchanger with a thermal energy storage medium, specifically a PCM thermal battery, with engineered thermal properties to enhance charging and discharging rates. To control the thermal properties of the storage materials, PCM composites enhanced with aluminum and graphite foams are characterized and tested under various charging conditions to guide the design of thermal batteries. Experiments are performed to verify the salient features of the foams that control thermal charging rates along with thermal conductivity, density, and latent heat of the composite. Additionally, numerical models are developed and validated to predict the time

to fully charge the battery. This fundamental work is used to guide the optimized design of a thermal battery for integration as the condenser in a vapor compression refrigeration cycle to minimize heat released to the ambient during operation. Component-level performance studies of the thermal battery are completed.

CHAPTER 1. INTRODUCTION

1.1 Background

Heat is a byproduct of all processes that use energy as well as machines that do work due to component inefficiencies and the laws of thermodynamics. Examples include a refrigerator releasing warm air while condensing a refrigerant to provide cooling or a combustion engine releasing heat into the environment during the conversion of chemical to mechanical energy. If this heat remains uncaptured and not put to practical use, it is considered waste heat as it is rejected to the environment. In combination with the development of more efficient technologies to minimize waste heat release, waste heat recovery systems are being developed to further reduce energy consumption and carbon dioxide emissions. Though waste heat has a lower utility than the original source, it is estimated that more than half of the energy produced each year is rejected as waste heat into the environment [1]. Additionally, captured and reused waste heat is an emission free substitute for additional fuels or electricity. By developing methods to better harness this energy, it can either be immediately utilized in other industrial and domestic processes to enhance numerous thermodynamic cycles or stored for later usage.

There are three essential components of waste heat recovery: an accessible source of waste heat, a technology to recover the waste heat, and an end use for the recovered heat. The source of waste heat can be classified based on its temperature range: high (> 650°C), medium (230-650°C), and low (< 230°C). Heat exchanger technologies that recover waste heat include recuperators, regenerators, passive air preheaters, and waste heat boilers. The recovered heat can either be reused within the same process or transferred

to another process [2]. Ways of reusing heat locally include using combustion exhaust gases to preheat combustion air or feed water in industrial boilers. Alternately, the heat can be transferred to another process; for example, a heat exchanger could be used to transfer heat from combustion exhaust gases to hot air needed for a drying oven. Such methods for recovering waste heat can help facilities significantly reduce their fossil fuel consumption, as well as reduce associated operating costs and pollutant emissions [2].

In addition to being used locally or transferred to another thermal process, waste heat can be used to produce electricity [2]. The development of more efficient and cost effective methods to convert heat to power has been an area of much research and technological development [3-6]. This conversion can either occur by using the thermal stream to create mechanical work which, in turn, creates power, or the direct conversion of thermal to electrical energy. As depicted in Figure 1.1 and Figure 1.2, technologies such as combined heat and power and electricity co-generation have been developed to create power from mechanical work. Examples of direct electrical conversion devices include thermoelectric generation and piezoelectric power generation.

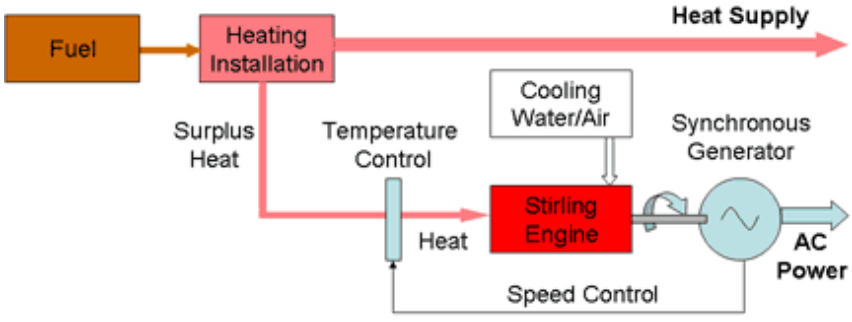

Figure 1.1. Combined heat and power [6].

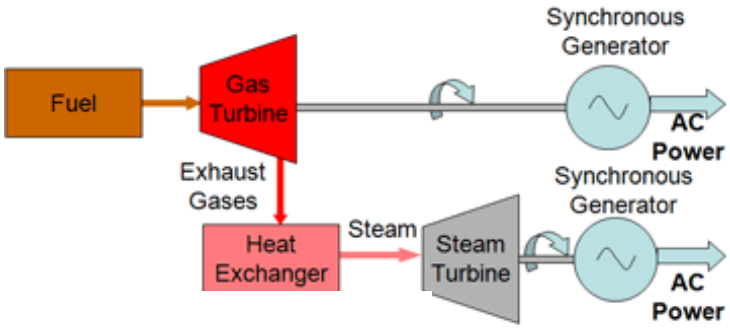

Figure 1.2. Electricity co-generation [6].

Though waste heat recovery systems are frequently implemented in conditions where high and medium temperature (≥ 230°C) streams are present, the feasibility greatly decreases in the low temperature range due to constraints of temperature limits and costs of recovery equipment. However, since up to 60% of unrecovered waste heat in industrial applications is in the low temperature range [2], and an even greater percent in residential applications, the need to develop more effective heat exchangers is imperative to recover and reuse this wasted energy. Examples of waste heat recovery systems for low temperature applications include deep economizers, direct and indirect contact condensation recovery, transport membrane condenser, drain recovery, and heat pumps [2]. Figure 1.3 depicts a direct contact condensation heat recovery unit, and Figure 1.4 shows a drain water heat recovery system. In both cases, the performance of each of the systems is dependent on heat exchanger design, especially for these low temperature applications where efficient heat transfer is imperative for the feasibility of the system.

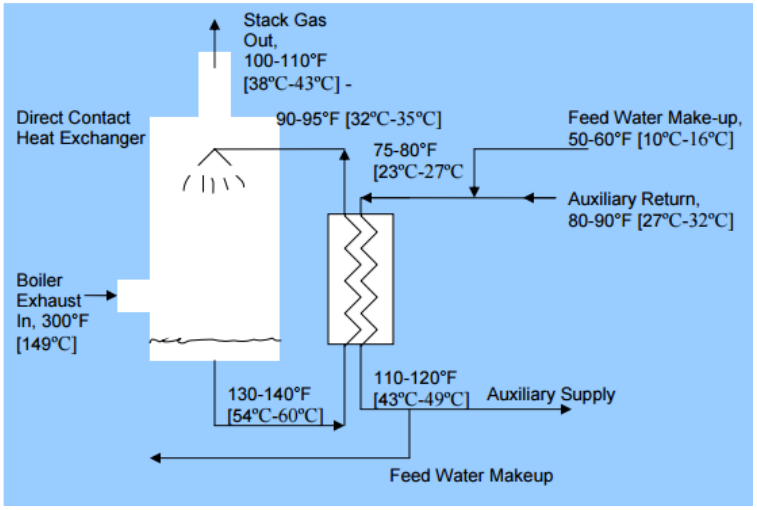

Figure 1.3. Direct contact condensation heat recovery [2].

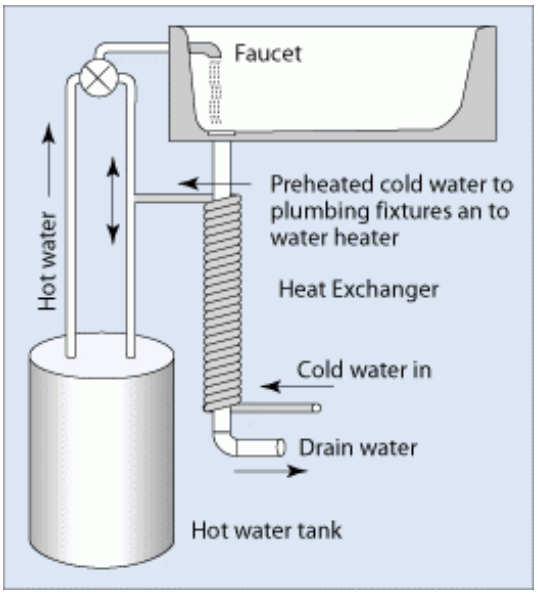

Figure 1.4. Diagram of a drain water heat recovery system [7].

Not only is the technology to recover waste heat important, but having an end use for the energy is also required of an effective waste heat recovery system. In all prior examples the energy is directly used – reused in the same system, transferred to another process, or converted to electricity. However, a crucial link between waste heat production

and utilization remains: thermal energy storage. Without storage, waste heat recovered from thermodynamic systems must be immediately applied to existing energy needs or the heat is lost to the environment. This is especially an issue for low-temperature intermittent waste heat streams or renewable energy such as solar heat. Therefore, the development of technologies to store thermal energy is a crucial hurdle to overcome in the effort to bridge the gap between heat generation and consumption.

1.2 Thermal Energy Storage

Thermal energy storage is a technology that stores thermal energy by heating or cooling a storage medium so that the stored energy can be used at a later time for heating, cooling, or power generation. The development of thermal energy storage is critical to the success of any intermittent energy source in meeting energy demand. Not only does this technology allow for decoupling supply from demand, but it also reduces energy costs, increases flexibility of operation by avoiding partial load operation or operation at other suboptimal times, and shifts demand over time to reduce peak loads [8]. Since the ability to store thermal energy is required for using low-temperature waste heat effectively, enhancement in thermal energy storage systems is imperative.

As Figure 1.5 illustrates, there are three primary methods of storing thermal energy. The storage capacity potential of chemical storage, sensible heat storage (water), and latent heat storage (PCM) is also depicted in Figure 1.6. Of these options, latent heat thermal storage systems (LHTSS) are considered the most promising due to their high energy storage density (5 to 14 times higher than sensible heat systems [9, 10]). Though thermo-chemical materials (TCM) have higher storage capacity than latent heat storage materials,

they are also much more expensive and add significant design complexity. Additionally, they are not applicable for systems that require a storage temperature less than 50°C. The low energy density of sensible heat storage materials requires a large volume to store the necessary energy as well as proper heat exchanger design to discharge thermal energy at a constant temperature. For these reasons, this research is focused on latent heat thermal storage materials.

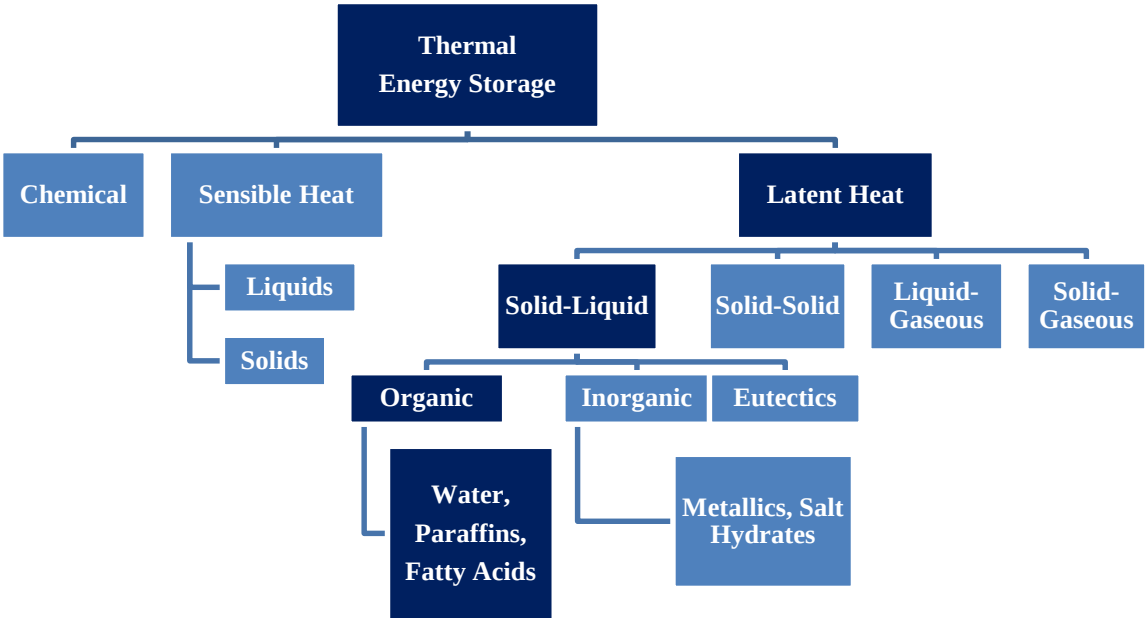

Figure 1.5. Classification of thermal energy storage materials [9, 11-13].

Materials that can store thermal energy as latent heat are called phase change materials, since the thermal energy is stored or released as a material transitions between solid, liquid, or gas phases. This conversion occurs over a nearly isothermal temperature range corresponding to the phase-transition temperature [9, 12, 14]. Although solid-solid phase change materials, which store energy through crystalline structure changes, offer the advantage of less stringent container requirements and limited volume change, they also

have lower latent heat values. Liquid-gas and solid-gas PCMs have higher latent heat values than solid-liquid PCMs; however, they require advanced storage containers that can handle the large volume changes. Solid-liquid PCMs are most widely used in the development of LHTSS due to their comparatively high latent heat values and minimal volume change during phase transition, which reflects in ease of container and system design [9, 15].

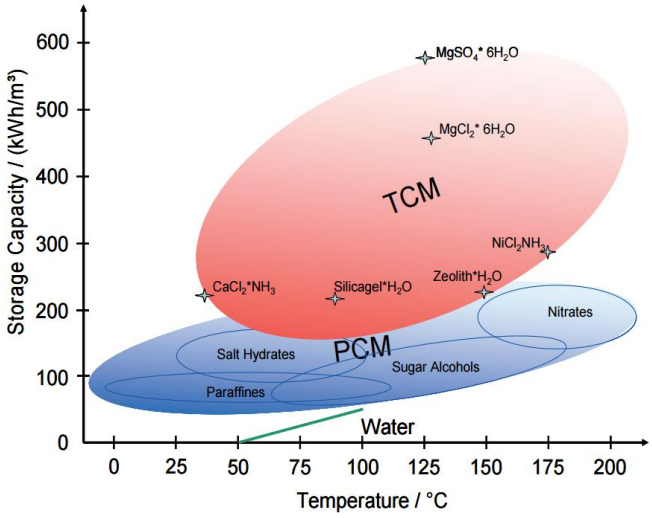

Figure 1.6. Storage capacity vs. temperature for sensible, latent, and thermo-chemical thermal energy storage [13].

The development of a latent heat thermal storage system to capture, store, and reuse waste heat must possess at least the three following basic components [15]:

1. A heat exchanging surface for transferring heat from the heat source to the PCM and from the PCM to the heat sink
2. A proper containment system that houses the PCM

3. A PCM that undergoes a solid-to-liquid phase transition in the required operating temperature range

Recent examples of heat exchanger design research that address the first two concerns include research with PCMs inside direct-contact or shell and tube heat exchangers to understand how the addition of PCM impacts the temperature and rate of heat storage [16, 17], designing and testing an air-PCM heat exchanger for building ventilation coupled to energy storage [18], and developing an air-PCM heat exchanger for heating in greenhouses [19]. There has even been research on the use of phase change heat exchangers to help offset heat on spacecraft to enable better temperature regulation on future missions [20].

Though the performance of thermal energy storage systems depends considerably on its specific application and operational needs, one common barrier of all systems is the capability of the storage material. Critical properties of these storage materials include the temperature at which the PCM melts, amount of thermal energy the PCM can store, the rate at which the PCM can transfer energy in and out of the system, and the cost. Additionally, the supercooling and phase separation should be minimized. After determining the operating temperature, the choice of PCM is based on the latent heat and thermal conductivity to optimize the energy storage and the thermal charging rate. Consideration of chemical properties helps to minimize cost as safety measures are unnecessary to stabilize the materials.

For low temperature applications, the use of organic solid-liquid PCMs to create thermal batteries presents several advantages including their high latent heat, minimal

volume change, non-corrosive nature, minimal supercooling, and ability to melt congruently (without phase separation), which result in safe and reliable thermal energy storage and discharge [21]. Organic solid-liquid PCMs can be further classified as paraffins or non-paraffins. Paraffins exhibit many desirable characteristics as PCMs for low temperature storage applications. This category of hydrocarbon materials, which ranges from hexadecane ($C_{16}H_{34}$) to hexacontane ($C_{60}H_{122}$), is known for being stable, compatible with various materials to prevent corrosion, and non-toxic. In general, both the melting point and latent heat of fusion increase with the number of carbon atoms or chain length [12]. Non-paraffins, which include esters, fatty acids, alcohols, glycols and water, may also be of interest due to the availability of materials with wider melting temperature ranges.

The main disadvantage of all organic phase change materials is their low thermal conductivity, which results in long transients for thermally charging and discharging the material. To increase the rate of heat transfer, solutions such as extended surfaces, microencapsulation of the PCM, and introduction of high conductivity foams or nanoparticles within the PCM to increase the thermal conductivity of the composite have been proposed in literature. The saturation of foams with PCM has been shown to have the greatest enhancement on thermal performance. Extended surfaces are limited by small surface area to volume ratios, microencapsulation is expensive, and nanoparticles introduce instability issues in cyclic conditions.

Enhancing the thermal conductivity of PCM is a promising method to improve the thermal energy storage and discharge rate [22]. However, there is a need to better understand the thermal charging performance of PCM composites as a function of PCM and composite parameters such as thermal conductivity, viscosity, enhancement material

surface area or density, heat capacity, and cost. For example, how does thermal conductivity or surface area of the enhancement material impact the thermal charging rate? Does the density or surface area of the enhancement material or viscosity of the PCM inhibit natural convection in the liquid phase, and, if so, does this discredit the use of enhancement materials?

Additionally, there is a need to understand the impact of enhancement under various operating conditions. In general, such additions to the PCM system aim to minimize the impact on the stable, high latent heat capacity, and low cost PCM, while increasing the rate of thermal transport. However, solutions for thermal management of small electronics with pulsed operation are different than those for waste heat recovery from hot air ducts required to reclaim heat continuously. This suggests comparisons not only based on thermal conductivity and latent heat measurements found in literature, but also the importance of the rate of thermal charging under a specified boundary condition as well as cost of the system. Guided by this discussion, what are the metrics of comparison that should be used in the design of thermal batteries, and how can nondimensionalization be used to simplify the design process?

The optimization of thermal batteries for various applications requires validated numerical models to expedite the design process. However, the current lack of available models to easily predict the charging time for thermal battery composites formed with various enhancement materials hinders the implementation of this technology. What are the different approaches for modeling the transient response of PCM composites, and how do geometric properties of the enhancement material impact the validity of a heterogeneous or homogenized microstructure assumption? Is a full finite-element transient model

required to capture the thermal charging time or is it possible to use homogenization to predict the thermal performance?

Though the introduction of enhancement materials increases the thermal charging, the composite latent heat is decreased. Through experiments and validated models, this optimization between charging time and energy density can better be understood, but how do these enhanced systems perform in applications? Additionally, how can the design of the thermal battery be leveraged to not only optimize for the thermal storage application, but also reduce commercialization concerns such as production lead-time and cost? Pure PCMs have been studied in combination with heat exchangers for use in latent heat thermal storage systems to enhance various energy technologies as either centralized or distributed systems [12]. Centralized applications include district heating or cooling systems, large industrial plants, combined heat and power plants, or renewable power plants, whereas distributed systems are mostly applied in domestic or commercial buildings to capture waste heat for water and space heating or cooling [13]. Other uses, such as PCM integration in air ducts, heat pumps [23], and water heaters, utilize these materials as thermal storage materials for pre-heating or, conversely, in electrical heating, as materials to assist with thermal management through cooling the electrical components. In these applications, not only is the performance of the system a barrier to implementation, but the cost of the system is of concern.

1.3 Dissertation Outline

In this dissertation, the use of enhanced thermal batteries to capture waste heat is investigated to understand how material properties and heat exchanger design impacts the

feasibility and performance of the latent heat storage system. Chapter 2 provides an in-depth review of the thermal charging enhancement methods. This includes an explanation of the advantages and disadvantages of each approach followed by an introduction of the primary enhancement materials studied in Chapters 3 and 4. Chapter 3 reports on the impact of surface area and natural convection of PCM composites on the thermal charging rate when exposed to various boundary conditions. Metrics of comparison are discussed. In addition to latent heat and thermal conductivity, the energy storage performance and energy storage cost are used to compare all composites under various boundary conditions. Additionally, dimensionless parameters are developed, and the applicability is demonstrated by comparing reported experiments to results of various enhancement methods and boundary conditions found in literature.

These experimental results are used to validate computational models in Chapter 4. The impact of surface area on the homogenous material assumption is discussed. Models of various enhanced PCM composites and their experimental validation are explored. In Chapter 5, this experimental and computational work is used to guide the design of a phase change thermal battery installed in a heat exchanger to store heat removed from a refrigerant, effectively acting as a condenser, in a vapor compression refrigeration system. Constraints of cost and size are specifically addressed by optimizing the heat capacity and thermal conductivity of the PCM composite. Methods of reducing production lead-time and cost are discussed. Chapter 6 concludes and proposes future work to further the development of latent heat thermal storage systems for low temperature applications.

The integration of thermal batteries in heat exchangers to capture, store, and reuse waste heat is dependent on engineering stable materials that have suitable properties and

understanding how these properties impact the design of the heat exchanger. By studying the impact of various thermal charging enhancement methods, this work supports the effort of developing organic, non-corrosive, non-toxic, chemically stable, and low cost PCM for use in thermal energy storage systems.

CHAPTER 2. THERMAL CHARGING ENHANCEMENT REVIEW

2.1 Introduction

As discussed in Chapter 1, the primary concern facing the use of organic PCMs as thermal batteries in advanced heat exchangers is the limited rate of thermal charging and discharging because of the low thermal conductivity of the PCM. The advantages of organic PCMs, precisely the stable and inexpensive nature, have led a focus on methods to increase the thermal charging rate of PCMs, while maintaining the characteristic high latent heat. Such methods include the use of extended surfaces, microencapsulation of the PCM, and introduction of high conductivity foams or nanoparticles within the PCM to increase the thermal conductivity of the composite. Generally, extended surfaces are used to reduce the thermal resistance between the heat transfer fluid and the PCM, while microencapsulation, nanoparticles, and foams are used to reduce the thermal resistance of the PCM itself [24].

2.2 Extended Surfaces

Extended surfaces, specifically fins, provide additional surface area to transfer heat in and out of the PCM. Fins have been studied on both the inside and outside of the PCM cavity wall as presented in Figure 2.1.

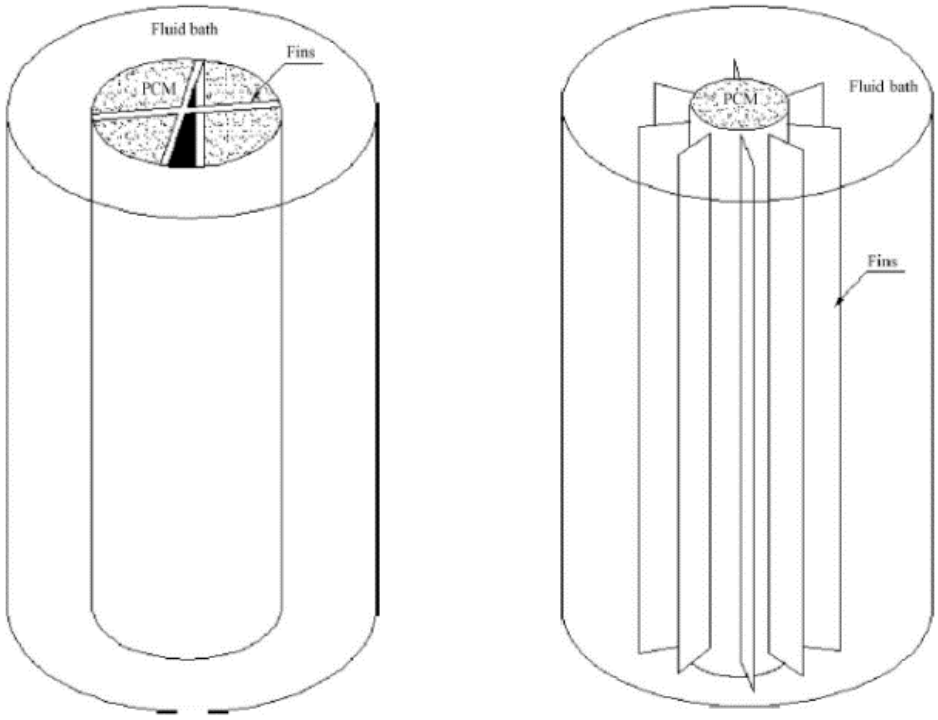

Figure 2.1. LHTSS with internal (left) and external (right) vertical fins [25].

Since the efficiency of the finned system is dependent on the rate of heat transfer, the location of the fins is generally based on the relative heat transfer coefficient. In most of the systems, the PCM side heat transfer coefficient is less than that of the heat transfer fluid side, and, thus, it is a general practice that fins are on PCM side [25]. Examples of fins published in literature, specifically annual and vertical fins, are depicted in Figure 2.2, and horizontal fins are shown in Figure 2.5 (left).

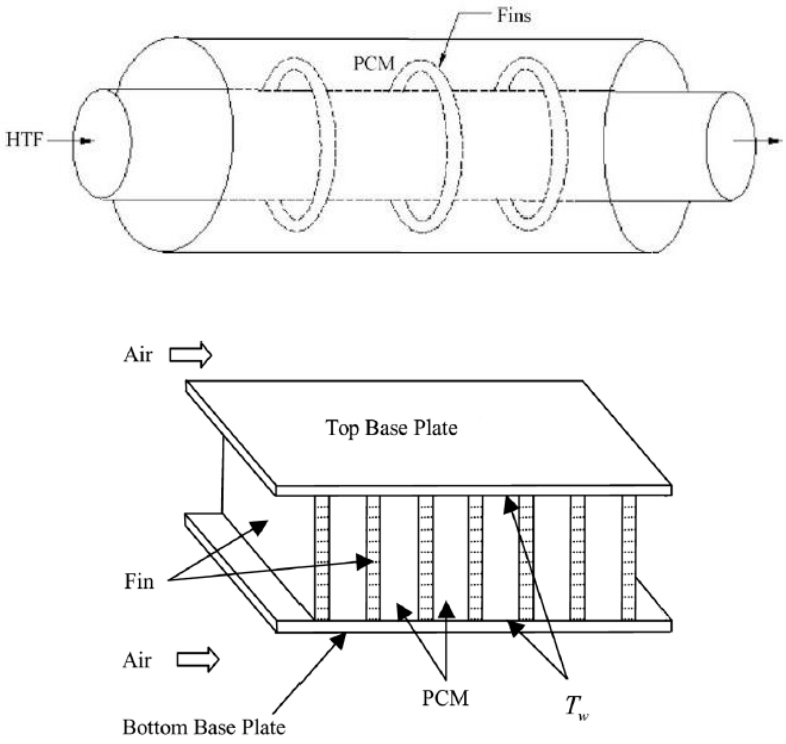

Figure 2.2. LHTSS with annual fins [26] (top); LHTSS with vertical fins [27] (bottom).

The two mechanisms of heat transfer that occur in PCM during melting and solidification are conduction and natural convection. During melting, heat is transferred to the solid PCM by conduction and then by natural convection as the PCM liquefies. This is because the solid region moves away from the heat transfer surface, and the thickness of the liquid region increases near the heat transfer surface as shown experimentally in Figure 2.3. Since the thermal conductivity of liquid PCM is less than that of solid PCM (for example, k_l = 0.17 W/m·K, k_s = 0.35 W/m·K for T_{melt} = 64°C [14]), the heat transfer by conduction reduces as the charging process continues. Conversely, as the PCM solidifies during the discharging process, conduction becomes the dominant form of heat transfer [25].

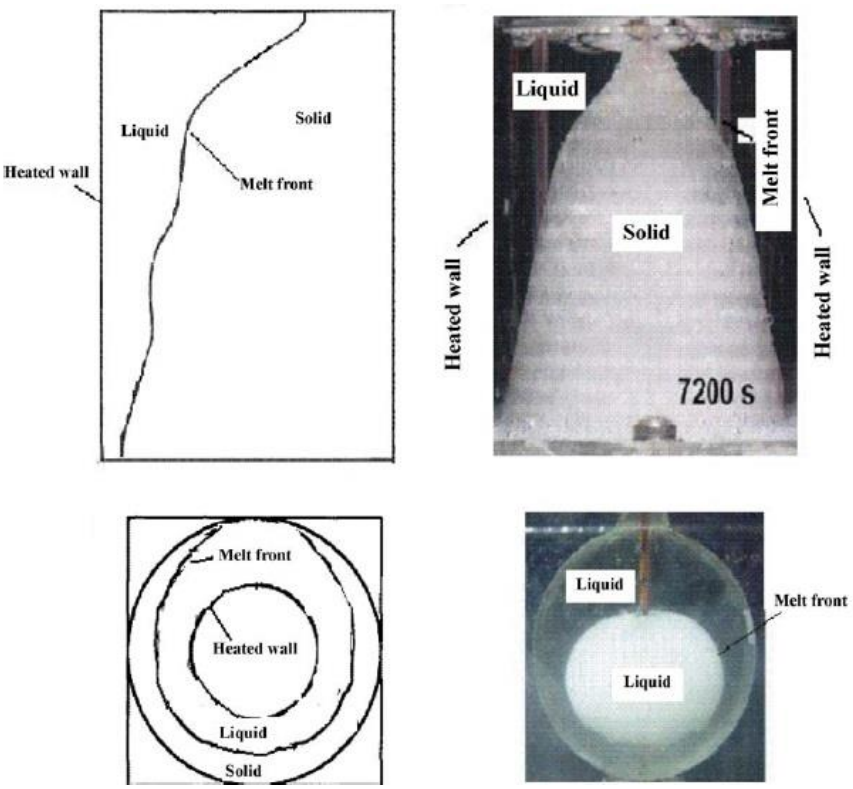

Figure 2.3. Natural convection dominated melting process: rectangular system (top left [28]); cylindrical system (top right [29]); cylindrical annulus (bottom left [30]); spherical system (bottom right [31]) adapted from [25].

As can be seen experimentally in Figure 2.3 and computationally in Figure 2.4, the location of the melt front is not uniform throughout the system because of its dependence on natural convection. Since the melting process in pure PCM is dominated by natural convection, the presence of fins is focused on improving the natural convection (due to the lower thermal conductivity in the molten state) as well as the conduction rate [25].

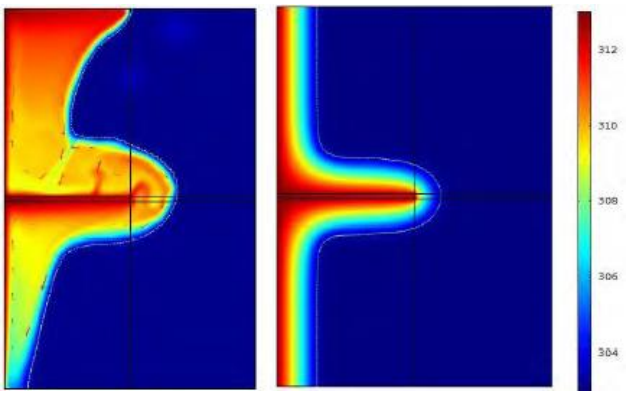

Figure 2.4. Temperature distribution for one fin system accounting for heat conduction and natural convention (left) and accounting for heat conduction only (right) [32].

When considering internal fins to increase the thermal performance of the PCM, the effect on each heat transfer mechanism and the associated impact on thermal response must be understood. For example, published literature has discussed the impact of the insertion of horizontal fins into a vertical cavity filled with paraffin wax as depicted in Figure 2.5. Issues addressed include how the fins interrupt the natural convection movement during melting (Figure 2.5 (right)), whether they inhibit the thermal charging rate or if the additional heat transfer surface compensates for impeding the natural convective motion, and how the additional heat transfer surface assists during solidification when conduction is the main mechanism of heat transfer. Published work has focused on understanding such tradeoffs with finned systems, including how heat transfer mechanisms during the phase change processes depend upon the configuration and orientation of the system and fins [25, 27, 33-38].

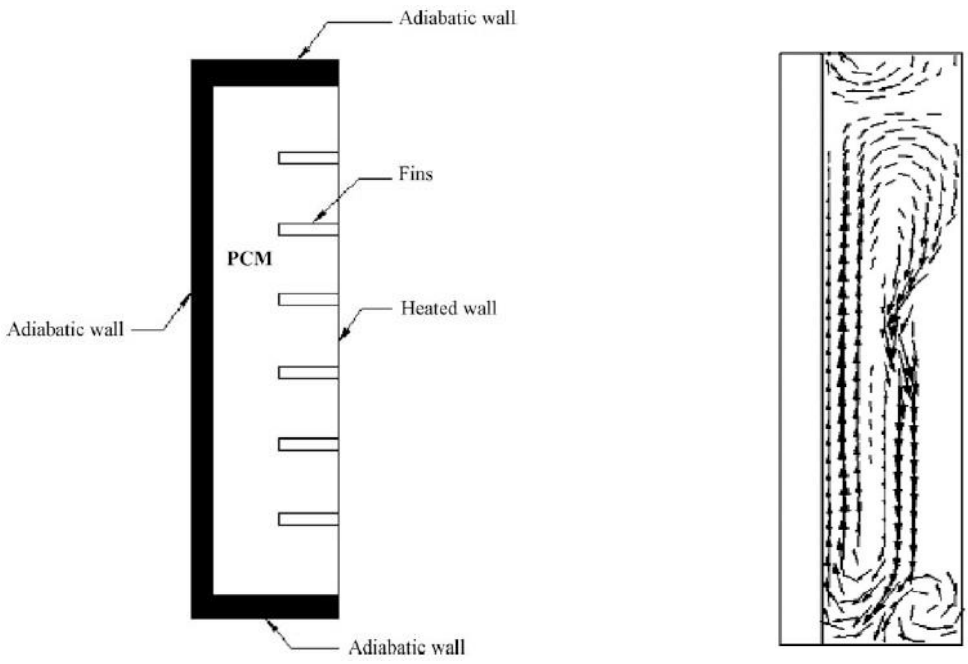

Figure 2.5. LHTSS with vertical fins [36] (left); fluid motion during melting [25, 39] (right).

Computational and experimental research has focused on the design of finned systems to understand the relationship between the orientation of the heated wall(s), finned structures, and the entire unit. Additionally, studies have looked at the relationship between the number, dimension, and orientation of the fins and the thermal charging and discharging rate. Examples of optimizing the number and orientation are shown in Figure 2.6 and Figure 2.7. Other studies compared pinned, longitudinal, and axial fin orientations [40, 41] or parallel and crossed fins [42] (Figure 2.8) on the heat transfer rate within the PCM.

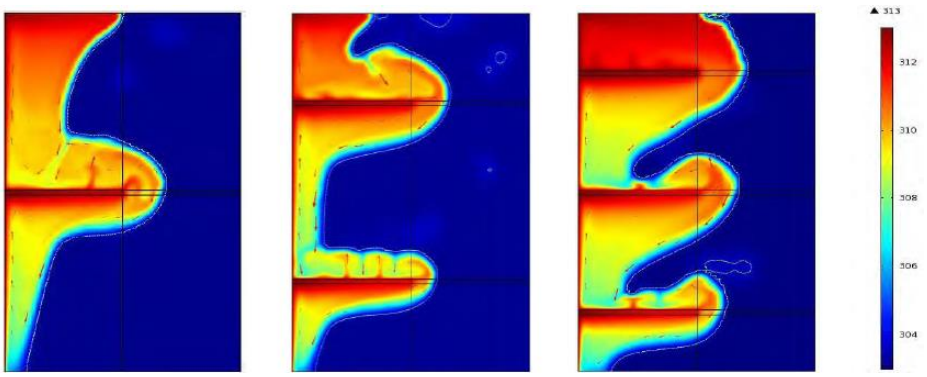

Figure 2.6. Temperature distribution and melting front for finned systems having 1 fin (left), 2 fins (middle), and 3 fins (right) [32].

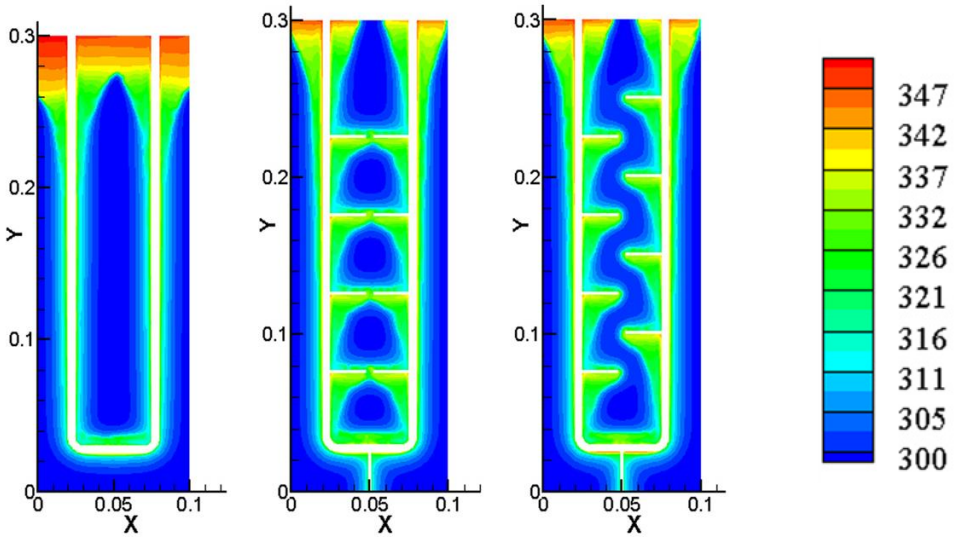

Figure 2.7. Temperature contour for U-tube design (left); U-tube with inline fins (middle); U-tube with staggered fins (right) after 300 seconds, temperature in Kelvin [43].

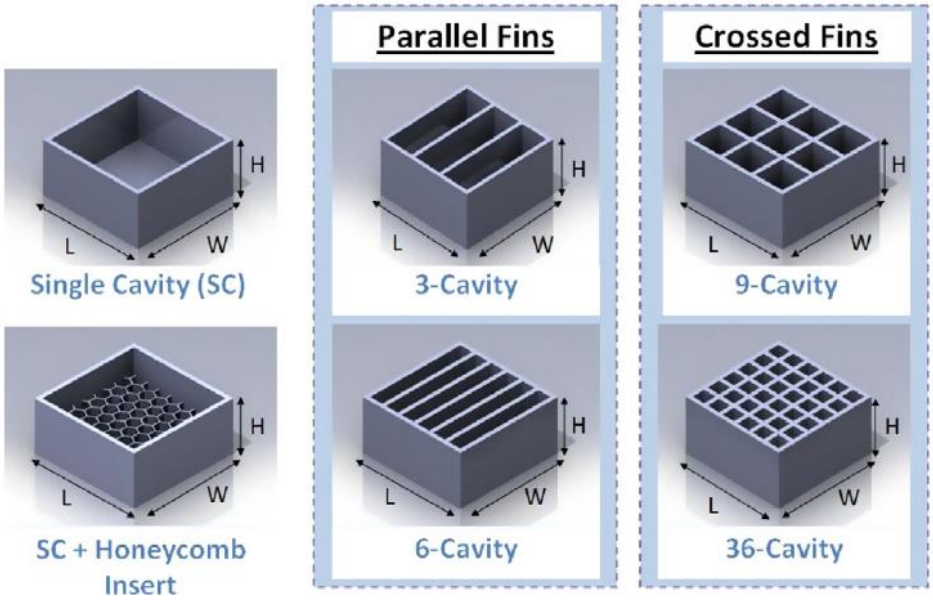

Figure 2.8. Six types of heat sink designs tested [42].

In general, the heat transfer enhancement is reported to increase with an increase in the number of fins, which corresponds to a decrease in the distance between the adjacent fins [26, 27, 36, 38]. However, an increase in the number of internal fins will not linearly contribute to an increase in thermal performance because natural convection is diminished within the smaller fin gap volume [44]. Additionally, as the number of fins increase, the total amount of latent energy stored by the system decreases since each fin replaces available volume of the PCM.

Extended surfaces provide a simple and low cost (due to ease of fabrication) method of enhancing charging performance of thermal batteries [45]. However, this thermal enhancement technique also adds considerable weight to the system as well as additional size constraints for the system to accommodate finned structures. Although fins provide a thermal performance enhancement, one of the main restrictions on performance remains

the low thermal conductivity of the PCM. As Figure 2.7 indicates, although fins increase the thermal charging of the system, the temperature distribution is very disproportionate. Therefore, methods of not only increasing the heat transfer area, but also reducing the maximum distance from the heat transfer surface to the PCM have been explored.

2.3 Microencapsulation

Microencapsulation is one such method of improving the thermal performance of the PCM by minimizing the radial path length from the enhancement material to the PCM. With this method, the PCM becomes a core enveloped within a solid shell structure (Figure 2.9) made of a wide range of materials including natural and synthetic polymers [25]. The shell of microcapsules can protect the core material from interacting with the heat transfer fluid, which enhances the stability of the PCMs, while potentially improving the heat transfer efficiency because of the large surface-to-volume ratio [46].

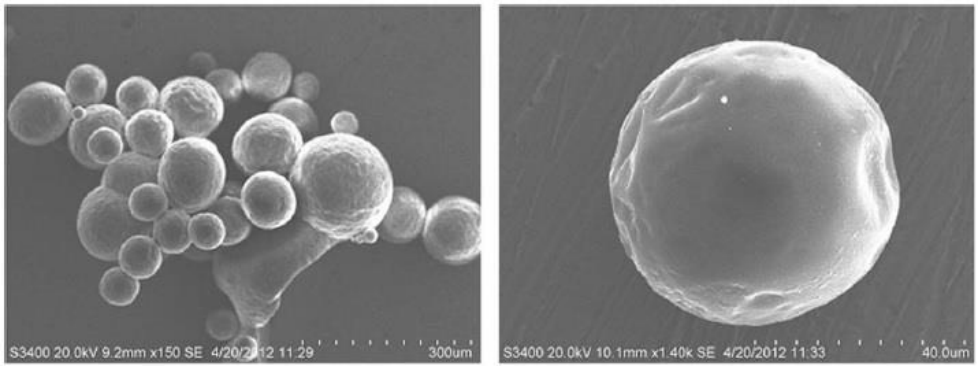

Figure 2.9. SEM photographs of microencapsulated paraffin wax in silicon dioxide [46].

Two main issues exist with microencapsulation: cost and material properties of the shell. Microcapsules can be prepared by several methods such as interfacial polycondensation, spray drying, coacervation, suspension polymerization, and in-situ polymerization [46]. This additional processing adds considerable cost and production time to the system, especially when working with an inexpensive and commercially available material such as paraffin wax. Additionally, some shell materials have been found to be flammable and release poisonous gas while others have poor mechanical properties, which results in cracking of the shell [46]. Various studies have shown that silicon dioxide [46, 47] and polymethylmethacrylate [48, 49] are viable options from a materials perspective, but were reported to reduce the latent heat by up to 49% [46, 48].

Based on these concerns, is it apparent that if a microencapsulated PCM should replace the relatively cheaper non-enhanced PCM, then a substantial thermal charging enhancement must be realized. It has been reported that heat transfer is enhanced by up to 37% as compared to pure PCM during constant heat flux tests [47, 49]. However, when considering the cost and reduction in latent heat, this improvement does not appear to be feasible.

The final option to increase thermal performance by increasing thermal conductivity of the PCM is advantageous, specifically for the development of low cost and organic commercial latent heat thermal storage systems. By increasing the thermal conductivity of the PCM, micro-scale methods are not necessary to minimize the distance from the heat source to the PCM and fins are not required to increase the heat transfer area.

2.4 Thermal Conductivity Enhancement

Thermal conductivity enhancement techniques have focused on saturating high conductivity porous materials with PCM or dispersing high conductivity particles in the PCM [25, 50, 51]. Aluminum, copper, and graphite are the most common materials used in literature to produce particles and porous foams that are subsequently incorporated in PCM to form thermal batteries with high energy and power density [52-60]. The intention is to increase the thermal charging and discharging without the addition of considerable size, weight, or cost as well as to more evenly distribute heat throughout the system. High conductivity nanoparticle and porous foams will be reviewed. For further information, Zhang *et al.* [61] recently published an extensive review on composite phase change materials.

2.4.1 High conductivity nanoparticles

Nanoparticles of aluminum, copper, and graphite mixed with PCM have been reported in literature [52-54, 62, 63]. When the performance of graphite nanoparticles is compared to that of denser materials such as aluminum or copper at similar concentrations [52-59], graphite is found to be the optimum thermal conductivity enhancement material. This is due to its high thermal conductivity paired with low density and compatibility with organic PCM, which allows for the largest conductivity enhancement and lowest material concentration [56, 64, 65].

Three geometries of graphite nanoparticles imbedded within PCM are found in literature: nanotubes, nanofibers, and nanoplatelets, though graphite nanoplatelets appear to be the most effective carbon filler [64-72]. Graphite nanoplatelets exhibit the highest

increase in thermal conductivity as a function of weight percent due to the increased surface area, which improves the conductive network within the composite PCM. However, specified alignment of carbon nanoplatelets in the PCM cannot be guaranteed. This limits the thermal conductivity enhancement, particularly in the liquid phase.

As Jegadheeswaran and Pohekar summarize [25], the dispersion of nanoparticles within PCM (via shear mixing or sonication) is a simpler thermal conductivity enhancement method than PCM integration into porous material since saturation is not dependent on an open-cell pore structure. Additionally, graphite nanoplatelet/PCM composites are inexpensive and can be prepared with limited lab experience and equipment. However, the main issue with the use of graphite nanoplatelets to increase the thermal conductivity is the stability of the nanoparticles in the liquid PCM. The stability of these suspensions during melting and solidification of the PCM is a concern as settling or sedimentation of the fillers will change the effective thermal conductivity.

In an attempt to improve the stability, researchers have utilized dispersants, specifically sodium dodecylbenzenesulfonate, which has shown some success in paraffin wax systems with aluminum and copper nanoparticles [57, 62] as well as octadecylphosphonic acid to stabilize graphite nanoplatelets in paraffin wax [73, 74]. However, the use of such dispersants reduces the latent heat of the composite. Additionally, even though a maximum thermal conductivity enhancement of 2.5 W/m·K has been reported [65], contact resistance between the nanoparticles impacts the thermal charging response of the composite. As shown in Figure 2.10, graphite nanoparticles significantly underperform graphite foams at the same wt% due to the increased resistance between the

nanoparticles. This suggests that nanoparticles are severely limited in their ability to increase the thermal charging response of PCM based thermal batteries.

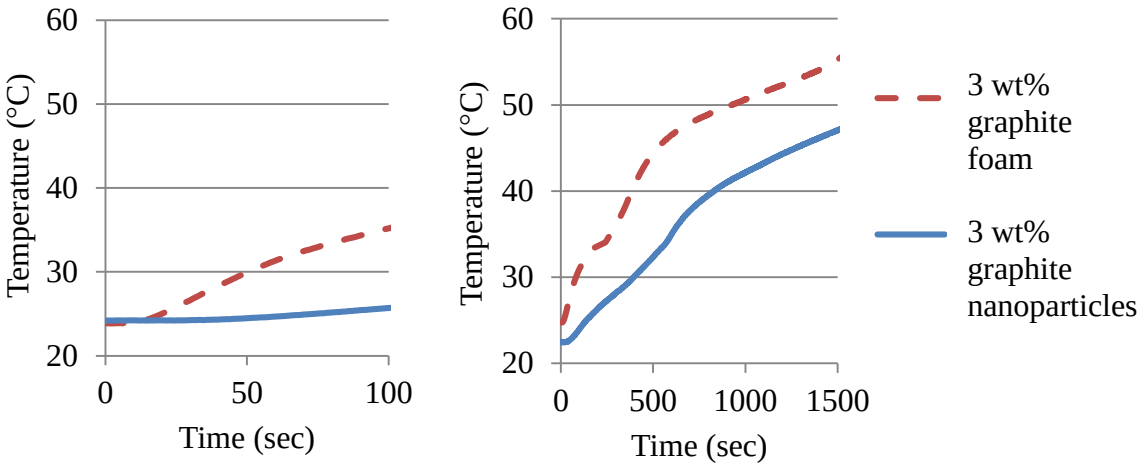

Figure 2.10. Bottom temperature of thermal charging experiments under 1.55 W/cm^2 (left) and 0.39 W/cm^2 (right) [73].

2.4.2 High conductivity metal foams

Open-cell metal foams are commonly made by injecting a gas into molten metal, such as copper or aluminum, to form bubbles that produce interconnected pores of the foam. PCM can then be absorbed into the foam to form a high conductivity composite. Foams are characterized by two primary parameters: relative density and pore size. Relative density is the density of the foam divided by the density of the solid parent material of the struts. This parameter controls the ligament cross-section shape and size as seen in Figure 2.11. As the relative density increases, the thermal conductivity of the composite increases, but the latent heat decreases.

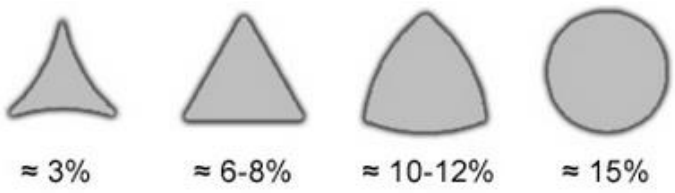

Figure 2.11. Ligament cross sections [75].

The second identification parameter for porous foams is pore density. Every gas bubble in the metal forms a cell consists of about 14 reticulated windows, as depicted in Figure 2.12. Each window is referred to as a pore. In any given bubble, the pores actually are of two or three different characteristic sizes and shapes, but for material designation purposes, they are simplified to an average size and circular shape [75]. The number of these pores in one inch of the foam then designates the foam pore density and is quantified by pores per inch (PPI). Examples of typical pores per inch include 5, 10, 20, and 40 PPI.

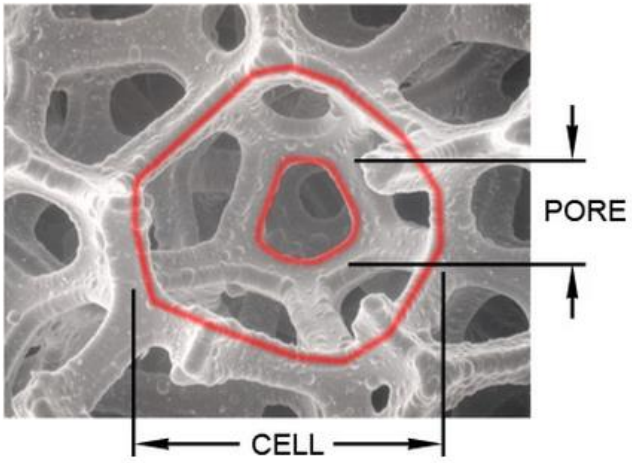

Figure 2.12. Structure of foams [75].

Both the pore density and the relative density have an influence on the specific surface area. As the pore density increases, the diameter of each pore decreases and the overall surface area of the foam increases. Similarly, as the relative density increases, the redistribution of aluminum within the foam ligaments results in an increase in the surface area. A high specific surface area allows for increased contact with the PCM. The specific surface area as a function of pore density and relative density can be seen in Figure 2.13.

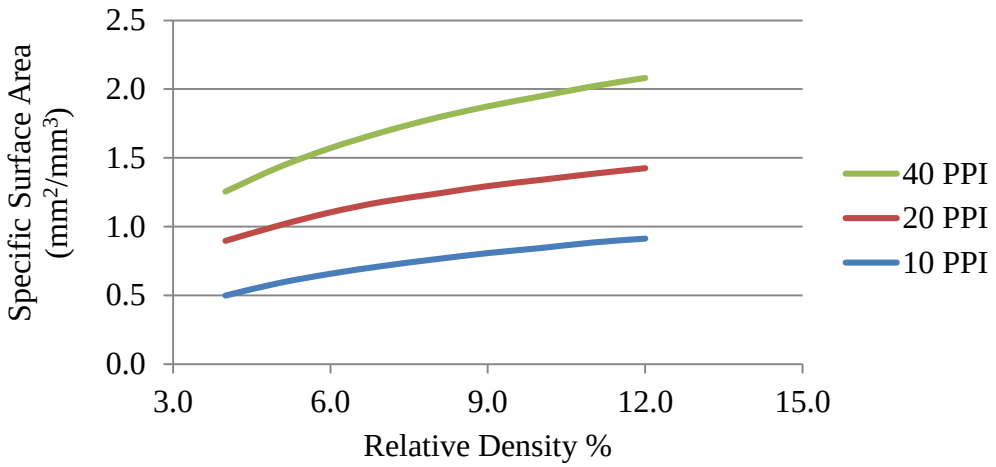

Figure 2.13. Specific surface area of Duocel® metal foams [75].

Metal foams are attractive thermal enhancement materials due to their stiffness/strength properties, high thermal conductivity, high surface area densities, and continuous interconnected pore structure [25, 76]. Saturation of metal foams with liquid PCM has been reported with and without vacuum assistance. Micro-foams with a pore diameter less than <1 mm benefit from the use of a vacuum during saturation, whereas foams with a pore size ≥ 1 mm do not require a vacuum for full saturation [61].

Research with PCMs integrated in open-cell metal foams describes the impact on thermal charging by measuring the decrease in melting time of the PCM [77, 78] or the decrease in temperature at the junction of the heat sink and the latent heat thermal storage system [79, 80]. Copper and aluminum foams have been computationally and experimentally studied [55, 58, 59, 79, 81]. Copper foams have been found to decrease the melting time of the PCM up to a factor of 10 and reduce the junction temperature by more than 50% [58, 59]. Similar experiments have been conducted with aluminum foams [77, 79], though the associated impact on thermal charging is less than copper foams due to the 50% decrease in bulk material thermal conductivity. However, this performance is countered by additional cost and weight of the composite.

2.4.3 High conductivity graphite matrix

Graphite is known for its high thermal conductivity and low density, which makes it a good candidate for improving thermal conductivity of organic PCMs. Additionally, this material has been suggested to decrease the volume change of PCM during the solid to liquid phase change and offers no corrosion problems [82]. For some applications, graphite is of specific interest because of its anisotropic nature, which allows the heat transfer to be focused in the direction of interest.

PCM can be enhanced with a matrix of graphite that is produced from various forms including: graphite powder, micron graphite flake, mesophase pitch, expanded natural graphite (EG), and compressed expanded natural graphite (CENG). Studies report on different methods of producing the foams as well as the impact of the mass of graphite present in the sample volume, which is measured by bulk density (kg/m^3), on the thermal

conductivity and latent heat of the composite. Graphite powder and micron graphite flake are not commonly used because of their limited impact on thermal conductivity. For example, a graphite matrix of 417 kg/m^3 produced from pressing graphite powder and saturated with paraffin wax exhibits a thermal conductivity of 1.1 W/m·K [83], whereas the thermal conductivity of paraffin has been reported to increase by more than an order of magnitude (from 0.2 W/m·K to 50-70 W/m·K) with the addition of a CENG foam [21, 84]. The most common and effective methods of mesophase pitch-based graphite foams, EG, and CENG will be further discussed.

2.4.3.1 Mesophase pitch-based carbon foam

Mesophase pitch-based graphite foams are produced through a controlled process of heating, pressurizing, and further heating of a mesophase pitch precursor that creates a highly aligned porous graphite structure. As shown in Figure 2.14, the foam typically exhibits uniformly shaped bubbles with a normal distribution. The average pore size, orientation, and distribution is determined primarily by the pitch viscosity and processing pressure during foaming. Additionally, the mesophase foam will have a preferred orientation of crystals in the z-direction with accompanying anisotropic properties compared to those in the x-y plane, even though the visual physical structure may not be anisotropic [85]. Because of the open and interconnected pore structure, this foam can be saturated with PCM to create a high conductivity composite. Warzoha *et al.* [86] studied saturation with and without vacuum assistance. Submersion of the foam resulted in a saturation ratio of 75%, whereas, within a vacuum, the saturation ratio increased to almost 100%.

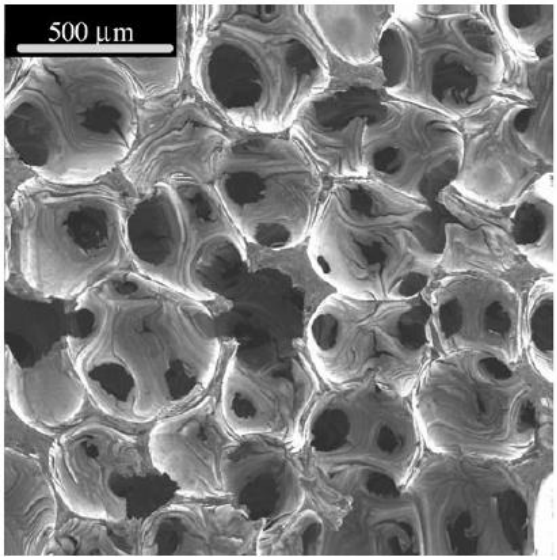

Figure 2.14. SEM images of mesophase pitch-based foams [85].

Studies with mesophase pitch-based graphite foams include characterization of thermophysical properties as well as the impact on thermal charging of PCMs. For example, thermal conductivity at a density of 450 kg/m^3 has been reported to be 149 W/m·K in the direction of aligned of crystals, while 42 W/m·K transverse to the alignment [85]. Mesalhy *et al.* [87] conducted numerical and experimental studies to predict the thermal characteristics of mesophase pitch-based graphite foams saturated with PCM. Zhong *et al.* [60] used mesophase pitch-based graphite foams with different thermal properties and pore sizes to increase the thermal conductivity of paraffin wax for latent heat thermal storage systems. It was found that the thermal conductivity of the graphite/paraffin foam can be enhanced up to 180 times that of pure paraffin wax.

Although mesophase pitch-based graphite foams increase the thermal charging performance of PCMs, there are issues that inhibit their suitability to low temperature applications. In addition to the high pressure (1000 psi), high temperature (1000 °C), and

oxygen-free environment [85] required of formation, the introduction of mesophase pitch-based graphite foams greatly impacts the composite latent heat due to their high density. Reported data suggests that the density range is 200 – 600 kg/m^3 [85, 88], and Zhong *et al.* [60] reported that foams between 200 kg/m^3 and 570 kg/m^3 decrease the latent heat 24% to 55%, respectively. Similar results were reported by Song *et al.* [89]. Though mesophase pitch-based graphite foams are a promising solution to thermal storage and thermal management in high temperature or high heat flux applications where the high thermal conductivity is more important than the composite energy density [60, 87, 89], other types graphite foams may be more promising for low temperature applications.

2.4.3.2 Expanded natural graphite

Expanded natural graphite is produced from natural graphite flake that has been chemically treated and then thermally exfoliated. By introducing an acid, such as sulfuric or nitric acid, to the graphite flake, each of the layers of the graphite flake are chemically detached (Figure 2.15). Since each flake is held together by weak van der Waals bonds, the addition of heat (microwave or furnace) splits it apart into a worm-like accordion structure (Figure 2.16) [51, 90, 91]. The EG can then be mixed with PCM to form a composite thermal storage system.

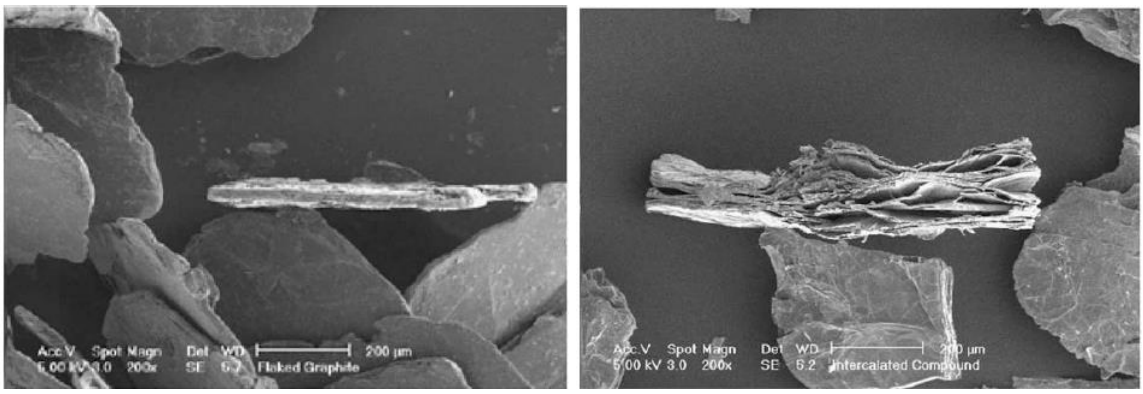

Figure 2.15. SEM photographs of flake graphite (left) and graphite intercalated compound after acid washing and drying (right), both with 200x magnification [51].

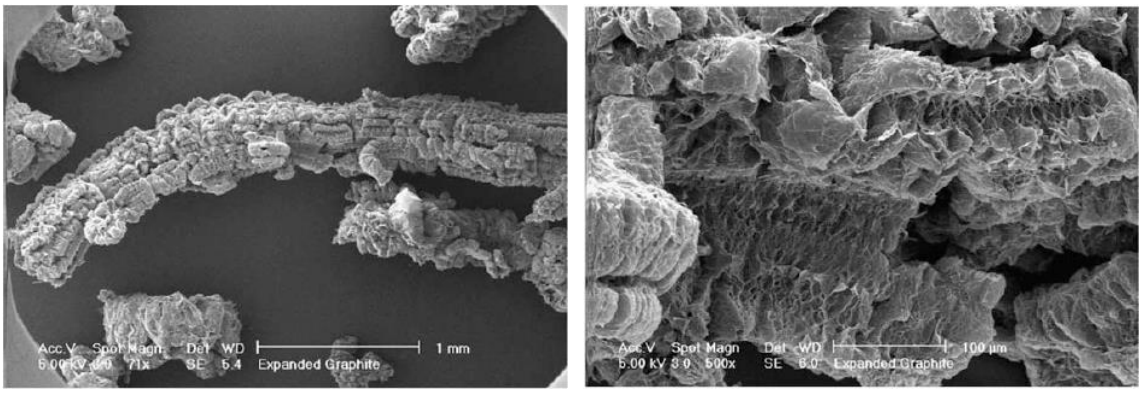

Figure 2.16. SEM pictures of EG at 71x magnification (left) and 500x magnification (right) [51].

The thermal conductivity enhancement and impact on latent heat have been discussed specifically by Sari and Karaipekli [91], Yin *et al.* [92], Xia *et al.* [93], and Zhang *et al.* [93]. For example, a 10 wt% EG sample increased the thermal conductivity by 100%, decreased the latent heat by 8%, and decreased the melting time by 32% [91]. Though expanded graphite offers improvement in thermal conductivity of the PCM, this system does not take advantage of the anisotropic nature of graphite. By compressing the expanded natural graphite system, a significant increase in thermal conductivity can be realized.

2.4.3.3 Compressed expanded natural graphite

Compressed expanded natural graphite is produced by compressing the expanded graphite into a compact porous foam. In doing so, the directional thermal conductivity of graphite can be used to maximize the performance of the system. PCM can then be absorbed into the foam through capillary forces between the liquid PCM and the CENG to form a highly conductive composite [51]. Saturation with and without a vacuum has been reported, but the use of a vacuum reduces the time required for full saturation [61]. One of the benefits of using this material is that the EG can be compacted into various shapes to form stable graphite matrices without using any binding materials due to the mechanical interlocking of the worms [51].

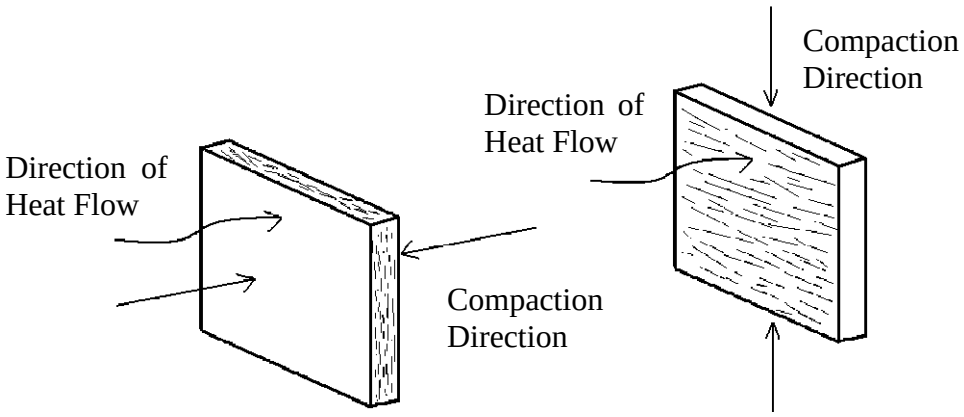

Figure 2.17. Schematic of compaction methods with respect to direction of heat flow during thermal conductivity tests [51].

As shown in Figure 2.17, thermal conductivity measurements can either be measured in the direction of compaction or perpendicular to the direction of compaction. The thermal conductivity of composites formed with CENG bulk densities greater than 50 kg/m^3 are found to be impacted by the anisotropy of the compressed graphite as discussed

by Mills *et al.* [51], Py *et al.* [21], Haillot *et al.* [84, 94] and shown in Figure 2.18. Thermal conductivity of the sample in the compression direction is less than in the direction perpendicular to the compression direction. For example, the thermal conductivity of CENG foam with a bulk density of 350 kg/m^3 has been reported to be 70 W/m·K in the direction perpendicular to compaction, while it is 10 W/m·K in the compression direction [21]. Typical CENG foams range between 50 kg/m^3 and 350 kg/m^3, the lower value a limit of mechanical strength of the matrix and the upper value limited by the permeability necessary to absorb PCM [21].

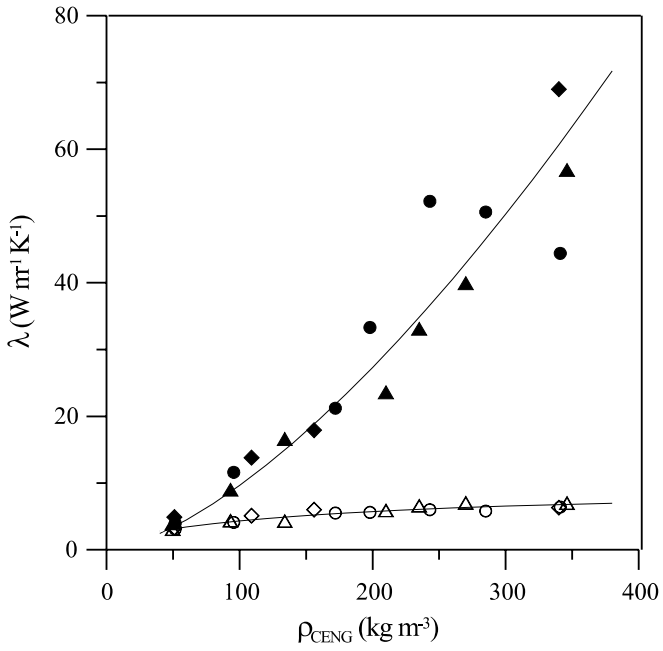

Figure 2.18. CENG thermal conductivities versus bulk graphite matrix density; perpendicular to compression (solid), parallel to compression (open) [21].

CENG foam is primarily considered a method of increasing thermal conductivity for PCM due to its large thermal conductivity, high surface area to volume ratio, and small density. It also can be formed into various shapes and easily molded to the heat transfer

surface, which allows contact between the composite and exchanger wall without the use of expensive thermal epoxies. However, disadvantages to using CENG for thermal conductivity enhancement are introduced due to the production technique. As the EG is compacted, some of the pores will be closed during compression forming voids of trapped air that are impenetrable by PCM. By studying the amount of PCM absorbed by the sample compared to the theoretical maximum, Py *et al.* [21] found that the higher the bulk density, the greater the volume of closed pores. Additionally, the time to saturate a matrix of graphite with PCM takes longer than an open cellular material [51]. Furthermore, graphite is not as rigid as metal and may not be adequately robust for certain applications.

2.5 Research Outline

The goal of this research is to improve the performance of space conditioning systems through innovative heat exchanger design with thermal energy storage. The integration of a thermal battery in a condenser offers a method of decoupling heat removal from a condensing refrigerant and heat release into the ambient space. The design of such a condenser requires knowledge of thermal charging behavior for PCM composites as well as adhering to constraints of size, mass, heat capacity, thermal charging rate, refrigerant charge, and cost required of the unit. This effort necessitates PCM material characterization, thermal charging experiments with numerical model validation, and system-level performance optimization and assessments.

Due to the low temperature application (<60°C), organic PCMs are of interest because of their stable, non-corrosive, and non-toxic nature. To increase the thermal charging response of organic PCMs, increasing the composite thermal conductivity by

saturating metal or graphite foam with PCM has been shown to have the greatest impact. Extended surfaces are limited by small surface area to volume ratios, microencapsulation is expensive, and nanoparticles introduce instability issues in cyclic conditions.

Research with PCMs integrated in metal foams typically describes the impact on thermal charging by measuring the decrease in melting time of the PCM [58, 78] or the decrease in temperature at the junction of the heat sink and the latent heat thermal storage system [79, 80]. Composites of graphite foams saturated with PCM are generally compared solely through thermal conductivity measurements [21, 51]. In general, both additions to the PCM system aim to minimize the impact on the high latent heat capacity and low cost PCM, while increasing the rate of thermal transport. However, various methods of thermal charging enhancement combined with a lack of standard testing procedures suggests a need for a systematic comparative study. Additionally, the quantification of thermal charging improvement based on thermal conductivity or melting time common of present literature disregards another imperative parameter of thermal batteries: thermal energy storage density.

This work will approach the optimized design of thermal batteries based on both thermal response and energy density through the following objectives:

1) Compare the thermal charging enhancement of organic solid-liquid PCM with aluminum foam and graphite foam. Properties of thermal enhancement materials are summarized in Table 2.1. Aluminum foam was chosen over copper foam based on density, and CENG foam was used due to the ability to achieve lower densities than mesophase pitch-based graphite foam, which results in less impact on latent

heat. Thermal charging experiments for aluminum and graphite foam PCM composites will be conducted under different boundary conditions. These experiments and analysis will inform the choice of enhancement material for large-scale battery development.

Table 2.1. Properties of various thermal enhancement materials.

	Limit	Bulk Density (kg/m^3)	Relative Density %	Bulk Apparent Conductivity (W/m·K)	% Decrease Latent Heat
Aluminum foam [75]	Lower	81	3	1.7	3%
	Upper	351	13	7.2	13%
Copper foam [75]	Lower	270	3	4.0	3%
	Upper	1170	13	17.2	13%
Mesophase pitch-based graphite foam [60, 85]	Lower	200	9	50.0	24%
	Upper	570	26	150.0	55%
CENG graphite foam [22, 60]	Lower	50	2	5.0	4%
	Upper	350	16	70.0	35%

2) Develop validated numerical models to simulate the thermal charging of each system.
3) Use the validated model to optimize the thermal storage system, specifically minimize volume, mass, refrigerant charge, and cost, by studying the impact of PCM thermophysical properties on these design objectives. In this work, a phase change thermal battery is designed to store 170W of condenser waste heat over a 2-hour period, or 1224 kJ of thermal energy. Copper refrigerant tubing and R134a are to be used in the refrigeration cycle.

4) Component-level experimental testing in a controlled loop for further model validation and system-level battery production.

Chapter 3 will report on a comparative experimental study of aluminum and graphite foam. Following thermal conductivity, latent heat, melting temperature, and viscosity characterization of each PCM and PCM composite, thermal charging experiments are conducted for various aluminum and graphite foams under 1.55 W/cm^2 and 0.39 W/cm^2. Experiments are also conducted with the composite exposed to 60°C to study the thermal charging response under a constant temperature condition near the PCM melting temperature.

The impact of surface area, natural convection, and boundary condition on the thermal charging rate is experimentally studied by varying aluminum foam pore size, graphite bulk density, PCM viscosity, and applied heat flux or temperature. By using a standard experimental configuration, thermal charging enhancement of the foams is compared based on four metrics: composite latent heat, thermal conductivity, time to end of melt, and junction temperature between the heater and the sample. To relate all metrics, two dimensionless parameters are defined to compare diffusive transport and energy storage to junction temperature. Finally, the energy storage cost is calculated for each composite.

Chapter 4 will report on two numerical models developed to predict charging behavior without relying on experiments. Modeling latent heat thermal storage materials introduces a non-linearity into the heat transfer problem since thermal energy is stored or released at a nearly constant temperature during phase change. Due to the complexity of

the phase change problem, analytical solutions are limited to one-dimensional analysis with constant properties. To study 2D and 3D phase change phenomena and include variation in the thermal properties as a function of temperature, numerical models are employed. The impact of surface area on the homogenous material assumption is explored. Aluminum foam models and graphite foam models are developed and validated for use in thermal battery design.

An effective properties model is found to accurately represent the graphite foam; however, due to the large pore size of metal foams and the nonlinear phase change process, this approximation is not valid for the open-cell foam system. This work discusses the development of a geometrically accurate open-cell foam model and demonstrates its applicability in phase change modeling. Using both 3D phase change modeling and experimental data for comparison, an energy storage model is developed and validated for metal foam composites. In addition to significantly reducing the computational complexity of modeling open-cell foam systems, this model can be adapted for multiple phase changes or non-isothermal phase change because it is based on the amount of energy absorbed over time instead of the discrete nature of the temperature distribution within the system.

Chapter 5 will discuss the large-scale battery development. This includes an optimization study, component-level experimental testing and model validation, and system-level battery production and integration in a vapor compression system. Methods of reducing production time and cost are discussed and demonstrated. Chapter 6 suggests further research guided by the work presented in Chapter 3, 4, and 5. This will also discuss current ongoing work regarding the design of a higher capacity thermal battery.

CHAPTER 3. THERMAL CHARGING EXPERIMENTS

As discussed in Chapter 2, the design of effective thermal batteries with phase change materials (PCM) relies on the addition of materials with high thermal conductivity and specific surface area to increase the rate of thermal charging and discharging. This chapter discusses a comparative experimental study between two such enhancement materials, namely aluminum and compressed expanded natural graphite foams, saturated with phase change material. A common test platform is used, which makes comparison of experimental data more feasible, unlike what is often found in the literature between different PCM thermal storage systems. Questions this chapter seeks to address include the impact of the pore size on the thermal charging rate for metal foams, the impact of carbon density on the thermal charging rate of graphite foams, and the performance of all systems under high and low heat fluxes and constant temperature boundary conditions. Additional investigations include the impact of PCM viscosity and thermal interface material. By providing this rich set of data under controlled conditions, a better understanding of the enhancement of metal and graphite foams on PCM thermal charging will be revealed, specifically through various performance metrics presented.

3.1 Thermal Charging Literature Review

Recall from 2.4.2, open-cell metal foams are classified based on pore density and relative density. Pore density (measured as pores per inch, PPI) describes the diameter of each pore. Typical values range from 10 PPI to 40 PPI. As the number of pores per unit length increases, the diameter of each pore decreases and the overall surface area of the foam increases. Relative density, defined as the density of the foam divided by the density

of the solid parent material, identifies the amount of metal compared to the amount of PCM. Relative densities of most metallic foams vary from 3% to 13%. Research with metal foams saturated with PCM typically describes the impact of these two parameters by measuring the decrease in melting time of the PCM [58, 78] or the decrease in temperature at the junction of the heat sink and the latent heat thermal storage system [79, 80].

As a phase change material is moving between the solid and liquid phase, the two primary modes of heat transfer are conduction and natural convection. The introduction of metal foam impedes natural convection in the liquid phase depending on orientation of the heat source, but the conductive foam network greatly improves the thermal charging as compared to relying on natural convection and diffusion within a pure PCM system. However, for foams with large pores, an additional complexity of natural convection within the pore must be considered in the design of the thermal battery. There is an inherent tradeoff between natural convection and conduction as a function of the relative density and pore density of the foam. As the surface area increases to promote conduction within the system, the size of the pore decreases, therefore, limiting the natural convection within the pore.

Some of the previous work discussing the impact of pore density and relative density on natural convection and conduction is shown in Figure 3.1 and Table 3.1. Although all studies presented in Table 3.1 agree that the addition of metallic foams improves the rate of thermal charging of PCM, various heat flux magnitudes, orientations, sample geometries, and PCMs have been used. This variation in test conditions makes it challenging to draw conclusions regarding the impact of pore density and relative density as well as the impact of natural convection within the system on the thermal charging rates.

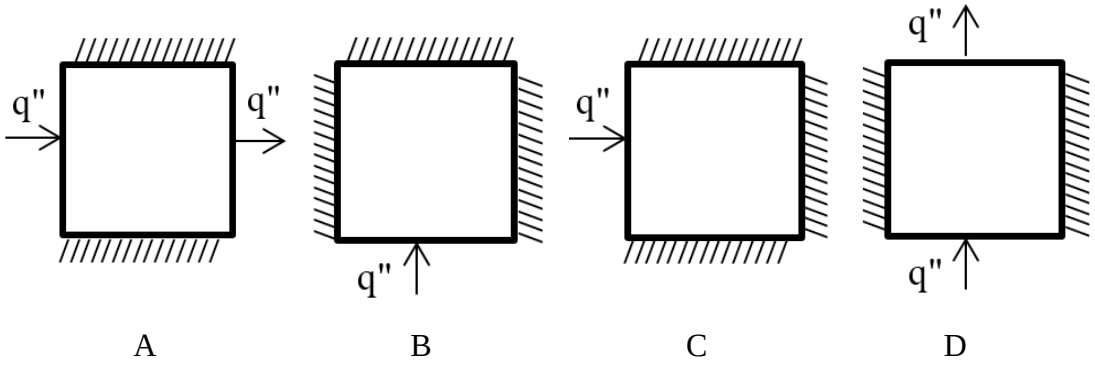

Figure 3.1. Thermal charging boundary conditions described in Table 3.1.

Table 3.1. Sample of thermal charging experiments reported in literature.

	Study	Condition	Diagram
A	**Lafdi *et al.* [79, 95]**	0.3 W/cm^2 Pore Density: 10, 20, 40 PPI Relative Density: 3.4%, 6.6%, 11.6%	5.1 x 10.2 x 10.2 cm
B	**Zhao *et al.* [58]** **Tian, Zhao [81]**	0.2 W/cm^2 Pore Density: 10, 30 PPI Relative Density: 5.0%, 15.0%	20.0 x 12.0 x 2.5 cm
C	**Chen *et al.* [96]**	0.6 W/cm^2 Pore Density: 10 PPI Relative Density: 8.6%	6.0 x 6.0 x 2.2 cm
D	**Chintakrinda *et al.* [64]**	1.9 W/cm^2, 5.8 W/cm^2, 11.6 W/cm^2 Pore Density: 40 PPI Relative Density: 9%	5.1 x 5.1 x 5.1 cm

Lafdi *et al.* [79, 95], Zhao *et al.* [58], and Tian and Zhao [81] studied metal foam/PCM composites exposed to constant heat flux conditions. The study conducted by Lafdi *et al.* [79, 95] used a PCM with a melting temperature between 26°C-29°C and a viscosity at 50°C of 0.003 Pa·s. Each aluminum foam was attached to a 0.3 W/cm^2 heated surface with thermal grease. In the work by Zhao *et al.* [58], and Tian and Zhao [81], the PCM melting temperature ranged between 48°C and 62°C, and the copper foams were

sintered to the 0.2 W/cm^2 heated surface. Viscosity was not reported. These studies discuss the impact of pore density and relative density on the junction temperature and melting time or time to steady state.

It was found that metal foams with a higher relative density decreased the junction temperature due to greater conduction through the composite. Regarding the impact of pore density on junction temperature, Zhao *et al.* [58] and Tian and Zhao [81] found that a higher pore density decreased the junction temperature, while Lafdi *et al.* [79, 95] showed that it increased the junction temperature. When studying the impact on the melting time, Zhao *et al.* [58] and Tian and Zhao [81] found that foams with a higher pore density resulted in a greater reduction of melting time, while a higher relative density increased the melting time. Though Lafdi *et al.* [79, 95] do not discuss melting time, it is summarized that higher pore density and higher relative density increased the time to steady state due to inhibited convection within the pores. Finally, in a recent study by Mancin *et al.* [97] (melting temperature 53°C, viscosity not reported), it was concluded that pore density did not affect the thermal response under 0.6 W/cm^2, 1.3 W/cm^2, and 1.9 W/cm^2. It is noted the use of different viscosities, thermal interface materials, and heat fluxes in these studies may lead to the differences in reported results. Overall, these studies show that there can be a complex dependence of the thermal charging performance of metal foam/PCM composites on the geometry, constituent properties, and thermal boundary conditions. Thus, comparisons between reported experiments in the literature must be done carefully.

In addition to studies on the impact of pore and relative density on the thermal performance of PCMs, supplemental literature discusses the integration of such open-cell foam/PCM composites in thermal management or storage systems. Applications include

the use in solar collectors [78], thermal energy storage systems [59], and heat sinks for electronics cooling [95, 98, 99]. Chen *et al.* [78] found that the addition of 10% relative density aluminum foams (PPI not reported) in paraffin had a significant impact on the heat transfer and melting rate of the PCM in a flat plate solar collector. Siahpush *et al.* [59] computationally studied how 5% relative density (PPI not reported) copper foam enhanced the heat transfer performance in a cylindrical solid/liquid phase change thermal energy storage system and found that both the melting and solidification intervals decreased. This result contradicts a study summarized by Hong and Herling [100] which found that the time to cool down was increased through the introduction of copper foam. The discrepancy can be explained through the experimental setup: Siahpush *et al.* [59] started with a uniform temperature liquid composite system and then actively cooled the system where as Hong and Herling [100] passively cooled the composite system which had already been heated to a base temperature of 100°C. Since Hong and Herling began the cooling experiments after heating the system until the base temperature reached 100°C, the higher conductive systems had a more uniform temperature throughout the sample as well as more energy absorbed. This resulted in a longer time to release the energy absorbed.

Trelles and Dufly [98] as well as Lafdi *et al.* [95] reported on the use of porous aluminum foams for electronics cooling. Trelles and Dufly [98] considered 10%, 20%, and 40% relative densities (PPI not reported) and Lafdi *et al.* [95] studied 3%, 6%, 10%, and 12% for each pore density, 5, 10, 20, and 40 PPI. Both studies found that the use of aluminum foams in the PCM heat sink decreased the maximum temperature, which can lead to better performance in the device. Additionally, Khateeb *et al.* [99] studied the use of aluminum foam saturated with paraffin wax in passive thermal management systems for

the lithium-ion battery of an electric scooter. They found that the use of the composite PCM system enhanced the performance of the battery by helping to maintain temperature uniformity in lithium-ion batteries without the use of active cooling components which are neither compact nor lightweight.

Thermal charging studies comparing graphite foams and aluminum foams also have been conducted. Chintakrinda *et al.* [64] studied the impact of mesophase foam and aluminum foam under high heat fluxes. A 9% relative density aluminum foam and 39% relative density graphite foam were compared using heat flux boundary conditions of 5.8 W/cm^2 and 11.6 W/cm^2. By comparing the time to fully melt the system, it was found that the graphite foam outperformed the aluminum foam under both heat fluxes. However, the latent heat capacity of the composites was not discussed, which is an important factor in the total energy storage of the battery. The lower latent heat of the high relative density graphite foam reduces the time to melt since the system is not capable of storing as much energy as the aluminum foam composite. In another study, Zhao and Wu [77] concluded that 5% relative density copper foams outperformed graphite foam made with 3.0 wt% expanded graphite flake due to the higher conductivity of the copper foam. Similarly, Zhou and Zhao [101] concluded that copper foam outperformed composites made of 3.0, 6.0, and 9.0 wt% expanded graphite.

As discussed in 2.4.3.3, though expanded graphite flake offers an improvement in thermal conductivity of the PCM, by compressing the flake, a significant increase in thermal conductivity can be realized [51, 91]. The amount of expanded natural graphite flake used in CENG is measured by bulk density, or the mass of graphite in the sample volume. This graphite composite, referred to as compressed expanded natural graphite

(CENG) foam, can then be saturated with PCM to form a highly conductive composite [51]. Composites of CENG foam saturated with PCM are generally compared through composite thermal conductivity and latent heat measurements [21, 51].

Saturation of the CENG foam is impacted by the compression because the pores can either spilt or collapse when the EG is compressed, potentially forming closed voids that are impenetrable by PCM. By studying the amount of PCM absorbed by the sample compared to the theoretical maximum, Py *et al.* [21] concluded that the higher the bulk density, the greater the volume of closed pores, which can result in a loss in mass of PCM contained in the composite and, ultimately, the thermal storage capacity. Additionally, Balima *et al.* [102] found that pore collapse is dependent on compression force as well as compression direction. While a higher compression force required of a greater CENG bulk density increased pore collapse, this phenomenon was found more significant in the direction parallel to compression.

While latent heat of the PCM decreases with an increase in CENG bulk density due to the addition of graphite as well air contained within closed pores formed during the compression process [21], the thermal conductivity of the PCM increases [21, 51, 94]. Recall that the thermal conductivity of composites formed with CENG bulk densities greater than 50 kg/m^3 is found to be anisotropic: thermal conductivity of the sample in the compression direction is less than in the direction perpendicular to the compression by as much as a factor of 7 [21]. This arises due to the preferred orientation of the graphite flakes transverse to the compression direction.

In addition to studying the influence of CENG bulk density on the storage properties of the PCM composite, applications such as thermal management of a battery pack and thermal storage in a solar hot water system have been considered. In these applied experiments [51, 60, 103], CENG bulk densities of 210 kg/m^3, 150 kg/m^3, and 70 kg/m^3 were studied. These three experiments discuss thermal charging of the CENG/PCM composites, but comparison of the effectiveness of the CENG is only considered in terms of the thermal conductivity, while no consideration of the varying heat capacity is given.

Although these studies agree that the addition of metal foams and CENG foams improves the rate of thermal charging of PCM, a direct comparison between the experiments in the literature is often difficult. In addition to the use of different boundary conditions for the thermal charging, various relative or bulk densities, sample geometries, PCM viscosities, and performance metrics are reported on the tested systems. Additionally, to date, no CENG thermal charging studies for different boundary conditions and bulk densities have been found. Due to the lack of a standardized methodology for testing these thermal storage materials, it would be beneficial to perform comparisons of metal and CENG-based phase change composites using a standard experimental setup and orientation and over the same thermal boundary conditions to better understand the factors that govern thermal charging rates in foam/PCM composites.

In this chapter a comparative study on the thermal charging enhancement of PCM thermal storage systems is presented, specifically focusing on composites of aluminum foam and CENG foam saturated with PCM. A standard sample with a constant heat flux or temperature on one boundary and insulated sides is used to determine the charging rate of the composite foam structures. Through this research, the impact of PCM viscosity, heat

flux magnitude, and thermal contact resistance between the heater and PCM on the thermal charging rate for aluminum foams of various pore densities is addressed. Next, a focus is placed on how the thermal charging enhancement of CENG foams compare to aluminum foams under various heat fluxes. The use of phase change materials is especially superior when the temperature difference between storing and releasing heat is small to maximize the amount of heat stored during the phase change. Therefore, thermal charging experiments are also conducted under a constant temperature of 60°C for a PCM that undergoes solid-liquid melting at 55°C. The impact on thermal charging for all systems is discussed by relating to both the decrease in melting time as well as the decrease in junction temperature between the heater and the PCM composite. Additionally, the latent heat, thermal conductivity, and costs of the composites are considered. This work will be used to guide the design of a thermal batteries with engineered thermal properties to enhance charging and discharging rates for use in space conditioning systems.

3.2 Experimental Description

3.2.1 Material selection

Two organic waxes with different viscosities were selected as the PCMs due to their non-corrosive nature and ability to melt congruently (without phase separation), which results in safe and reliable performance [21]. Technical grade waxes (Aldrich, melting point 54°C and PureTemp, melting point 37°C) were used as received. Material properties for the waxes are listed in Table 3.2. The transition temperatures and latent heat of each PCM were measured using the differential scanning calorimetry (DSC) technique (TA Instruments Q2000) with a heating and cooling speed of 5°C/minute and a sample

mass of 10.0 mg. DSC curves for each PCM are shown in Figure 3.2. The smaller peaks of the paraffin wax represent a solid-solid transition where the orthorhombic crystal structure (hard and brittle) of the paraffin transforms in a hexagonal crystal structure (softer and shows plasticity). PT37 does not exhibit a solid-solid transition. Both PCMs undergo a solid-liquid transition as seen by the large peaks in both graphs.

The latent heat during melt and solidification is represented by the area under the endothermic bottom curve and exothermic top curve, respectively. Solid-solid and solid-liquid transition temperatures were determined by the respective temperatures at each apex of the endothermic DSC curve while ramping from 20°C to 60°C or 80°C, depending on the melting temperature. As PT37 does not undergo solid-solid phase change, only the solid-liquid values are listed. The viscosity of PCM was measured using a parallel plate rheometer (TA Instruments ARES) with a shear rate of 300/sec, and a hot disk thermal constant analyzer (Hot Disk TPS 2500 S) was used to characterize the PCM thermal conductivity [93].

Table 3.2. Properties of PCM used in experimentation.

	Transition Temperature (°C)		**Thermal Conductivity at 20°C (W/mK)**	**Viscosity (Pa·s)**	**Latent Heat (J/g)**	
	Solid-solid	Solid-liquid			Solid-solid	Solid-liquid
Paraffin Wax	35.4	55.2	0.28	0.0066 (at 80°C)	31.2	132.2
PT37	-	37.0	0.25	0.0034 (at 60°C)	-	210.0

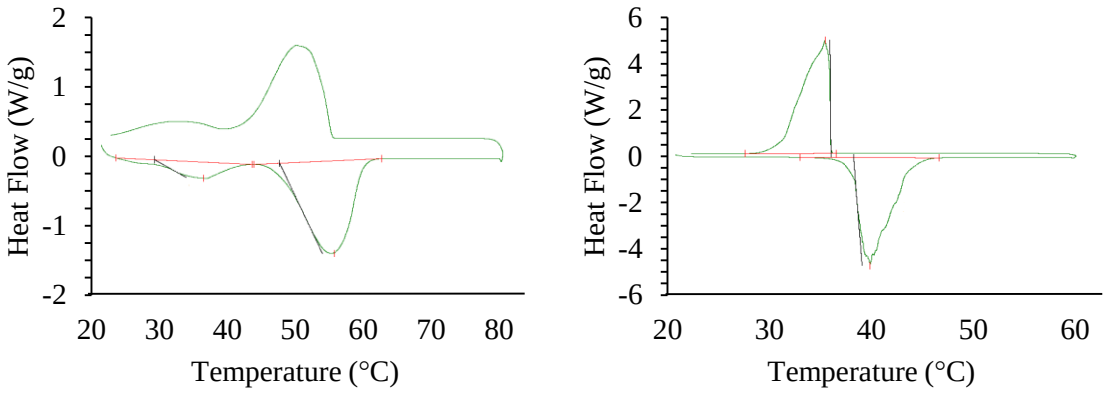

Figure 3.2. DSC curves of paraffin wax (left) and PT37 (right).

Aluminum foams (Duocel 6061T6) were acquired in three different pore densities: 10, 20, and 40 PPI. The relative density of each sample was measured and listed in Table 3.3. Exfoliated graphite (Asbury Carbons 3772) was used as received. This expandable graphite was heated in a 1000 W microwave over two 30 second intervals to complete the expansion process. An optical image of the expanded graphite (EG) is shown in Figure 3.3 (left). Each worm of expanded graphite was approximately 1.5-2.0 mm long and about 0.4 mm wide. The morphology of the expanded graphite was examined using a Hitachi VP 3700 variable pressure scanning electron microscope (SEM).

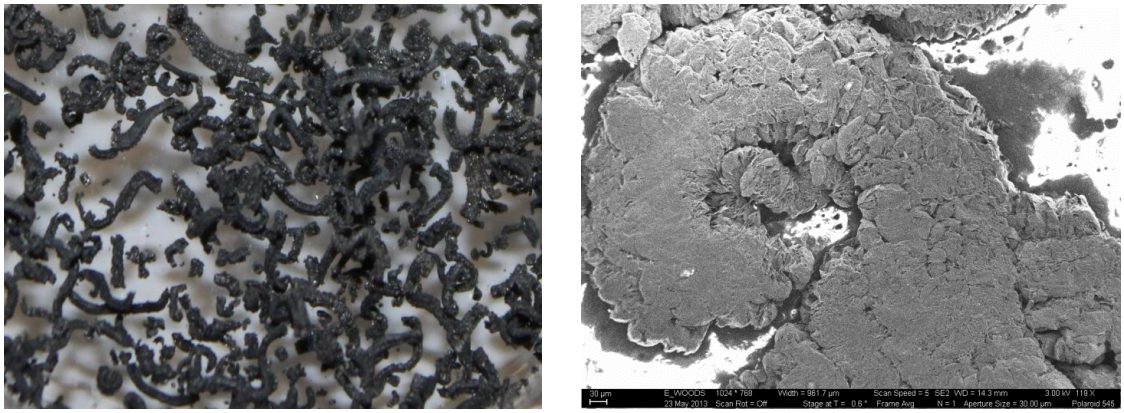

Figure 3.3. Optical image of EG (left); SEM image of EG at 119x magnification (right).

Each expanded graphite worm is an accordion style connection of graphene layers that have been separated during the heating under microwave energy and the release of the intercalated acid. An SEM image of EG at 119x magnification is shown in Figure 3.3 (right), while Figure 3.4 presents images at 1080x and 4020x magnification showing the expanded volume between the graphite layers.

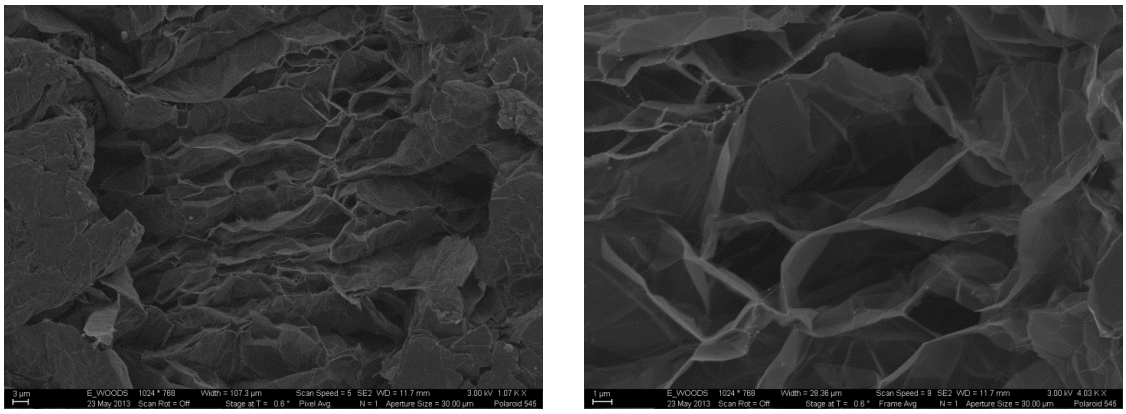

Figure 3.4. SEM images of EG at 1080x (left) and 4030x (right) magnification.

After the expansion process, the EG was manually compacted to the desired CENG bulk density by compressing in a stainless steel mold shown in Figure 3.5 (left). EG was

loaded into the cylindrical container and then compressed until the plunger was flush to the top of the container, forming a sample of volume 1.2×10^{-4} m^3. By measuring the mass of EG in the compression system, samples with bulk densities of 23, 50, 100, and 143 kg/m^3 were formed.

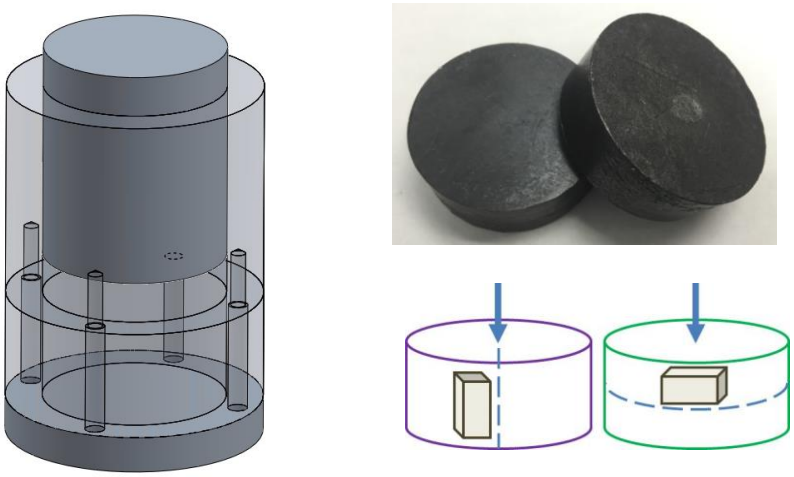

Figure 3.5. Compression system used to form samples (left); composite sample (top right); schematic of sample measurement orientations (bottom right).

The plunger was then removed and the PCM was introduced to the compressed graphite in the bottom section of the mold to form the CENG composites. Two methods of PCM saturation were compared: a liquid PCM method and a solid PCM method. The liquid PCM method refers to CENG saturation by pouring liquid wax into the container, allowing the setup to equilibrate at 80°C inside of a vacuum furnace, and then pulling a 635 mmHg vacuum to remove air within the CENG. A second approach, the solid PCM method, refers to placing a solid block of PCM on top of the CENG and then placing the setup inside of a vacuum furnace at 80°C and immediately pulling the 635 mmHg vacuum.

The solid PCM method was found to be superior to the liquid PCM method because trapped air within the CENG was removed before the foam was saturated with PCM. With the liquid PCM method, it was found that the air being removed from the CENG through the PCM broke the CENG apart due to the resistance from the wax and resulted in lower thermal conductivity. After saturation, the excess PCM was poured from the mold to prevent supersaturation as the PCM cooled and constricted. The solid CENG composite was removed from the mold as shown in Figure 3.5 (top right) and used in thermal conductivity and latent heat measurements as well as thermal charging experiments.

3.3 Sample Preparation

The aluminum foam samples were cut into rectangular portions with sides of 2.54 cm and a thickness of 1.27 cm. Initial experiments studied the impact of the thermal interface material between the heat source and the aluminum foam saturated with paraffin wax on the thermal charging rate. Two thermal interface materials, thermal grease (3.5 W/m·K) and thermal epoxy (2.5 W/m·K), were used to attach a square 0.15 cm thick aluminum heat spreader to the aluminum foam. While the thermal epoxy directly attached the aluminum foam to the aluminum plate, the thermal grease was evenly distributed between the top of the composite and the aluminum plate. During preparation of the thermal grease samples, each aluminum foam was placed into an acrylic test container and then liquid paraffin was poured into the container to saturate the foam. After the paraffin had cooled, 0.4 g of thermal grease was spread onto an aluminum plate and then placed on top of the sample.

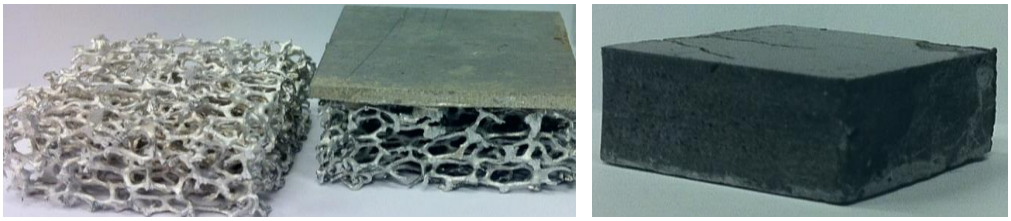

Figure 3.6. Aluminum foam before and after the attachment of the aluminum plate (left); CENG/PCM foam (right).

To form the epoxy samples, thermal epoxy was spread on the aluminum plate and then permanently bonded to the aluminum foam. Figure 3.6 (left) depicts the aluminum before and after the epoxy process. To prepare the thermal epoxy aluminum foam systems for experimental testing, each sample was reheated on a hotplate at 80°C for 10 minutes and then immediately placed into the top portion of the test setup. The setup was oriented with the aluminum plate on the bottom, and liquid paraffin was poured into the setup. A piece of aluminum foil was immediately placed on top and then the bottom of the test container was placed on top of the aluminum foil. To ensure that the space formed due to constriction during solidification was between the heater and the composite to accommodate expansion during melting, the sample was immediately turned over. The sample was allowed to cool, and excess paraffin was removed.

Following the study of thermal interface materials, aluminum foams saturated with paraffin wax and PT37 were prepared to compare the impact of pore density on the thermal charging rate for different viscosity PCMs under various heat fluxes. Thermal epoxy was used as the thermal interface material in order to provide comparable results between the various experiments. Constant temperature experiments were conducted with paraffin wax samples prepared with thermal grease.

Experiments with aluminum foam samples focused on understanding the impact of thermal interface material, heat flux magnitude, PCM viscosity, and pore density on the thermal charging rate of the composite. Additionally, constant temperature experiments were conducted for various pore densities. Experiments with thermal grease and paraffin wax for various aluminum foam pore densities and boundary conditions were then compared to similar experiments with CENG foam of various bulk densities. Thermal grease was used since thermal epoxy cannot bond the CENG/PCM composite to the aluminum plate. Paraffin wax was used to saturate all CENG foams. Due to the compression process required to form the CENG, natural convection within each pore is minimized, so a study of viscosity was not conducted. The saturated CENG composite was cut into rectangular portions with sides of 2.54 cm and a thickness of 1.27 cm as shown in Figure 3.6 (right), similar to the aluminum foam composites. Thermal grease was spread on an aluminum heat spreader plate and placed on top of the sample.

3.4 Sample Characterization

3.4.1 Aluminium foams

Four metrics were used to compare all composites – thermal conductivity, latent heat, junction temperature, and time to end of melt. The approximate thermal conductivity of the foam is estimated according to the following equation,

$$k_{foam} = k_{bulk} \times \text{relative density} \times 0.33 \quad (1)$$

where k_{bulk} = bulk conductivity of the metal, and relative density = relative density of the foam [64]. The 0.33 coefficient represents the foam structure geometry or "tortuosity"

factor [75]. It is noted that there are numerous correlations proposed to determine the effective thermal conductivity of metal foams saturated with PCM, and that values determined by Equation 1 for the given relative densities agree with published literature for aluminum foams [104]. Further information on the effective thermal conductivity calculation can be found in 4.2.3.

The approximate thermal conductivity of each foam is listed in Table 3.3 based on a bulk 6061-T6 aluminum thermal conductivity of 200 W/m·K and a relative density of 8.7%, 8.8%, 9.5% (234, 237, 258 kg/m^3). Since the aluminum foam is an open-cell structure, the latent heat of the system can be calculated by using a volume fraction assumption (Equation 2) with bulk PCM latent heats of 163.4 J/g and 210.0 J/g. Properties of the aluminum foam composites are summarized in Table 3.3.

$$L_{composite} = L_{PCM} \times \text{(1-relative density)} \quad (2)$$

Table 3.3. Properties of aluminum foam composites.

Wax	**Aluminum Foam** Relative Density, Pore Density, Bulk Density	**Thermal Conductivity at 20°C (W/m·K)**	**Latent Heat (J/g)**	**Solid-Liquid Melting Temperature (°C)**
Paraffin Wax	9.5%, 10 PPI, 258 kg/m^3	6.3	147.8	55.2
	8.8%, 20 PPI 237 kg/m^3	5.8	149.0	55.2
	8.7%, 40 PPI, 234 kg/m^3	5.8	149.2	55.2
PT37	9.5%, 10 PPI 258 kg/m^3	6.3	189.9	37.0
	8.7%, 40 PPI 234 kg/m^3	5.8	191.8	37.0

3.4.2 CENG foams

During preparation of the CENG composite, saturation with paraffin wax was verified by determining the percent void volume through the measurement of the mass of paraffin in the composite compared to the predicted mass of paraffin based on the known volume and density. It was found that the longer the composite was held under vacuum during paraffin infiltration, the more time the paraffin had to advance through the tortuous network of the CENG to saturate the foam. In Figure 3.7 (left), the 50 kg/m^3 and 100 kg/m^3 composites show the trend of decreasing void with an increase of time in vacuum. The 100 kg/m^3 composite also indicates a lower limit of about 10% for the percent void, while the 143 kg/m^3 composites show the repeatability of two different CENG samples in the vacuum for the same period of time. Even though samples were placed in vacuum for 20

hours or more, the percent void is shown to increase as the CENG bulk density increases due the larger number of closed pores formed during the graphite compression process.

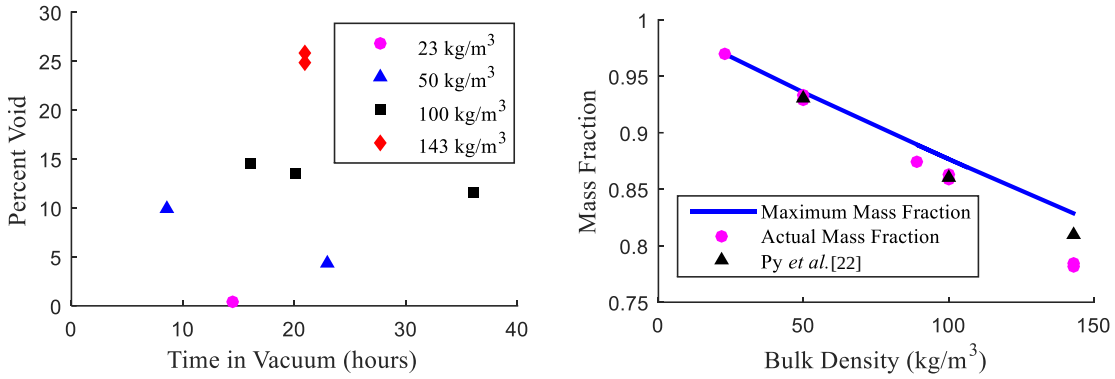

Figure 3.7. Percent void (±3%) as a function of time in the vacuum (left); mass fraction (±1%) as a function of CENG bulk density (right).

The mass fraction of the paraffin in the composites, calculated as the mass of paraffin divided by the mass of the sample, is compared to data reported by Py *et al.* [21] in Figure 3.7 (right). Though viscosity is not reported in Py *et al.* [21], generally the viscosity decreases with a decrease in melting temperature. Therefore, the data from Py *et al.* [21] repeated in Figure 3.7 (right) is for a melting temperature of 73°C as a comparison to the PCM used in this work that melts at 55°C. The mass fraction data similar to Py *et al.* [21] was also reported by Mills *et al.* [51] for a melting temperature of 50°C. The maximum mass fraction refers to the mass fraction limit if no voids existed in the composite. The impact of percent void is shown by the difference between the actual mass fraction data and the maximum mass fraction. The difference between the actual mass fraction of the composites used in this study and those reported by Py *et al.* [21], specifically for 143 kg/m^3, is posed to be a result of the volume of composite and the time allowed for the composite to absorb paraffin. The volume of each the composites reported in Figure 3.7 is

120 cm^3, while the samples used by Py *et al.* [21] and Mills *et al.* [51] were 15.6 cm^3 and 1.8 cm^3, respectively. Mills *et al.* [51] also prepared samples with a volume of 49 cm^3 and noted a decrease in mass fraction similar to the trend shown in Figure 5 (right). It is noted that the viscosity of the PCM used in this work may also have an impact on the actual mass fraction; however, the work by Py *et al.* [21] indicates that closed pores as a result of the compression process at high bulk densities are an issue for any viscosity PCM.

Similar to the pure PCMs, thermal conductivity of each CENG composite was measured at 20°C, while the composite latent heat and melting temperature were measured by ramping from 20°C to 80°C. For the higher bulk densities, 100 kg/m^3 and 143 kg/m^3, anisotropy of the CENG was considered in the thermal conductivity measurements: thermal conductivity was measured along both cylinder axes of Figure 3.5 (bottom right), where the arrow represents the compression direction.

Thermal conductivity of the composites is reported in Figure 3.8 (left) and Table 3.4. Higher thermal conductivity is exhibited for 100 kg/m^3 and 143 kg/m^3 samples that were measured perpendicular to the direction of compression. This is consistent with previously published data [21, 51, 94]. Latent heat of the composites is reported in Figure 3.8 (right) by comparing the measured latent heat the composites to that of pure paraffin wax. The raw data is reported in Table 3.4. The data indicates that the latent heat of composites start to significantly decrease at a CENG bulk density of 100 kg/m^3. It is postulated that this effect is a result of increased graphite volume in the system combined with an increased number of closed pores formed during the compression process.

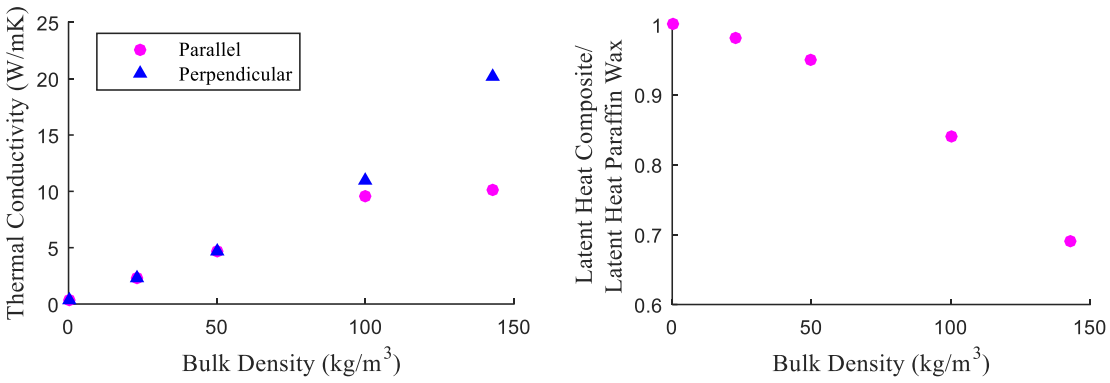

Figure 3.8. Thermal conductivity (±2%) as a function of CENG bulk density and compression (left); Latent heat (±4%) as a function of CENG bulk density (right).

Table 3.4. Properties of CENG foam composites with respect to the bulk density.

CENG Foam Bulk Density (kg/m^3)	Thermal Conductivity at 20°C (W/m·K)	Latent Heat (J/g)	Solid-Liquid Melting Temperature (°C)
0	0.3	163.4	55.2
23	2.3	161.9	56.3
50	4.7	157.0	56.3
100	9.6	136.4	54.5
143	10.1 (‖), 20.2 (⊥)	111.1	53.8

Following material characterization, rectangular thermal charging experimental samples (2.54 x 2.54 x 1.27 cm) were cut from the disks used in thermal conductivity measurements. Anisotropy of the CENG was considered for 143 kg/m^3 composites during the thermal charging experiments as shown by the rectangular blocks of Figure 3.5 (bottom right).

3.5 Thermal Charing Experiment Setup

All aluminum foam and CENG foam composites were tested in a similar thermal charging experimental setup. The acrylic test container measured 5.08 cm x 5.08 cm x 2.54 cm and was designed in two separate pieces, each 5.08 cm x 5.08 cm and 1.27 cm thick, for simple loading and unloading of the samples as shown in Figure 3.9 (left). The top acrylic piece was made with a 2.54 cm x 2.54 cm hole into which the foam/PCM composite was placed. The bottom acrylic piece was solid. Thin film heaters with an adhesive backing and maximum output of 1.55 W/cm^2 were used as a heat source. The adhesive heater was placed on top of the 0.15 cm thick aluminum square plate, separated from the sample with the thermal interface material (TIM).

The heater was oriented on top of the experimental sample to minimize leakage during testing. Since PCM expands during melting, a small air pocket is necessary to accommodate the expansion. This void will remain at the top of the composite since air is less dense than wax. If the heater is orientated such that heat travels through the sample against the gravity direction, the air pocket will not be located between the heater and the wax. Therefore, as the wax melts, the expansion will not occur within the air pocket and eventually force the heater and foam apart. This introduces an additional complexity when considering the orientation of the heater. It suggests that PCM thermal storage systems should be designed such that the heat source orientation enables volume expansion during melting.

K-type thermocouples of diameter 0.025 cm were used in conjunction with a data acquisition unit via a 20-channel multiplexer to record the thermocouple temperatures. The

heaters were powered using an Agilent E3649A DC power supply during constant heat flux experiments. For constant temperature experiments, a Lakeshore 331 temperature controller was used. For all experiments, two thermocouples were placed under the heater to measure the top temperature of the sample and two additional thermocouples were placed at the bottom of the sample as shown in Figure 3.9 (right). The bottom thermocouples were evenly spaced between the sides of the sample and, for aluminum foam experiments, positioned in the middle of foam pores. A piece of oil resistant rubber was then placed on top of the heater to prevent leakage and minimize heat losses. A progression of images depicting this process is shown in Figure 3.10. Finally, the entire system was placed inside of an insulated box.

For each experiment, the top (or junction) and bottom temperatures of the sample were recorded over time. It was confirmed that temperature profiles on top of the aluminum plate and under the aluminum plate were the same over time due to the high conductivity of the aluminum. Comparison of the rate at which each portion of the sample increased in temperature relates to the thermal charging performance of the system. Values presented for junction temperature and melting time represent averaged values over two repeated experiments per boundary condition and density.

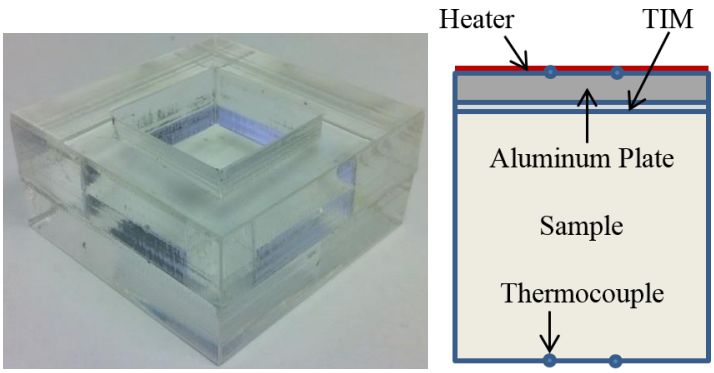

Figure 3.9. Test setup (left); Schematic of test setup for thermal charging experiments (right).

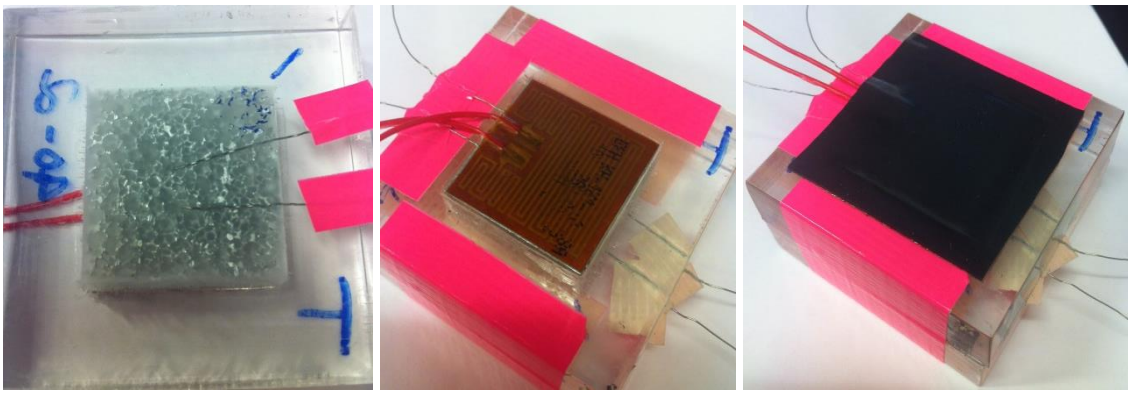

Figure 3.10. Progression of preparation of aluminum foams for testing.

3.6 Results and Discussion – Constant Heat Flux

3.6.1 Aluminium foam composites

3.6.1.1 Impact of thermal interface material on thermal charging

Thermal charging experiments were conducted for pure paraffin as well as aluminum foams with two different thermal interface materials. A baseline case of paraffin exposed to 1.55 W/cm^2 is represented in Figure 3.11. The poor thermal charging

performance of paraffin wax is implied by the difference in the rate of temperature change between the top and the bottom temperatures. The experiment was terminated after only 100 seconds because of a 100°C limit for the acrylic material.

As illustrated in Figure 3.11, aluminum foams significantly increase the thermal charging performance of paraffin wax. For all aluminum foam bottom temperature data lines, the initial steep temperature slope indicates the sensible heating portion of paraffin followed by a non-linear temperature change during solid-solid latent heat storage around 35°C. This leads into a short sensible heating portion followed by the almost flat temperature profile of the solid-liquid phase change around 45°C. The shift to a steeper slope around 55°C indicates the period when melting has ended and the paraffin continues storing thermal energy as sensible heat. The impact of each aluminum foam on thermal performance is measured by the time of this change from solid-liquid latent to sensible heat storage. This metric is referred to as time to end of melt.

To find the time to end of melt for each system, the maximum difference between the top and bottom temperature of the sample was calculated. The time and top and bottom temperatures associated when this maximum temperature difference occurred were recorded and used to compare the three systems. Note that a shorter time to end of melt coincides with better thermal charging. The junction temperature between the heat source and the foam sample at the end of melt is indicated by the top temperature recorded. The lower the junction temperature at the end of the melting process, the more efficient the foam is at distributing heat throughout the composite system. Finally, the bottom temperature was compared to the expected melting range of 53-55°C based on DSC results.

To quantify the impact of the thermal interface material on the thermal charging rate and junction temperature, thermal charging experiments were compared for samples fabricated using thermal grease and thermal epoxy. Results for 10 PPI, 20 PPI, and 40 PPI aluminum foams saturated with paraffin wax, bonded with thermal epoxy, and exposed to 1.55 W/cm^2 are presented in Figure 3.11 and summarized in Table 3.5. The maximum percent error was calculated to be 4% of the time to end of melt. The impact of the thermal interface material on the time to end of melt and junction temperature can be seen in Table 3.5. The results indicate that 40 PPI outperforms 10 PPI and 20 PPI by about 15% for both thermal interface materials based on time to end of melt and that the top temperature decreases with an increase in pore density. Additional comparison of the impact of thermal interface material selection on each pore density indicates that thermal epoxy results in a decrease in time to end of melt, while thermal grease results in a lower junction temperature.

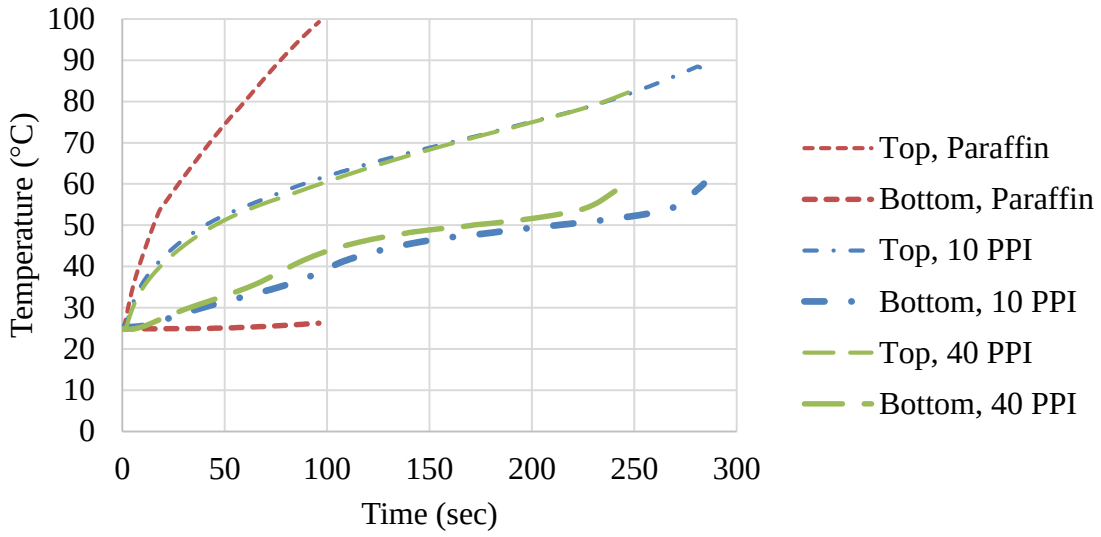

Figure 3.11. Thermal charging performance of 10 and 40 PPI (9% relative density) aluminum foams with thermal epoxy under 1.55 W/cm^2.

Table 3.5. Summary of data presented in Figure 3.11.

	10 PPI		**20 PPI**		**40 PPI**	
Thermal Interface Material	Epoxy	Grease	Epoxy	Grease	Epoxy	Grease
Time to End of Melt (sec)	271	296	253	268	225	254
Bottom Temperature (°C)	54.7	54.6	53.6	54.9	54.0	55.0
Top Temperature (°C)	86.5	84.8	85.0	83.6	78.3	75.2
Temperature Difference (°C)	31.8	30.2	31.4	28.7	24.3	20.2

As seen by the above experiments, 40 PPI foams outperforms 10 PPI and 20 PPI with a heat flux of 1.55 W/cm^2 through comparison of the reduction in time to end of melt as well as the lower junction temperature measurements. Since the pore density has a significant impact on specific surface area [75], these results indicate that the larger specific surface area of 40 PPI foam increases the heat diffusion into the aluminum foam composite

samples. Therefore, for high heat fluxes, the impact of conduction exceeds that of natural convection, and a system should be designed with maximum specific surface area density.

Experimental data also indicates that the type of thermal interface material impacts the thermal response of the composite samples. While thermal epoxy results in a faster melting response, thermal grease exhibits a lower junction temperature. It is suggested that this is due to the bonding method of each thermal interface material. Thermal epoxy provides a better contact between the aluminum foam and the heater to increase heat distribution into the system. However, thermal grease is evenly spread on top of the foam composite, which results in better distribution of the heat at the interface between the composite and heater. This difference is important when considering the application of latent heat systems. For thermal management applications, such as electronics cooling, minimizing the junction temperature is a priority. However, for thermal storage solutions, decreasing the time to melt is the primary concern. The remaining experiments were conducted with thermal epoxy samples.

3.6.1.2 Impact of heat flux on thermal charging

For all prior experiments, a constant heat flux of 1.55 W/cm^2 was used for the thermal charging experiments. As previously mentioned, lower heat fluxes between 0.2 W/cm^2 and 0.3 W/cm^2 have been used in literature, but there is a lack of comparison between different heat fluxes and the impact on thermal charging performance of foams with different pore densities. Table 3.6 and Figure 3.12 summarize experiments conducted with 40 PPI and 10 PPI foams under three constant heat flux conditions – 1.55 W/cm^2, 0.78 W/cm^2, and 0.39 W/cm^2 – to develop an understanding of the impact of heat flux on the

relative thermal performance of each system. The maximum percent error was calculated to be 4% of the time to end of melt.

Table 3.6. Time to end of melt for 10 PPI and 40 PPI aluminum foams (9% relative density) under heat fluxes of 1.55 W/cm^2, 0.78 W/cm^2, and 0.39 W/cm^2.

Aluminum Foam Pore Density	Applied Heat Flux (W/cm^2)	Time to End of Melt (sec)	Bottom Temperature (°C)	Top Temperature (°C)
10 PPI	0.39 W/cm^2	1369	53.9	60.0
	0.78 W/cm^2	552	53.8	70.2
	1.55 W/cm^2	271	54.7	86.5
40 PPI	0.39 W/cm^2	1372	53.6	59.7
	0.78 W/cm^2	505	53.6	65.0
	1.55 W/cm^2	225	54.0	78.3

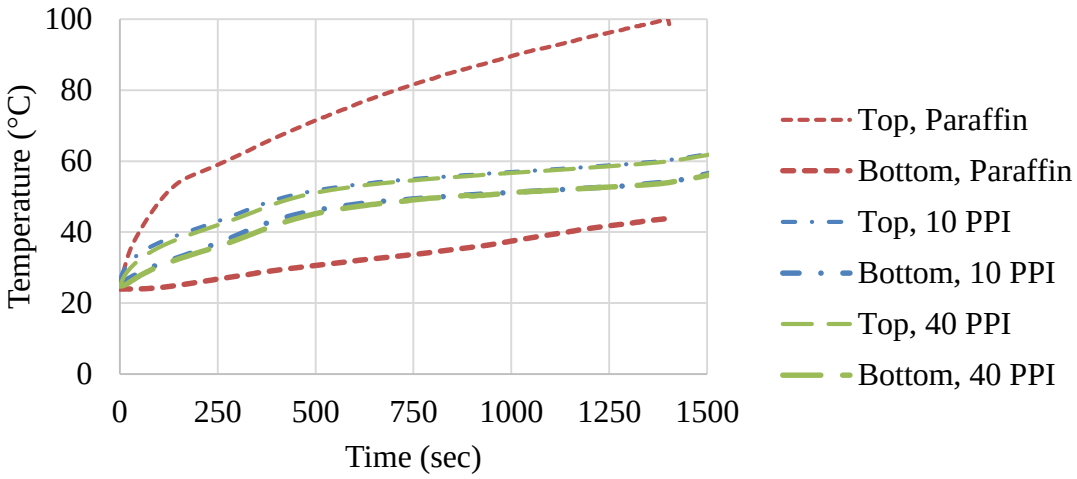

Figure 3.12. Thermal charging performance of 10 and 40 PPI (9% relative density) aluminum foams with thermal epoxy under 0.39 W/cm^2.

The 40 PPI foam outperforms 10 PPI exposed to 1.55 W/cm^2 by 17% based on time to end of melt while decreasing the junction temperature by 8.2°C. With a similar comparison between the two foams with 0.78 W/cm^2, it is found that 40 PPI outperforms 10 PPI by 8.5% and 5.2°C. This finding led to a study with 0.39 W/cm^2 to compare the thermal charging response if the heat flux was reduced (Figure 3.12). The results indicate that 10 PPI and 40 PPI perform similarly under 0.39 W/cm^2 conditions as measured by both the time to melt and junction temperature. This indicates that as the heat flux is further reduced, the benefit from the additional heat transfer area of the larger PPI foam decreases.

3.6.1.3 Impact of viscosity on thermal charging

To study the impact of viscosity, the thermal charging of aluminum foams saturated with paraffin wax (μ = 0.0066 Pa·s) was compared to PT37 (μ = 0.0034 Pa·s). The thermal response is shown in Figure 3.13 and data is summarized in Table 3.7. The difference in the melting behavior of the paraffin wax, which undergoes both solid-solid and solid-liquid phase change, compared to just the solid-liquid phase change of the PT37 is shown in the graphs of Figure 3.13. The two temperature inflections of the paraffin wax correspond to the solid-solid and solid-liquid phase change, whereas the single inflection of the PT37 corresponds to the solid-liquid phase change. Recall that the solid-liquid phase change for paraffin wax occurs around 55°C, while PT37 transitions at 37°C.

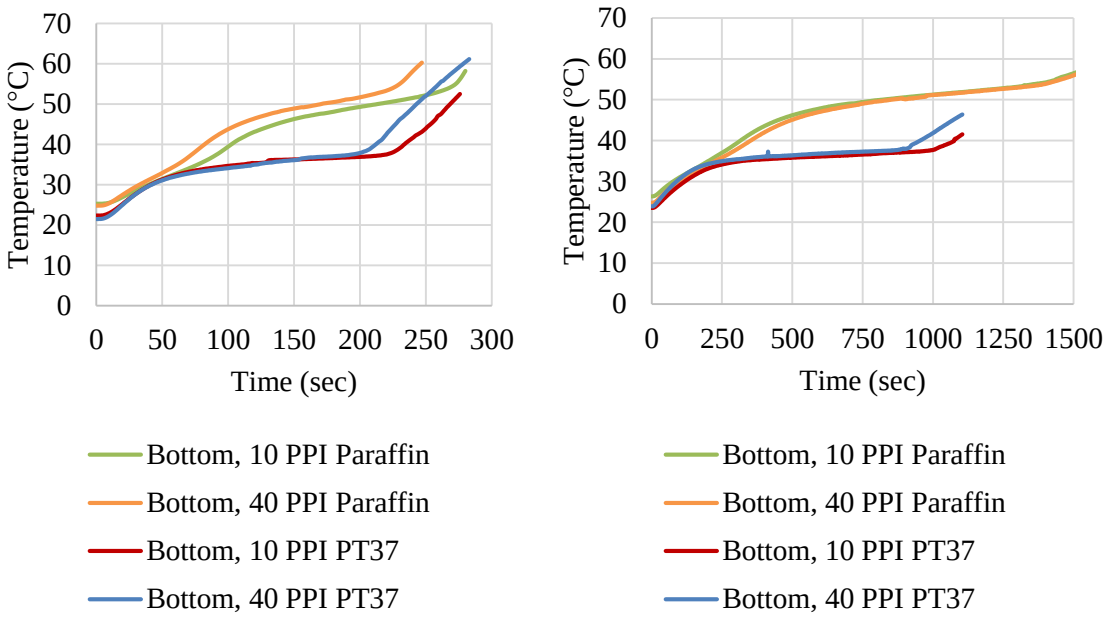

Figure 3.13. Thermal charging performance of 40 PPI and 10 PPI aluminum foams saturated with paraffin wax and PT37 under 1.55 W/cm^2 (left) and 0.39 W/cm^2 (right).

Table 3.7. Time to end of melt for 10 PPI and 40 PPI aluminum foams (9% relative density) with paraffin wax and PT37 under heat fluxes of 1.55 W/cm^2 and 0.39 W/cm^2.

Aluminum Foam Pore Density	**Applied Heat Flux (W/cm^2)**	**Time to End of Melt (sec)**		**Bottom Temperature (°C)**		**Top Temperature (°C)**	
		Paraffin	PT37	Paraffin	PT37	Paraffin	PT37
10 PPI	0.39	1369	1038	53.9	38.2	60.0	44.8
	1.55	271	229	54.7	39.1	86.5	69.8
40 PPI	0.39	1372	908	53.6	37.4	59.7	43.2
	1.55	225	202	54.0	38.3	78.3	62.6

As shown in Figure 3.13 and Table 3.7, the increased surface area of higher pore density foam is beneficial for both faster charging and a decrease in the junction temperature for systems saturated with paraffin wax and PT37 exposed to 1.55 W/cm^2.

However, when exposed to 0.39 W/cm^2, the influence of increased surface area differs: 10 PPI and 40 PPI foams saturated with paraffin wax charge at a similar rate, but when saturated with PT37, 40 PPI charges faster than 10 PPI.

It is hypothesized that this occurs due to the difference in viscosity and the difference in junction temperature at end of melt for the two PCMs, both of which impact the natural convection within the pores. The impact of natural convection compared to that of conduction on the heat transfer can be related through use of the Raleigh number (Equation 3). Recently, Jackson *et al.* [105] and Zhao *et al.* [106] independently found that convection is constrained and can be assumed negligible when the Ra $\leq 10^4$.

$$Ra = \frac{\left(g * \beta_{PCM} * \ H^3 * \left(T_{junction} - T_{melt}\right)\right)}{\alpha_{PCM} * \nu_{PCM}} \tag{3}$$

where,

g = gravity (9.81 m/s^2)

β_{PCM} = thermal expansion coefficient of PCM [1/K]

H = height [m]

α_{PCM} = thermal diffusivity [m^2/s]

ν_{PCM} = kinematic viscosity [m^2/s]

$T_{junction}$ = Junction temperature at time to end of melt [K]

T_{melt} = Melting temperature [K]

Zhao *et al.* [106] studied the impact of the Raleigh number and pore size through use of the Fourier number and Stefan number defined in Equation 4 and 5.

$$Fo = \frac{\alpha t}{H^2} \tag{4}$$

$$Ste = \frac{c_p \left| T_{junction} - T_{melt} \right|}{L} \tag{5}$$

where,

α = thermal diffusivity of the liquid PCM [m^2/s]

t = time [s]

H = height [m]

c_p = specific heat of liquid PCM [J/kg·K]

L = latent heat of PCM [J/kg]

$T_{junction}$ = Junction temperature at time to end of melt [K]

T_{melt} = Melting temperature [K]

As discussed by Zhao *et al.* [106], higher pore density results in larger internal surfaces for heat transfer. As shown by Figure 3.14 (left), the melting time decreases with an increase in pore density due to the greater surface area. Additionally, the difference between melting time of the PCMs in metal foams with different pore densities tends to be smaller as the Rayleigh number increases as shown in Figure 3.14 (left) due to the influence of natural convection.

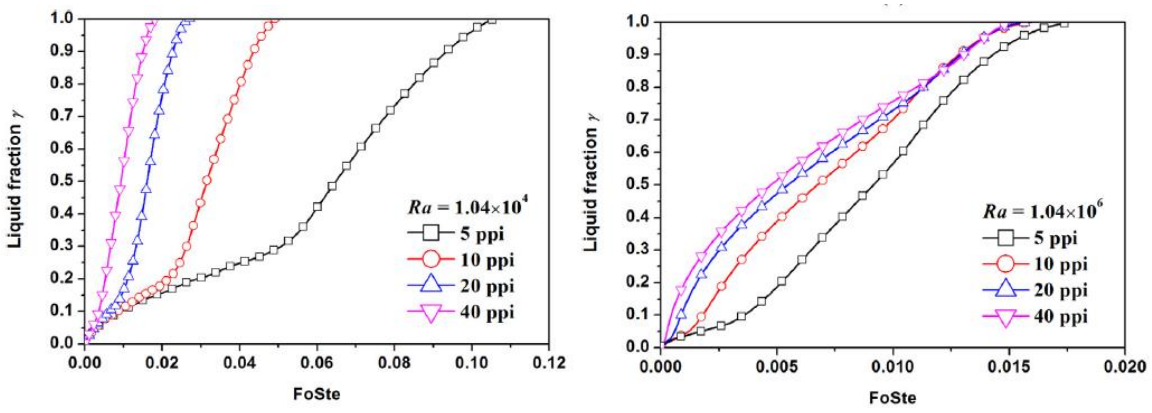

Figure 3.14. Effective of pore density on the melting evolution of PCM [106].

The Fourier number, Stefan number, and liquid fraction number have been calculated for the data of Figure 3.13 to compare to the results of Zhao *et al.* [106]. Though all properties are not available for the experimental PCMs to calculate the Raleigh number for each experiment, inferences can be made based on the results in Figure 3.14. First, by comparing all data for the less viscous PT37 (Figure 3.15) to the respective data of the greater viscosity paraffin wax (Figure 3.16), the impact of viscosity is suggested. It is noted that the data lines of PT37 have a smaller deviation than those of paraffin wax, suggesting that natural convection plays more of a role in the heat transfer for the lower viscosity systems (based on Figure 3.14). However, the dominance of conduction heat transfer for the PT37 systems is suggested by the increase in liquid fraction of the 40 PPI systems under both heat fluxes (purple and blue lines) as compared to the respective 10 PPI systems (red and green lines). Additionally, since the rate of increase in liquid fraction under 0.39 W/cm^2 (dashed lines) for each PPI is greater than that of 1.55 W/cm^2 (solid lines), this suggests that additional heat transfer due to natural convection is more important at lower heat fluxes.

The primary difference between the PT37 data and the paraffin wax data is the response of the 40 PPI system under 0.39 W/cm^2 in relation to the other systems. The PT37 data demonstrates that the heat transfer due to natural convection is more important at lower heat fluxes, however, the paraffin wax data shows that this influence of natural convection decreases since both dashed lines follow the same trend. This suggests that the tortuosity of the higher pore density foam prevents increased heat transfer from natural convection for high viscosity PCMs, leading to similar performance for 10 PPI and 40 PPI foams under low heat fluxes.

To summarize this discussion, for the lower viscosity PCM (PT37), the higher pore density offers improvement in the thermal charge rate under both heat fluxes since the main mode of heat transfer is conduction. However, the data does indicate the presence of natural convection, especially at a lower heat flux. For the higher viscosity paraffin wax, the main mode of heat transfer is conduction and the added influence of natural convection at lower heat fluxes is reduced. This suggests a trade-off between higher surface area (higher pore density) and natural convection (lower pore density).

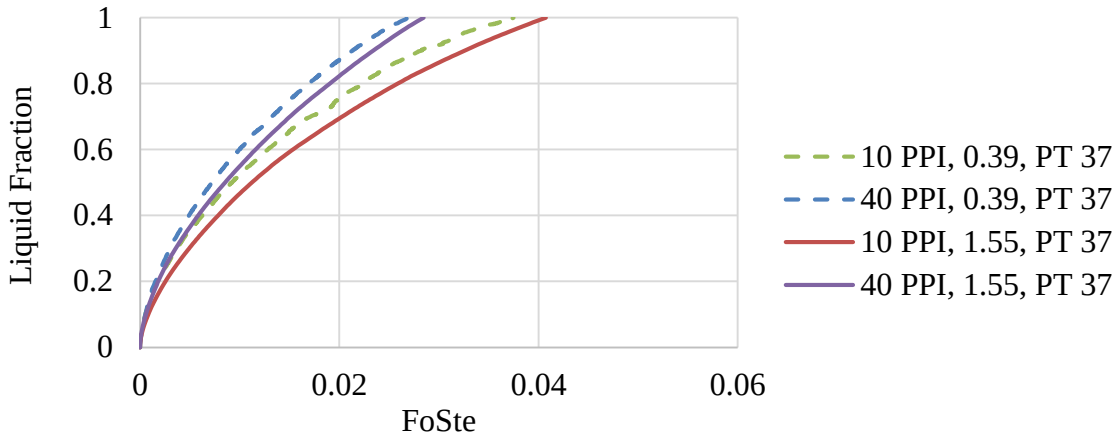

Figure 3.15. Effect of heat flux and pore density on the melting evolution of PT37.

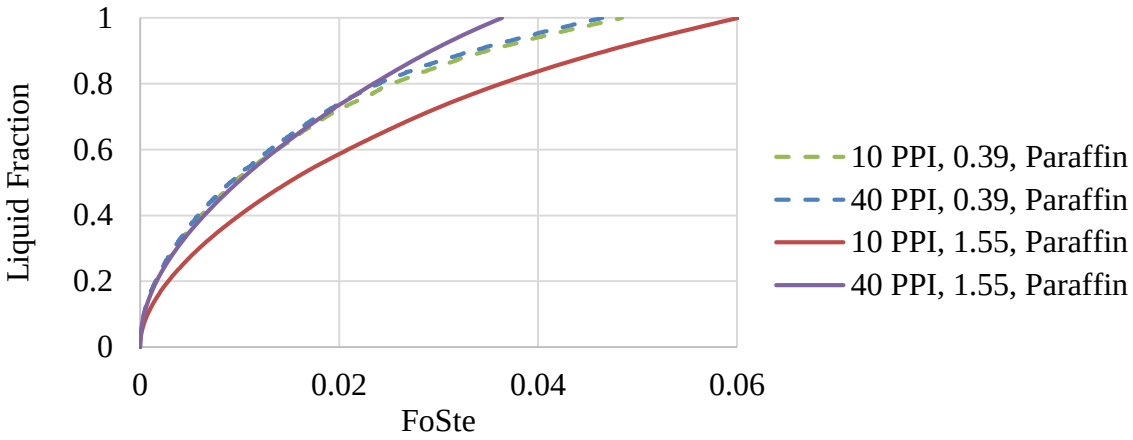

Figure 3.16. Effect of heat flux and pore density on the melting evolution of paraffin wax.

3.6.2 CENG foam composites

3.6.2.1 Impact of bulk density on thermal charging

Thermal charging experiments were conducted for all CENG/paraffin wax composites listed in Table 3.4. Similar to aluminum foam composites, the time to end of melt and junction temperature were recorded and used to compare the influence of the CENG foam on the thermal charging performance. Paraffin wax and thermal grease were

used in all experiments. Composites with a graphite bulk density of 143 kg/m^3 were experimentally studied with the heat flow both perpendicular (⊥) and parallel (||) to the compression direction. Recall from Table 3.4 that the perpendicular thermal conductivity measurement is twice that of the parallel thermal conductivity. Figure 3.17 presents the thermal charging curves for 23, 100, and 143⊥ kg/m^3 composites, and Table 3.8 lists experimental results for all composites. The maximum percent error was calculated to be 4% of the time to end of melt. The improved conduction through the system due to the higher thermal conductivity of denser graphite composites can be seen through the decrease in time to end of melt as well as the decrease in the top temperature. For both heat fluxes, the 143⊥ kg/m^3 composite has the shortest time to end of melt and lowest junction temperature. It is noted that the decrease in time to end of melt is a result of both the high thermal conductivity and lower latent heat capacity due to the addition of graphite.

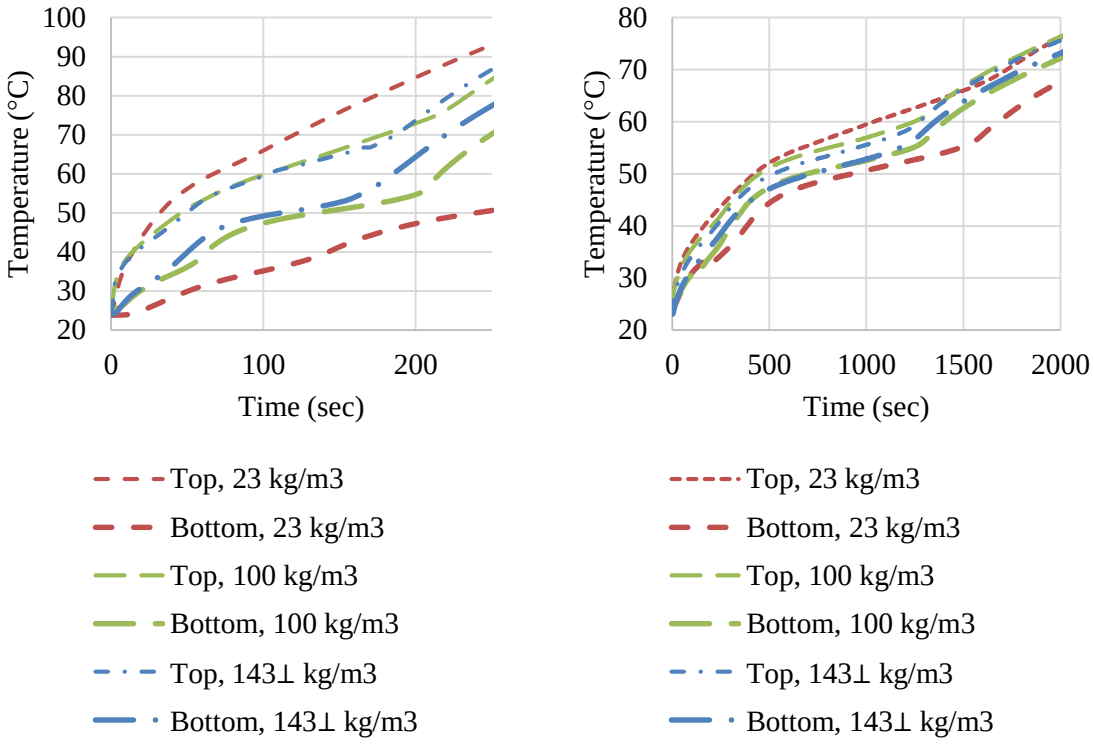

Figure 3.17. Thermal charging performance of 23, 100, and 143⊥ kg/m^3 CENG foams saturated with paraffin wax under 1.55 W/cm^2 (left) and 0.39 W/cm^2 (right).

Table 3.8. Time to end of melt for CENG foams saturated with paraffin wax under 1.55 W/cm^2 and 0.39 W/cm^2.

CENG Foam Bulk Density (kg/m^3)	Applied Heat Flux (W/cm^2)	Time to End of Melt (sec)	Bottom Temperature (°C)	Top Temperature (°C)
23	1.55	355	56.3	100.0
	0.39	1557	56.3	66.8
50	1.55	243	56.2	83.4
	0.39	1379	56.2	63.0
100	1.55	198	54.5	72.6
	0.39	1200	54.5	59.4
143⊥	1.55	158	53.7	65.7
	0.39	1084	53.8	56.6
143‖	1.55	169	53.8	73.3
	0.39	1091	53.8	58.7

3.7 Results and Discussion – Constant Temperature

In constant temperature applications, the choice of PCM melting temperature near the applied temperature ensures that a majority of the thermal energy transferred to the composite is stored as latent heat. To explore the impact of aluminum foams and CENG foams on the charging response for composites exposed to a constant temperature heat source, the PCM was chosen as paraffin wax (T_{melt} = 55°C) and the applied temperature was 60°C. The same thermal charging experimental setup (Figure 3.9 and Figure 3.10) and experimental samples as discussed for the constant heat flux experiments were used for this study. Thermal grease was used in all experiments to provide comparable results between the aluminum foam and CENG foam thermal charging response. All composite properties reported in Table 3.3 and Table 3.4 remain for the systems studied and are repeated in Table 3.9.

Table 3.9. Properties of aluminum foam and CENG foam composites saturated with paraffin wax.

CENG or Aluminum Foam Density	Thermal Conductivity (W/m·K)	Latent Heat (J/g)	Solid-Liquid Melting Temperature (°C)
CENG, 0 kg/m^3	0.3	163.4	55.2
CENG, 23 kg/m^3	2.3	161.9	56.3
CENG, 50 kg/m^3	4.7	157.0	56.3
CENG, 100 kg/m^3	9.6	136.4	54.5
CENG, 143 kg/m^3	10.1 (∥), 20.2 (⊥)	111.1	53.8
9.5%, 10 PPI, 258 kg/m^3	6.3	147.8	55.2
8.7%, 40 PPI, 234 kg/m^3	5.8	149.2	55.2

To characterize aluminum foam and CENG foam composites, reported data includes the bottom transient temperature profile during charging, the time at which the PCM completed melt, and the bottom and top temperature of the composite at the end of melt. The time to end of melt was measured based on when the bottom temperature reached the solid-liquid melting temperature shown in Table 3.9 from DSC measurements. Therefore, the bottom temperature reported for both the aluminum foam and CENG foam systems in Table 3.10 and Table 3.11 is the same as Table 3.9 and is included as a confirmation. Additionally, the top temperature reported as the time to melt is expected to be near the applied temperature of 60°C.

The poor thermal charging performance of paraffin wax as well as the enhanced charging rate as a result of the addition of aluminum foams is shown by the transient bottom temperature profiles in Figure 3.18. The data presented in Figure 3.18 and Table 3.10 show that 40 PPI foams increase the rate of charging better than the 10 PPI systems as shown by

a 34% decrease in the time to end of melt. The maximum percent error was calculated to be 7% of the time to end of melt.

Similar to constant heat flux experiments, this data suggests that the conductive heat transfer due to the high surface area of the 40 PPI system is more important to the overall heat transfer than natural convection, particularly present in the 10 PPI system due to the larger pore size. It is noted that the top temperature profile of the pure paraffin wax increases faster than that of the 40 PPI and 10 PPI systems. This is due to the poor conduction during charging of the pure PCM, which forms an insulating layer between the heater and the PCM since the thermal conductivity of liquid PCM is less the solid. The thermal barrier decreases the rate in which energy can move through the composite, thereby increasing the temperature of the top surface faster.

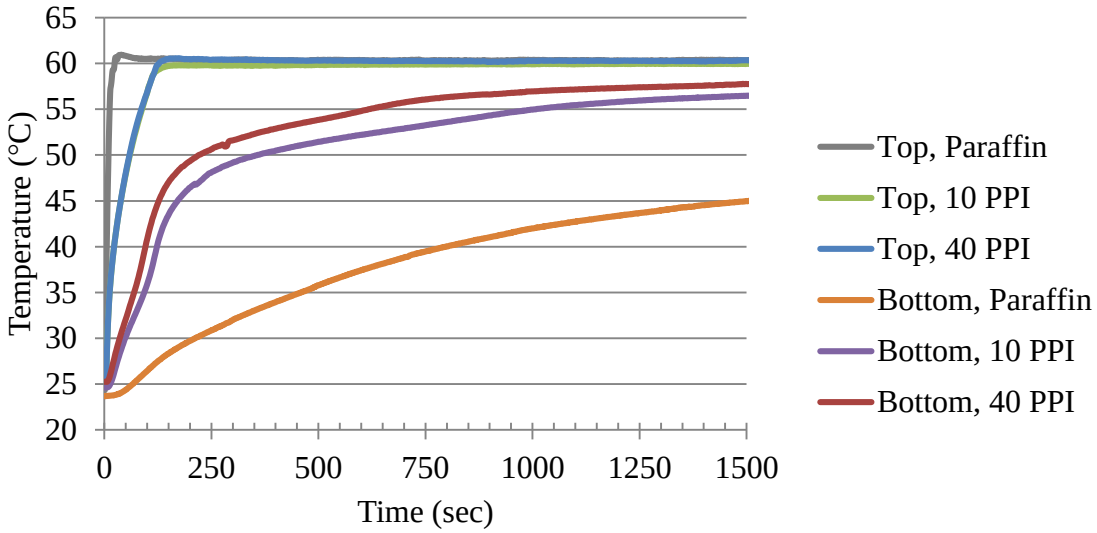

Figure 3.18. Thermal charging performance of paraffin wax as well as 10 PPI and 40 PPI aluminum foams (9% relative density) saturated with paraffin wax under 60°C.

Table 3.10. Time to end of melt for paraffin wax as well as 10 PPI and 40 PPI aluminum foams (9% relative density) with paraffin wax and PT37 under 60°C.

Aluminum Foam Pore Density	Time to End of Melt (sec)	Bottom Temperature (°C)	Top Temperature (°C)
10 PPI	986	55.2	60.3
40 PPI	646	55.2	59.9

Thermal charging experiments for CENG/paraffin wax composites is shown in Figure 3.19 and Table 3.11. The maximum percent error was calculated to be 4% of the time to end of melt. As the bulk density increases, the time to melt decreases. However, similar to the constant heat flux results, the percent improvement in time to end of melt decreases as the bulk density increases. For example, increasing the bulk density from 23 kg/m^3 to 50 kg/m^3 decreases the time to end of melt by 49%, but the decrease from 100 kg/m^3 to 143⊥ kg/m^3 and 143‖ kg/m^3 is 30% and 13%, respectively. It is also noted that, though not as defined as the paraffin wax data, the 23 kg/m^3 top temperature does increase slightly faster than the higher bulk density samples. This is due to the lower thermal conductivity of the composite, which increases the thermal resistance between the heater and the sample.

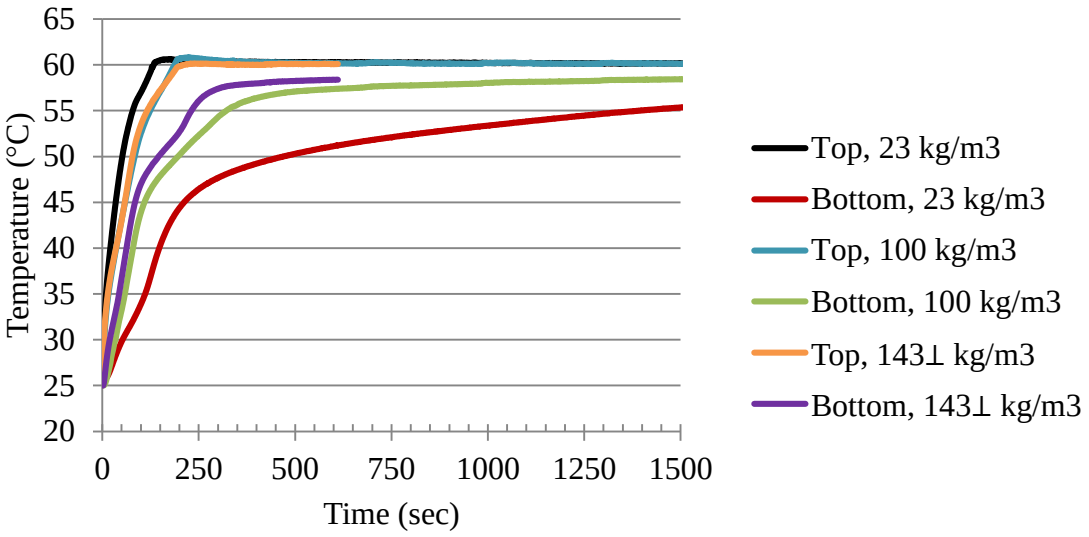

Figure 3.19. Thermal charging performance of 23, 100, and 143⊥ kg/m^3 CENG foams saturated with paraffin wax under 60°C.

Table 3.11. Time to end of melt for CENG foams saturated with paraffin wax under 60°C.

CENG Foam Bulk Density (kg/m^3)	Time to End of Melt (sec)	Bottom Temperature (°C)	Top Temperature (°C)
23	1906	56.3	60.2
50	965	56.3	60.4
100	305	54.5	60.3
143⊥	215	53.8	60.0
143‖	266	53.8	60.0

3.8 Aluminum Foam and CENG Foam Comparison

As previously discussed, the addition of a high conductivity material to increase the composite thermal conductivity decreases the latent heat of the composite. For aluminum foams, the composite latent heat was calculated based on the volume fraction due to the

open-cell geometry (Table 3.3). Additionally, the thermal conductivity was approximated based on the relative density and bulk thermal conductivity of the metal. For CENG foams, the latent heat decreases due to the addition of graphite and the formation of voids during the compression process. To characterize these samples, the latent heat and thermal conductivity was measured (Table 3.4). A comparison of composite latent heat and thermal conductivity for paraffin wax composites used in this study is shown in Figure 3.20. Recall that the relative density of open-cell foam ranges from 3-13%. The blue line represents the range of thermal conductivity and latent heat for composites formed with aluminum foam based on this relative density range. This limitation shows that for applications that require a higher conductivity composite, either a higher conductivity metal, such as copper, or graphite are required. Assuming a copper thermal conductivity of 400 W/m·K and using Equation 1, the limitation for copper foams ranging from 3-13% relative density is shown by the dashed green line in Figure 3.20. Though the 13% relative density copper foam composite has a similar latent heat decrease with a higher thermal conductivity than the 100 kg/m^3 graphite composite, the cost and density of copper foams constrains many applications.

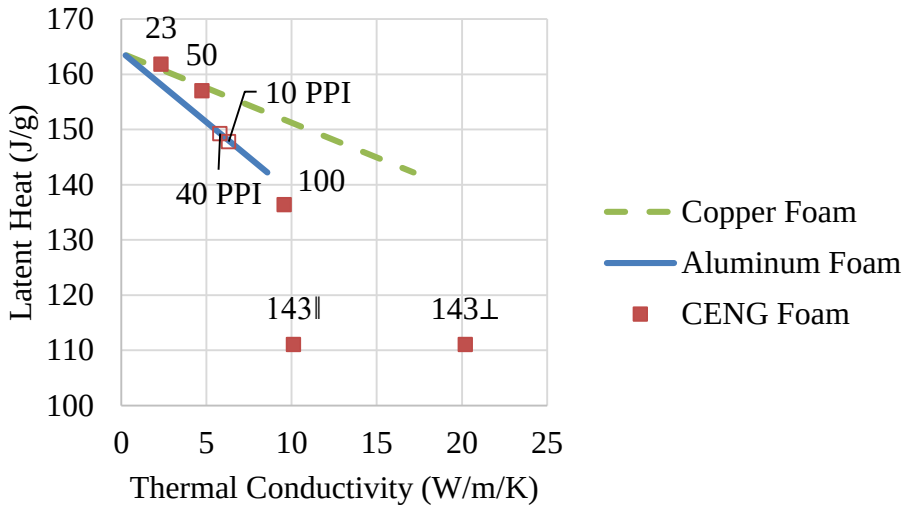

Figure 3.20. Thermal conductivity and latent heat of CENG and metal foam composites formed with paraffin wax. Solid represents CENG and open represents aluminum.

3.8.1 Constant heat flux

The junction temperature and time to end of melt for each graphite and aluminum foam is compared to the respective composite thermal conductivity in Figure 3.21. As the thermal conductivity increases, the junction temperature and time to end of melt decrease, but both tend toward a lower limit. For the experimental volume, a thermal conductivity beyond 10 W/m·K has limited impact on the thermal charging performance. This suggests that, in thermal battery design, systems approach a practical limit where the additional thermal conductivity does not provide improved performance.

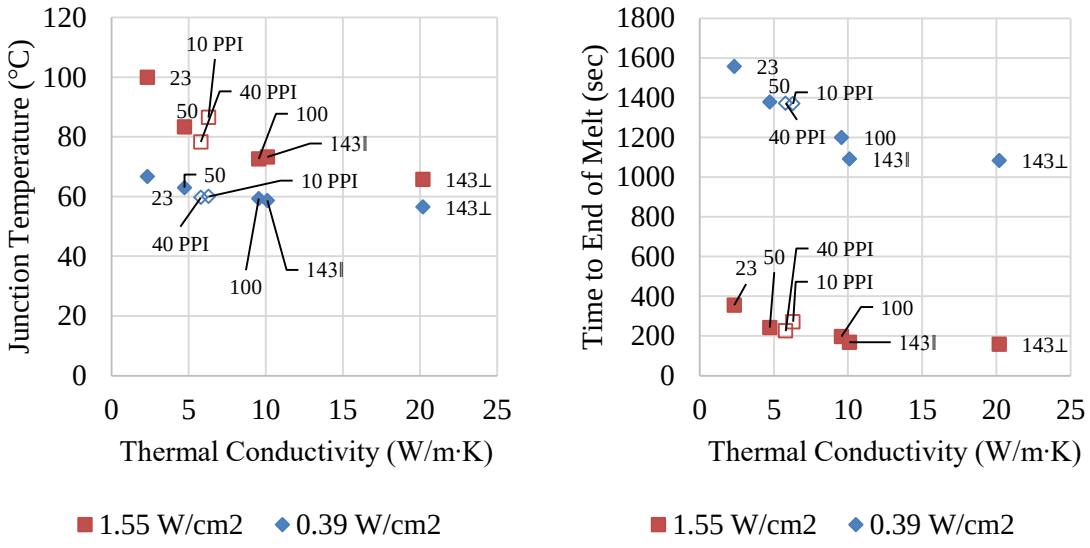

Figure 3.21. Junction temperature (left) and time to end of melt (right) compared to thermal conductivity of CENG and metal foam composites formed with paraffin wax. Solid represents CENG and open represents aluminum.

In addition to the junction temperature and rate of charge, many thermal battery applications are constrained by the weight of the system. Figure 3.22 compares the junction temperature (left) and the time of melt (right) to the bulk density of aluminum foams and CENG foams. It can be seen that the higher bulk density of aluminum foam does not provide additional benefit compared to CENG foams in terms of impact on junction temperature and time to end of melt. It is posited that the improved charging rate of CENG foams compared to aluminum foams is due to both the higher bulk thermal conductivity and the small pore size which increases the specific surface area of the foam. Pore sizes of aluminum foams range from 2 mm (40 PPI) to 4 mm (10 PPI), whereas the pore diameter of CENG foams has been reported to about be 1µm [21].

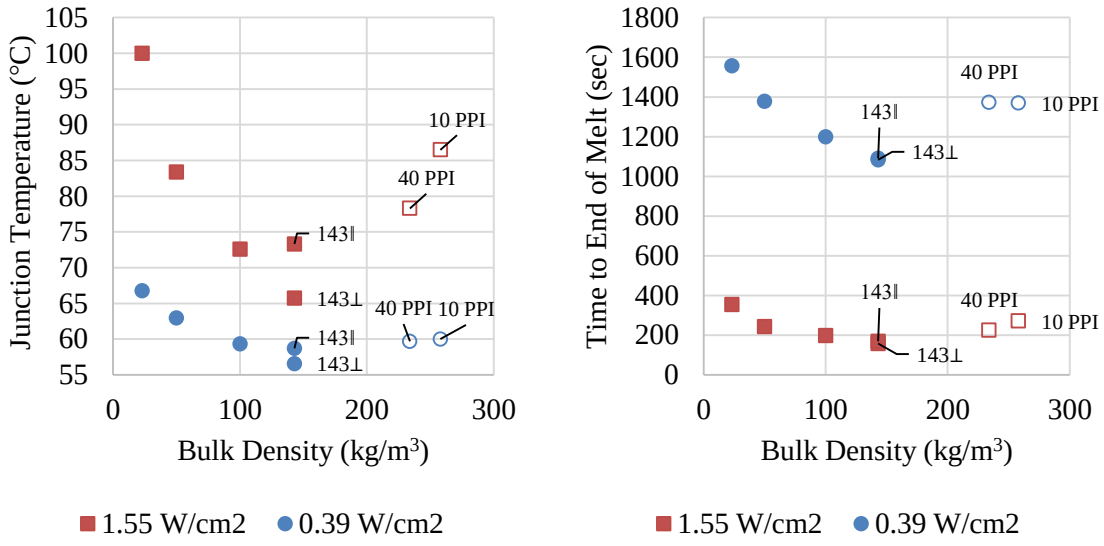

Figure 3.22. Juction temperature vs bulk density (left); Time to end of melt vs bulk density (right). Solid represents CENG and open represents aluminum.

3.8.1.1 Non-dimensional analysis

With the use of dimensionless parameters, Figure 3.20 through Figure 3.22 can be combined into a single plot using a dimensionless temperature and Fourier number [24, 37, 107]. The Fourier number, defined as the diffusive transport divided by the energy storage, takes into account the density, time to melt, thermal conductivity, height, and energy stored. By modifying the energy storage to account for both the sensible and latent heat storage, the parameters can be compared to a dimensionless temperature to account for material properties and thermal charging response. The modified Fourier number and dimensionless temperature used in this analysis are shown below:

$$Fo = \frac{k\, t_{melt}}{\rho H^2 \left(c_p + \frac{L}{T_{melt} - T_i}\right)} \tag{6}$$

$$\Theta = \frac{T_{junction} - T_{melt}}{T_{melt} - T_i} \quad (7)$$

For each experiment, the Fourier number and dimensionless temperature were calculated based on the composite thermal conductivity, latent heat, and melting temperature reported in Table 3.3 and Table 3.4 and the time to melt and junction temperature reported in Table 3.7 and Table 3.8. Composite density and specific heat were calculated based on a volume fraction assumption with the material properties listed in Table 3.12, and the volume fractions derived from the respective bulk densities and geometry previously reported. Recall that height of the samples was 1.27 cm, and experiments were conducted with heat fluxes of 1.55 W/cm^2 and 0.39 W/cm^2.

Table 3.12. Assumed thermophysical properties of paraffin, aluminum, copper, and graphite.

	Density (kg/m^3)	**Specific Heat (J/kg·K)**
Paraffin	910	2200
Aluminum	2700	910
Copper	8960	390
Graphite	2260	711

As shown by the log-log plot in Figure 3.23, a power law relates the Fourier number and the dimensionless temperature for constant heat flux conditions. Not only does this relationship hold for the aluminum and CENG foam experimental data presented in this work, but published experimental data for aluminum foam and copper foam (Table 3.13) is also included. This suggests that the use of the Fourier number and dimensionless temperature can simplify the complicated relationship between composite thermophysical

properties and charging response for porous foam/PCM composites. This relationship can also assist in the design of thermal batteries where limitations of heat flux, junction temperature, mass, or required energy storage are often defined and other system parameters such as the required composite thermal conductivity or system height to meet system constraints must be determined.

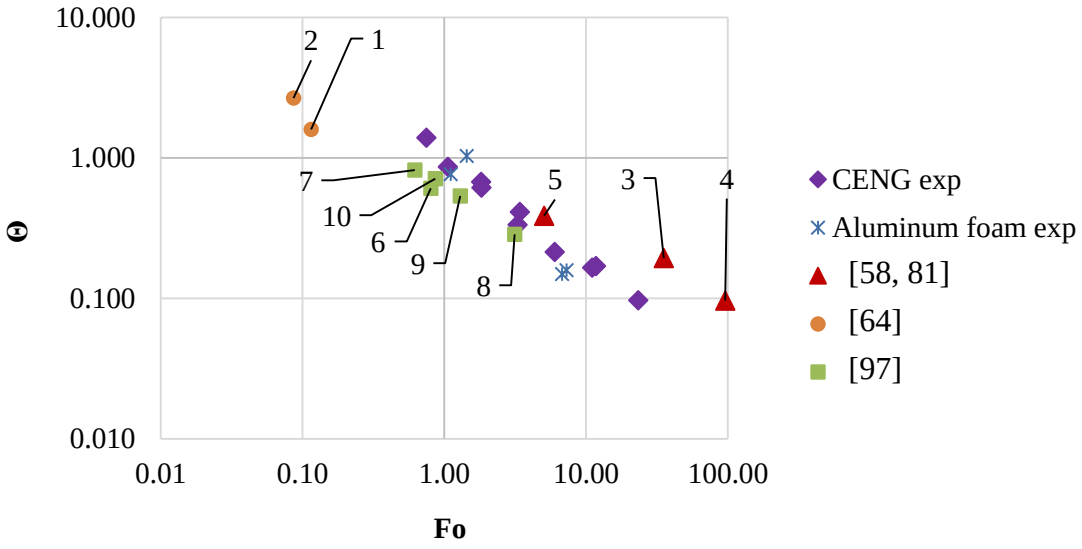

Figure 3.23. Fourier number compared to dimensionless temperature for porous foams saturated with PCM.

Table 3.13. Information on materials used in Figure 3.23.

ID	Source	Composite Details	Latent Heat (J/g) (Eq. 2)	Thermal Conductivity (W/m·K) (Eq. 1)	Time to Melt (sec)	Junction Temperature (°C)
1	Chintakrinda *et al.* [64]	9%, 40 PPI aluminum 5.8 W/cm^2	200.2	5.9	480	100.4 (linear interpolation from Table 2)
2	Chintakrinda *et al.* [64]	9%, 40 PPI aluminum 11.6 W/cm^2	200.2	5.9	360	131.5 (linear interpolation from Table 3)
3	Tian and Zhao [81]	5%, 40 PPI copper 0.16 W/cm^2	172.0	6.6	3100 (estimated based on Fig. 8)	62.0
4	Tian and Zhao [81]	15%, 40 PPI copper 0.2 W/cm^2	153.9	19.8	3850 (estimated based on Fig. 8)	59.0
5	Zhao *et al.* [58]	5%, 10 PPI copper 0.2 W/cm^2	172.0	6.6	4000 (estimated based on Fig. 4 (a))	68.0
6	Mancin *et al.* [97]	6.4%, 40 PPI aluminum 1.9 W/cm^2	186.8*	4.2	2000 (estimated based on Fig. 9)	70
7	Mancin *et al.* [97]	6.6%, 10 PPI aluminum 1.3 W/cm^2	187.2*	4.2	1550 (estimated based on Fig. 9)	76
8	Mancin *et al.* [97]	6.5%, 5 PPI aluminum 0.6 W/cm^2	187.0*	4.2	4000 (estimated based on Fig. 6)	61
9	Mancin *et al.* [97]	6.5%, 5 PPI aluminum 1.3 W/cm^2	187.0*	4.2	1650 (estimated based on Fig. 8)	68
10	Mancin *et al.* [97]	6.5%, 5 PPI aluminum 1.9 W/cm^2	187.0*	4.2	1100 (estimated based on Fig. 8)	73

* PCM latent heat not reported; assumed 200 J/g.

3.8.2 Constant temperature

Similar to the constant heat flux experiments, the time to end of melt for each graphite and aluminum foam is compared to the respective composite thermal conductivity and bulk density in Figure 3.24. The junction temperature is not reported, as is it near 60°C for all constant temperature experiments. Similar trends are reported for the constant temperature experiments as the constant heat flux experiments. As the thermal conductivity increases, the time to end of melt decreases, but tends toward a lower limit, suggesting that a practical limit exists where the additional thermal conductivity does not provide improved performance. Additionally, the higher bulk density of aluminum foam does not provide additional benefit compared to CENG foams in terms of decrease on time to end of melt. Non-dimensional analysis was not completed for the constant temperature experimental data since the non-dimensional temperature is the same for all systems due to the similar applied temperature and similar melting temperature.

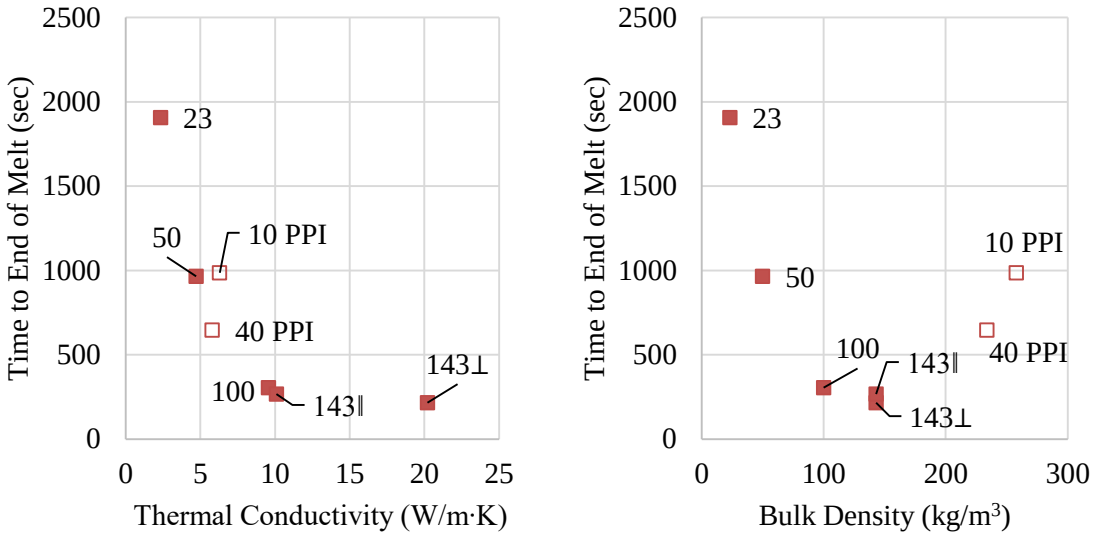

Figure 3.24. Time to end of melt compared to thermal conductivity (left) and bulk density (right) of CENG and metal foam composites formed with paraffin wax. Solid represents CENG and open represents aluminum.

In terms of thermal charging rate, junction temperature, and composite mass, Figure 3.20 through Figure 3.22 and Figure 3.24 highlight that CENG foams are superior to aluminum foams. For a constant heat flux condition, Figure 3.23 suggests a power relationship between the Fourier number and the dimensionless temperature defined in Equation 6 and Equation 7 for porous systems saturated with PCM.

It is acknowledged that metal foams outperform CENG foams in some aspects. First the production of CENG foam results in the formation of closed pores, whereas open-cell metal foams can be fully saturated with PCM. This is an issue especially for high bulk density CENG foams, which can impact the latent heat of the composite. Additionally, metal foam offers structural stability, whereas CENG foam is easily machined so that is can accommodate various geometries. However, metal foams are more expensive than

CENG foams. To consider the issue of latent heat and cost, two additions metrics, energy storage performance and energy storage cost, will be used to compare all composites.

3.9 Energy Storage Performance and Energy Storage Cost

Thermal charging experiments conducted for various aluminum and graphite foams discussed in 3.6 and 3.7 are used to compare the energy storage rate and cost for each of the composites. Data is analyzed by comparing the amount of energy stored as latent heat divided by the time to end of melt as a function of the material bulk density to quantify the energy storage performance. Additionally, the energy storage cost is calculated by dividing the bulk material cost by the latent heat of each of the composites. As provided from the manufacturers, the high volume cost of aluminum foam and CENG foam is $12/kg and $5/kg, respectively.

The relation between energy storage cost and energy storage performance is presented separately for each boundary conditions in Figure 3.25, Figure 3.26, and Figure 3.27. A high energy storage performance and low energy storage cost is preferential. The data presented in Figure 3.25 through Figure 3.27 indicates that CENG foam is superior to aluminum foam based on both thermal charging enhancement and cost. This data also demonstrates the need for analysis tools to guide the optimized thermal battery design based on the application. Most notably, the 143⊥ kg/m^3 and 143|| kg/m^3 composites move from a high energy storage performance to a low energy storage performance when comparing 60°C and 1.55 W/cm^2 to 0.39 W/cm^2 due to the impact on latent heat combined with limited impact on thermal charging rate as compared to other composites. Furthermore, it is noted that the range of energy storage performance values is highest for

60°C and decreases for 1.55 W/cm^2 and 0.39 W/cm^2. This suggests that optimization of the thermal battery based on charging performance is most critical for temperature conditions near the PCM melting temperature or high heat fluxes. As demonstrated by the comparison between energy storage cost and energy storage performance, CENG foams are superior when designing thermal batteries to maximize the charging response and energy density as well as minimize the cost.

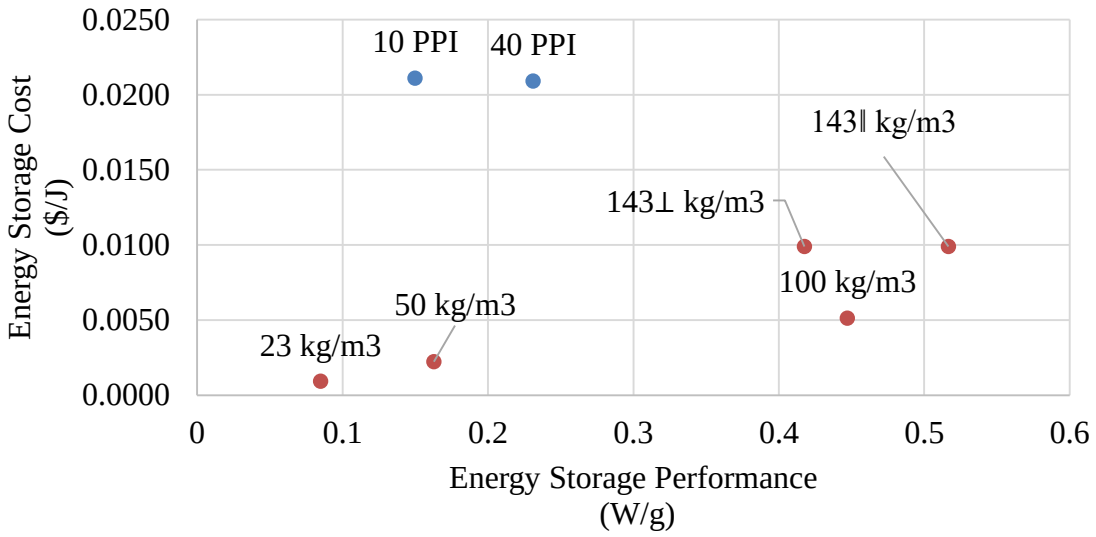

Figure 3.25. Comparison of energy storage performance to energy storage cost for aluminum foam (blue) and CENG foam (red) for experiments exposed to 60°C.

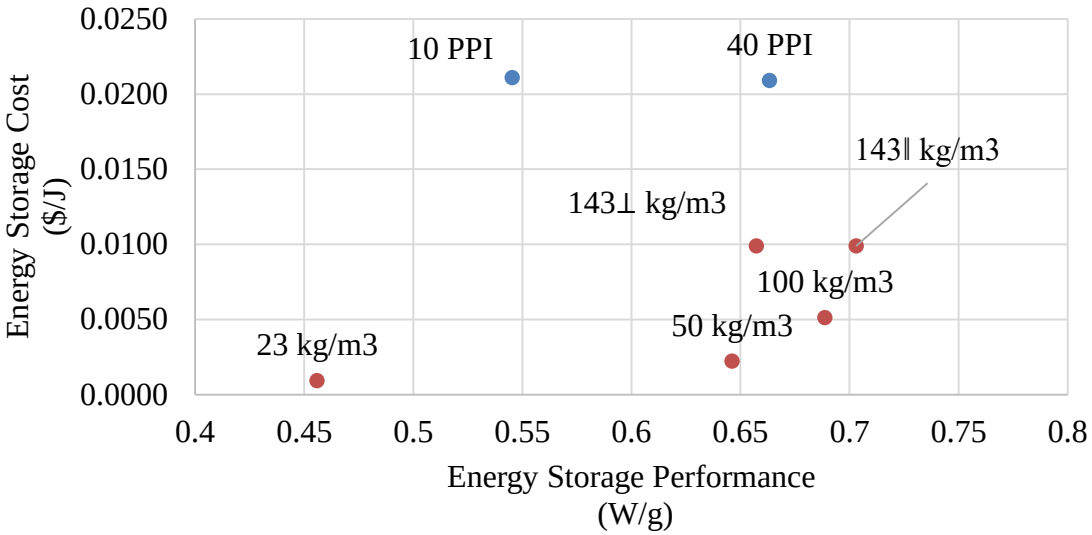

Figure 3.26. Comparison of energy storage performance to energy storage cost for aluminum foam (blue) and CENG foam (red) for experiments exposed to 1.55 W/cm^2.

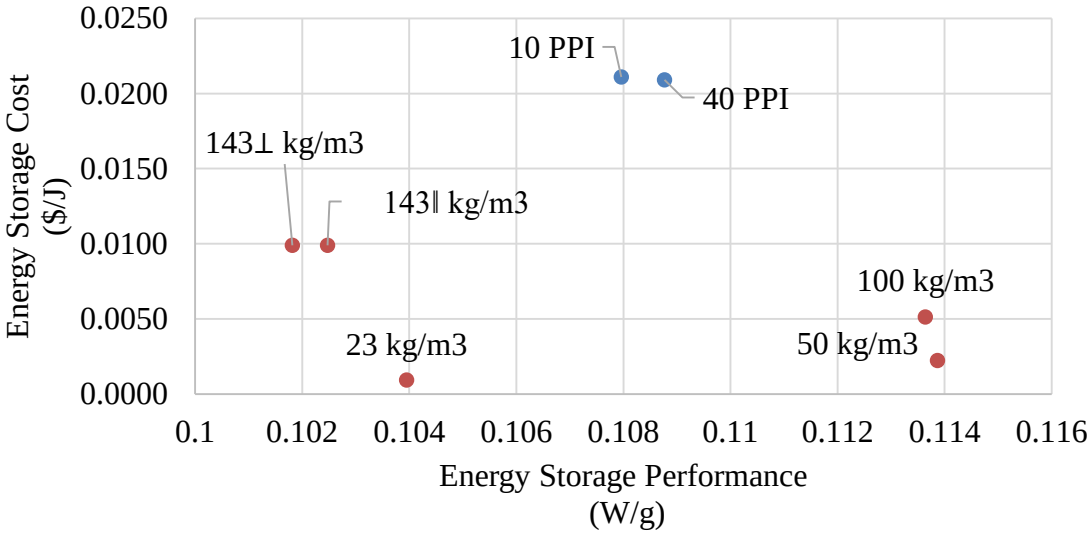

Figure 3.27. Comparison of energy storage performance to energy storage cost for aluminum foam (blue) and CENG foam (red) for experiments exposed to 0.39 W/cm^2.

3.9.1 Energy Storage Performance of CENG Foams

The energy storage performance of CENG foams is further discussed to demonstrate the concept of an optimized design based on charging rate and energy density. Recall that the decrease in time to end of melt for CENG foams is a result of both the increase in thermal conductivity and lower latent heat capacity due to the addition of graphite. At high bulk densities, closed pores formed during compression also decrease the composite latent heat. The combined effect of these two properties on the thermal charging rate can be seen in Figure 3.21 and Figure 3.22.

Even though the increase in thermal conductivity associated with an increase in CENG bulk density results in a decrease in time to end of melt, this relationship is not proportional. For example, under 1.55 W/cm^2, the 104% increase in thermal conductivity from 50 kg/m^3 to 100 kg/m^3 results in a decrease in time to end of melt by 19%. Further comparison of the 5% increase in thermal conductivity from 100 kg/m^3 to 143|| kg/m^3, results in a decrease in time to end of melt by 15%. The similar impact on melting time with a limited impact on thermal conductivity is due to the decrease in latent heat of the composite as shown in Figure 3.8 (right); a lower latent reduces the amount of energy stored during phase change, which results in a faster phase change transition. Furthermore, the 100% increase in thermal conductivity between 143|| kg/m^3 and 143⊥ kg/m^3 samples only decreases the charging rate by 7%. This suggests that comparing CENG composites based only on thermal conductivity is an insufficient metric to understand their thermal charging performance. Additionally, it is important to normalize the thermal charging rate by the composite latent heat since the amount of energy a composite can store will impact the thermal charging rate.

To determine the CENG bulk density threshold for each boundary condition, the time to end of melt and the latent heat measurements were used to find the energy storage performance. The calculated maximum percent error is 7% of the energy storage value. By comparing the rate of increase in energy storage for each boundary condition (constant temperature or constant heat flux), the tradeoff between increased rate of thermal charging and decrease in latent heat is presented. As shown in Figure 3.28, for the experimental sample, the benefit of additional graphite beyond 100 kg/m^3 for samples exposed to any boundary condition has limited impact on the energy storage performance. Additionally, the use of a CENG bulk density greater than 100 kg/m^3 actually decreases the energy storage performance for samples measured parallel to compression of the composite as a result of decrease in latent heat. Based on this discussion, it is apparent that the tradeoff between thermal conductivity and latent heat must be considered in thermal battery design with CENG composites. After a numerical model is validated with this experimental data, optimization will further be explored analytically in 4.5.

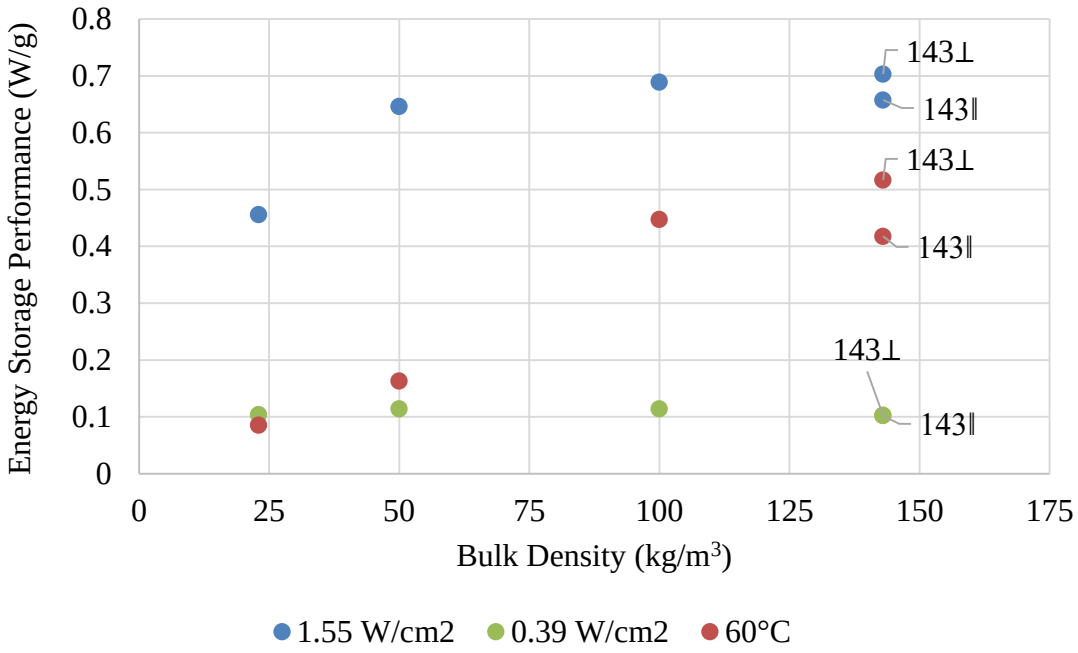

Figure 3.28. Energy storage performance as a function of the CENG bulk density for different constant heat flux and constant temperature boundary conditions.

3.10 Thermal Charging Experiment Conclusion

Phase change materials provide high thermal energy storage density for the development of thermal storage systems and advanced thermal management design. Thermal charging rates can be enhanced by the use of aluminum and CENG foams. This chapter addressed the impact of PCM viscosity, boundary condition, and thermal interface material on the junction temperature and time to end of melt for aluminum foams of various pore densities. Additionally, a comparative study on the thermal charging enhancement of CENG foams and aluminum foams under various boundary conditions was reported.

For constant heat flux experiments, it was found that high pore density aluminum foams outperformed other metal foams under high heat fluxes because of increased conduction due to greater specific surface area. This result was seen in both systems with

thermal grease and thermal epoxy and suggests a system of high pore density/high specific surface area. The impact of thermal interface material selection was shown through comparisons of junction temperature and time to end of melt. While thermal epoxy resulted in a faster temperature response, thermal grease exhibited a lower junction temperature. Under low heat fluxes, it was shown that not only the pore density, but also the PCM viscosity, impacted the response. High pore density metal foams resulted in a faster time to end of melt for all heat fluxes with low viscosity PCMs. Though high pore density foams saturated with high viscosity PCMs were superior when exposed to high heat fluxes, their thermal charging rate was similar to low pore density foams under low heat fluxes due to inhibition of natural convection. The impact of bulk density on thermal charging rate of CENG composites under various bulk densities was also reported. Finally, the charging performance of all composites exposed to a constant temperature near the melting temperature was discussed.

Following thermal charging experiments for aluminum and CENG foams, these systems were compared in terms of measured composite thermal conductivity and latent heat as well as experimentally determined junction temperature and time to end of melt. It was shown that the thermal charging enhancement of CENG foams is superior to that of aluminum foams on the basis of thermal charging rate, junction temperature, mass, and cost due to high thermal conductivity, low density, and small pore size. For constant heat flux experiments, a power law was found to relate the Fourier number and dimensionless temperature.

The importance of normalizing the thermal charging rate by the composite latent heat since the amount of energy a composite can store will impact the response was

discussed. Additionally, the energy storage cost was considered in the comparison of aluminum foams and CENG foams. Chapter 4 will discuss further modeling efforts to better understand these parameters and their impact on optimizing the design of thermal batteries for specific applications. This work will be used in Chapter 5 to guide the design of a thermal batteries with engineered thermal properties to enhance charging and discharging rates for use in space conditioning systems.

CHAPTER 4. THERMAL CHARGING MODELING

Continued research and development of enhanced latent heat thermal storage and management requires efficient and accurate modeling of such systems. As suggested experimentally in Chapter 3, a practical limit exists for all boundary conditions where an increase in thermal conductivity is no longer a benefit for thermal battery design when both energy density and storage rate are of interest. However, this limit is dependent on various material and system-level parameters that are application specific. The ability to model the thermal charging performance of thermal batteries enhanced by metal foams or graphite foams is important for the optimization of systems for specific applications.

The objective of this chapter is to explore the current state of models for thermal charging of phase change materials and to develop methods that improve their accuracy and allow for a reduced order formulation for the prediction of charging and discharging times. First, the chapter discusses transient modeling of phase change materials and methods to calculate effective properties such as thermal conductivity, which is often used to compare PCMs and PCM composites. The issue of heterogeneous and homogenized microstructures is also addressed, which leads to different approaches for modeling the transient response of metal foam/PCM and CENG/PCM composites. Finally, models of various enhanced PCM composites and their experimental validation are explored provide in order to make accurate and meaningful comparisons between systems and to offer modeling approaches that will be used later in the design of PCM composites for waste heat storage.

4.1 Modeling Phase Change Materials

Modeling latent heat thermal storage materials introduces a non-linearity into the heat transfer problem since thermal energy is stored or released at a constant temperature during phase change. As summarized by Iten and Liu [108], during the phase change process, a boundary develops between the two phases which advances through the material based on the rate of latent heat being absorbed or released at the boundary. In order to describe the temperature distribution through the homogenous medium, the evolution of the boundary through the material must be understood. This moving boundary problem, referred to as the Stefan problem, can be solved analytically, though only feasible for basic 1D analysis, or numerically.

The most common 1D analytical solution to the Stefan problem, referred to as the Neumann solution, is developed by imposing two boundary conditions on the phase change boundary [108]. In addition to a constant temperature condition, $T_{solid} = T_{liquid} = T_{melt}$, at the phase change boundary, an energy balance is written such that the net heat flux across the boundary is equal to the energy being absorbed as latent heat as shown in Equation 8 where L is the latent heat of fusion and X is the location of the phase change interface. The material occupies the domain $-\infty < x < \infty$ where at $x = 0$ the system is isothermal in that for $x < 0$ and $x > 0$ the material is solid and liquid, respectively.

$$k_{solid}\frac{\partial T_{solid}}{\partial x} - k_{liquid}\frac{\partial T_{lqiuid}}{\partial x} = L\rho\frac{dX(t)}{dt} \tag{8}$$

Along with appropriate boundary and initial conditions, conservation of energy can be applied to both the liquid (Equation 9) and solid (Equation 10) domains to fully define

the system as discussed in [109, 110] with no heat generation and temperature independent properties. In Equations 9 and 10, ρ is the density, c_p is the specific heat, k is the thermal conductivity. A diagram of the Neumann solution is shown in Figure 4.1.

$$\rho_{liquid} c_{p_{liquid}} \left(\frac{\partial T_{liquid}}{\partial t} + \vec{v} \cdot \nabla T_{liquid} \right) = \nabla (k_{liquid} \nabla T_{liquid}) \tag{9}$$

$$\rho_{solid} c_{p_{solid}} \left(\frac{\partial T_{solid}}{\partial t} \right) = \nabla (k_{solid} \nabla T_{solid}) \tag{10}$$

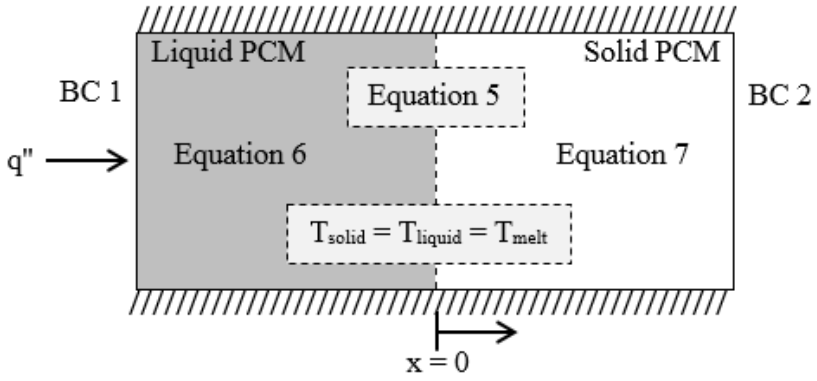

Figure 4.1. Diagram of Neumann solution for 1D phase change solution.

To account for natural convection, conservation of mass and momentum can be applied to the liquid region. Lamberg *et al.* [109] suggests to use the Boussinesq approximation (density variation is only important in the buoyancy term) to model the buoyancy forces. This approximation in combination with the continuity and Navier-Stokes equations to model fluid flow is shown in Equation 11 and Equation 12, where ρ is the density, $\vec{v}$ the velocity of the liquid PCM, p the pressure, μ the dynamic viscosity, $\vec{g}$ the gravity vector, β the coefficient of thermal expansion, T_o the reference temperature, c_p the specific heat, k the heat conductivity and T_{liquid} the temperature of the liquid PCM.

$$\nabla \cdot \vec{v} = 0 \tag{11}$$

$$\rho \frac{\partial \vec{v}}{\partial t} + \rho(\vec{v} \cdot \nabla)\vec{v} = -\nabla p + \mu \nabla^2 \vec{v} + \rho \vec{g} \beta (T_{liquid} - T_0) \tag{12}$$

Due to the complexity of the phase change problem, analytical solutions are limited to basic one-dimensional analysis with constant properties. To study 2D and 3D phase change phenomena and include variation in the thermal properties as a function of temperature, numerical models are employed. The two most common solution methods are referred to as the enthalpy method and the effective heat capacity method [108].

The enthalpy method and the effective heat capacity method reformulate the Stefan problem such that the phase change boundary is not explicitly tracked through the material. This is advantageous because, in reality, multiple phase changes can occur in a material over a non-isothermal temperature range, such as solid-solid crystalline rearrangement later followed by solid-liquid phase change at a higher temperature [109]. For the enthalpy method, a function, $h(T)$, is defined as the sum of the sensible heat and the latent heat required for the phase change. By inserting $h(T) = \int_{T_{melt}}^{T} \rho c_p \, dT + \rho f(T) L$ where $f(T)$ is the local liquid fraction defined as $f(T) = \frac{T - T_{solid}}{T_{liquid} - T_{solid}}$, the Equations 9 and 10 can be simplified,

$$\left(\frac{\partial h(T)}{\partial t} + \vec{v} \cdot \nabla T_{liquid}\right) = \nabla(k_{liquid} \nabla T_{liquid}) \tag{13}$$

$$\left(\frac{\partial h(T)}{\partial t}\right) = \nabla(k_{solid} \nabla T_{solid}) \tag{14}$$

One way to account for natural convection within the system is to introduce a heat transfer coefficient (h_c), thereby describing heat transfer through the system with appropriate boundary conditions without the mass and momentum conservation equations [109].

$$\rho \frac{\partial h(T)}{\partial t} + h_c \nabla T = \nabla(k \nabla T) \tag{15}$$

In Equation 15, $h(T)$ is the enthalpy function and h_c is the heat transfer convection coefficient determined such as in the work of Lamberg and Siren [111]. With the appropriate boundary and initial conditions, this relation fully defines the phase change problem. This equation can also be written as shown by Equation 16.

$$\rho c_p(T) \frac{\partial T}{\partial t} + h_c \nabla T = \nabla(k \nabla T) \tag{16}$$

As a result of non-isothermal phase change, there are three phase regions that correspond to a solid zone, liquid zone, and an intermediate mushy zone in between the solid and liquid phases. This mushy zone, as shown in Figure 4.2, also prevents sharp discontinuities that may create some numerical instabilities. Table 4.1 presents the three definitions of $h(T)$ as well as the thermal conductivity as defined for each region [108, 112] which would be inserted into Equation 15. Recall that the phase change may occur over a range of temperature, denoted by ΔT. Additionally, the melting temperature is described as T_{melt} such that $T_{solid} = (T_{melt} - \Delta T/2)$ and $T_{liquid} = (T_{melt} + \Delta T/2)$.

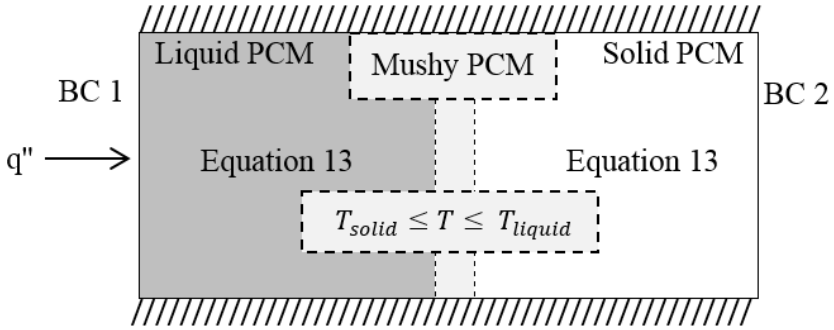

Figure 4.2. Diagram of enthalpy method for 1D phase change solution

Table 4.1. Description of functions used in enthalpy formulation.

Phase	**Enthalpy Formulation $h(T)$**	**Thermal Conductivity Relation**	**Applicable Temperature Range**
Solid	$\int_{T_m}^{T} \rho_{solid} c_{p_{solid}} \, dT$	$k = k_{solid}$	$T < T_{solid}$
Mushy	$\int_{T_m}^{T} \rho f(T) L$	$k = k_{solid} + \left(\frac{k_{liquid} - k_{solid}}{T_{liquid} - T_{solid}}\right)(T - T_{solid})$	$T_{solid} \leq T \leq T_{liquid}$
Liquid	$\int_{T_m}^{T} \rho_{liquid} c_{p_{liquid}} \, dT + \rho f(T) L$	$k = k_{liquid}$	$T > T_{liquid}$

The third method of solving the Stefan program is similar to the enthalpy method in that temperature dependent properties can be accounted for as well as a non-isothermal phase transition. The effective heat capacity method adjusts the energy equation (Equation 15) of the enthalpy method by noting that $\frac{\partial h}{\partial t} = \frac{\partial h}{\partial T}\frac{\partial T}{\partial t} = c_p \frac{\partial T}{\partial t}$.

$$\rho c_p \frac{\partial T}{\partial t} + h_c \nabla T = \nabla(k \nabla T) \tag{17}$$

where,

$$c_p = \begin{cases} c_{p_{solid}} & T < T_{solid} \\ c_{p_{eff}} & T_{solid} \leq T \leq T_{liquid} \\ c_{p_{liquid}} & T > T_{liquid} \end{cases}$$

$$c_{p_{eff}} = \frac{L}{(T_{liquid} - T_{solid})} + \frac{c_{p_{solid}} + c_{p_{liquid}}}{2}$$

As Equation 17 shows, the effective heat capacity of the material, $c_{p_{eff}}$, is directly proportional to the stored and released energy during phase change and inversely proportional to the phase change temperature range. Lamberg *et al.* [109] summarized these two methods of solving the Stefan problem and included the following graph to describe the difference between the two methods. Figure 4.3 depicts the difference in the heat capacity calculation for the enthalpy method and the effective heat capacity method with two different temperature ranges, denoted by dT.

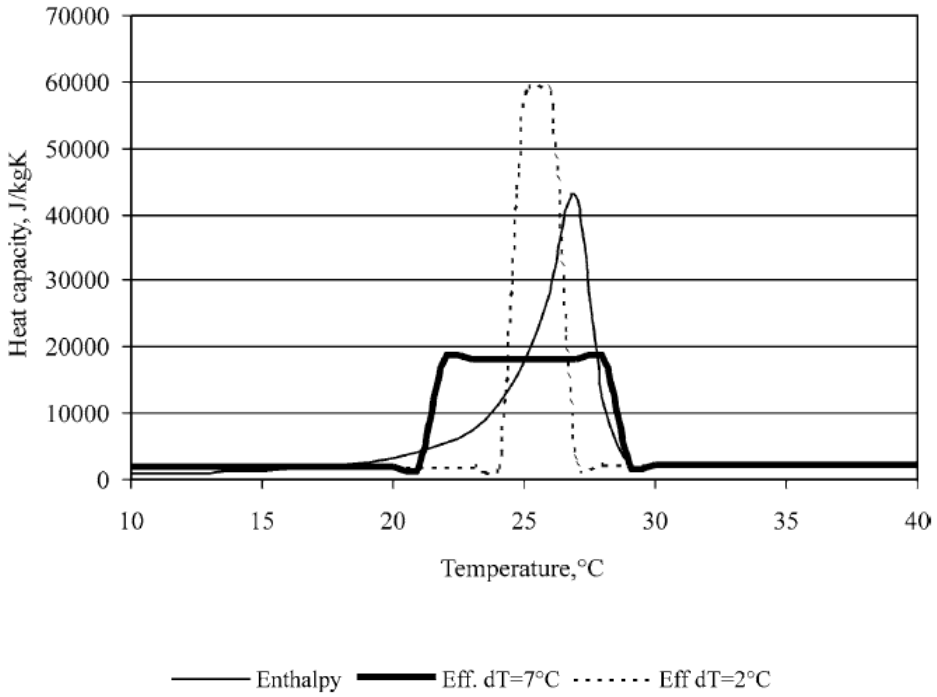

Figure 4.3. The specific heat capacities in the melting process for the enthalpy and heat capacity methods [109].

Most numerical studies of phase change in pure PCM use either the enthalpy method or effective heat capacity method to model phase change in the 2D or 3D transient heat transfer problem. Lamberg *et al.* [109] found that for small temperature ranges, the effective heat capacity method is more precise than the enthalpy method, though both provide good approximations of the phase change behavior. Additional studies can be found summarized by Iten and Liu [108] as well as Dutil *et al.* [112] which provide thorough lists of numerical studies of pure PCM in various geometries.

As geometries and applications become more complicated, the use of computational modeling software, such as COMSOL and FLUENT, is becoming more common to solve 3D transient heat transfer problems. For example, Ye *et al.* [113], Dolado

et al. [114], and Raj and Velraj [115] used FLUENT to study fluid flow and heat transfer behavior in PCM latent heat thermal units. Studies were also completed in COMSOL by Murray and Groulx [116] as well as Liu and Groulx [32].

4.2 Modeling Phase Change Materials Enhanced with Porous Foams

The enthalpy method and the effective heat capacity method can be extended to study the heat transfer within porous foams saturated with a phase change material. There are two methods of studying this composite material heat transfer problem: using a volume averaging technique by incorporating the relative density (γ) of the foam in the thermophysical properties or to model the foam geometry saturated with PCM via SOLIDWORKS, COMSOL, FLUENT, etc. with computing ability to tolerate the simulation complexity. First, volume averaging techniques for open-cell foams will be discussed (4.2.1) followed by CENG foams (4.2.2) and then the use of modeling software packages in 4.4.

4.2.1 Modeling open-cell metal foams

The volume averaging technique uses the relative density of the material to adjust the thermophysical properties of each unique material in the system by its respective volume in the composite [78, 81]. When modeling the PCM and the foam separately, heat transfer between the two materials can be modeled by Newton's law of cooling with an interstitial heat transfer coefficient (h_{sf}) and the surface area between the foam and the PCM (a_{sf}) [117].

Some numerical studies do consider the impact of natural convection [78, 118], but a simplifying assumption made for heat transfer in porous media with phase change is that natural convection is suppressed within the porous material [117, 119]. As discussed in 3.6.1.3, Zhao *et at.* [106] found that a Rayleigh number is a significant parameter to describe the intensity of natural convection, and natural convection is insignificant for cases when the $Ra \leq 10^4$. Experiments reported 3.6.1.3 suggest the dominance of conduction as well as the limited influence of natural convection, especially for higher viscosity PCMs.

Other studies that focus on the impact of natural convection include Chen *et al.* [96] who conducted an experimental and numerical study simulating both conduction and natural convection for 9 PPI, 8.63% relative density aluminum foam on the melting behavior of phase change material. It was found that heat transport within the foam/PCM composite was dominated by conduction. Similarly, Tian and Zhao [81] experimented with various relative densities (5% and 15%) and pore densities (10 PPI and 30 PPI) of copper foam and found that the velocity driven by buoyancy force is so small due to high viscosity of the PCM and high flow resistance in the metal foams that the natural convection fails to produce dominant influence on heat transfer. Furthermore, Kota *et al.* [120] summarize that due to small pores, which reduces the effect of gravity by inducing a capillary effect, and the large surface area to volume ratio, natural convection in the melt is insignificant.

With the assumption that natural convection can be neglected in the heat transfer analysis, the governing equations can be rewritten for transient conduction as shown by Equation 18 and Equation 19.

$$(\gamma)(\rho c_p)_{foam}\frac{\partial T_{foam}}{\partial t} = \nabla \cdot \left(k_{foam_{eff}} \nabla T_{foam}\right) - a_{sf} h_{sf}\left(T_{foam} - T_{PCM}\right) \quad (18)$$

$$(1-\gamma)\left(\rho c_p\right)_{PCM}\left(\frac{\partial T_{PCM}}{\partial t}\right) + (1-\gamma)(\rho_{PCM} L)\frac{df}{dt} = \nabla \cdot \left(k_{PCM_{eff}} \nabla T_{PCM}\right) + a_{sf} h_{sf}\left(T_{foam} - T_{PCM}\right) \quad (18)$$

In Equation 18 and Equation 19, γ is the relative density, $k_{foam_{eff}}$, a_{sf}, and h_{sf} are the effective thermal conductivity of the foam, surface area per unit volume of the foam, and the heat transfer coefficient between the solid and PCM, respectively. Additionally, $k_{PCM_{eff}}$ is the effective thermal conductivity of the PCM, L is the heat of fusion of the PCM, and f is the liquid fraction. All of these parameters depend on the structure of the porous medium and the volume fractions of each material.

Both the specific surface area, a_{sf}, and the heat transfer coefficient, h_{sf}, and are highly dependent on the foam structure. Specific surface area can be estimated based on geometric parameters [80, 121-123], while the heat transfer coefficient can be estimated based on empirical correlations [78, 81, 106, 123]. A summary of the correlations for inter-phase heat transfer was published by Zhang *et al.* [61]. The estimation of effective thermal conductivities for the PCM and foam is an area of much attention and will be discussed in 4.2.3. Energy stored in the PCM in solid, mushy, and liquid phase can then be solved through either the enthalpy method [81, 124, 125] or the specific heat capacity method [78].

To further simplify this transient heat conduction problem, consider the temperature gradient between the foam and the paraffin. As Equations 18 and 19 indicate,

the heat flux from the foam into the paraffin provides a necessary condition to satisfy conservation of energy. However, if thermal equilibrium is established between the boundary of the paraffin and the foam, these two equations can be written as a one-temperature model as shown in Equation 20.

$$\left[(1-\gamma)(\rho c_p)_{PCM} + (\gamma)(\rho c_p)_{foam}\right]\frac{\partial T}{\partial t} + (1-\gamma)(\rho_{PCM} L)\frac{df}{dt} = \nabla \cdot (k_{composite} \nabla T) \tag{20}$$

To calculate the energy stored in the PCM in solid, mushy, and liquid phase, either the enthalpy method [38, 96, 126] or the specific heat capacity method [120, 127] can be used. Note that, similar to the energy equation, the enthalpy or specific heat must be adjusted using the volume averaging technique. For example, the effective heat capacity method would adjust Equation 20 as shown by Equation 21. Recall that the melting temperature is described as T_{melt} such that $T_{solid} = (T_{melt} - \Delta T/2)$ and $T_{liquid} = (T_{melt} + \Delta T/2)$. The composite thermal conductivity will be discussed in 4.2.3.

$$\left[(1-\gamma)(\rho c_p)_{PCM} + (\gamma)(\rho c_p)_{foam}\right]\frac{\partial T}{\partial t} = \nabla \cdot (k_{eff} \nabla T) \tag{21}$$

where,

$$(\rho c_p)_{PCM} = \begin{cases} \rho c_{p_{solidPCM}} & T < T_{solid} \\ \rho c_{p_{eff}} & T_{solid} \leq T \leq T_{liquid} \\ \rho c_{p_{liquidPCM}} & T > T_{liquid} \end{cases}$$

$$c_{p_{eff}} = \frac{L}{(\Delta T)} + \frac{c_{p_{solidPCM}} + c_{p_{liquidPCM}}}{2}$$

Various studies use the one and two-temperature models to simulate heat transfer in open-cell foam/PCM composites. As recently summarized by Zhang *et al.* [61], though early studies assume local thermal equilibrium between the porous structure and PCM, due to the existence of the interface between solid porous phase and PCM, a thermal resistance exists across the boundary. Therefore, the effect of thermal non-equilibrium must be taken into consideration, meaning that a two-temperature model is considered more accurate than a one-temperature model.

4.2.2 Modeling CENG foams

Modeling open-cell metal foam/PCM composites is complicated by the large open-cell pore structure, which requires effective thermal conductivity correlations to be discussed in 4.2.3, as well as the two-temperature model to simulate heat transfer. However, the small pore size of graphite foam as a result of the compaction process allows the composite to be modeled with the one-temperature model as a homogenous medium by Equation 21. This means that the thermophysical properties are adjusted as a function of the bulk density [128-132] and natural convection is negligible [131, 133]. The composite thermal conductivity and latent heat can either be directly measured or based on correlations with bulk density [60, 129, 131].

Luo *et al.* [132] found good correlation between a one-temperature 3D model with directional thermal conductivities and experimental data. It was summarized that the larger the thermal conductivity along the direction of the heat flow, the more uniform the temperature distribution and the shorter the time for melting the composite PCM. Other one-temperature models discussed by Wang *et al.* [131] (2D model) and Greco *et al.* [129]

and Zhao *et al.* [130] (3D models) with directional dependent thermal conductivities also studied the impact of anisotropy on the charging response of CENG composites. Both constant heat flux [130, 132] and constant temperature [128, 129, 131] have been considered, and results are generally reported through transient temperature and transient melting front profiles. For all studies, heat transfer was greater in the direction of higher thermal conductivity, similar to Luo *et al.* [132].

4.2.3 Effective thermal conductivity and the homogenous assumption

The primary difference between modeling open-cell metal foams and CENG foam composites is the effective thermal conductivity approximation required of the two-temperature model (Equations 18 and 19) or the one-temperature model (Equation 20). While pore size, relative density, and temperature have been found to impact the thermal conductivity of open-cell metal foams, the measured composite thermal conductivity can be used to model CENG as a homogenous medium.

To better understand the limit of pore size on the homogenous material assumption, a 2D porous geometry has been studied in COMSOL composed of PCM and aluminum with varying pore sizes. The properties used in this simulation are shown in Table 4.2. During all simulations, the following assumptions were made:

1) Natural convection and radiation negligible; conduction only.
2) Applied temperature is 50°C.
3) The foam is fully saturated with PCM and there is no volume change of PCM.

Table 4.2. Properties of PCM and aluminum used in model.

	Phase Change Temperature	Density (kg/m^3)	Specific Heat (J/kg·K)	Thermal Conductivity (W/m·K)	Latent Heat (J/g)
PCM	38°C, ΔT = 6°C	920	2210	0.25	210
Aluminum	-	2700	900	200	-

Starting with a square of sides 10 mm, 90% of the area was partitioned into an inner square and assigned properties of the PCM, while the remaining material was assigned properties of the aluminum. The single pore geometry is shown in Figure 4.4 (upper left). To study the impact of pore size, the number of inner squares was continually increased, though 90% of the area remained PCM as shown in Figure 4.4. A temperature was applied to the top boundary, while the remaining sides were insulated. The initial temperature was 25°C, and the applied temperature was 50°C. A schematic of the initial and boundary conditions is shown in Figure 4.5. Geometric properties of each of the systems modeled are shown in Table 4.3.

Table 4.3. Geometric properties of foams used in simulation.

	Specific Surface Area (mm/mm^2)	Cell Side Length (mm)
1 block	0.379	9.487
4 blocks	0.759	4.743
9 blocks	1.138	3.175
16 blocks	1.518	1.723
100 blocks	3.795	0.949
625 blocks	9.487	0.379
2500 blocks	18.974	0.190

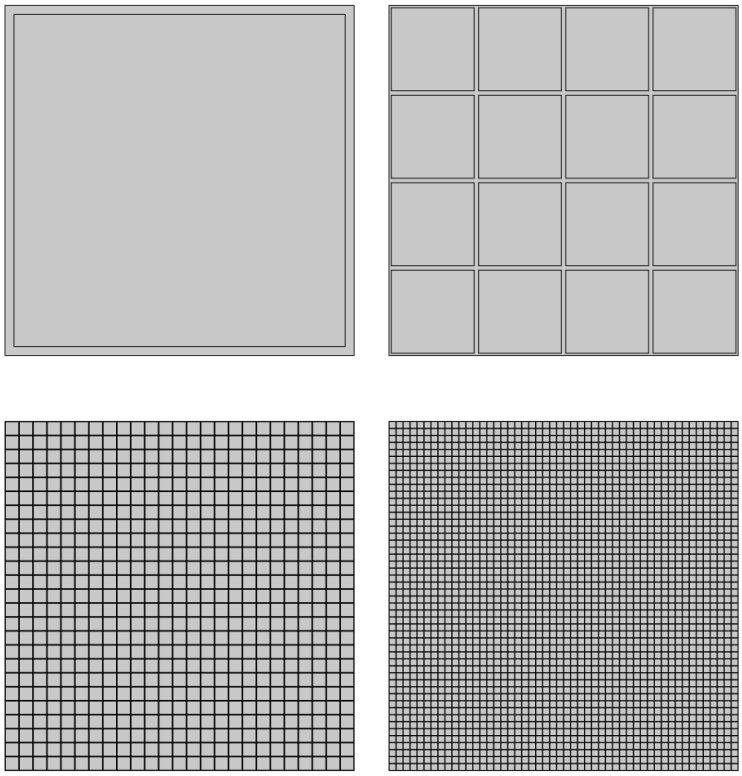

Figure 4.4. Geometry used in model: 1 pore (upper left), 16 pores (upper right), 625 pores (lower left), 2500 pores (lower right).

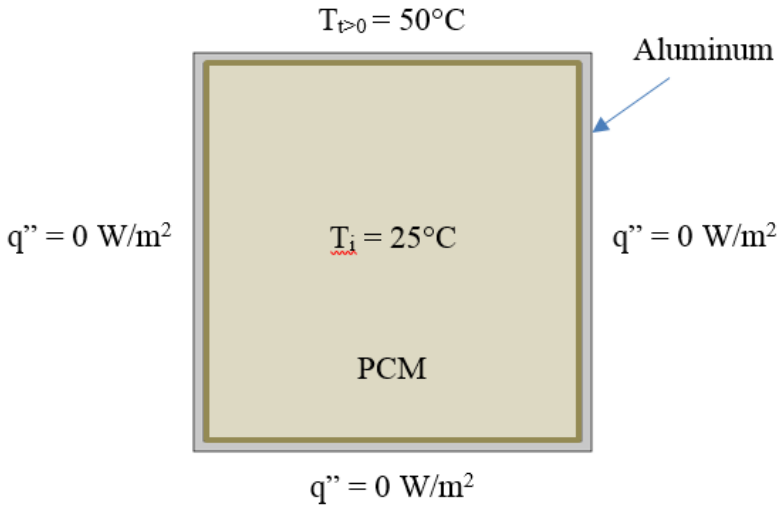

Figure 4.5. Schematic of the initial and boundary conditions.

The results were analyzed in three ways. First, the temperature distribution at 50 seconds is shown in Figure 4.6. In a homogenous material with the applied temperature only on the top boundary, the temperature distribution would not vary in the horizontal (X) direction. Particularly for the 1 block and 16 block systems, the change in temperature in both the horizontal and vertical direction indicates that the impact of the pore size and temperature must be considered in an effective thermal conductivity calculation to accurately capture the thermal charging response.

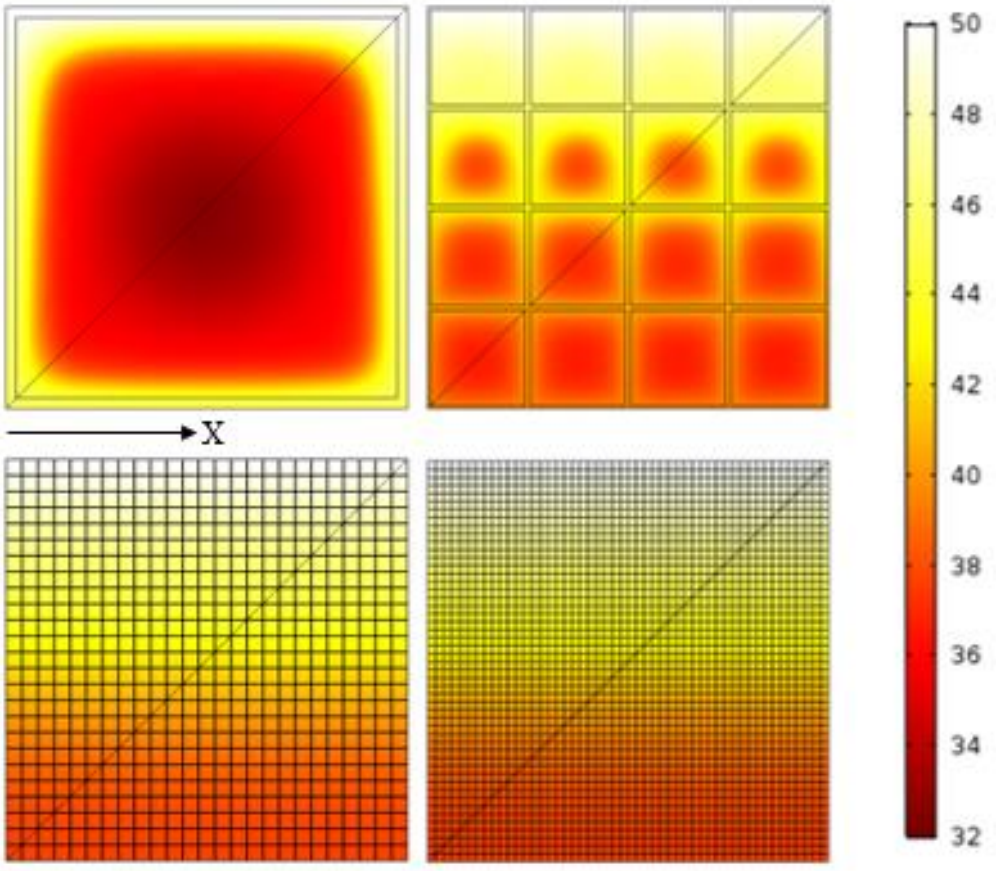

Figure 4.6. Temperature distributions for each geometry at 50 seconds: 1 pore (upper left), 16 pores (upper right), 625 pores (lower left), 2500 pores (lower right).

Another way to study the results is to graph the temperature along the diagonal line for each of the geometries in Figure 4.6 as shown in Figure 4.7. The red and blue lines represent the temperature distribution of the 1 block and 16 block systems, respectively. The variation along the x-coordinate indicates the presence of the PCM and reiterates that an effective conductivity purely based on relative density would not represent the material.

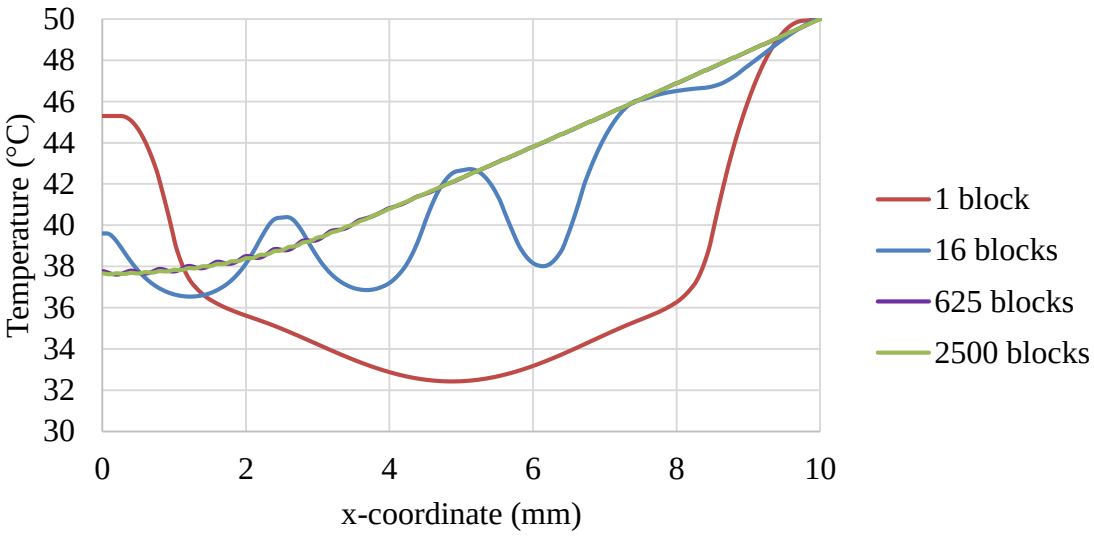

Figure 4.7. Temperature profile along diagonal for each system in Figure 4.6.

As the number of blocks increases, the temperature profile steadies as shown by the purple and green lines of the 625 and 2500 blocks. Slight variation is seen in the temperature profile of the 625 block systems, while the 2500 block system is steady. Note that the change in slope of both the 625 and 2500 block systems occurs at x = 2 mm, which corresponds to the edge of the material that is undergoing phase change.

These results can also be used to compare the temperature profile deviation from that of a homogeneous system as a function of specific surface area, calculated from pore

size. The first step is to determine the effective thermal conductivity of this system. This is done by modeling the entire 10 mm square block as homogeneous material with the density and specific heat adjusted by volume fraction and varying the thermal conductivity until good correlation is exhibited with the 2500 block system. The effective thermal conductivity found to represent this system is k_{eff} = 14 W/m·K. The temperature distribution is shown in Figure 4.8 and Figure 4.9.

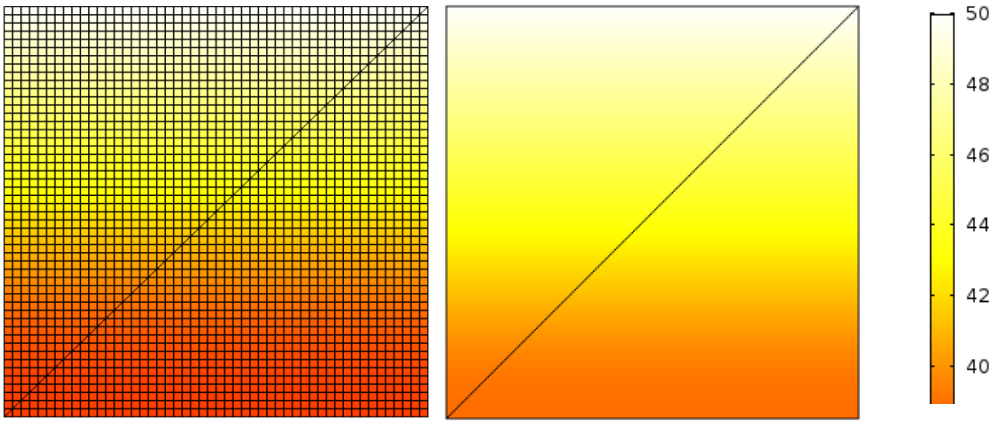

Figure 4.8. Temperature distribution of 2500 blocks (left) and the homogenous system (right) at 50 seconds.

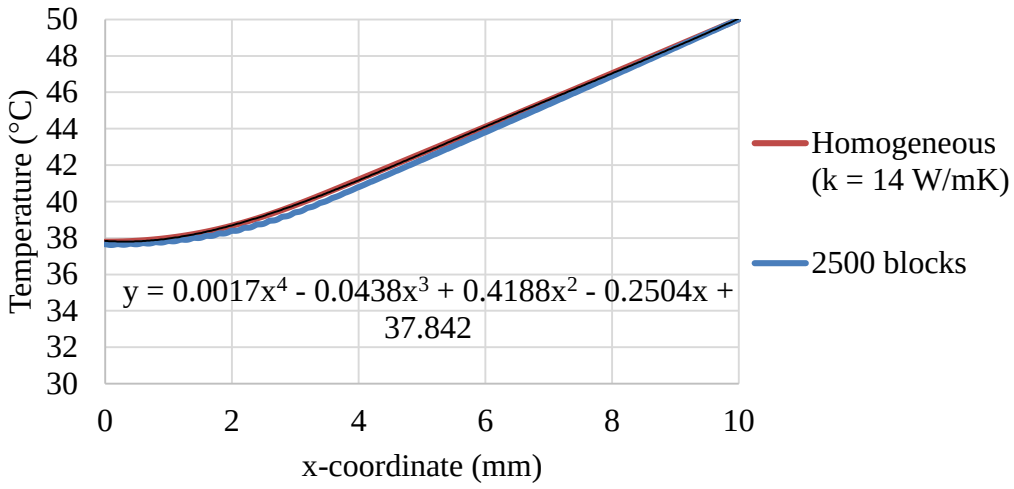

Figure 4.9. Comparison of 2500 blocks model and homogeneous system.

Next, the 4th order polynomial trend line of the homogenous medium was found as shown in Figure 4.9. Using this trend line, the deviation of the temperature across the x-coordinate for each of the modeled pore systems was determined. This is graphed in Figure 4.10 as a function of specific surface area and pore size listed in Table 4.3. Recall from 3.8 that the diameter of open-cell foams varies between 2 and 4 mm, whereas the diameter of CENG pores is about 1 µm. According to Figure 4.10 (right), a pore size below 0.4 mm can be considered a homogeneous system as there is little deviation from a homogenous medium. It is acknowledged that the 2D geometry modeled is not a geometrically accurate representation of open-cell metal foams, but it does indicate the importance of cell size or specific surface on the ability to represent a porous foam/PCM composite with an effective thermal conductivity that is not dependent on pore size.

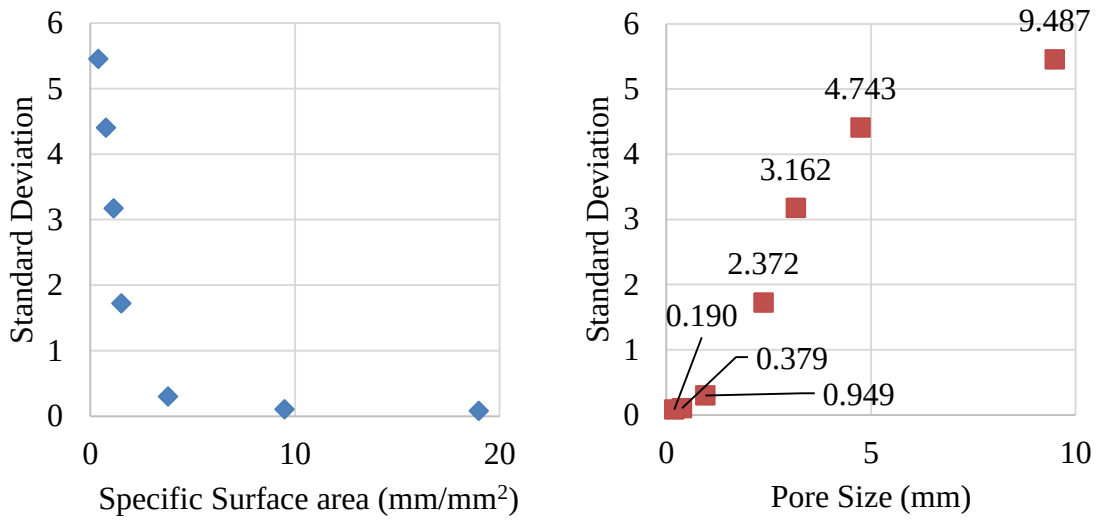

Figure 4.10. Impact of surface area (left) and pore size (right) on the standard deviation of the temperature profile as compared to a homogenous material.

The final method of confirming the impact of pore size on effective thermal conductivity is by exploring the time to fully charge or the time for the entire system to reach 50°C. The charging rate is dependent to two main variables – how much the energy the composite can store and the rate that it charges. Since the amount of aluminum and PCM is that same in each geometry in Figure 4.4, the energy density remains constant. Therefore, any change in the transient heat flux profile is due to the composite thermal conductivity. As shown in Figure 4.11, the 1 block and 16 blocks systems have different transient heat flux profiles, while the 625 and 2500 block systems have similar profiles. Again, this indicates that a pore size below 0.4 mm (625 blocks) can be considered a homogeneous system.

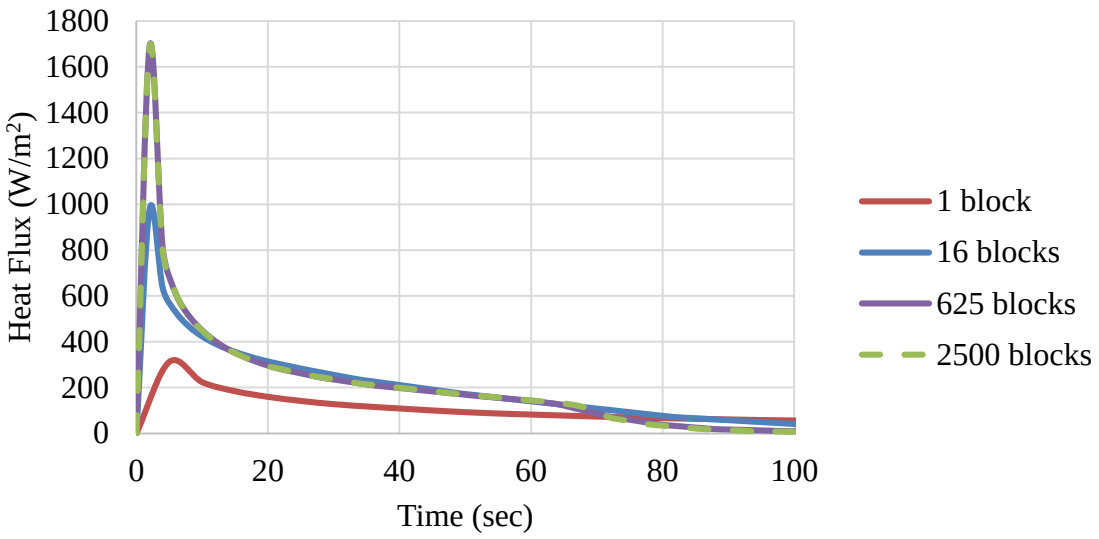

Figure 4.11. Transient heat flux profile for each system in Figure 4.6.

The discussion of effective metal foam/PCM conductivities will begin with the most basic models. It is known that the effective thermal conductivity of a foam/PCM system will fall between the range calculated through the parallel and series models.

$$k_{eff_{parallel}} = (1-\gamma)k_{PCM} + (\gamma)k_{metal} \tag{22}$$

$$k_{eff_{series}} = \left(\frac{(1-\gamma)}{k_{PCM}} + \frac{\gamma}{k_{metal}}\right)^{-1} \tag{23}$$

Some of the most simplifying examples that do not consider impact of pore size include Chen *et al.* [78] who used a two-temperature model with effective conductivities of the foam and PCM adjusted by the relative densities: $k_{foam_{eff}} = \gamma k_{metal}$ and $k_{PCM_{eff}} = (1-\gamma)k_{PCM}$. Similarly, Kota *et al.* [120] used a one-temperature model with the effective thermal conductivity calculated with the rule of mixtures, $k_{eff} =$

$(1-\gamma)k_{PCM} + \gamma k_{metal}$. A geometric mean model ($k_{eff} = k_{PCM}^{(1-\gamma)} k_{metal}^{(\gamma)}$) has also been proposed [61].

However, various works suggest that these are imprecise estimates as they are solely dependent on the relative density. Hong and Herling [55] summarize that the effective thermal conductivity estimated using the rule of mixtures can be inaccurate since the same relative density can be obtained for metal foams with different surface area densities based on the pore density. It is suggested that for a better representation of the metal foam/PCM composite, the thermal conductivity either be measured, or an effective thermal conductivity correlation be developed that includes parameters for the surface area density as well as relative density. Even the experiments reported in Chapter 3 show that the charging response is not just dependent on relative density, but the size of the pore as well.

There are commercially available devices such as laser flash [134] and transient plane source [135, 136] techniques to measure the thermal conductivity of materials. However, measuring the effective thermal conductivity of composite PCMs fabricated with porous structures results in large uncertainties due to the surface roughness and anisotropic features of the foam ($k_{metal} \gg k_{PCM}$) [137]. To overcome this issue, the one-dimensional steady-state heat conduction approach, based on Fourier's law, has been used to determine the effective thermal conductivity under steady-state conditions [55, 61, 137-140]. Examples of this technique are shown in Figure 4.12 where a sample is placed between a hot and cold surface, temperatures are measured over time, and the effective thermal conductivity is defined as,

$$k_{eff} = q'' \frac{\Delta x}{\Delta T} \tag{24}$$

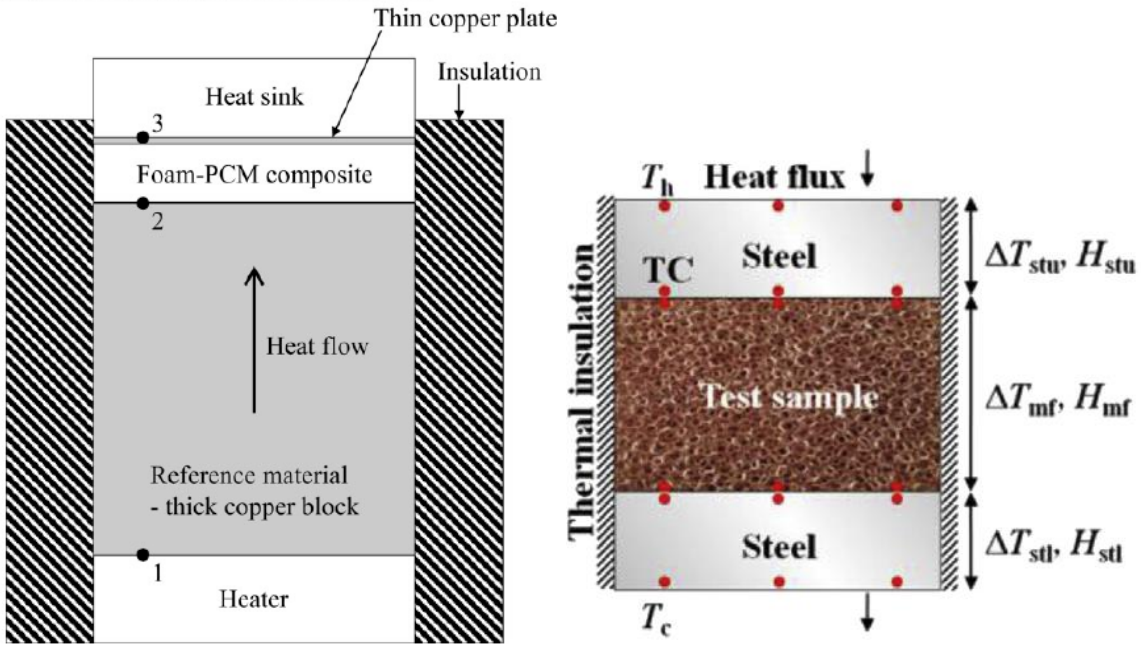

Figure 4.12. Typical experimental setup of effective thermal conductivity measurement by one-dimensional steady-state heat conduction method [55, 139].

Xiao *et al.* [141] used the above method to measure the thermal conductivity of copper and nickel foams, both with 5% relative density and 1.0–5.0 mm pore sizes, saturated with paraffin. The effective thermal conductivity was increased from 0.3 W/m·K of pure paraffin to 4.9 W/m·K of copper foam/paraffin foam composite PCM, and to 0.95–1.3 W/m·K of nickel foam/paraffin foam composite PCM. In another study, Xiao *et al.* [137] further investigated copper and nickel foams with different relative densities and pore sizes. For copper foam, the results revealed the highest effective thermal conductivity of 16.01 W/m·K with 11% relative density and 1.0 mm pore size; for nickel foam, the highest effective thermal conductivity was 2.33 W/m·K with 9% relative density and 1.0 mm pore

size. Furthermore, the authors pointed out that the effective thermal conductivity of composite PCM increased with a decrease of relative density and was hardly affected by pore size. It is noted that the PCM remained solid in all measurements.

Similarly, Hong and Herling [55] measured the thermal conductivity of aluminum foam/paraffin composites with the setup shown in Figure 4.12. The aluminum foams had relative densities of 7–8%, while the pore size was in the range of 0.5–2.0 mm. Results were reported with a normalized effective thermal conductivity, which was the ratio of effective thermal conductivity to that of the pure PCM. The normalized effective thermal conductivity increased as the PCM moved from the solid state to liquid state. The authors attributed this increment to the better contact between the metal foam and liquid PCM. Different from the conclusion drawn by Xiao *et al.* [137], it is shown that the effective thermal conductivity increased with the reduction of aluminum pore size, in particular when the pore size was 0.5 mm. This inconsistency of the effect of the pore size on the thermal conductivity of composite PCM suggests the need for further investigation.

Instead of relying on experimental data, other estimates have been developed based on geometric relationships of the foam structure and the thermal conductivity of the foam and PCM. The goal is to include the effect of pore size, relative density, and material properties in an effective thermal conductivity of the composite. Such correlations have been either based on 2D or 3D unit cell geometries.

One such 2D example is from Calmidi and Mahajan [142]. By using the unit cell shown in Figure 4.13 (left) and the geometric relations shown in Figure 4.13 (right), the effective thermal conductivity correlation shown in Equation 25 was developed, where k_s

and k_f represents the bulk conductivity of the metal and PCM, respectively. This has been used in numerous open-cell foam/PCM studies [59, 81, 106, 143]. Bhattacharya *et al.* [144] also developed an effective conductivity correlation with a 2D geometry that was used by Yang *et al.* [125] to model a metal foam/PCM composite with the one-temperature model.

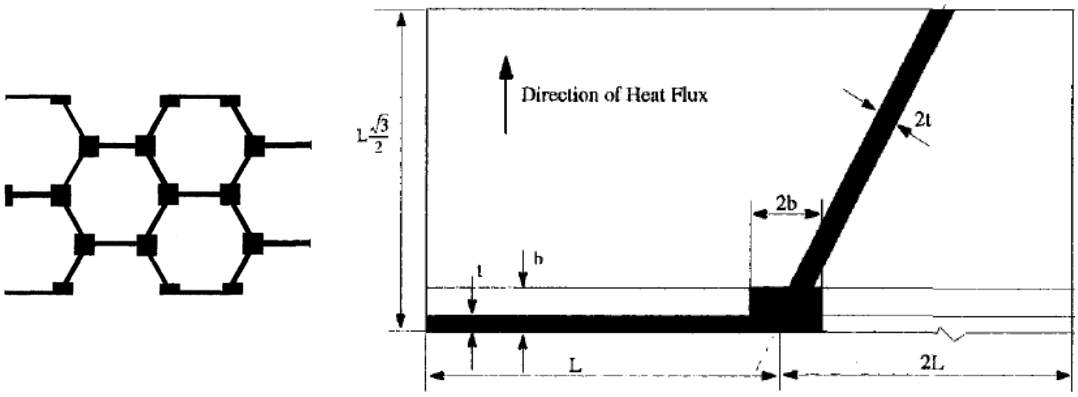

Figure 4.13. Hexagonal structure of the metal matrix (left) and representative unit cell according to the model of Calmidi and Mahajan [142].

$$k_{eff} = \left(\left(\frac{2}{\sqrt{3}} \right) \left(\frac{r\left(\frac{b}{L}\right)}{k_f + \left(1 + \frac{b}{L}\right)\frac{(k_s - k_f)}{3}} + \frac{(1-r)\left(\frac{b}{L}\right)}{k_f + \frac{2}{3}\left(\frac{b}{L}\right)(k_s - k_f)} + \frac{\frac{\sqrt{3}}{2} - \frac{b}{L}}{k_f + \frac{4r}{3\sqrt{3}}\left(\frac{b}{L}\right)(k_s - k_f)} \right) \right)^{-1} \tag{25}$$

More recently, 3D unit cell geometries have been used to develop a correlation for the foam effective thermal conductivity based on a tetradecahedron geometry. Although,

on the microscale, metals form in BCC, FCC, or HCP crystal structures, on the macroscale, bubbles in the creation of metallic foams form to minimize surface area. This is the basis of the Kelvin structure, which is a tetradecahedron geometry made of 14 faces (eight hexagonal and six squares) [121]. One of the most common correlations using this geometry (Figure 4.14) was developed by Boomsma and Poulikakos [145] assuming cylinder ligaments and cubic nodes as shown in Figure 4.14 (right).

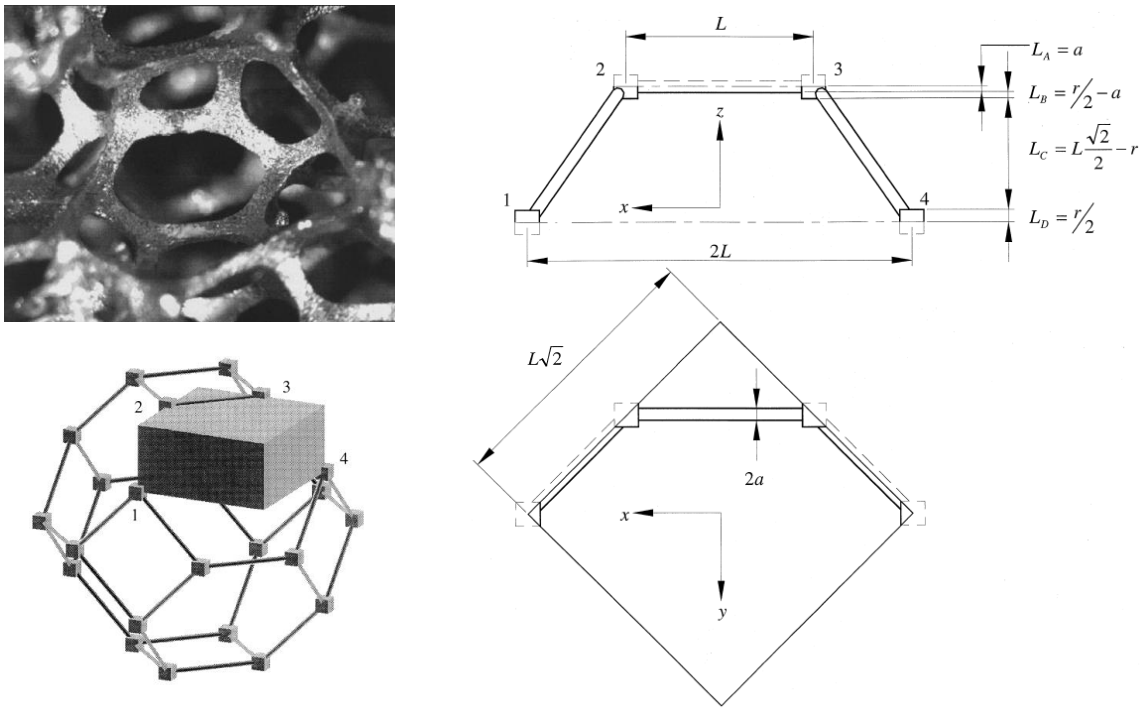

Figure 4.14. Single tetrakaidecahedron cell in an aluminum foam (top left); tetrakaidecahedron modeled with cylindrical ligaments and cubic nodes (bottom left); geometrical breakdown of the unit cell of the tetrakaidecahedron (right) [145].

The effective thermal conductivity was defined as Equation 26 where the definitions of R_A, R_B, R_c, R_d can be found in [145].

$$k_{eff} = \frac{\sqrt{2}}{2(R_A + R_B + R_c + R_d)} \tag{26}$$

The Boomsma and Poulikakos effective thermal conductivity model has been used many numerical studies that model open-cell foams saturated with PCM [58, 80, 81, 119, 123, 146, 147]. Other effective thermal conductivity correlations based on 3D geometric models include Dai *et al.* [148] and Yang *et al.* [149]. A summary of literature that uses effective thermal conductivity correlation in numerical simulation is shown in Table 4.4 along with the reference of the correlation. Studies that use the one-temperature model calculate the effective thermal conductivity for the composite directly from the correlation,

$$k_{composite} = k_{eff} \tag{27}$$

Studies that use the two-temperature model calculate the effective thermal conductivity for the PCM and foam separately, specifically,

$$k_{foam_{eff}} = k_{eff} \mid k_{PCM} = 0 \tag{28}$$

$$k_{PCM_{eff}} = k_{eff} \mid k_{metal} = 0 \tag{29}$$

Table 4.4. Summary of numerical studies using effective thermal conductivity correlations.

Reference	Model	k_{eff} correlation
Chen *et al.* [78]	2 temperature	Rule of mixtures
Kota *et al.* [120]	1 temperature	Rule of mixtures
Du and Ding [119]	1 temperature	Boomsma and Poulikakos [145]
Tian and Zhao [81]	2 temperature	Boomsma and Poulikakos [145]
Yang *et al.* [125]	1 temperature	Bhattacharya *et al.* [144]
Zhao *et al.* [106]	2 temperature	Calmidi and Mahajan [142]
Li *et al.* [80]	2 temperature	Boomsma and Poulikakos [145]
Siahpush *et al.* [59]	1 temperature	Calmidi and Mahajan [142]
Tian and Zhao [150]	2 temperature	Boomsma and Poulikakos [145]
Zhang *et al.* [123]	2 temperature	Boomsma and Poulikakos [145]
Yang and Garimella [124]	2 temperature	Bhattacharya *et al.* [144]
Zhu *et al*. [146]	2 temperature	Boomsma and Poulikakos [145]

Based on experimental work, it is generally accepted that the heat transfer area, measured as specific surface area, is of prime importance when studying the thermal charging and discharging of open-cell foams saturated with PCM [55, 58, 79, 104]. Therefore, when effective thermal conductivities are determined based on a geometric model, accurate representation of the open-cell foam is imperative. A primary issue with the geometric models discussed above is the difference in assumptions surrounding the ligament structure, ligament orientation, and effect of filling medium, which impact the effective thermal conductivity calculation. Figure 4.15 depicts how the difference in geometric model assumptions impacts the effective conductivity calculation as a function of porosity (1.0 – relative density) for various models found in literature.

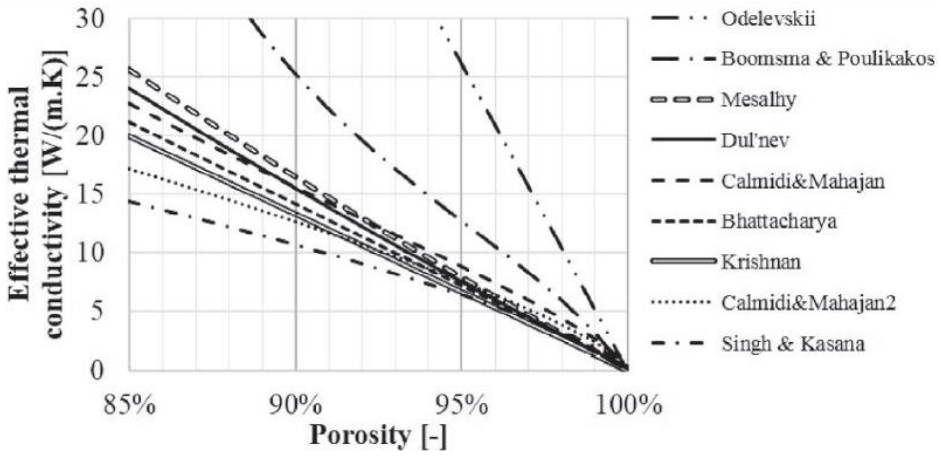

Figure 4.15. Analytical and empirical models for the evaluation of the effective thermal conductivity of a high porosity copper foam saturated with paraffin [104].

Recently, Yao *et al.* [139] developed a thermal conductivity correlation to improve upon the simplifying assumptions of past models, specifically (1) relatively simple ligament structure, (2) effect of ligament orientation is ignored, (3) effect of filling medium is ignored. A summary of the proposed model and improvement on past work is shown in Table 4.5. The use of tri-prism ligaments refers to the assumed shape of the foam ligaments. As shown by the SEM image of copper foam ligaments in Figure 4.16, this is a better approximation of the shape of ligaments than the circular ligament used in the past.

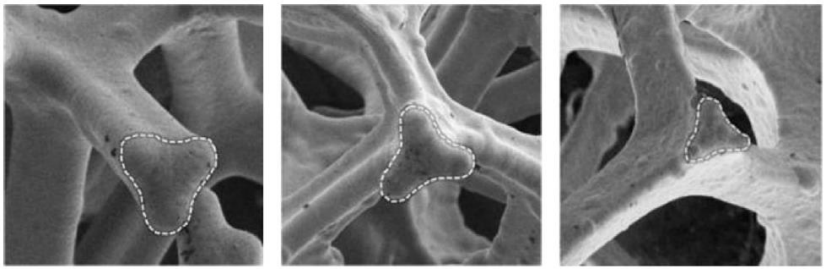

Figure 4.16. SEM images of copper foam at different relative densities [139].

Table 4.5. Main characteristics of different effective thermal conductivity models for open-cell metal foams; adapted from Yao *et al.* [139].

Model	Main characteristics
Yao *et al.* [139]	• 3D tetrakaidecahedron with concave tri-prism ligaments and four-pyramids nodes • Containing no additional empirical parameter • Considering effect of ligament orientation • Considering effect of filling medium
Boomsma and Poulikako [145]	• 3D tetrakaidecahedron with cylinder ligaments and cubic nodes • Containing additional empirical parameter • Ignoring effect of ligament orientation • Considering effect of filling medium
Dai *et al.*[148]	• 3D tetrakaidecahedron with cylinder ligaments and cubic nodes • Containing additional empirical parameter • Considering effect of ligament orientation • Considering effect of filling medium
Yang *et al.*[149]	• 3D tetrakaidecahedron with cylinder ligaments and without nodes • Containing no additional empirical parameter • Considering effect of ligament orientation • Ignoring effect of filling medium
Calmidi and Mahajan [142]	• 2D hexagon with cylinder ligaments and square nodes • Containing additional empirical parameter • Ignoring effect of ligament orientation • Considering effect of filling medium

In addition to calculating the effective thermal conductivity from geometric correlations, Yao *et al.* [139] and Xiao *et al.* [137] also conducted one dimensional heat transfer experiments as shown in Figure 4.12 for copper, aluminum, and nickel foams. In both cases, the respective geometric models agreed well with the effective thermal conductivity measurements. Specifically for Yao *et al.* [139], the average deviations from the experimental data was within 10%, which was reasoned to be a result of the more realistic foam structure. However, both of these experiments were conducted with the PCM

only in the solid state. The impact of surface area is most important during phase change, which was not captured in these solid state experiments. Additionally, though the effective thermal conductivities are based on a geometrically accurate foam model, comparison of modeled surface area as a function of pore density or relative density to actual foams has yet to be discussed.

Thus far, three methods of determining the effective thermal conductivity of an open-cell metal foam/PCM composite have been discussed: commercially available devices (not feasible for most composite foam systems), use of Fourier's law in a steady state measuring device, and estimation based on geometric relations. As summarized by Fleming *et al.* [151], steady state investigations, whether theoretical or experimental, tend to conclude that the effective thermal conductivity is primarily dependent on porosity and the respective material thermal conductivities, but not the foam pore size [137, 142, 144, 145]. These findings are consistent with effective medium theory if the interfacial resistances are negligible [152, 153]. However, studies focused on phase change do find dependence on pore size [55, 79, 80]. For a given porosity, a smaller pore size results in higher pore density and will enhance heat transfer via higher specific surface area [55]. This was also shown in Chapter 3. For melting, this effect may be somewhat mitigated by natural convection suppression, but nevertheless, there exists a pore dependence [79, 80]. Aside from natural convection, the reason for the apparent conflict between steady state and phase change studies is due to local thermal non-equilibrium [153]. To accommodate local thermal non-equilibrium, two-temperature models have been reported as reviewed in 4.2.1. However, such an approach does not lend readily to determination of effective thermal conductivity values that can be used for quick performance evaluation.

To overcome the issue of thermal non-equilibrium dependence, a fourth approach to estimate the effective thermal conductivity of open-cell foams saturated with PCM has recently been proposed: first develop a foam model and then incorporate the structural model into a 3D phase change simulation. This method couples the heat transfer between the foam matrix and the PCM, without needing the assumption of local thermal equilibrium and any empirical interstitial heat transfer coefficient for closure [118]. From this 3D pore-scale simulation, an effective thermal conductivity can be calculated by fitting a volume averaged model to the 3D simulation. Once the effective thermal conductivity is estimated from the realistic simulation, a one or two-temperature can be used.

Open-cell metallic foam geometries can either be developed by assuming a lattice structure (body centered cubic, BCC [117, 154], hexagonal close-packed, HCP [155], or face centered cubic, FCC [156]) or by using one of the minimal surface area models such as the Kelvin [157], Weaire-Phelan [122, 157, 158] or other cell structures [121, 159] and then incorporating into a modeling software. Recently, Hu and Patnaik. [117] used FLUENT and Sundarram *et al.* [156] used COMSOL to study open-cell foams saturated with PCM with BCC and FCC foam models, respectively.

In addition to direct simulation with the BCC foam model saturated with PCM, Hu and Patnaik [117] used the 3D phase change simulations to fit an effective thermal conductivity value to the data. It was found that both a one and two-temperature model compared well to direct simulation with an effective thermal conductivity calculated from the Progelhoff method. For the two-temperature model, $k_{foam_{eff}} = (\gamma)^{\alpha} k_{foam}$ and $k_{PCM_{eff}} = (1-\gamma) k_{PCM}$ and for the one-temperature model, $k_{eff} = (\gamma)^{\alpha} k_{foam} + (1 -$

$\gamma)k_{PCM}$. In both cases, setting $\alpha = 1.31$ minimized the error between the transient temperature profile of the direct simulation and the volume averaged simulation. This work suggests that developing a correlation for the effective thermal conductivity based on a 3D phase change simulation eliminates error due to local thermal non-equilibrium and allows the use of a one-temperature model with volume averaged properties and an effective thermal conductivity. This reduces the computational complexity and estimation of the interstitial heat transfer coefficient; however, the accuracy of the BCC model compared to experimental foams was not discussed.

Similar numerical analysis was reported by Feng *et al.* [118] with a Kelvin/BCC hybrid foam model. As discussed by Hu and Patnaik [117], a volume averaged one-temperature model was found to be suitable once the effective thermal conductivity was determined from the 3D simulation, however, the accuracy of the foam geometry was not discussed. Fleming *et al.* [151] experimentally and numerically studied an aluminum foam enhanced latent heat storage system. Numerical analysis with a simplified Kelvin structure was conducted to determine the effective thermal conductivity of the system by comparing to experimental data. The effective thermal conductivity was found to be notably different that other steady state correlation would predict. This lack of agreement was attributed the local thermal non-equilibrium during transient heat transfer assumed by past correlations.

4.3 Modeling Summary

Modeling the performance of metallic foams saturated by phase change material is complicated by the nonlinear nature of the phase change process as well as the non-homogeneity of the system. Accounting for local non-equilibrium between the foam and the PCM is imperative when studying the effective thermal conductivity of the composite. Additionally, a geometrically accurate foam model is cruical in pore-size models, as the surface area greatly impacts the heat transfer. Once an effective thermal conductivity is determined from pore-scale simulations, a one-temperature model can accurately predict the performance of an oepn-cell foam/PCM composite. Though past studies have used Kelvin based foam structures, no study has addressesd the accuracy of this foam compared to surface area data. Unlike metal foam composites, the small pore size of graphite foam as a result of the compaction process allows the composite to be modeled with the one-temperature model as a homogenous medium.

The following two sections will discuss efforts to model and validate aluminum foam and CENG foam models. Acknowledging that specific surface area is an important parameter in determining the effective thermal conductivity of metal foams, a geometrically accurate open-cell foam model is developed and then used in 3D phase change simulations and validated by experimental results. Such a method provides details of the temperature distribution within the inhomogeneous composite system. While such detailed information can be useful for determining the state of charge and the rate of heat transfer at any instant in time, a simpler approach that provides the time to charge or discharge the system can be quite useful in order to estimate the performance of thermal storage systems.

This work extends the one-temperature model approach to an effective properties model referred to as the effective energy storage model. By developing effective density, heat capacity, and thermal conductivity properties for the foam/PCM composite, this 3D non-linear heat transfer problem is converted to a 1D linear system. This method can be adapted for multiple phase changes or non-isothermal phase change because it is based on the amount of energy absorbed over time instead of the temperature distribution within the system. This method is especially useful for thermal storage systems when the amount of energy stored, not temperature distribution, is important. The goal is to further streamline the analysis of composite PCM heat transfer for heat exchanger design. Similarly, CENG foams models are developed and validated with experiments.

4.4 Validation of Aluminum Foam Models

Recall that open-cell foams are classified based on pore density and relative density. Pore density (measured as pores per inch, PPI) describes the diameter of each pore. As the number of pores per unit length increases, the diameter of each pore decreases and the overall surface area of the foam increases. Relative density, defined as the density of the foam divided by the density of the solid parent material, identifies the amount of metal compared to the amount of PCM. The following graph (repeated from 2.4.2) summarizes the relationship between relative density, PPI, and specific surface area [75].

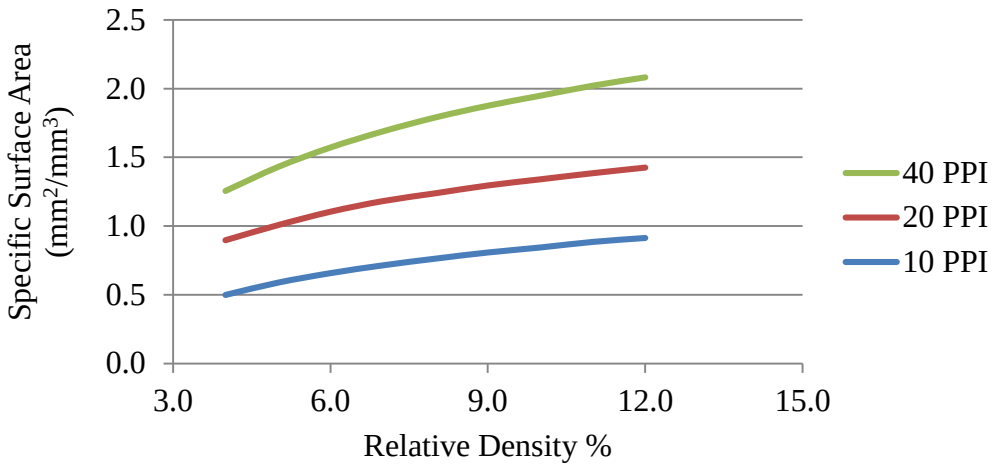

Figure 4.17. Specific surface area of Duocel® metal foams [75].

In previous studies using open-cell foam/PCM composites, only the BCC model or a modified Kelvin geometry has been used to model the foam structure [117, 118, 151, 154], and no studies compare the predictions between specific surface area versus relative density. In this study, both the BCC model and Kelvin structure were modeled as shown in Figure 4.18, but the Kelvin structure was found to match the relative density versus specific surface area more accurately, as shown in Figure 4.20 and was used in further modeling. Note that the Kelvin structure shown below is different than past work. Instead of extruding along each ligament, Feng *et al.* [118] removed a sphere from the Kelvin structure, essentially forming a Kelvin/BCC hybrid model. Additionally, Fleming *et al.* [151] assumed spherical nodes at each of the ligament joints.

The foam structure was developed in SOLIDWORKS so that the relative density and specific surface area could be adjusted through the size and shape of the ligaments, while the pore size could be changed through the dimensions of the unit cell. This unit cell can be duplicated to form a foam of any dimension as shown in Figure 4.19.

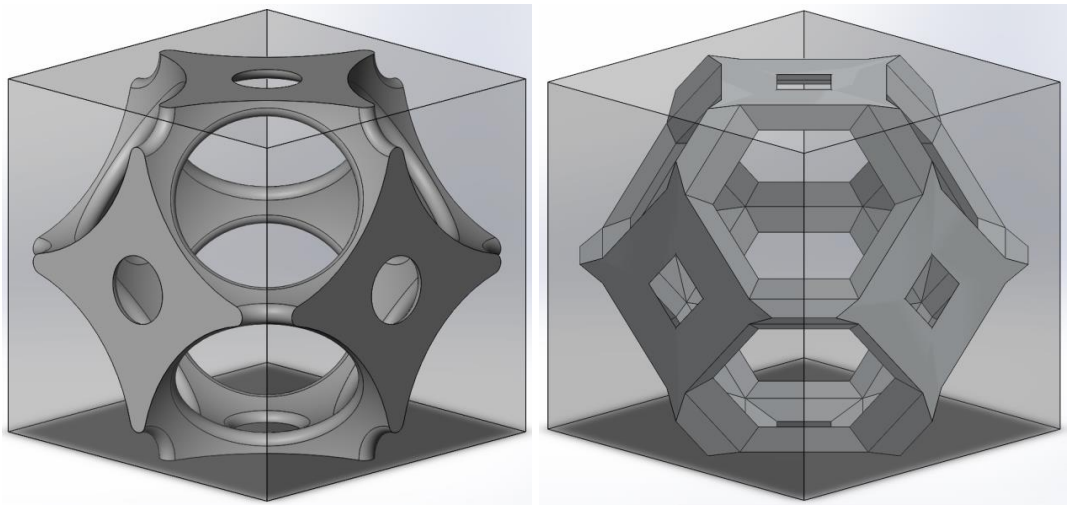

Figure 4.18. Depiction of the BCC foam model (left); Kelvin structure (right).

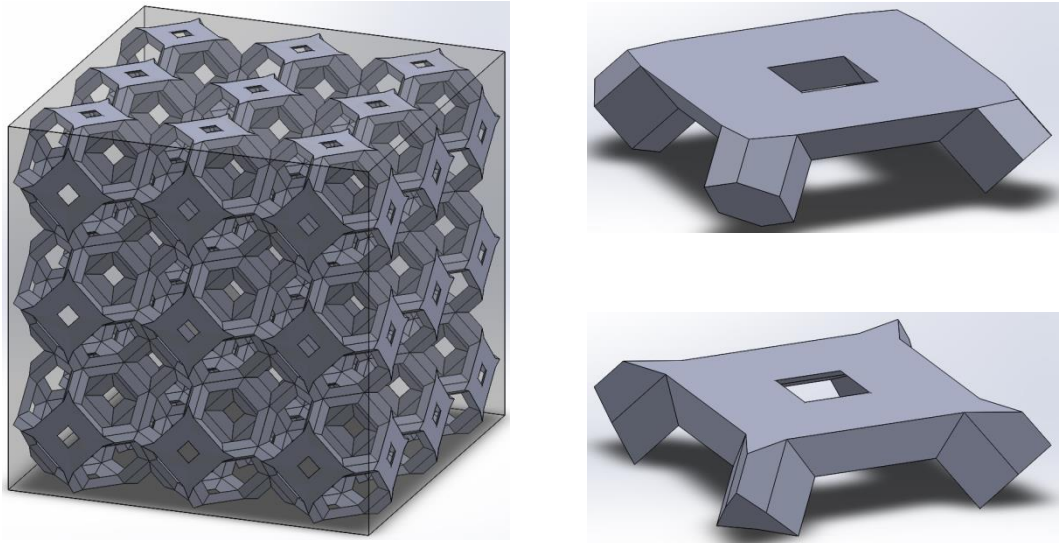

Figure 4.19. Foam constructed of Kelvin structure unit cells (left); ligaments for 13% relative density (top right) and 7% relative density (bottom right).

The foam model was compared to experimental data for both 10 PPI and 40 PPI aluminum open-cell foams (Figure 4.20). Note that the 40 PPI BCC model is not shown because the surface area for each relative density was about twice the experimental data. Although various use of the Kelvin structure to model foams exists in literature [157], no

use of this method has been found in combination with modeling phase change thermal systems as well as comparison to existing specific surface area and relative density data.

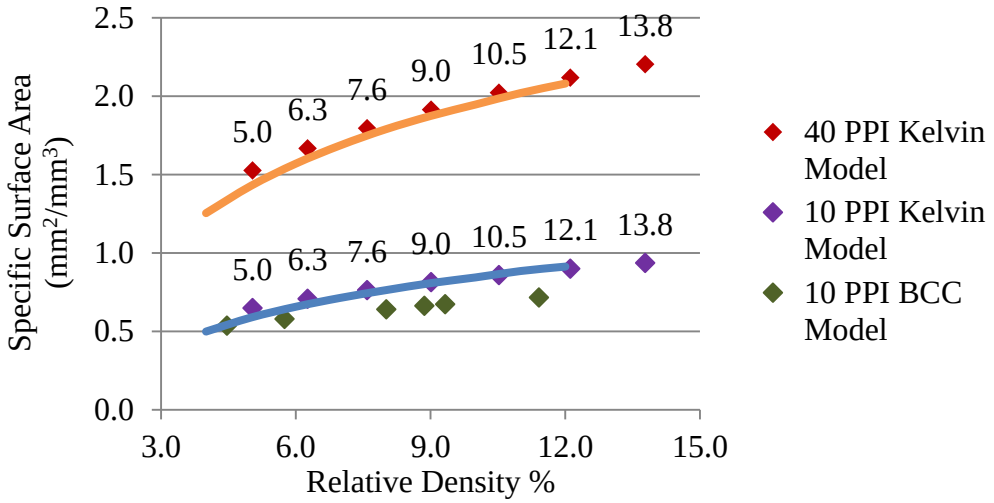

Figure 4.20. Comparison of foam model to geometric data [75].

After developing an accurate model of the foam, the geometry was imported into COMSOL 4.4 for various heat transfer analyses. In general, this effort intends to build on work with the one-temperature model previously discussed by modeling the composite foam/PCM system at the pore-sale, developing correlations for the thermophysical properties, and then validating the one-temperature approximation with experimental data. Additionally, an effective properties model referred to as the effective energy storage model is proposed to simplify thermal charging simulations for constant temperature conditions based on tracking the energy being stored over time instead of discrete temperature distributions. Recall the one-temperature equation for the specific heat approximation discussed in 4.2.1,

$$\left[(1-\gamma)(\rho c_p)_{PCM} + (\gamma)(\rho c_p)_{foam}\right]\frac{\partial T}{\partial t} = \nabla \cdot (k_{eff}\nabla T) \tag{30}$$

where,

$$(\rho c_p)_{PCM} = \begin{cases} \rho c_{p_{solidPCM}} & T < T_{solid} \\ \rho c_{p_{eff}} & T_{solid} \leq T \leq T_{liquid} \\ \rho c_{p_{liquidPCM}} & T > T_{liquid} \end{cases}$$

$$c_{p_{eff}} = \frac{L}{(\Delta T)} + \frac{c_{p_{solidPCM}} + c_{p_{liquidPCM}}}{2}$$

For this model, both the latent heat and sensible heat storage are calculated independently. Instead of calculating these two terms separately, the effective energy storage model uses the one-temperature approximation where the total energy is calculated over time, without specifying latent or specific heat, thereby turning this non-linear phase change problem into a linear transient heat transfer problem,

$$(\rho_{eff} c_{eff})\frac{\partial T}{\partial t} = \nabla \cdot (k_{eff}\nabla T) \tag{31}$$

This method is especially useful for thermal storage systems exposed to a constant temperature when the amount of energy stored, not temperature distribution, is important. The effective density is defined similar to the one-temperature model; however, the effective specific heat is redefined to include the latent heat. This method is then validated with paraffin wax and aluminum foam experimental data. To summarize, the steps involved in this analysis include:

1) Using the geometrically accurate foam geometry, perform finite-element 3D phase change simulations to study the thermal charging of 10 PPI and 40 PPI aluminum foams (9% relative density) exposed to 60°C and 80°C. Both the rate of energy storage and temperature distribution will be reported.
2) Define effective properties for the effective energy storage model.
    a) Effective specific heat and effective density are defined based on volume averaging. After being confirmed for a non-phase change system, the effective specific heat is redefined to include both the sensible and latent energy storage. These definitions are verified by comparing total energy stored from the 3D phase change model to that of the effective energy storage model.
    b) Effective thermal conductivity is calculated by minimizing the difference between the rate of energy storage for the 3D model and the effective energy storage model. Fleming *et al*. [151] developed an effective thermal conductivity for a single pore density, relative density, and temperature condition. In this work, the impact of relative density and temperature on the thermal conductivity is explored.
3) Validation of the effective energy storage model with experimental data.

The geometry used for the 3D phase change simulations is shown in Figure 4.21. A symmetry argument was used to reduce to one-fourth the original size as shown in Figure 4.21 (right). The unit cell for 10 PPI measured 4.0 mm x 2.0 mm x 2.0 mm, while the unit cell for 40 PPI measured 1.7 mm x 0.85 mm x 0.85 mm.

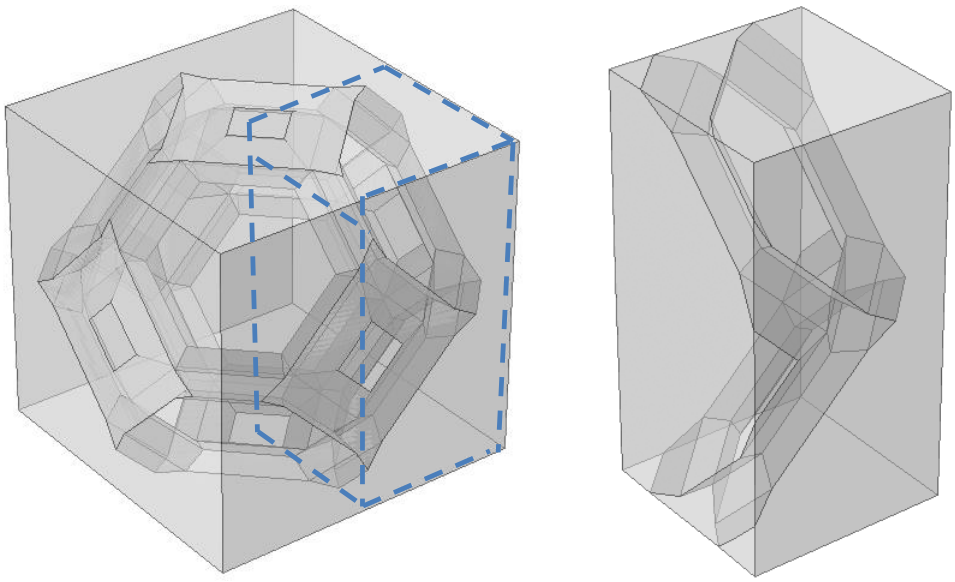

Figure 4.21. Original 9% relative density foam (left); Symmetric unit model used during simulations (right).

Due to the difference in pore size for the 10 PPI and 40 PPI foams, the unit cell volumes differ, which is reflected in the total energy stored in the unit volume. Therefore, the 40 PPI volume was adjusted to be the same as the 10 PPI unit cell. As shown in Figure 4.22, the volume of each sample is 16 mm^3 (4mm x 2mm x 2mm). Since the volume of aluminum in each sample is 1.44 mm^3, the relative density is confirmed to be 9%. During all simulations, the following assumptions were made:

1) Natural convection and radiation negligible; heat transfer is conduction only.
2) Applied temperature is greater than the melting temperature.
3) The PCM is initially in the solid phase.
4) The PCM and foam are homogenous and isotropic and have no property degradation with time.
5) The foam is fully saturated with PCM and there is no volume change of PCM.

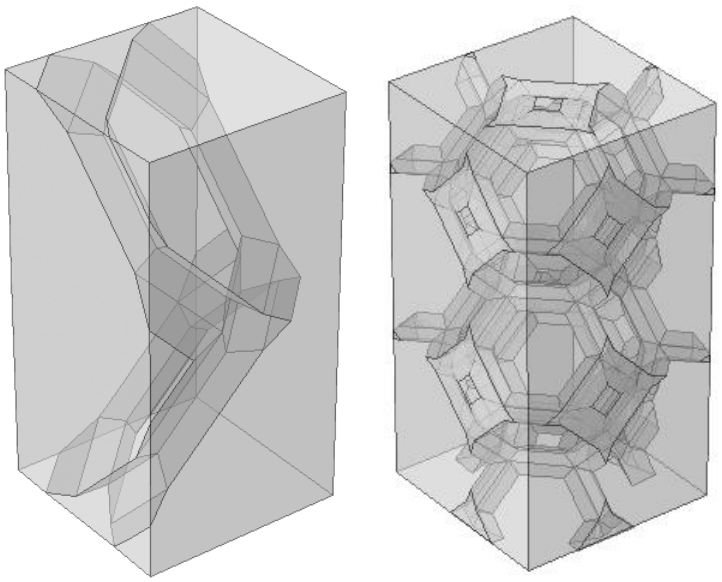

Figure 4.22. 10 PPI (left) and 40 PPI (right) geometries of similar volume (16 mm^3).

The first step in this study was to conduct finite-element 3D phase change simulations. The effective heat capacity method was used to model the PCM. Material properties are defined in Table 4.6. In addition to the prior assumptions, further simplifications were made during the first set of models for the proof of concept:

1) The thermophysical properties of the PCM and foam material are independent of temperature and are the same for solid and liquid phases.
2) Phase transition occurs at 55°C over a ΔT of 2°C. There is only one phase change period between solid and liquid with a latent heat of 150 kJ/kg (approximation of paraffin wax).

Table 4.6. Material properties for aluminum and paraffin wax used during simulations.

	Aluminum	Paraffin Wax
Density (kg/m^3)	2700	910
Specific heat (J/kg·K)	900	2500
Thermal conductivity (W/m·K)	200	0.25

After importing the foam geometry from SOLIDWORKS into COMSOL, a step temperature was applied to the top surface of the geometry as shown in Figure 4.23 (left) that ramped from ambient conditions (25°C) to the applied temperature within 10 seconds. Applied temperature conditions of 60°C and 80°C were studied, and the remaining sides were insulated. Figure 4.23 (right) shows the status of the PCM after 50 seconds. The red space represents solid, while the blue space represents liquid. The negative space in the geometry represents the aluminum foam. Example charging data for the 10 PPI foam is shown in Figure 4.24. The energy storage was calculated by integrating the heat flux across the top surface over time. The temperature data represents the temperature at the lower right corner as shown by the green circle in Figure 4.23 (right). The phase change process can be seen by the transition from sensible heating to latent heating when the temperature profile changes slope at 55°C. Following phase change, the temperature profile returns to a positive slope during the end of sensible heating.

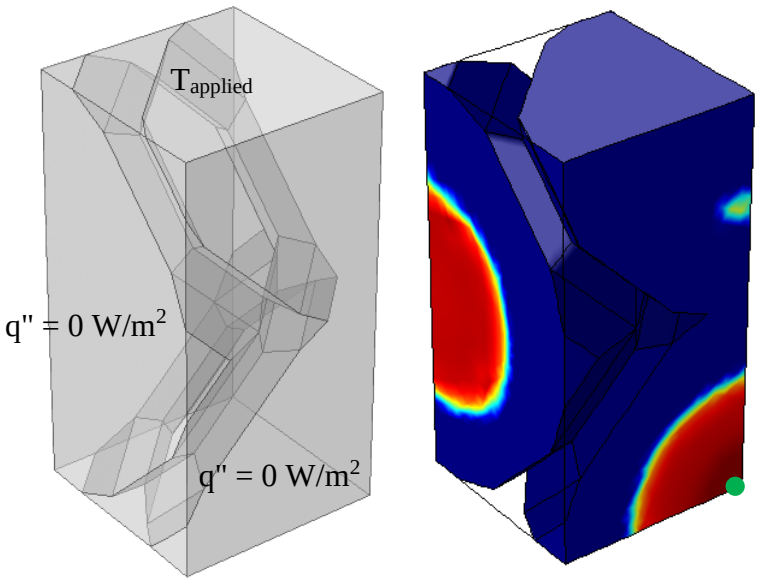

Figure 4.23. SOLIDWORKS geometry with boundary conditions (left); PCM during phase change after 50 seconds (right).

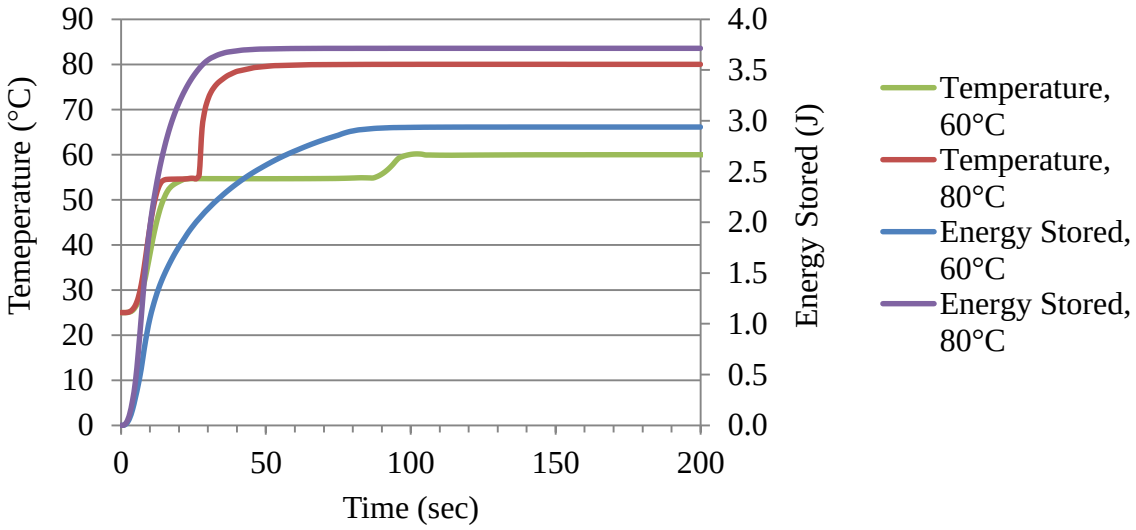

Figure 4.24. Energy storage and bottom temperature over time for 10 PPI unit cell system with phase change under two applied temperatures (right).

The next step in this study was to determine the proper estimations for effective density and specific heat in a unit cell based on comparison to the 3D model. For this first

analysis, phase change is not considered. Then these approximations were used to study the proposed specific heat concept, which combines the sensible heat storage with latent heat storage. As previously discussed, the rule of mixtures has been used to calculate effective specific heat and density in past work. However, it is noted that the rule of mixtures is a volumetric relationship, and when working with a mass property such as specific heat, this approximation may not be valid for two materials with different densities. To determine if the density fractions should be considered in the calculation of effective specific heat, initial simulations were completed without phase change such that the effective specific heat was defined in Equation 32 and Equation 33 where γ is the relative density,

$$c_{p_{eff}} = (1-\gamma)c_{p_{PCM}} + (\gamma)c_{p_{foam}} \tag{32}$$

$$c_{p_{eff}} = (1-\gamma)\frac{\rho_{PCM}}{\rho_{eff}}c_{p_{PCM}} + (\gamma)\frac{\rho_{foam}}{\rho_{eff}}c_{p_{foam}} \tag{33}$$

Similar to the 3D phase change simulations, adiabatic boundary conditions were defined for all surfaces except for the top surface as shown in Figure 4.23 (left). A step temperature was applied to the top surface which ramped from ambient conditions (25°C) to the applied temperature (40°C) within 10 seconds. Energy stored over time for a 9% aluminum foam unit system is calculated from the simulation. The steady state energy storage is also calculated through Equation 34 where ρ_{eff} and $c_{p_{eff}}$ are defined in Table 4.7.

$$E_{stored_{Sensible}} = \left(\rho_{eff} c_{p_{eff}}\right) * V * \Delta T \quad (34)$$

The energy stored calculated from the simulation and Equation 34 are compared to determine the proper effective calculation for specific heat. As shown by comparison of the energy stored of the modeled foam systems in Figure 4.25 and the effective property calculations in Table 4.7, the energy stored in a non-phase change block can be accurately estimated with the rule of mixtures effective density formulation and effective specific heat formulation that includes the density fraction. This result was repeated through additional trials with various applied temperatures for both 10 PPI and 40 PPI.

Table 4.7. Effective energy storage calculation for 10 PPI and 40 PPI unit cell 9% relative density aluminum foam/paraffin systems exposed to 40°C.

	$\boldsymbol{\rho_{eff}}$	$\boldsymbol{c_{p_{eff}}}$	$\boldsymbol{E_{stored_{Sensible}}}$ **(J)**
10 PPI	$\rho_{eff} = (1-\gamma)\rho_{PCM} + (\gamma)\rho_{foam}$	Equation (32)	0.61
		Equation (33)	0.55
40 PPI	$\rho_{eff} = (1-\gamma)\rho_{PCM} + (\gamma)\rho_{foam}$	Equation (33)	0.55

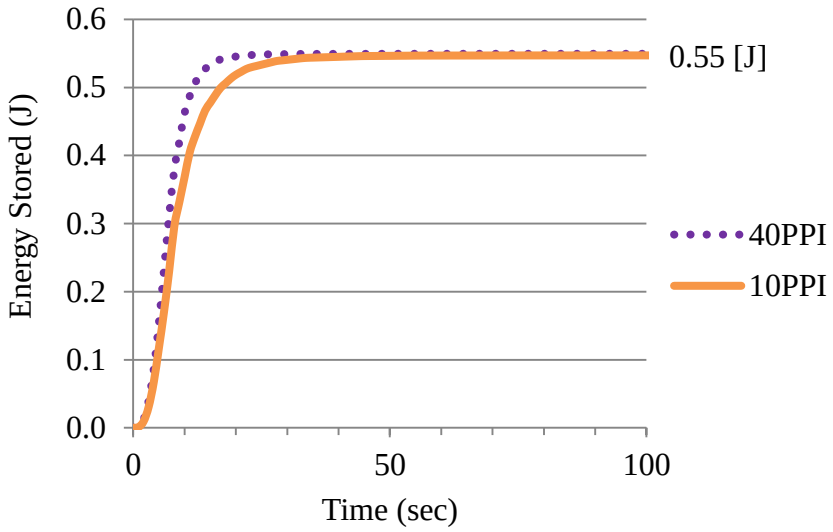

Figure 4.25. Energy storage over time for 10 PPI and 40 PPI unit cell 9% relative density aluminum foam/paraffin systems exposed to 40°C.

Next, the model was redefined to include phase change of the paraffin to study the impact of latent heat storage on the total energy storage over time. Recall the assumed phase transition occurs at 55°C over a ΔT of 2°C. There is only one phase change period between solid and liquid with a latent heat of 150 kJ/kg (approximation of paraffin wax). In general, energy absorbed during phase change can be written as,

$$E_{stored_{Latent}} = (1-\gamma) * V * \rho_{PCM} * L \tag{35}$$

where L is the latent heat of the PCM. The total energy stored can be expressed as,

$$E_{total} = E_{stored_{Sensible}} + E_{stored_{Latent}} \tag{36}$$

An effective heat storage term, φ, for both sensible and latent heat can be developed as,

$$\varphi = \frac{E_{total}}{\rho_{eff} * V * \Delta T} \tag{37}$$

where V and ΔT are volume and difference between applied temperature and initial temperature. By inserting the definitions from Equations 34 and 35 into Equation 36, Equation 37 can be rewritten as

$$\varphi = c_{p_{eff}} + \frac{(1-\gamma) * L * \rho_{PCM}}{\Delta T * \rho_{eff}} \tag{38}$$

Through this process, the foam/PCM system can now be represented in a linear manner with $(\rho_{eff}\varphi)\frac{\partial T}{\partial t}$ as summarized in Table 4.8 and depicted in Figure 4.26.

Table 4.8. Summary of volume averaging model and the energy storage model.

	Energy Storage	
Volume Averaging Model	$\left[(1-\gamma)(\rho c_p)_{PCM} + (\gamma)(\rho c_p)_{foam}\right]\frac{\partial T}{\partial t}$	$(\rho c_p)_{PCM} = \begin{cases} \rho c_{p_{solidPCM}} & T < T_{solid} \\ \rho\left[\frac{L}{(\Delta T)} + (\rho c_p)_{PCM}\right] & T_{solid} \le T \le T_{liquid} \\ \rho c_{p_{liquidPCM}} & T > T_{liquid} \end{cases}$
Effective Energy Storage Model	$(\rho_{eff}\varphi)\frac{\partial T}{\partial t}$	$\rho_{eff} = (1-\gamma)\rho_{PCM} + (\gamma)\rho_{foam}$ $\varphi = c_{p_{eff}} + \frac{(1-\gamma) * L * \rho_{PCM}}{\Delta T * \rho_{eff}}$ $c_{p_{eff}} = (1-\gamma)\frac{\rho_{PCM}}{\rho_{eff}} c_{p_{PCM}} + (\gamma)\frac{\rho_{foam}}{\rho_{eff}} c_{p_{foam}}$

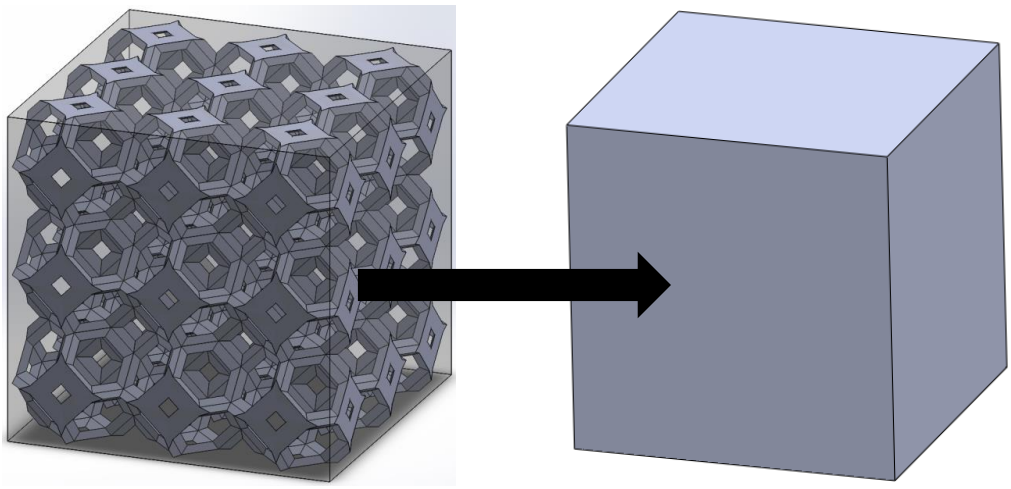

Figure 4.26. Depiction of the effective energy storage model.

The effective energy storage model is used to calculate the energy storage in a unit cell for the 9% aluminum 10 PPI foam, paraffin system. Similar to past conditions, a step temperature was applied to the top of the unit cell while all other sides remained adiabatic. Comparison of the energy stored from the effective energy storage model to that of the 3D phase change model from Figure 4.24 is shown in Table 4.9.

Table 4.9. Comparison of effective energy storage calculation for 10 PPI aluminum foams saturated with paraffin wax unit cell to 3D phase change simulations.

	Energy Stored (J)	
	60°C	80°C
Effective Energy Storage Model	2.93	3.66
3D Simulation	2.95	3.71
Error	0.68%	1.35%

With the small error in energy storage, the accuracy of the effective heat capacity and effective density calculations is demonstrated. The final effective property that must be discussed is the effective thermal conductivity. As shown in Figure 4.25, when 10 PPI, 9% relative density and 40 PPI, 9% relative density foams are placed under identical boundary conditions, 40 PPI responds faster than 10 PPI. This indicates that the thermal charging rate, reflected by the system's thermal conductivity is affected by the pore density, not just by the relative density. This relationship was explored, and it was realized that effective thermal conductivity depends on more than just the pore density and relative density, but it also depends on the temperature.

The effective thermal conductivity for each system was calculated by minimizing the error between the thermal charging rate of the 3D phase change model to the effective energy storage model. As shown in Figure 4.27, the effective thermal conductivity of 10 PPI, 9% relative density aluminum foam exposed to 60°C is 1.5 W/m·K, while under 80°C it is 3.0 W/m·K.

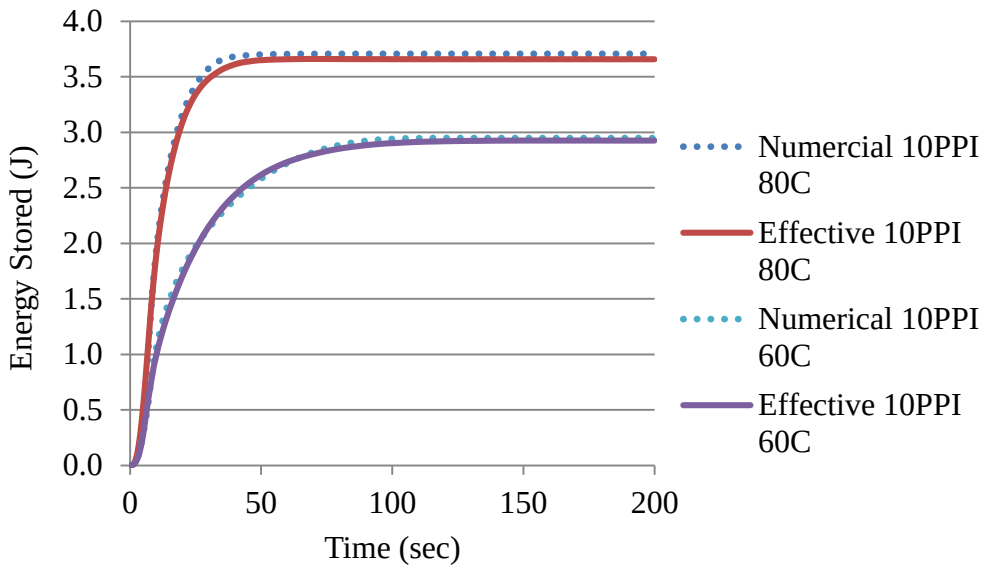

Figure 4.27. Energy storage over time comparison for the numerical phase change simulation and the effective energy storage model.

Next the relationship between relative density, temperature, effective thermal conductivity, and amount of energy stored is explored. As shown in Figure 4.28, the highest effective thermal conductivity is exhibited with the applied temperature of 40°C which means that the system has not undergone phase change. This is explained by analyzing the impact of phase change on the rate of energy moving through the system. Since the system is not undergoing phase change, no energy is being absorbed by this process, which results in a high effective thermal conductivity. When the system does undergo phase change (exposure to 60°C and 80°C), 80°C has a higher effective thermal conductivity than 60°C. This is due to the increased temperature gradient present within the system which results in energy moving through the system at a higher rate.

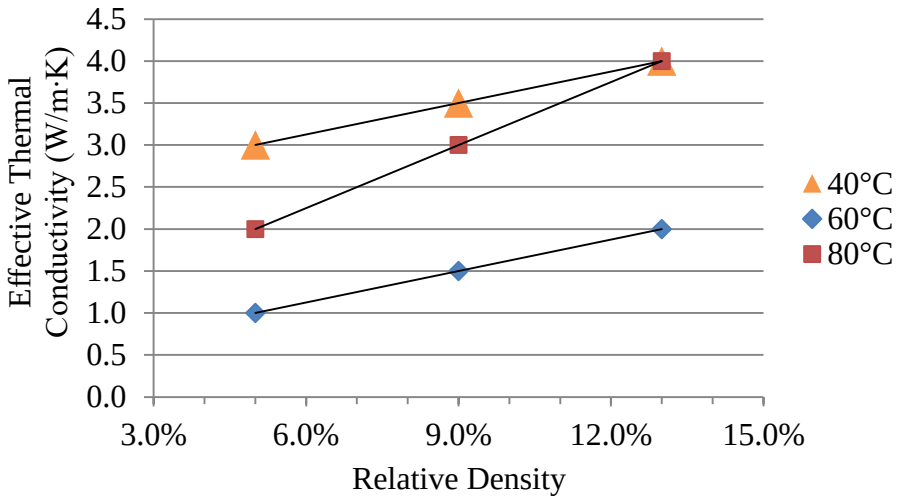

Figure 4.28. Thermal conductivity as a function of relative density and temperature for 10 PPI aluminum foam/paraffin composite system.

Based on the results in Figure 4.28, systems exposed to 40°C have the largest thermal conductivity. However, to fully understand the potential of these systems, not only the thermal conductivity should be considered, but also the amount of energy stored. An example of the amount of energy stored is presented in Table 4.10 for 9% relative density composite systems. The amount of energy stored for the 60°C phase change system is 7x more than the non-phase change system, while the 80°C is 8x. Though both phase change systems store significantly more energy than the non-phase change system, the 80°C system only stores 20% more energy since additional energy storage beyond the 60°C system is sensible heat.

Table 4.10. Energy stored for various applied temperature - 10 PPI, 9% relative density aluminum foam/paraffin composite system

Applied Temperature (°C)	Thermal Conductivity (W/m·K)	Energy Stored (J)
40°C	3.5	0.55
60°C	1.5	3.74
80°C	3.0	4.48

Figure 4.27 and Figure 4.28 as well as Table 4.10 suggest that the effective thermal conductivity cannot be simply calculated via the rule of mixtures and, if other correlation methods are to be used, they must take into account the temperature, the pore density, and relative density. As a final example of the accuracy of the effective energy storage method, this model is validated with experimental data. As determined by the prior analysis, the effective thermal conductivity of 9%, 10 PPI aluminum foam systems exposed to 60°C and 80°C is 1.5 W/m·K and 3.0 W/m·K, respectively, while the effective specific heat and density are defined in Table 4.8. Required of the effective specific heat calculation is the latent heat of the material. As previously discussed, the benefit of the effective energy storage model is that the latent heat distribution for the solid-solid and solid-liquid transitions do not need to be independently defined as a function of their temperature. Only the total latent heat of the paraffin wax, determined via DSC in Table 3.2, needs to be known.

Modeled geometry represents the experimental geometry of a rectangular samples with sides of 2.54 cm and a thickness of 1.27 cm. Experimental data reported in Figure 3.18 is repeated in Figure 4.29 along with the results from the effective energy storage

model. The temperature profile presented is the bottom temperature of the modeled geometry over time. Though the effective model does not take into account phase change, a 10% error in time to steady state for both 60°C and 80°C indicates good agreement between the model and the experiment. As previously stated and shown by this analysis, the effective energy storage model is specifically useful when concerned about energy storage over time and not temperature distribution.

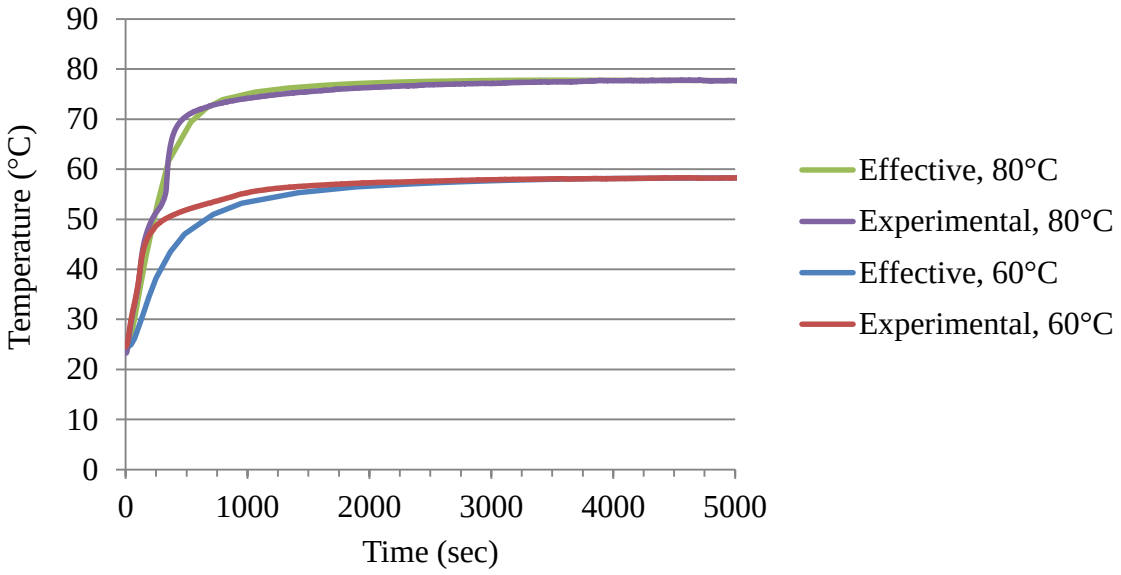

Figure 4.29. Comparison between experimental data and effective energy storage model bottom temperature profile.

4.4.1 Aluminium foam modeling summary

The effective energy storage model was presented as an accurate and efficient method of modeling porous foam/PCM systems. Rather than modeling sensible and latent heat separately, this model combines both thermal storage terms into an effective heat capacity calculation. As a result, the nonlinear 3D phase change problem is converted into

a 1D linear problem. This method is specifically useful in thermal energy storage applications where the amount of energy being stored over time is of interest.

Aluminum foam and paraffin wax properties were used in the demonstration of the model. Though the development of the effective heat capacity and effective density is straightforward, the effective thermal conductivity correlation is not. It was found that the effective thermal conductivity is dependent on temperature, the pore density, and relative density. Since both pore density and relative density are correlated to the specific surface area, an accurate structural foam model is necessary for the development of thermal conductivity correlations. It was found that a Kelvin structure model is a good approximation of the foam structure based on specific surface area versus relative density data. The effective energy storage model was compared to 3D phase change simulations with the Kelvin structure imported into COMSOL and only a small error was calculated. Not only does this model providing a way to represent the composite foam/PCM structure as a homogenous material, but, since the energy being stored is being calculated over time, multiple phase changes or various phase change temperature ranges can also be easily incorporated.

4.5 Validation of CENG Foam Models

When modeling aluminum foam/PCM systems, simplification of the foam with geometrically accurate effective properties offers a method of reducing the complexity of modeling the system. However, the small pore size of CENG allows the system to be modeled as a homogenous medium with the enthalpy method or the effective heat capacity approach [130], which does not require the simplifications of open-cell foams for expedient

analysis. As discussed in 4.2.2, density and specific heat can be adjusted as a function of the volume fraction, $\gamma = V_{foam}/V_{total}$, while latent heat and thermal conductivity can be measured or based on published correlations. Recall that Chapter 3 discussed the improved performance that CENG foams offer over aluminum foams to enhance the thermal charging rate of PCM, so it is of interest to investigate and validate the one-temperature model for this composite system for optimized battery design.

Assuming that natural convection is suppressed in the compressed pores, radiation is negligible, and thermal equilibrium exists between the boundary of the foam and PCM, the governing equation can be transformed with the effective heat capacity as Equation 39. Note that phase change may occur over a range of temperatures, denoted by ΔT, and that the melting temperature is described as T_{melt} such that $T_{solid} = (T_{melt} - \Delta T/2)$ and $T_{liquid} = (T_{melt} + \Delta T/2)$.

$$\left(\rho(T)c_p(T)\right)_{composite}\frac{\partial T}{\partial t} = \nabla\cdot\left(k_{composite}\nabla T\right) \tag{39}$$

or

$$\left[(1-\gamma)\left(\rho c_p\right)_{PCM} + (\gamma)\left(\rho c_p\right)_{graphite}\right]\frac{\partial T}{\partial t} = \nabla\cdot\left(k_{composite}\nabla T\right)$$

$$\left(\rho c_p\right)_{PCM} = \begin{cases} \left(\rho c_p\right)_{solidPCM} & T < T_{solid} \\ \left(\rho\left[\dfrac{L}{(\Delta T)} + c_p\right]\right)_{solidPCM} & T_{solid} \le T \le T_{liquid} \\ \left(\rho c_p\right)_{liquidPCM} & T > T_{liquid} \end{cases}$$

In this work, the effective heat capacity method with COMSOL is used to numerically model CENG foams saturated with paraffin wax. Since the intention is to fully characterize the CENG/PCM composite, this model requires knowledge of the density and specific heat in both the solid and liquid phase as well as latent heat and thermal conductivity of the composite. Density and specific heat for the solid and liquid pure PCM were obtained from the manufacturer. Volume fraction and percent void for each CENG foam was used to adjust both the specific heat and density to represent each composite. Latent heat and thermal conductivity are presented in Table 4.11 (repeated from Table 3.4). Additional properties used in the model are presented in Table 4.12 assuming $c_{p,graphite}$ = 711.0 J/kg·K and $\rho_{graphite}$ = 2260.0 kg/m^3. Note that, since the PCM of interest undergoes both a solid-solid and solid-liquid phase change, the thermophysical properties are presented for both the phase changes.

Table 4.11. Properties of CENG foam composites with respect to the bulk density.

CENG Bulk Density (kg/m^3)	**Thermal Conductivity at 20°C (W/m·K)**	**Latent Heat (J/g)**	**Solid-Liquid Melting Temperature (°C)**
0	0.3	163.4	55.2
23	2.3	161.9	56.3
50	4.7	157.0	56.3
100	9.6	136.4	54.5
143	10.1 (∥), 20.2 (⊥)	111.1	53.8

Table 4.12. Summary of CENG/PCM composites.

CENG Bulk Density (kg/m^3)	CENG Volume Fraction	Density (kg/m^3)		Specific Heat (J/kg·K)		Latent Heat (J/g)	
		Solid	Liquid	Solid	Liquid	Solid	Liquid
0	0.0%	910.0	740.0	2200.0	3000.0	31.2	132.2
23	1.0%	923.7	755.4	2162.9	2930.3	32.8	129.1
50	2.2%	939.7	773.4	2120.8	2852.1	31.2	125.8
100	4.4%	969.4	806.9	2046.5	2716.4	25.3	111.1
143	6.3%	995.5	836.3	1986.1	2608.5	19.8	91.3

The measurements and calculations of Table 4.11 and Table 4.12 are used in combination with Equation 39 to model the thermal charging performance of each composite with $\Delta T_{solid-solid}$ = 14°C and $\Delta T_{solid-liquid}$ = 13°C as calculated from DSC measurements. The modeled geometry is shown in Figure 4.30; a 0.5 mm layer of thermal grease separates the boundary condition applied to the top surface and the CENG/PCM sample, while the remaining sides are exposed to an external heat loss to represent the imperfect insulation of the acrylic experimental container. The initial temperature for the model is defined as the initial temperature of the composite in each respective experiment. The model is validated with prior experimental data by comparing the bottom temperature profile over time under various boundary conditions (60°C, 0.39 W/cm^2, and 1.55 W/cm^2) for various bulk densities of graphite (23, 50, 100, 143 kg/m^3). Figure 4.31 shows comparison of the 23 kg/m^3 and 100 kg/m^3 samples exposed to various boundary conditions.

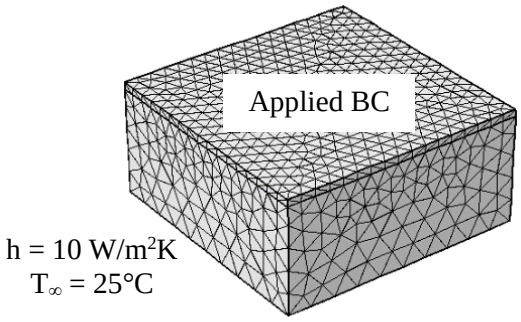

Figure 4.30. Modeled geometry 2.54 x 2.54 x 1.27 cm.

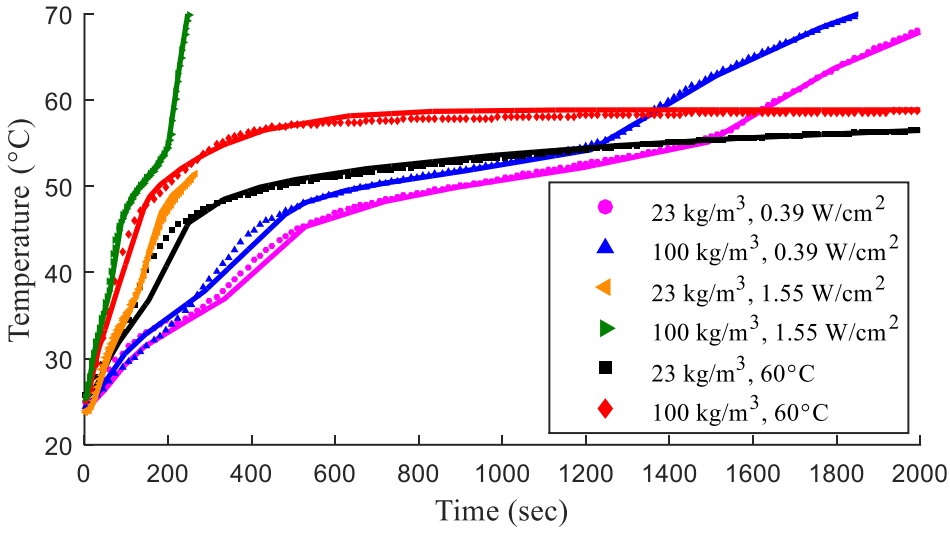

Figure 4.31. Comparison of model to experimental results. Solid and dotted lines represent numerical and experimental results, respectively.

The effective heat capacity assumes an even distribution of latent heat across the temperature range. Comparison of the DSC curve for paraffin wax compared to this assumption is shown in Figure 4.32. Approximating the normal distributions of latent heat from the DSC curve as average values in both phase change regimes has an implication on the modeled temperature profile. An example of solid-solid phase change is shown in

Figure 4.33. The discrepancy between the temperature profiles of the model and experiment can be attributed to the effective heat capacity assumption; the latent heat is assumed to be constant over the phase change temperature interval, but in reality, this property is a function of temperature.

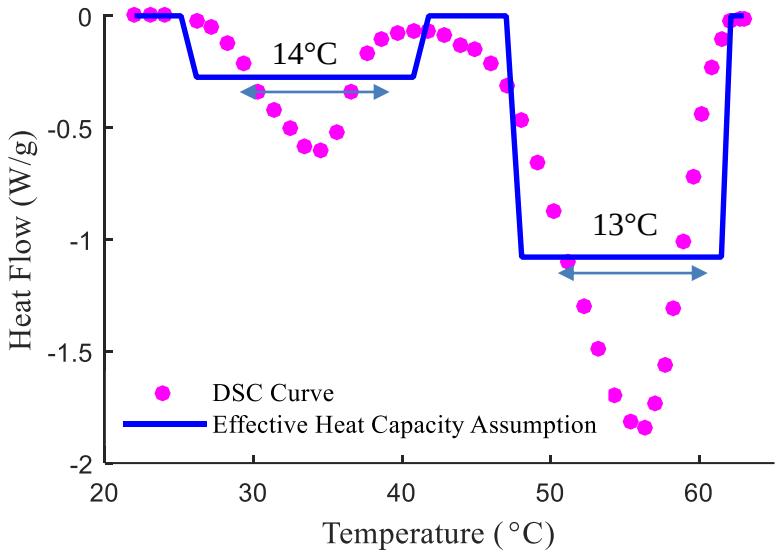

Figure 4.32. DSC curve compared to effective heat capacity assumption.

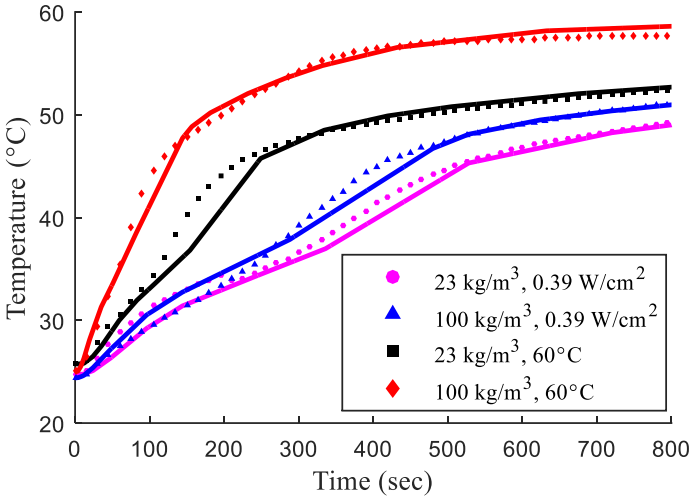

Figure 4.33. Solid and dotted lines represent numerical and experimental results, respectively.

While the effective heat capacity assumption impacts the temperature profiles in the solid-solid and solid-liquid phase change regimes, the validity of this model is suggested by comparing the time to end of melt. For all composites, there is less than 10% error between the time to end of melt of the model and the experiment. Since the time to fully melt the system is dependent on total latent heat capacity of the system as well as the temperature that the phase transition is complete, which are both accurately reflected in the effective heat capacity assumption, the effective heat capacity model is shown to be a valid model of CENG composites.

The use of the 3D geometry allows comparison of the thermal charging response of the anisotropic 143 kg/m^3 composites by defining the thermal conductivity as $[k_x, k_y, k_z]_{perpendicular}$ = [10.1, 10.1, 20.2] W/m·K and $[k_x, k_y, k_z]_{parallel}$ = [20.2, 20.2, 10.1] W/m·K. Figure 4.34 demonstrates the ability of the model to predict this anisotropic response as

well as confirms the limited additional benefit of the higher thermal conductivity graphite composite.

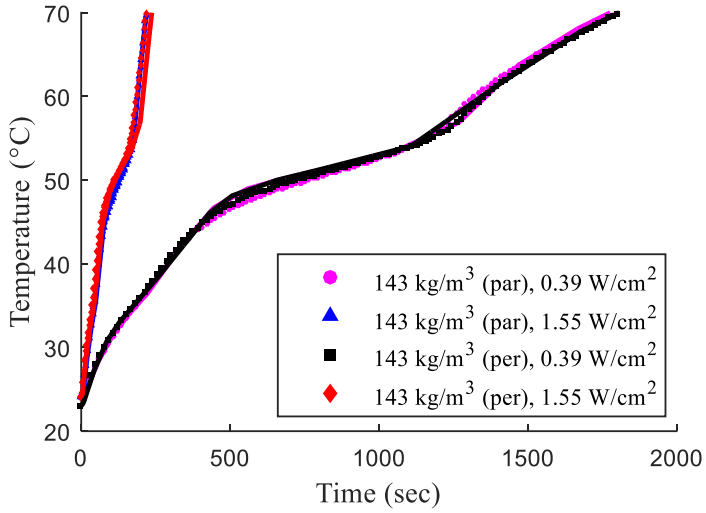

Figure 4.34. Comparison of model to experimental results for anisotropic graphite composites. Solid and dotted lines represent numerical and experimental results, respectively.

Both the experimental and modeling work in this study suggest that the addition of graphite beyond a CENG bulk density of 100 kg/m^3 has limited benefit on the energy storage performance of the experimental volume. Acknowledging that this practical CENG bulk density limit is height and boundary condition specific, the validated model was used to demonstrate the practical limit of CENG bulk density for systems of various heights and applied heat fluxes. Since the impact of height was the parameter of interest, the model geometry was simplified to a 2D problem as shown in Figure 4.35 with insulated sides and a lower convection boundary condition to represent imperfect insulation. The height, H, was varied between 1.27 cm and 50.8 cm.

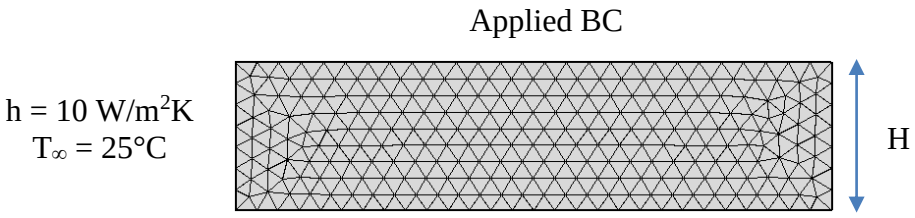

Figure 4.35. Modeled geometry 5.08 x H cm.

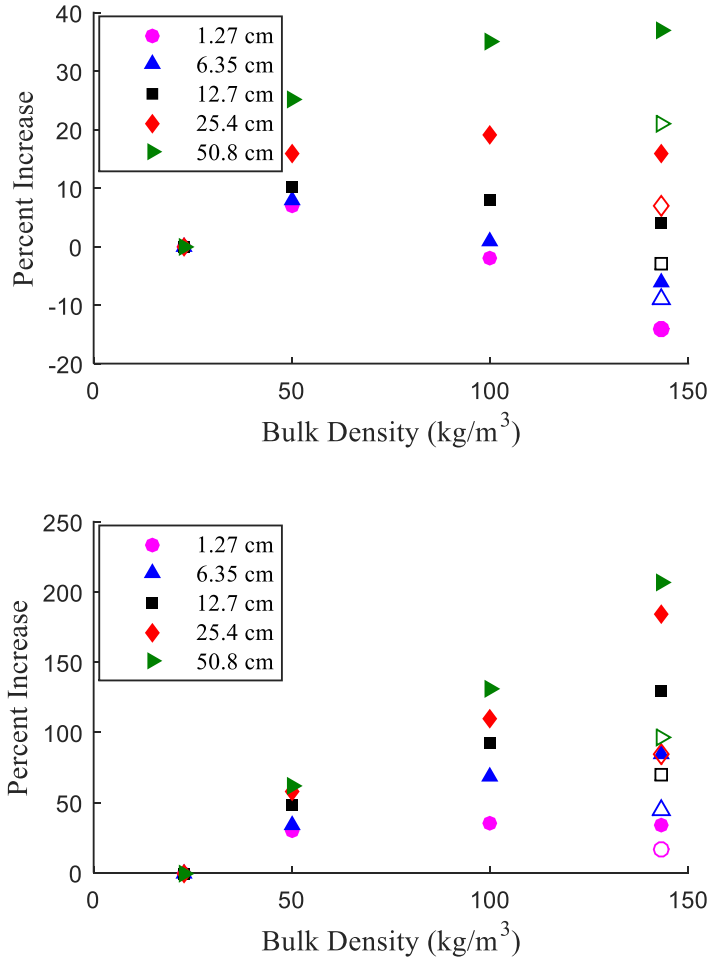

Figure 4.36. Energy storage performance percent increase compared to 23 kg/m^3: 0.2 W/cm^2 (top), 5.0 W/cm^2 (bottom).

Recall that the energy storage performance defined in 3.9 is the amount of energy stored as latent heat divided by the time to end of melt as a function of the material bulk density. The energy storage performance of CENG composites with bulk densities of 23 kg/m^3, 50 kg/m^3, 100 kg/m^3, 143|| kg/m^3, and 143⊥ kg/m^3 is compared for various heights and applied heat fluxes in Figure 4.36. The baseline is considered to be the energy storage performance of 23 kg/m^3. Note that 143|| and 143⊥ kg/m^3 composites are represented by open and closed data points, respectively, and that the energy storage performance percent increase of the perpendicular sample is always greater than the parallel due to the higher thermal conductivity. As Figure 4.36 (top) demonstrates, as the height increases for composites exposed to low heat fluxes, the optimum CENG bulk density also increases. Under 0.2 W/cm^2, 50 kg/m^3 is the optimum for the 1.27 cm sample, with both 143 kg/m^3 samples actually decreasing the energy storage performance compared to 23 kg/m^3 due to the lower latent heat of the composites. For 25.4 cm, the optimum CENG bulk density changes to 100 kg/m^3, and for 50.8 cm, 143⊥ kg/m^3 is preferable. As Figure 4.36 (bottom) demonstrates, the 143⊥ kg/m^3 composite is preferable for all composite heights exposed to 5.0 W/cm^2 due to the decrease in time to end of melt. The primary assumption in this analysis is the constant boundary condition. In applications with an intermediate heat source, the optimum CENG bulk density will increase; however, due to the decrease in latent heat as the thermal conductivity increases, an optimum CENG bulk density will always exist that maximizes both the thermal charging and energy storage.

The validated model has also been used to demonstrate the impact of the bulk density, height, and boundary condition on the time to end of melt. To compare all samples, the time to end of melt has been normalized by dividing by the composite height. The

normalized time to end of melt for CENG composites with bulk densities of 23 kg/m^3, 50 kg/m^3, 100 kg/m^3, 143|| kg/m^3, and 143⊥ kg/m^3 are compared for various applied heat fluxes in Figure 4.37. Note that 143|| kg/m^3 and 143⊥ kg/m^3 composites are represented by open and closed data points, respectively.

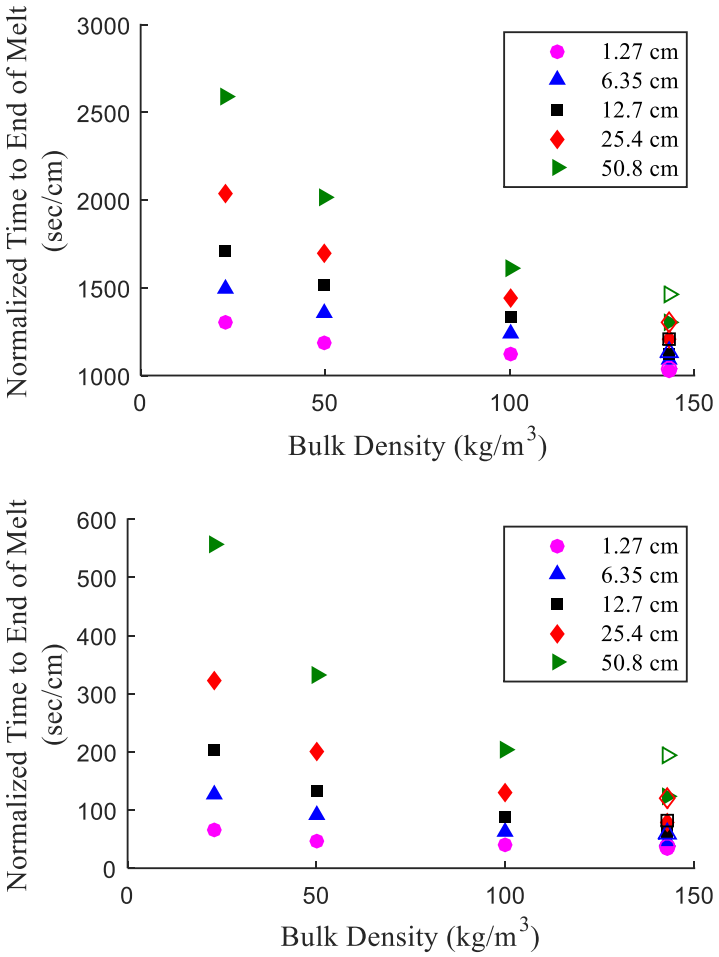

Figure 4.37. Normalized time to end of melt for various bulk densities: 0.2 W/cm^2 (left), 5.0 W/cm^2 (right).

As shown in Figure 4.37, the increase in CENG bulk density decreases the normalized time to end of melt for both heat fluxes. This decrease in time to end of melt is due to the increase in thermal conductivity as well as the decrease in latent heat as a result

of the addition of graphite (Figure 3.8). Comparison of the 100 kg/m^3 and 143‖ kg/m^3 data, which have similar thermal conductivities, demonstrates the impact of decreased latent heat: all 143‖ kg/m^3 samples have a normalized time to end of melt less than 100 kg/m^3 due to the decrease in thermal energy capacity. Additionally, comparison of the parallel and perpendicular samples for 143 kg/m^3 show that the higher thermal conductivity of the perpendicular sample results in a lower normalized time to end of melt as compared to the parallel sample. Figure 4.37 suggests that, for applications where the response rate is more important than the energy storage performance, a higher CENG bulk density is preferable; however, for many thermal storage applications, both the response rate and energy storage density are important parameters to consider.

4.5.1 CENG modeling summary

From experiments reported in 3.6.2.1, CENG foams outperform aluminum foam composites based on charging rate, energy density, and cost. Additionally, by calculating the energy storage performance for various boundary conditions and CENG bulk densities, it was shown that all systems approach a practical limit where an increase in CENG bulk density is no longer a benefit for thermal energy storage performance. In some cases, the anisotropic thermal conductivity for high bulk densities actually decreases the thermal storage performance because of the significant impact on latent heat due to the addition of graphite as well as the closed pores formed during compression. This introduces the need for a validated CENG model to study the impact of various parameters to optimize the CENG thermal battery for specific applications or constraints.

The experimental results were used to validate a 3D phase change model for CENG/PCM composites; the phase change moving boundary problem was solved using the effective heat capacity method and the addition of the graphite foam was represented with a combination of measured and volume averaged properties. This validated model was used to demonstrate the impact of size scale effects on the optimum bulk density.

Guided by this work, Chapter 5 will focus on developing design rules that consider constraints such as required energy capacity, volume, and response time that improve upon the common metrics of composite thermal conductivity and latent heat for thermal battery design. These guidelines will be used to optimize the design a large-scale thermal battery prototype for integration in a vapor compression cycle.

CHAPTER 5. OPTIMIZED THERMAL BATTERY DESIGN

The goal of this research is to improve the performance of space conditioning systems through thermal energy storage and innovative heat exchanger design. Improving the thermal charging of PCM through integration of aluminum foams and CENG foams was compared experimentally in Chapter 3. These results were used to validate models developed in Chapter 4. Due to the improved performance and lower cost of CENG foams, this material has been chosen as the method to increase the thermal charging rate of PCM.

The integration of a thermal battery in a condenser offers a method of decoupling heat removal from a condensing refrigerant and heat release into the ambient space. The final goal of this research is to design a phase change thermal battery to store 170W of condenser waste heat over a 2-hour period, or 1224 kJ of thermal energy. The design of such a condenser requires knowledge of thermal charging behavior for PCM composites as well as adhering to constraints of melting temperature, size, mass, heat capacity, thermal charging rate, refrigerant charge, and cost required of the unit. This necessitates an optimization of the CENG thermal battery bulk density to meet system constraints.

This chapter will first review optimization studies in literature for various PCM enhancement materials and applications. Following this discussion, PCM selection, design optimization, and fabrication will be reviewed along with how lessons learned during the first prototype are guiding the second prototype design specifically with issues of contact resistance and method of production.

5.1 Optimization Literature Review

The optimization of a thermal battery has been studied to meet various system constraints such as minimizing junction temperature [107, 160] or reducing fluid tube number [24]. Such studies reported in literature have focused on both thermal management and thermal storage applications of enhanced PCM thermal batteries.

Thermal management studies typically focus on electronics applications, where the goal is to maximize the operating time, while minimizing the junction temperature. For example, Baby and Balaji [107] experimentally compared the ability of 33, 72, and 120 pin fin heat sinks combined with PCM to minimize the junction temperature for thermal management of portable electronics. The geometry of the heat sink and pins were the same for each assembly as shown in Figure 5.1, so as the number of fins increased, the amount of PCM, and therefore the energy density, decreased. By applying various heat fluxes to the top of each pin fin assembly, it was determined that the 72 pin heat sink was optimal. This assembly minimized the junction temperature due to high conductivity from the pin fins, but also high energy density during phase change of the PCM. Optimization of pin fin geometry was also reported by Leland and Recktenwald [161]. In addition to pin fins, plate fins geometries have been optimized [127, 162, 163].

With a similar experimental setup where a heat flux is applied to one outer surface of a test sample and other sides remain insulated, Jiang *et al.* [160] experimentally studied the optimal density of expanded graphite combined with PCM for thermal management of Li-ion batteries. Mass fractions of expanded graphite were 3%, 6%, 9%, 12%, 16%, 20% and 30% were used, and it was determined that a mass fraction between 16-20% resulted

in the lowest temperature due to the high thermal conductivity and high energy density as shown in Figure 5.2.

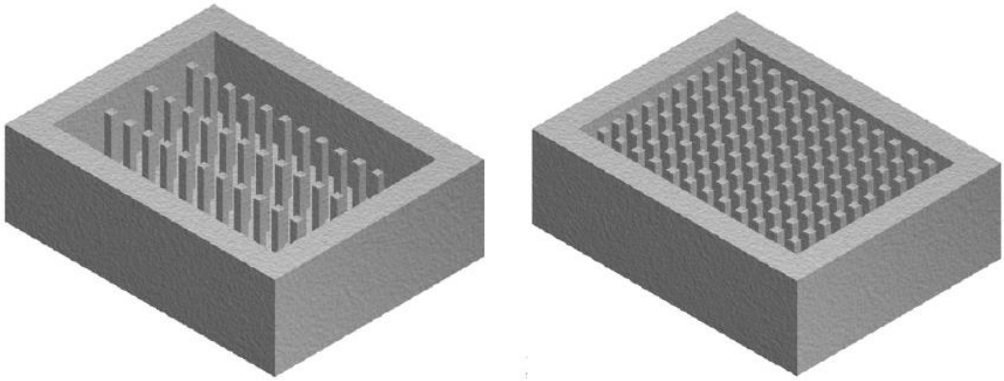

Figure 5.1. Isometric views of various heat sink assemblies [107].

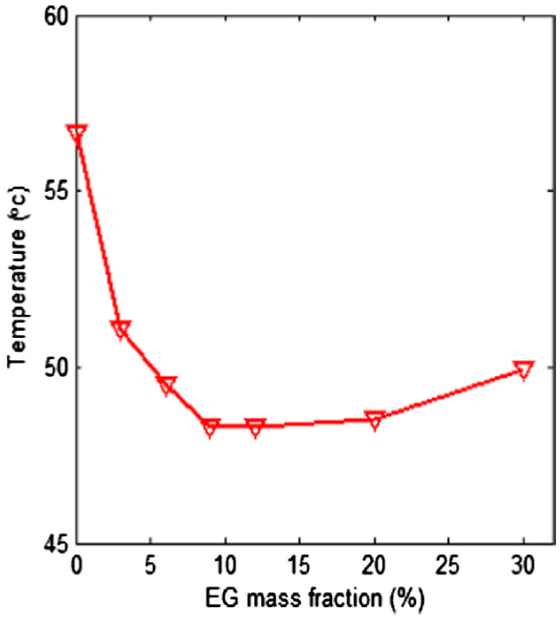

Figure 5.2. Volume-averaged temperatures of a battery with different EG mass fractions [160].

Thermal management applications generally study a geometry where a heat flux or temperature is applied to a surface and the other sides remain insulated to mimic installation in a device. Similarly, studies that focus on thermal storage applications use a geometry where the PCM thermal battery surrounds tubes through which a heat transfer fluid flows. An example is shown in Figure 5.3. Space surrounding each tube is filled with PCM or an enhanced PCM composite.

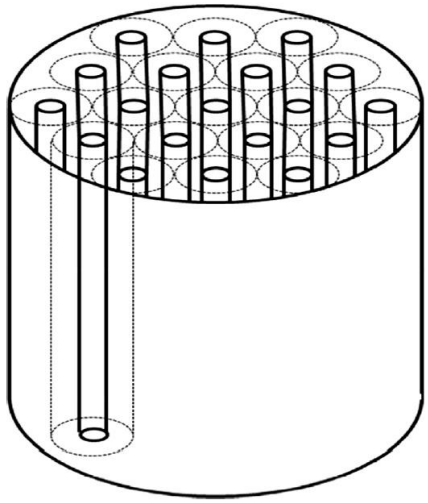

Figure 5.3. Configuration of a latent heat thermal storage system [24].

Thermal batteries used in storage applications are generally designed to store a defined amount of energy over a required period of time. For example, Kim *et al.* [24] and Zhao *et al.* [130] designed a latent heat storage system with mesophase pitch-based carbon foams saturated with PCM to store 75 MW and 100 MW of thermal energy over an 8-hour and 12-hour time period, respectively. A one-temperature model was used with effective properties to study the impact of graphite foam, heat transfer fluid velocity, pipe outer diameter, and pipe thickness on the phase change front progression through the material and the required number of pipes. The addition of graphite foam increased the thermal

conductivity and reduced surface area required for heat transfer. The surface area is impacted by number of tubes, outer diameter (OD), and thickness.

It was summarized that since the difference of PCM thermal conductivities between liquid phase and solid phase is generally small and natural convection is negligible for graphite foam/PCM composites, the charging process and the discharging process are similar. It was reported that a system with a pipe OD = 219.08 mm, a pipe wall thickness = 6.35 mm, a heat transfer fluid velocity = 0.5 m/s, and an effective thermal conductivity of the PCM/graphite foam combination = 30 W/m·K, the number of pipes was reduced by 10%, which corresponds to a substantial cost reduction [24]. Additionally, the pipe wall thickness was found to have insignificant effect on the system. No optimization studies with CENG/PCM within a heat exchanger have been found.

In addition to optimization studies that are focused on the impact of thermal enhancement material on the PCM, other studies have looked specifically at the impact of heat transfer velocity [24, 127, 164] and heat transfer fluid temperature [126, 164, 165] on the thermal charging response. With various heat exchanger designs (double pipe, fins, plates) saturated with PCM installed in a controlled experimental cycle, Medrano *et al.* [165] showed that by increasing the heat transfer fluid temperature, the melting temperature is reduced. This result has been shown in other studied with a shell and tube heat exchanger with pure PCM [126, 166] and PCM with finned tubes [23, 164].

Controlled test loops have also been used to demonstrate the impact of heat transfer fluid mass flow rate. It has been shown that the overall heat transfer rate to the PCM increases with an increase in the heat transfer fluid velocity [24, 127, 164]. However, the

effect of the heat transfer fluid velocity has been observed to be small in configurations having very few fins, owing to the large residual thermal resistance from the PCM [167].

Some studies have compared the effect of heat transfer fluid flow rate and temperature. Shon *et al.* [168] studied the impact of heat transfer fluid temperature and mass flow rate on the thermal charging response of a finned tube heat exchanger with PCM to store automotive coolant waste heat. It was determined that the absorption efficiency of a heat exchanger in a heat storage system using PCM was more strongly influenced by the heat transfer fluid flow rate than by the temperature. Alternatively, Korti and Tlemsani [169] determined for a coil surrounded by PCM that the heat transfer fluid flow rate does not have a great effect on the discharging phase compared to the charging phase, and that the inlet temperature has a great effect on the exchange performance.

It is acknowledged that the heat transfer fluid temperature and flow rate impact the thermal charging response, but when installed in thermodynamic cycles, these variables are dependent on the performance of the cycle. Therefore, the optimization conducted in this study is focused on the properties of the CENG/PCM composite (thermal conductivity, density, latent heat, and specific heat) and the associated impact on design constraints of the condenser (mass, volume, refrigerant charge, and cost).

5.2 Thermal Battery Application

As previously mentioned, a phase change thermal battery is to be designed and installed in the heat exchanger of a space conditioning device to store 170W of condenser waste heat over a 2-hour period, or 1224 kJ of thermal energy. The specific application is for the Roving Comforter (RoCo), an innovative personal thermal management technology

currently being developed at the University of Maryland in collaboration with Oak Ridge National Laboratory and Georgia Tech (ARPA-E Award Number: DE-AR0000530).

RoCo is a small, battery powered vapor compression cycle (Figure 5.4) mounted on a robotic platform. To provide cooling, a fan blows air over the evaporator and through a nozzle directed at the individual. Since RoCo is a portable device, it needs to store the condenser heat generated during operation. Latent heat storage through PCM offers a method to store this waste heat with minimal volume change and mass of the thermal battery. To minimize refrigerant charge (reduce environmental impact of R134a), mass (reduce the weight of the robot via copper mass to extend battery life), and cost (support RoCo as an affordable space conditioning option), it is of interest to increase the thermal charging rate through the addition of CENG. However, since the addition of any enhancement material decreases the composite latent heat, an optimization problem is presented to understand the impact of CENG bulk density on mass, volume, refrigerant charge, length of refrigerant tubes, and cost. The design objectives are shown in Table 5.1.

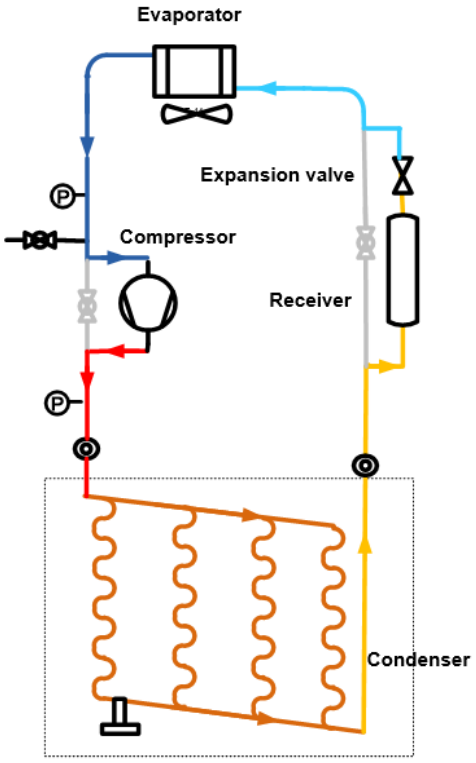

Figure 5.4. Vapor compression experimental cycle (personal communication with Yilin Du, University of Maryland)

Table 5.1. Design objectives of RoCo PCM condenser.

Weight and Volume	<5kg, <5L
Heat transfer capacity	170 W
Energy storage capacity	0.34 kWh
Phase change temperature	36°C – 40°C
Cost	<60$
Refrigerant charge	minimize

Though this is the first use of CENG to optimize the performance of a PCM thermal battery installed in a condenser, a few studies have considered the use of PCM in a condenser of a vapor compression cycle. As reviewed by Joybari *et al.* [170], the

advantages of using PCM as a condenser include higher COP, lower energy consumption, lower condensation temperature and pressure, and lower heat gain from condenser to ambient. However, it is noted that very few studies exist, and there is a need for more comprehensive analysis and investigation. One study was found that explores the use of enhanced PCM, specifically a microencapsulated PCM, integrated into a LHTSS in a conventional air conditioning system [171]. It was shown that the cooling loads of the refrigerator could be reduced by 46.3% and 9.6% for summer and winter, respectively.

5.3 PCM Selection

The first step in designing and building the CENG/PCM condenser is to conduct a market survey of PCMs that undergo melting in the desired melting range of 36°C-40°C. The choice of this temperature range is based on preliminary experiments that were conducted with a pure PCM condenser as well as the knowledge that the lower the melting temperature, the higher the COP of the system. Figure 5.5 presents a comparison of potential PCMs based on the retail cost required to store 1224 kJ of energy compared to the melting range. The retail cost ($/kg) is based on information from online suppliers, while the mass (kg) is based on the latent heat (J/kg). Multiplying the retail cost, required energy storage (1224 kJ), and dividing by the latent heat results in cost of the PCM required. It is noted that this is the upper cost limit as energy will be stored through both sensible and latent heating.

Though salt hydrates offer the lowest cost and highest energy density option, incongruent melting and supercooling result in phase separation, sedimentation, and hysteresis in the melting and solidification temperatures. Fatty acids, though mildly

corrosive, undergo congruent melting with little supercooling. Similarly, paraffins are non-corrosive with congruent melting and little supercooling. Initial effort will focus on PT37, while fatty acid combinations may be considered for future applications. Though not available for all PCMs, both the retail cost (solid circle) and high volume cost (open circle) are shown for PT37 as is it the current PCM under investigation.

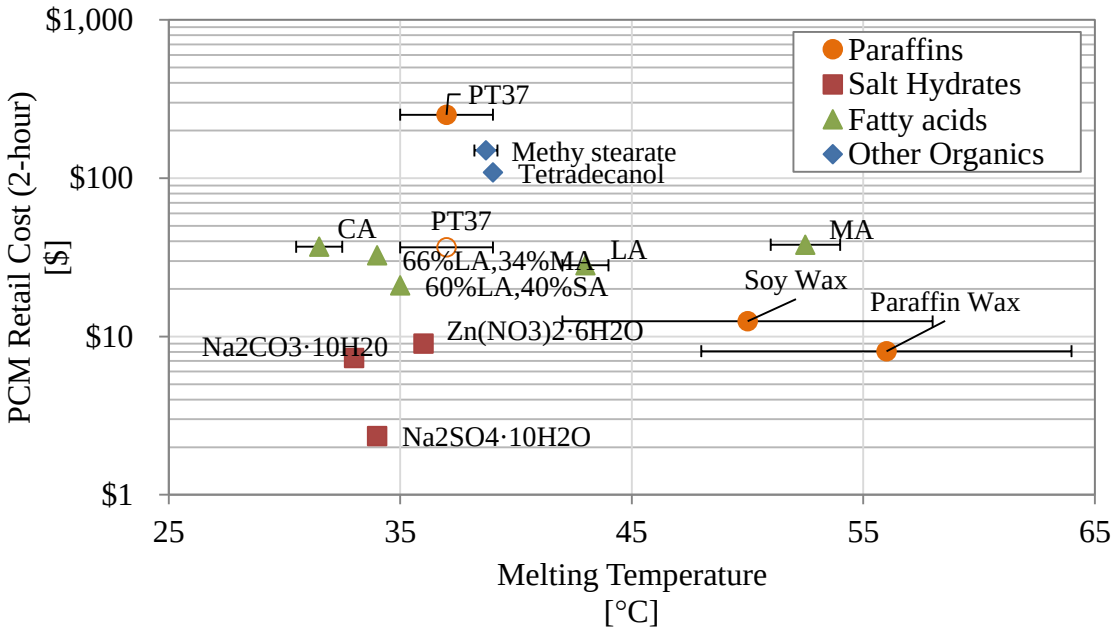

Figure 5.5. Cost of PCM requires of 2-hour design compared to the available PCM melting ranges.

Material properties for PT37 are shown in Table 5.2. The melting point, latent heat, and viscosity were measured as discussed in 3.2.1. The thermal conductivity, density, and specific heat were provided by the manufacturer.

Table 5.2. Properties of PureTemp 37 (PT37).

Melting Point		37°C
Latent Heat		210 J/g
Viscosity at 60°C		0.0034 Pa·s
Thermal Conductivity	solid liquid	0.25 W/m·K 0.15 W/m·K
Density	solid liquid	920 kg/m^3 840 kg/m^3
Specific Heat	solid liquid	2210 J/kg·K 2630 J/kg·K

5.4 CENG Battery Optimization

The next step in the design was to study the impact of various bulk densities on the system constraints of heat exchanger mass (PCM and refrigerant tubing), heat exchanger volume, refrigerant charge, and length of refrigerant tubes to meet the system performance requirements. The CENG model developed and validated in 4.2.2 is used to model the CENG composite. The specific heat and density are adjusted as a function of relative density, $\gamma = \frac{V_{graphite}}{V_{total}}$, as shown in Equation 40 and Equation 42, while the thermal conductivity and latent heat were based on previous work with paraffin wax.

$$\rho_{eff} = (1-\gamma)\rho_{PT37} + \gamma\rho_{graphite} \tag{40}$$

$$c_{p_{eff}} = (1-\gamma)\frac{\rho_{PT37}}{\rho_{eff}}c_{p_{PT37}} + (\gamma)\frac{\rho_{graphite}}{\rho_{eff}}c_{p_{graphite}} \tag{41}$$

Due to the low thermal conductivity of both paraffin wax and PT37, the composite thermal conductivity was assumed to be the same as paraffin wax composites for each bulk density reported in Table 3.4. Additionally, the decrease in latent heat because of both the CENG addition and voids determined through DSC measurements for paraffin wax was used to determine the latent heat of the CENG/PT37 composites. For example, the data reported in Table 3.4 indicates a 5% decrease in latent heat for CENG composites at 50 kg/m^3. Therefore, the latent heat of PT37 composites at 50 kg/m^3 is 95% of the original PCM (210 J/g) or 200 J/g. Following optimization, the thermal conductivity and latent heat were measured for the optimal PT37 composite to confirm these approximations.

Table 5.3. Properties of CENG/PT37 composites used in the optimization.

CENG Bulk Density (kg/m^3)	**CENG Relative Density**	**Density (kg/m^3)**		**Specific Heat (J/kg·K)**		**Latent Heat (J/g)**	**Thermal Conductivity (W/m·K)**
		Solid	Liquid	Solid	Liquid		
0	0.0%	920	840	2210	2630	210	0.25 (s); 0.15 (l)
11	0.5%	927	847	2192	2605	208	1.1
23	1.0%	934	854	2173	2578	205	2.3
50	2.2%	950	871	2131	2520	200	4.7
100	4.4%	979	903	2057	2417	176	9.6
143	6.3%	1005	930	1997	2335	145	20.2

The modeled geometry used in the optimization study is shown in Figure 5.6. The 3D model (Figure 5.6 (top left)) was reduced to a 2D model as shown in Figure 5.6 (lower left) since natural convection can be considered negligible and anisotropic properties of high bulk density system would be designed for the higher thermal conductivity to be in the radial direction. The inner tube represents the copper refrigerant tube. A symmetry

argument was used to reduce this unit cell to a quadrant as shown in Figure 5.6 (right). The applied refrigerant tube temperature is 48°C, which is based on initial experimentation conducted at the University of Maryland, while the remaining sides are insulated. For the initial prototype, thermal contact resistance between the refrigerant tube and the composite was not considered, but this assumption will be discussed in 5.6.

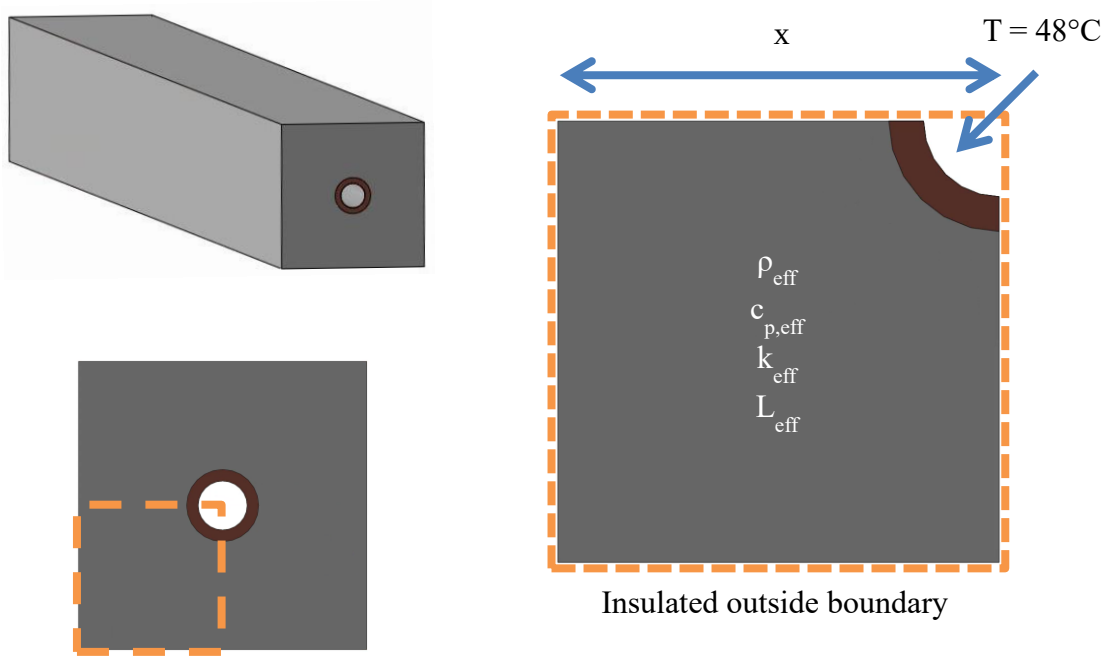

Figure 5.6. CENG modeled geometry.

To determine the graphite bulk density appropriate for the thermal battery, the effective properties model was used to find the melt distance, x, defined as the radial distance from the refrigerant tubing that PCM has undergone phase change after 2 hours as shown in Figure 5.6 (right). As the bulk density increases, the melt distance also increases due to the higher thermal conductivity as well as the lower latent heat. Figure 5.7 depicts the phase quality for pure PCM and 100 kg/m^3 CENG composite after 2 hours. Red

represents a quality of 1, which is liquid, while the darkest blue represents a quality of 0.5, which represents the PCM at 37°C. The thermal charging distance for the pure PCM and 100 kg/m^3 is 12 mm and 52 mm, respectively, which explains the difference in the size of the refrigerant tube compared to the size of the unit cell.

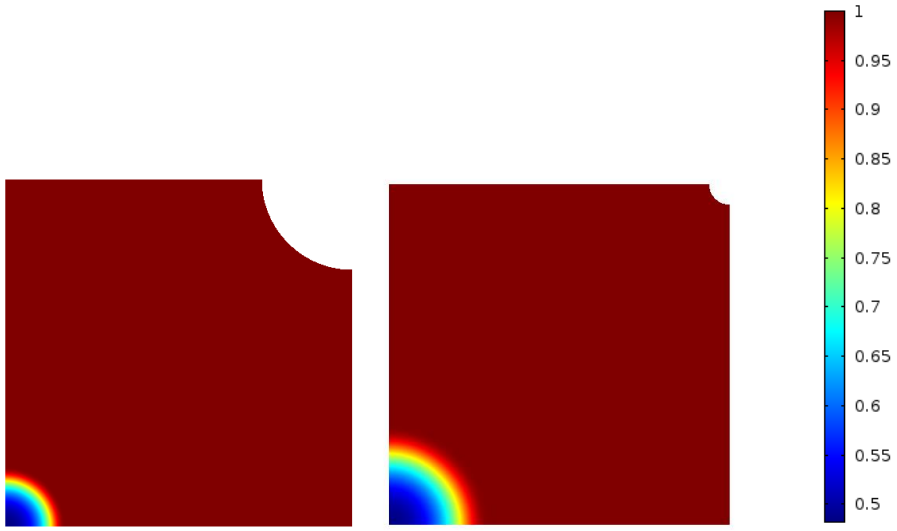

Figure 5.7. Thermal charging distance for 0 kg/m^3 (12 mm) and 100 kg/m^3 (52 mm) as determined by quality of the PCM after 2 hours.

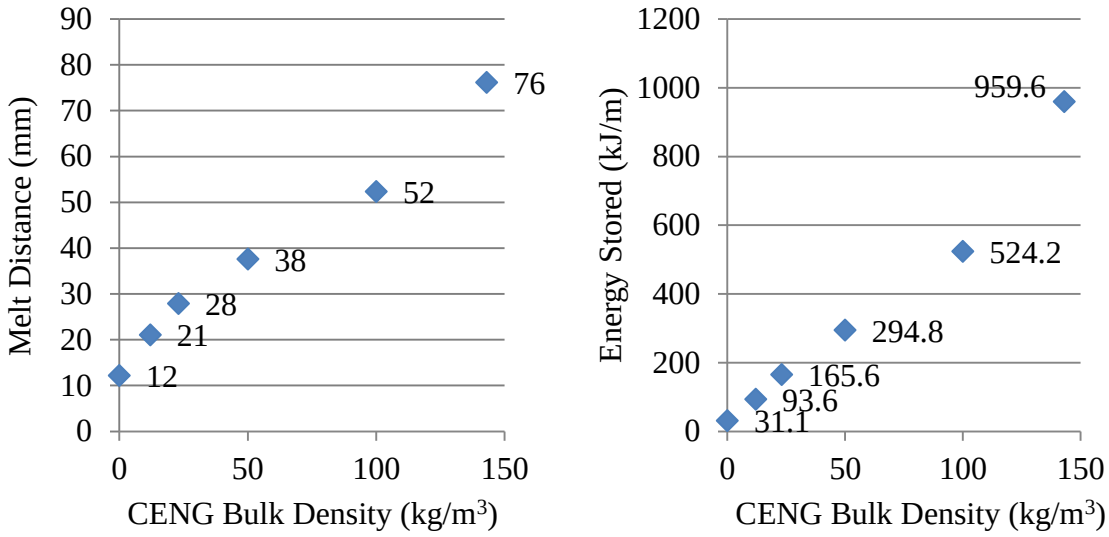

Figure 5.8. Thermal charging distance as a function of CENG bulk density.

The thermal charging distance for each CENG bulk density is summarized in Figure 5.8 (left). The energy stored in the quadrant was calculated by integrating the heat flux across the tube wall over time ($Q_{quad} = \iint q'' r d\phi dt$ [kJ/m]) and is shown in Figure 5.8 (right). The melt distance and energy stored as a function of bulk density were used to calculate the phase change heat exchanger (PCHX) mass and volume, refrigerant charge, and length of refrigerant tubes for a unit that stores 1224 kJ of thermal energy. For example, from the effective properties model, the thermal charging distance for pure PCM is determined to be 12 mm and the energy stored in the quadrant is 31.1 kJ/m. Therefore, energy stored in the cross-section is 124.4 kJ/m, and the length of PCM container required to store 1224 kJ of energy is 9.9 m. Based on this length, all other design variables (mass, volume, refrigerant charge, and length of refrigerant tube) can be calculated.

In general, as the bulk density increases, the higher thermal conductivity results in a greater melt distance that decreases the refrigerant charge and number of refrigerant

tubes. Furthermore, as the bulk density increases, the latent heat decreases due to closed pores as well as the addition of graphite as discussed in 3.4.2, which means that the mass and volume of the heat exchanger increases to store the required amount of energy. These considerations are summarized in the graph of Figure 5.9. Based on this analysis, a bulk density of 50 kg/m^3 has been chosen for the prototype thermal battery as it minimizes the PCHX mass and volume, while requires the lower limit of refrigerant tubing and charge.

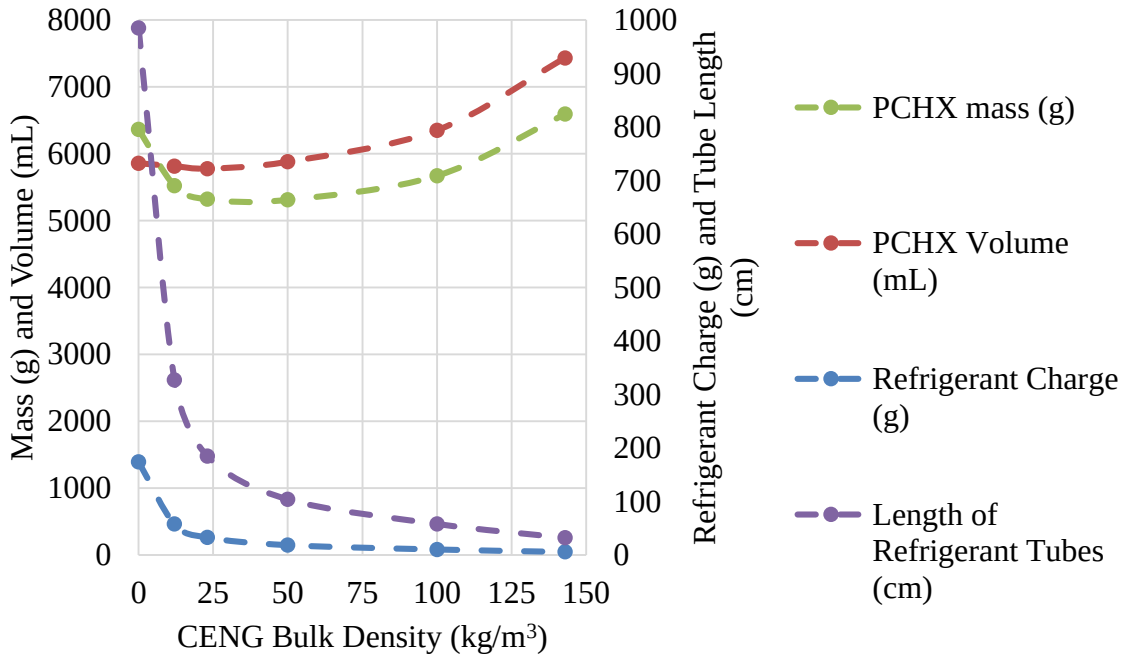

Figure 5.9. Summary the impact of CENG bulk density on design parameters.

The cost of the thermal battery as a function of CENG bulk density can be calculated with high volume costs of CENG ($2.3/kg) and PT37 ($6.4/kg) provided from the manufacturers, as well as high volume costs found online for copper refrigerant tubing and R134a. Other costs such as structure, frame, tooling, and overhead costs can be estimated to be 30% of the total cost based on the development of a CENG thermal storage

unit for an industrial application [172]. Reducing costs beyond required materials (PCM, CENG, copper, R134a) will be further discussed in 5.7.

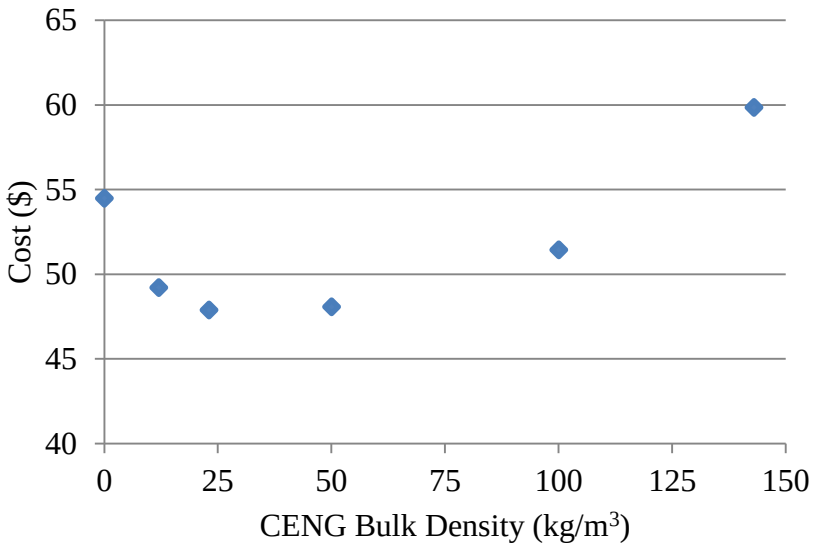

Figure 5.10. Cost of the CENG/PCM condenser as a function of CENG bulk density.

Comparison of the proposed constraints to the results from the optimized design is shown in Table 5.4. To meet the required volume of 5.9 L, it was decided to fabricate four individual 50 kg/m^3 rectangular blocks of 76 mm square cross-section and 260 mm length and then combine to form the thermal battery and provide the required refrigerant tube length of 104 cm.

Table 5.4. Proposed constraints compared to the optimized design.

	Proposed Constraints	Results from Optimized Design
Weight and Volume	<5kg, <5L	5.3kg, 5.9L
Heat transfer capacity	170 W	170 W
Energy storage capacity	0.34 kWh	0.34 kWh
Phase change temperature	36°C – 40°C	37°C
Cost	<60$	$47
Refrigerant charge (R134a liquid @ 30°C)	minimize	18g

Prior to fabrication of the full-scale prototype, small-scale samples were made with 50 kg/m^3 CENG and PT37 to measure the latent heat and thermal conductivity. These values were compared to assumed values based on past work with paraffin wax as shown in Table 5.5, which confirms the properties used during optimization modeling.

Table 5.5. Comparison of modeled and measured 50 kg/m^3 CENG/PCM composite.

	Modeled	Measured
Bulk density	50 kg/m^3	50 kg/m^3
Thermal conductivity at 20°C	4.7 W/m·K	4.8 W/m·K
Latent het	200 J/g	199.7 J/g
Melting temperature	37.0°C	38.5°C

5.5 CENG Battery Fabrication and Installation

An aluminum mold and plunger were designed and built to fabricate the CENG/PCM blocks. A schematic of this device is shown in Figure 5.11 (left). The fabrication process for each composite is as follows:

1. Load 74 grams of expanded graphite into the mold (this is the mass of EG required for 50 kg/m^3 composite)

    - After each load, shake the form to distribute the graphite evenly.
    - Intermittently compress the graphite to allow enough room in the mold for all of the material.
    - After loading 74 grams, completely compress the graphite to form the blocks (76mm x 76mm x 260mm) with 2 large clamps used to compress the plunger. The finished product in the form is shown in Figure 5.11 (right).

2. Load an excess amount of solid PCM

    - Loaded ~1700 grams of solid PT37 into the form. This is best accomplished by melting the PCM into rectangular molds and placing them into the mold after solid.

3. Saturate the foam

    - Place in furnace at 70°C with a 635mmHg vacuum for specified of time.
    - Remove the composite from the vacuum and allow the composite to cool prior to removing from form. The finished product is shown in Figure 5.12.

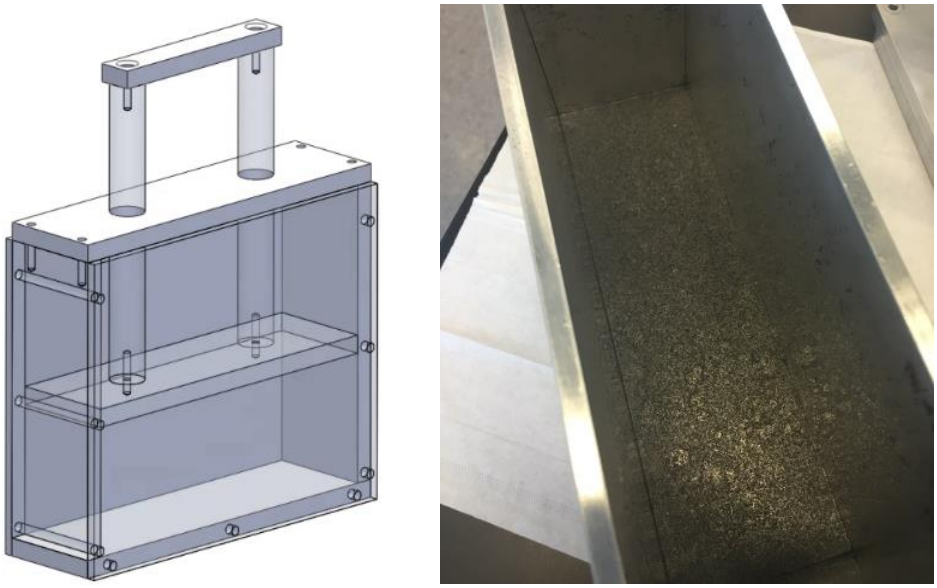

Figure 5.11. Schematic of mold and plunger (left); Compressed graphite in mold (right).

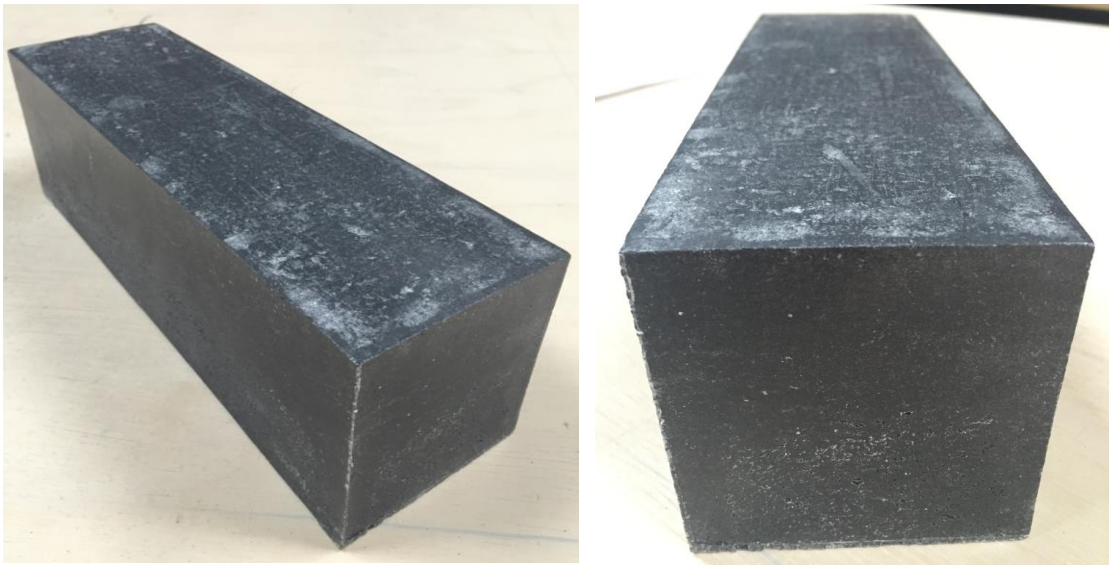

Figure 5.12. 50 kg/m^3 CENG/PT37 blocks (~76 mm x ~76mm x ~260mm); side view (left), front view (right).

Five CENG/PT37 blocks were produced and their properties are reported in Table 5.6. The time in the vacuum furnace was varied to understand the amount of time required to fully saturate the composite. Percent void was calculated by measuring the mass of PCM in the composite and dividing by the expected value based on the density and volume (Equation 42). The adjusted CENG bulk density was calculated to reflect the slight variation in width and height of the sample (Equation 43).

$$Percent\ void = \frac{mass_{PT37,\ measured}}{\rho_{PT37} V_{f,\ PT37}} \tag{42}$$

$$Bulk\ density = \frac{74\ g}{measured\ volume} \tag{43}$$

Table 5.6. Summary of 50 kg/m^3 CENG/PT37 blocks.

Composite	Weight (g)	Width (mm)	Height (mm)	Time in Vacuum Furnace (hr)	Percent Void	Adjusted CENG Bulk Density (kg/m^3)
1	1338.8	75.7	75.8	12.00	5.7%	49.6
2	1358.4	77.4	84.4	23.25	16.2%	43.6
3	1358.0	75.2	77.5	15.75	5.8%	48.9
4	1338.6	75.0	75.8	19.25	5.0%	50.0
5	1296.6	75.6	73.2	17.00	5.5%	51.4

All composites have similar geometries, percent void, and adjusted bulk densities except for Composite 2. During fabrication of this composite, the importance of keeping the composite within the mold during solidification was realized. Since the PCM contracts during solidication, removal of the mold too early results in stresses throughout the material due to temperature and density differences that impact the shape of the composite. Composite 2 was removed from the mold too early, and the stability of the geometry was compromised. All other samples were allowed to cool in the container. Composites 1, 3, 4, and 5 were installed in the condenser, while Composite 2 was used as a test case for the post-processing required of the composites prior to installation. It is also noted that all composites except for Composite 2 have a percent void around 6%. This is in good agreement with the samples made with paraffin wax in Figure 3.7 that had a void of 5% and suggests that 12 hours is an acceptable saturation time.

The container to house the CENG/PCM blocks to form the PCHX was designed (Figure 5.13 (left)) and 3D printed with polycarbonate (Figure 5.13 (right)). Figure 5.13 (left) shows how the four blocks were assembled within the conatiner. The copper refrigerant tube on the left is the inlet and the tube on the right is the outlet. The header shown on the top is mimicked on the bottom; a groove cut into the bottom of container allows space for this tubing. The main body was 3D printed (Figure 5.13 (right)), and the top cover was cut from acrylic.

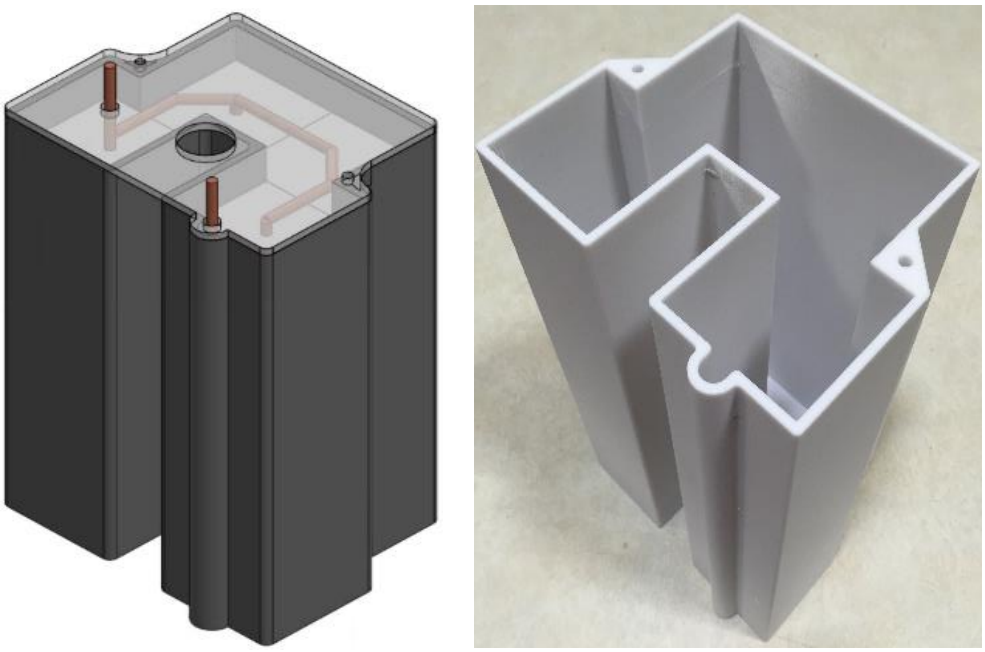

Figure 5.13. PCHX housing model (left); 3D printed container (right).

The blocks and 3D printed container were sent to the Univeristy of Maryland for post-processing and installation in the vapor compression experimental loop. Post-processing of the blocks includes cutting holes through the center for the refrigerant tube (Figure 5.14 (left)) and then cutting them in half to surround the tubing (Figure 5.14 (right)). Though feasible, this is an inefficient method of preparing the PCHX. Additionally, as shown in Figure 5.14 (right), cutting the blocks in half introduces gaps between the refrigerant tube and the composite, which will impact the thermal charging rate due to the low thermal conductivity of air.

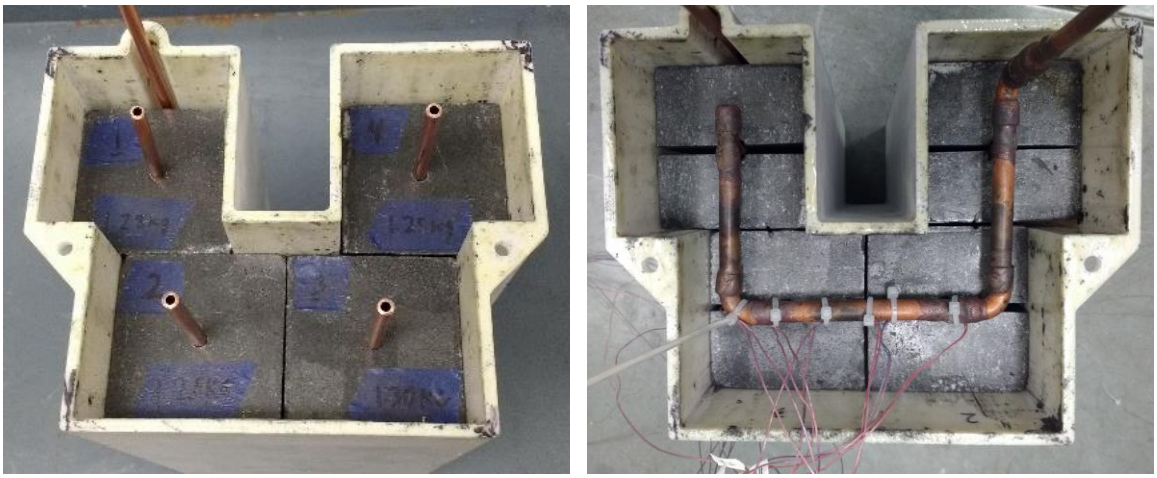

Figure 5.14. Images after drilling holes for copper tubing (right) and after cutting blocks in half (right).

Guided by these lessons learned, two efforts were explored: (1) redesigning the CENG/PCM production process and (2) designing a new production method. Redesigning the production process includes the positioning of a ¼" half-round in the bottom of the press prior to compression and the formation of half blocks, which can then be combined without any cutting or drilling to form the block shown in Figure 5.15. Designing the new production method will be discussed in 5.7, which will eliminate the need for extensive post-processing of the blocks prior to insertion in the PCHX housing.

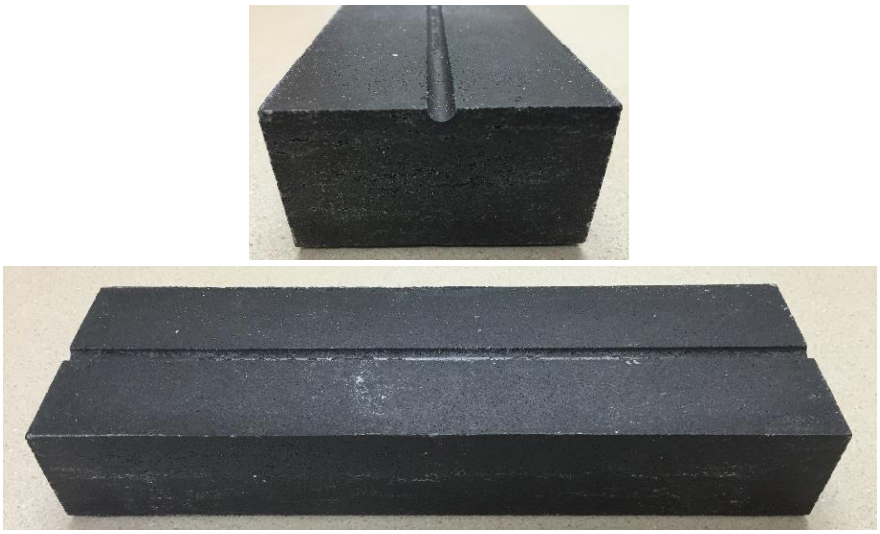

Figure 5.15. Image of the redesigned CENG/PCM block; front view (top), side view (bottom).

5.6 CENG Model Validation and Study of Contact Resistance

A key assumption made in the optimization study was negligible contact resistance between the refrigerant tube and the composite. To investigate the validity of this assumption, a small-scale 50 kg/m^3 CENG/PT37 thermal battery was fabricated and used in thermal charging experiments. The container was 3D printed with polycarbonate and designed to hold a 6.4 cm diameter, 3.8 cm tall composite, and with a 5 mm thick wall. The graphite was compressed within the container (Figure 5.16 (top left)) and then saturated with PT37. The percent void was calculated to be 8% based on weighing the sample before and after saturation. Then a hole was drilled (Figure 5.16 (top right)) and a copper tube was inserted through the composite (Figure 5.16 (bottom left)). Following installation of the lid and fittings required to connect to a constant temperature bath (Figure 5.16 (bottom right)), the test composite was installed into the experimental loop and

outfitted with thermocouples. Additional information on composite fabrication can be found in 5.7.

Figure 5.16. CENG within test container (top left); CENG following saturation and drilling of tube hole (top right); Installation of copper tube (bottom left); Final product (bottom right).

Thermocouples were installed to measure the composite temperature over time, the inlet and outlet fluid temperatures, ambient temperature, and the outer temperature of the PCHX plastic container. The composite was mounted so that the fluid moved in the vertical direction to allow confirmation of negligible natural convection within the sample through

comparison of transient temperature profiles as a function of height. Eight thermocouples were installed in the composite at varying depths and heights. Four thermocouples were installed near the bottom of the sample at depths of 0.50” and 0.25”, two thermocouples were installed in the middle at a depth of 0.50”, and two thermocouples were installed at the top of the sample at a depth of 0.25”. A schematic of the thermocouple location is shown in Figure 5.17.

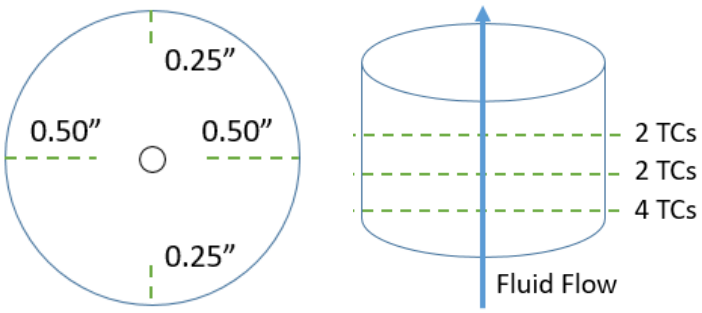

Figure 5.17. Thermocouple (TC) location for thermal charging experiments.

The test sample was installed in the experimental loop as shown in Figure 5.18. Connection to a constant temperature bath allowed the initial temperature for all experiments to be maintained at 32°C and the applied temperature to be 52°C. The experiment was conducted within an environmental chamber, and the ambient temperature was held at 32°C throughout the experiment.

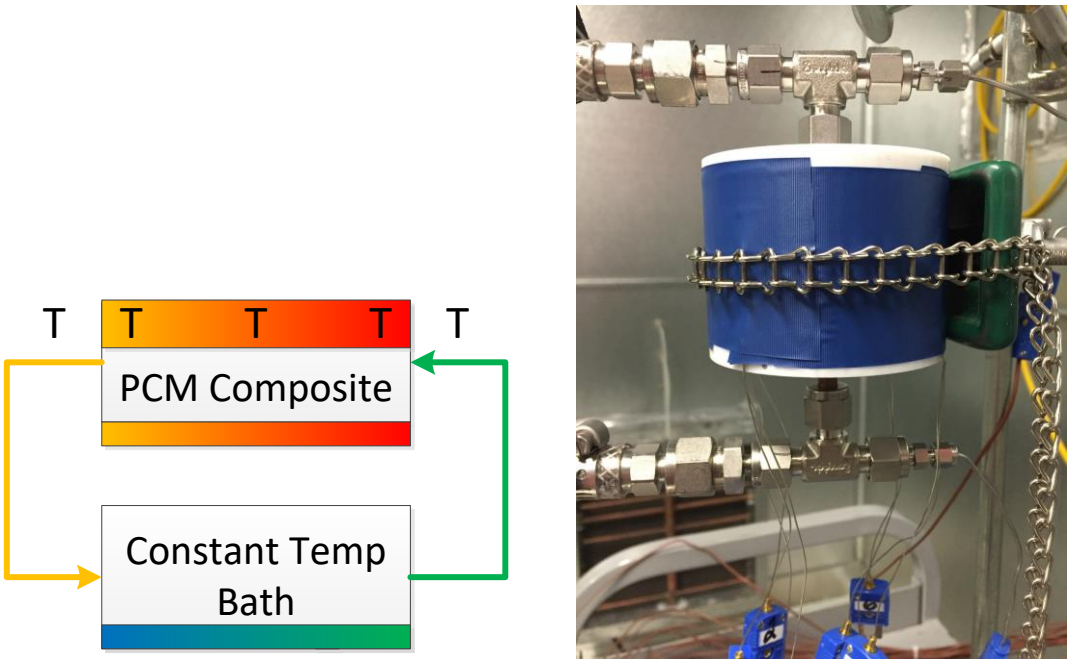

Figure 5.18. Schematic of experimental loop (left); Installation of 50 kg/m^3 CENG/PT37 test sample in experimental loop (right).

Example data for the 50 kg/m^3 CENG/PT37 sample is shown in Figure 5.19. Due to the high mass flow rate, the inlet and outlet temperatures are very similar. This means that a 2D model can be used, as the transient temperature profile is independent of location along the tube.

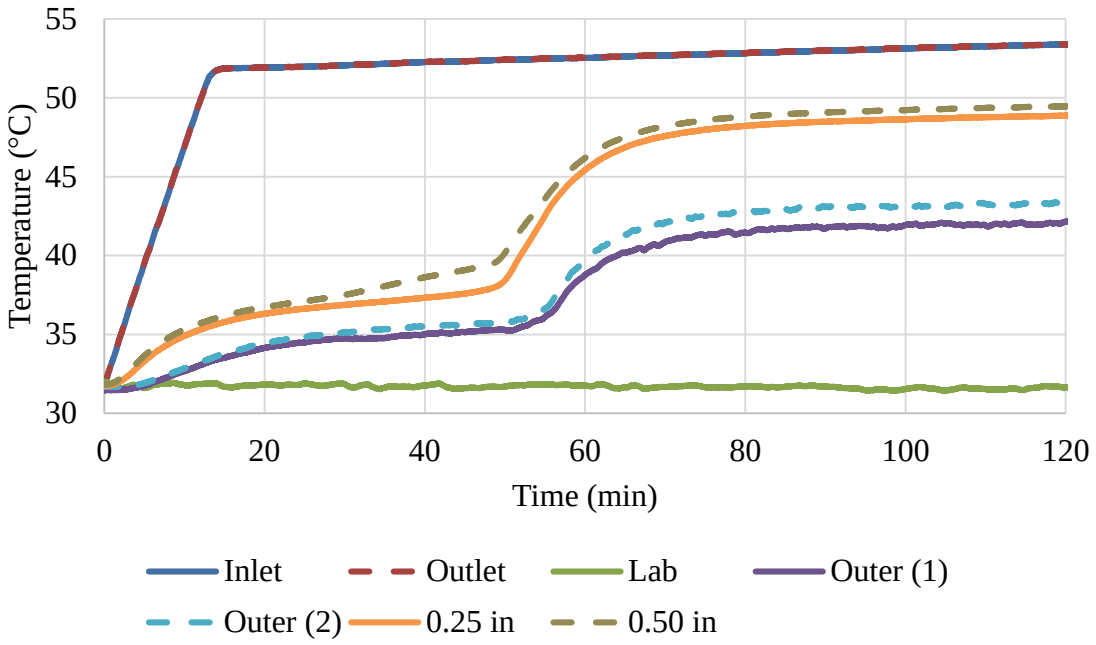

Figure 5.19. Example thermal charging data for 50 kg/m^3 CENG/PT37 composite.

Comparison of the transient temperature profiles as a function of depth is shown in Figure 5.20 for 0.50" (left) and 0.25" (right). Comparison of the bottom data to either the middle or top thermocouple data indicates that natural convection is negligible within the composite since the profiles do not vary with height. Additionally, the similar response of the 0.50" and 0.25" depths indicates that the high conductivity composite uniformly absorbs energy during melting.

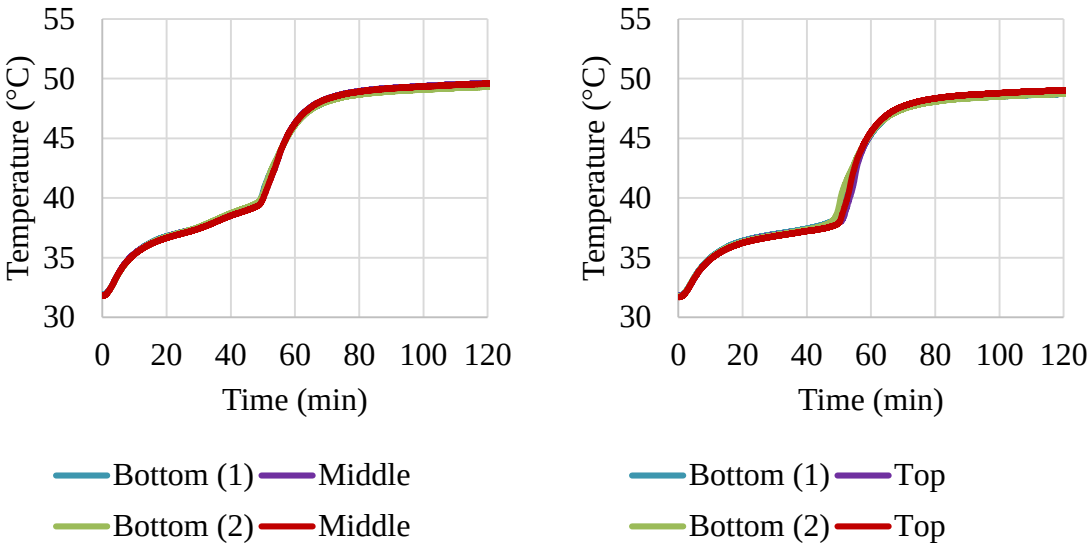

Figure 5.20. Transient temperature profiles as a function of depth – 0.50” (left), 0.25” (right).

The experiment was conducted three times, and bottom transient temperature profiles for experiment 2 and experiment 3 are compared in Figure 5.21. The similar profile for 0.50” and 0.25” confirms the repeatability and accuracy of the results. Additionally, it is noted that 0.50” in depth is about a degree warmer than 0.25”, which is expected based on their location respective to the refrigerant tube.

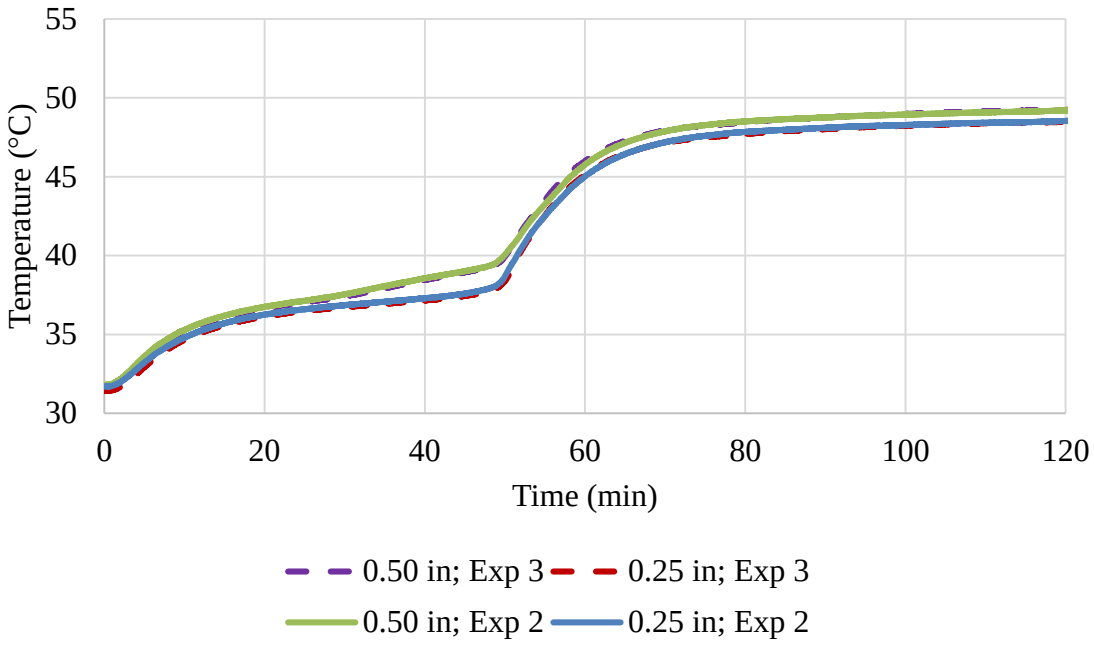

Figure 5.21. Bottom transient temperature profiles for various depths and trials.

These experimental results were used to validate the numerical model used during the optimization study reported in 5.4. The tube temperature and outer shell temperature recorded for the experiment were applied to the geometry shown in Figure 5.22 (right), while the properties reported in Table 5.3 of the 50 kg/m^3 CENG/PT37 composites were used to represent the thermal battery. A 0.25" OD copper tube was modeled on the interior with typical copper properties, and the 5 mm thick outer shell was assigned properties of plastic.

Comparison of the model and experiment is shown in Figure 5.22 (left) assuming perfect contact between the tube and the composite. The time to end of melt is over predicted by about 20%, which suggests the presence of contact resistance between the tube and the composite.

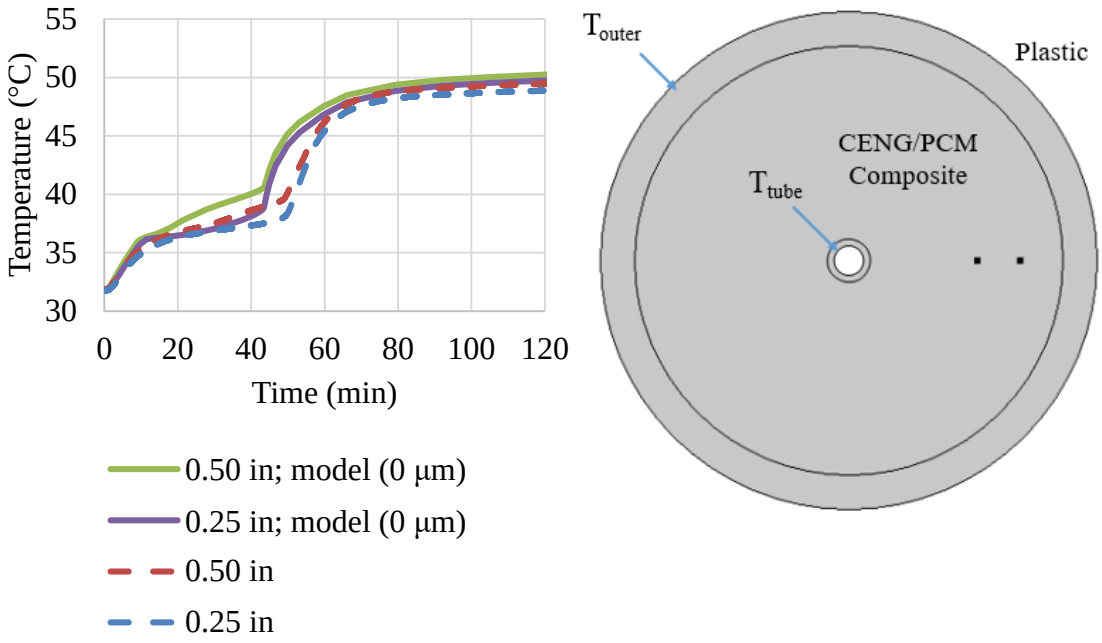

Figure 5.22. Comparison of experiment and model temperature profiles with no contact resistance.

Contact resistance is included in the model by adding a thin air layer between the tube and composite. As Figure 5.23 shows, the addition of a 7 μm air gap provides good correlation between the transient temperature profiles of the experiment and model. It is also noted that this makes physical sense as a tight fit is formed when the bore diameter is 3–10 μm greater than the rod.

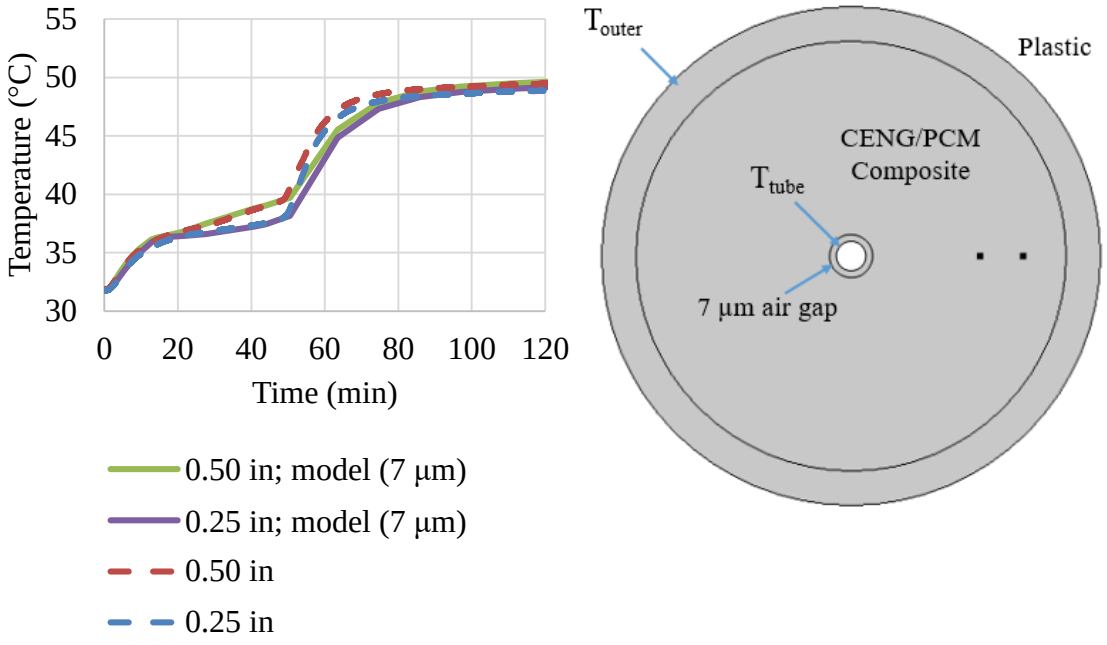

Figure 5.23. Comparison of experiment and model temperature profiles with a 7 µm air gap.

Even though the thin contact resistance was not included in the initial optimization, after revisiting this work, the addition of a 7 µm air gap does not change the optimal bulk density of 50 kg/m^3. However, recall that due to post-processing of the blocks, a gap >1 mm was formed between each tube and the composite as shown in Figure 5.14 and repeated in Figure 5.24 (bottom right). Compared to the 7 µm air gap shown in Figure 5.24 (top right), this is expected to significantly impact the thermal charging response. To demonstrate this impact, the transient temperature profile for the small-scale system with a 7 µm air gap is compared to a 1 mm gap in Figure 5.24 (left). As expected, the low thermal conductivity of the air significantly impacts the heat transfer. Therefore, methods of reducing this contact resistance explored will be discussed.

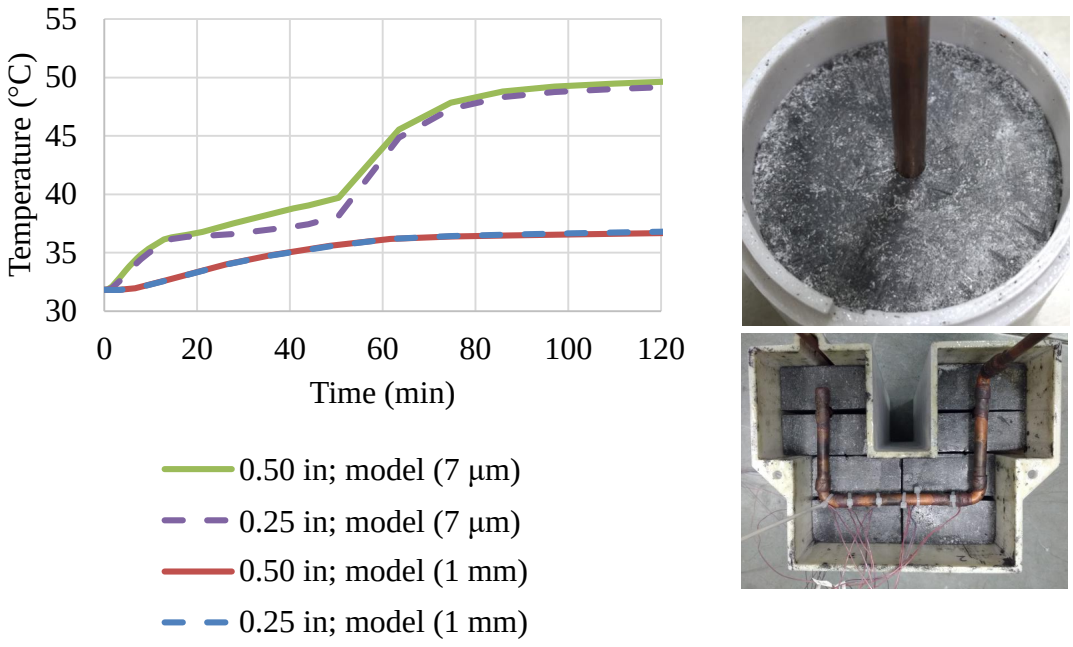

Figure 5.24. Comparison of transient temperature profile for 7 μm and 1 mm air gap.

5.7 In-situ Compression to Reduce Post-Processing

Currently, the formation of phase change material composites with compressed expanded graphite described in 5.5 follows a four-step process of (1) graphite compression, (2) PCM saturation, (3) composite post-processing, and (4) installation into a system for heat exchange and protection from leakage. Each of these phases of production typically requires separate equipment, requiring costly and time-consuming material handling between stages. Additionally, this post-processing may introduce undesirable issues such as material loss or addition of contact resistances, which can negatively impact the performance of the composites.

To overcome these issues, this section describes a novel production method using in-situ graphite compression within a prefabricated (including 3D printed) container which can accommodate vertical structures and some non-vertical structures, within certain limits. Compression within this container, followed by PCM saturation, eliminates the need for post-processing and minimizes contact resistance. This technique, which streamlines the production of phase change material composites made with compressed expanded graphite, was used to produce the experimental composites reported in 5.6, but will now be discussed in depth.

In-situ compression can occur within a setup that has four parts – a main housing, a reusable extension to hold the expanded graphite prior to compression, a reusable plunger, and a main housing cap. The extension, plunger, and main housing cap mate with the main housing. Both the extension and main housing cap are attached to the main housing with interlocking notches to provide secure contact as shown by the example housing in Figure 5.25. The plunger outer dimensions mimic the inner dimensions of both the extension and the main housing.

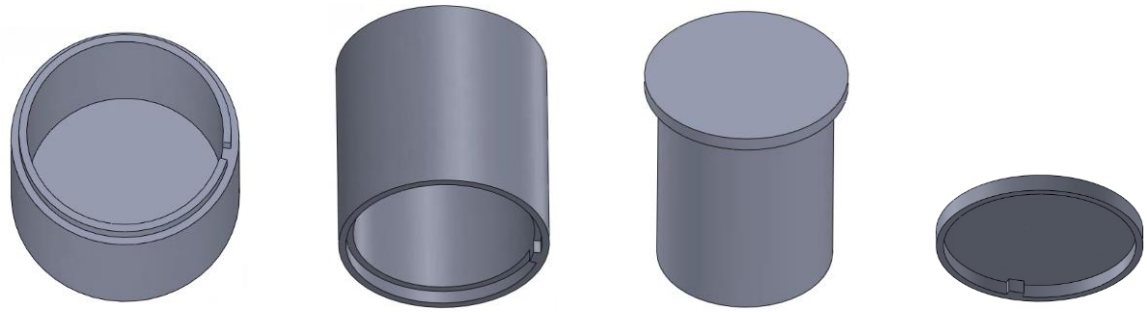

(A) (B) (C) (D)

Figure 5.25. Main housing (A); Reusable extension (B); Reusable plunger (C); Main housing cap (D).

A progression of images describing the process is shown in Figure 5.26. The reusable extension is shown as transparent to provide clarity. First, the extension is attached to the main housing (Figure 5.26 (A)). Next, a known mass of expanded graphite is loaded into the main housing/extension shell and compressed with the reusable plunger (Figure 5.26 (B-D)). The graphite is compressed to completely fill the volume of the main housing (Figure 5.26 (E)). This step is achieved with either a single or multiple compression effort. In the case of single compression, the proper amount of graphite is loaded at one time. In the case of multiple compression, the graphite is loaded multiple times in between subsequent compression. Multiple compressive steps may more evenly distribute the graphite for high density samples or accommodate more complex embedded geometry by using different plunger design for each compression step.

Following compression, the plunger is removed. PCM is placed on top of the compressed graphite, within the extension (Figure 5.26 (F)). The setup is heated to melt the PCM and saturate the composite. Saturation methods include, but are not limited to, the following:

- Placing the setup on a hot plate to melt the PCM and saturate the graphite foam via capillary forces.
- Placing the setup in a vacuum furnace to melt the PCM and saturate the graphite foam via capillary forces. Removing the air prior to saturation increases the rate of this process. The necessity of the vacuum and the length of time required for saturation is dependent on the PCM viscosity.
- Installing a port on the main housing to connect to a vacuum pump. After sealing the container with the compressed graphite and PCM inside, a vacuum would be pulled while the container is simultaneously heated.
- Preheat the graphite within the main housing and then simultaneously pour liquid PCM into the top of the setup while removing air through a port on the bottom. This will act as a plunger system to pull the liquid PCM through the graphite.

For the composites used in 5.6, the hot plate method was used, but it is noted that a vacuum may be required for full saturation of larger composites or for higher viscosity PCMs. Following saturation, the extension is removed (Figure 5.26 (G)) and the main housing cap is placed on top (Figure 5.26 (H)), resulting in a PCM/graphite composite. Holes can be drilled through this composite to accommodate heat transfer fluid tubes. Space between the composite and the main housing cap is designed to accommodate PCM expansion during melting. The prototype developed using the technique shown in Figure 5.16 is repeated in Figure 5.26 (I).

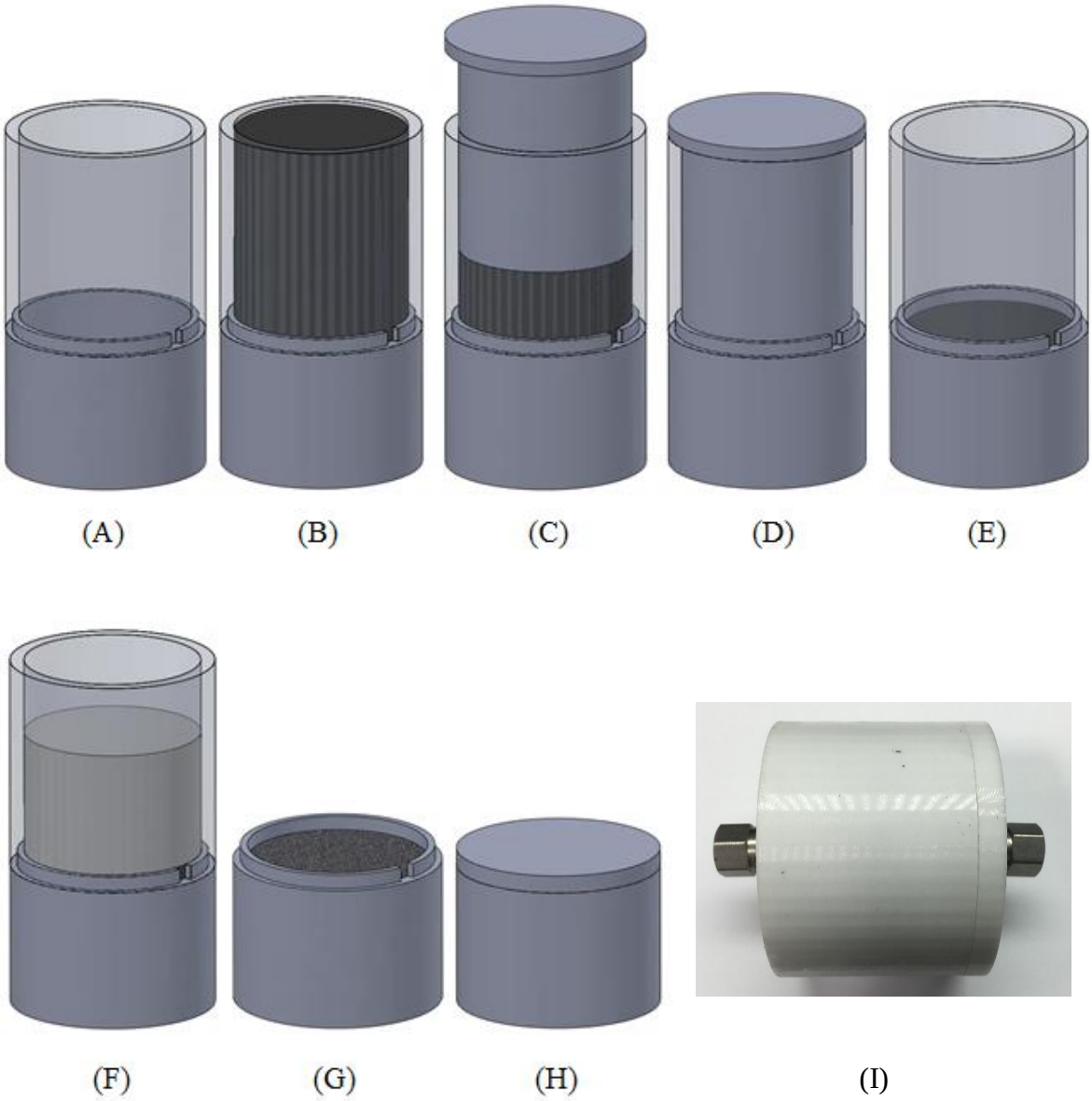

Figure 5.26. Progression of pictures demonstrating novel fabrication method with reduced post-processing for composite phase change material based on compressed expanded graphite.

This production method can also accommodate internal geometries such as heat transfer fluid tubes. The housing can be designed such that voids within the plunger compress around internal design features that are installed prior to graphite loading. Compressing around such internal features further reduces post-processing time and cost

and potentially reduces contact resistance. The example shown in Figure 5.27 demonstrates the ability to compress around vertical hollow tubes. After the hollow tubes (ID = x) are installed in the housing, a solid cylinder (OD = x) is placed inside each as a place holder (Figure 5.27 (A)). Graphite is loaded as previously described. The plunger is designed to accommodate the design feature during compression (Figure 5.27 (B-D)). Once the plunger and solid cylinder are removed, the final composite with vertical tubes (Figure 5.27 (E)) is covered with a main housing cap.

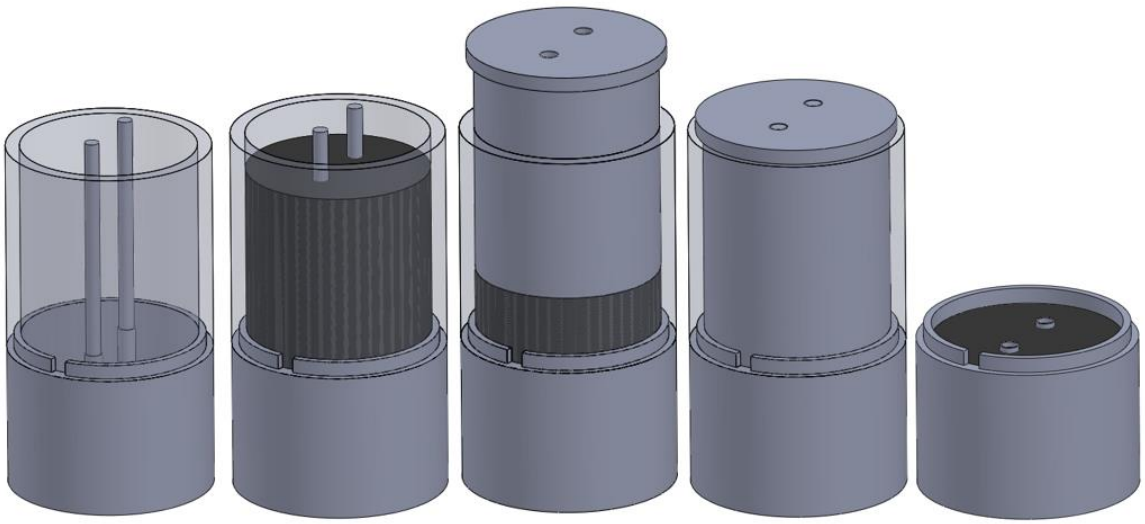

(A) (B) (C) (D) (E)

Figure 5.27. Progression of pictures demonstrating ability to conform to internal geometries.

Experimental composites were fabricated with the internal geometries method as shown in Figure 5.28.

Figure 5.28. Compression around internal geometry.

Composites made with both in-situ compression methods, drilling the hole post-saturation (A) and compressing around the heat transfer fluid tube (B), were tested in the experimental loop described in 5.6. Results are compared in Figure 5.29 for the temperature profile at a depth of 0.50”. The similar thermal charging performance indicates that compression around the tube does not result in a decrease in thermal resistance. However, since this method reduces the post-processing and results in similar charging performance as drilling the hole following saturation, it supports the use of in-situ compression with internal structures.

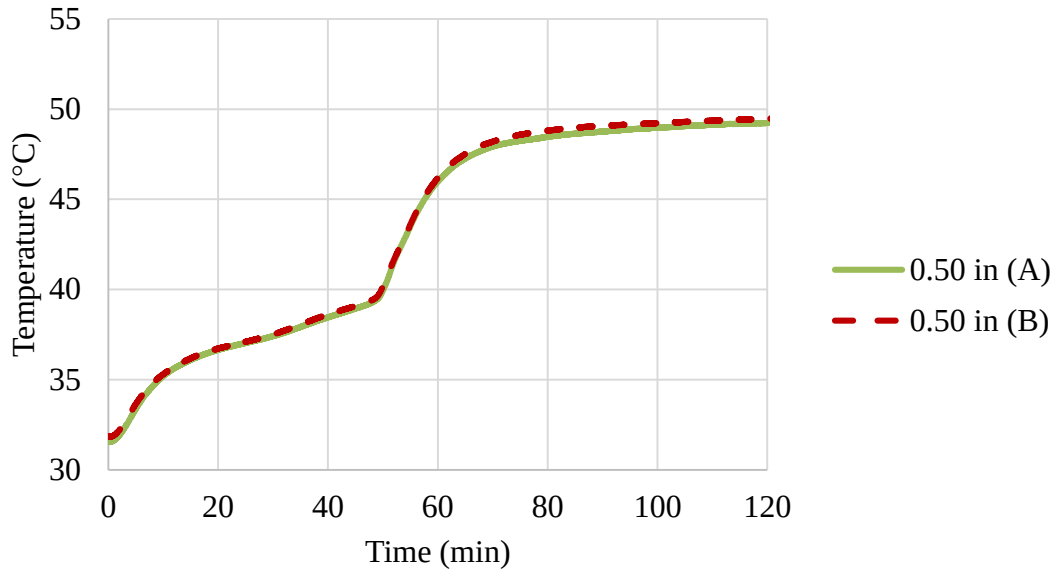

Figure 5.29. Comparison of in-situ compression with heat transfer fluid tube hole drilled following saturation (A) and graphite compression around tube (B).

5.8 Optimization and Fabrication Summary

In this chapter the optimization of a CENG/PT37 thermal battery with the validated model developed in Chapter 4 was discussed. Objectives considered were minimizing mass, volume and refrigerant charge, while maximizing energy density and thermal charging rate. A 50 kg/m^3 CENG/PCM prototype was fabricated and installed in vapor compression system to minimize heat released to the ambient. Issues of contact resistance and extensive post-processing were reviewed. The validated model was used to study the impact of contact resistance between the heat transfer fluid tube and the thermal battery composite. It was found that the tight fit required to slide the heat transfer fluid tube in and out of the composite resulted in a 7 μm air gap. Additionally, to resolve the issues of post-processing the prototype composites, specifically material loss, additional contact

resistance, and lead-time, a new method of in-situ compression was proposed and demonstrated.

CHAPTER 6. SUMMARY

The performance of space conditioning systems is reliant on the use of heat exchangers to absorb or reject heat from the thermodynamic cycle. This dependency implies that innovation in heat exchanger design is necessary to accommodate emerging high performance, compact, and low cost technology requirements. One such advancement is the insertion of an energy storage medium into the heat exchanger to act as a thermal battery, which allows the thermal exchange to occur on demand or when more expedient for an energy efficient application. By decoupling energy supply from demand, heat exchangers used in thermal energy storage can reduce peak demand, energy consumption, CO_2 emissions, and costs. Furthermore, the conversion and storage of variable energy in the form of thermal energy can also help increase the feasibility of renewables.

Thermal energy storage provides heat storage by cyclically charging and discharging a thermal energy storage material. The study of these thermal batteries is focused on appropriate material selection for different conditions and applications as well as the design of the heat storage unit. Though the containment system and heat exchanging surface are important components of this system, advancement in the field of thermal energy storage is greatly dependent on the continued development of suitable material composites with high energy density and high power density. Of specific interest are phase change materials (PCMs), which store thermal energy as latent heat over a nearly isothermal temperature range. Compared to sensible heat storage, properly chosen PCMs can store an order of magnitude more energy when undergoing phase change. Organic solid-liquid PCMs present several advantages including their high latent heat and minimum

volume change during transition, as well as being non-corrosive and their ability to melt without phase separation, which results in safe and reliable performance. However, their characteristic low thermal conductivity significantly limits the rate of thermal charging and discharging. Increasing the thermal performance of PCMs is crucial to the widespread adoption of thermal energy storage technologies.

To increase the rate of thermal charging and discharging, solutions such as extended surfaces, microencapsulation of the PCM, and introduction of high conductivity foams or nanoparticles within the PCM to increase the thermal conductivity of the composite have been proposed in literature. Increasing the composite thermal conductivity by saturating high conductivity foam has been shown to have the greatest impact on thermal charging response. Extended surfaces are limited by small surface area to volume ratios, microencapsulation is expensive, and nanoparticles introduce instability issues in cyclic conditions. Two common materials used to form conductive foams are metal and graphite. Compressed expanded natural graphite (CENG) foams are an attractive thermal enhancement material due to their high conductivity, low density, and machinability, while metal foams enhance the conductivity and add structural integrity to the PCM.

Research with PCMs integrated in metal foams typically describes the impact on thermal charging by measuring the decrease in melting time of the PCM or the decrease in temperature at the junction of the heat sink and the latent heat thermal storage systems. Composites of graphite foams saturated with PCM are generally compared solely through thermal conductivity and latent heat measurements. Because of these different performance metrics, it is difficult to compare these two forms of PCM thermal charging enhancement. In general, both additions to the PCM system aim to minimize the impact on the high latent

heat capacity and low cost PCM, while increasing the rate of thermal transport. In the design of thermal batteries for thermal energy storage, fulfilling this objective requires comparative experiments based on thermal conductivity and latent heat measurements as well as thermal charging enhancement, mass, and cost of the system. Additionally, the ability to model the thermal charging performance of thermal batteries enhanced by metal foams or graphite foams is important for the optimization of systems for specific applications.

6.1 Summary of Contributions

The main question addressed by this research is how to optimize a thermal battery based on enhancement material, size, mass, heat capacity, thermal charging rate, refrigerant charge, and cost for a specific application. A schematic of the tasks involved in this investigation is shown in Figure 6.1.

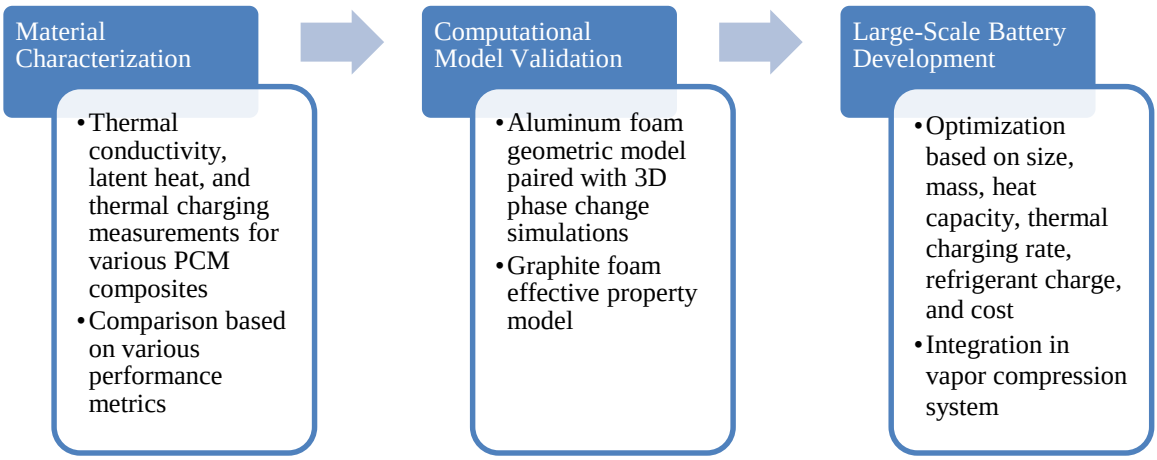

Figure 6.1. Overview of dissertation research.

The first task focused on thermal charging experiments for various aluminum foam and graphite foam PCM composites to compare how the systems respond under different boundary conditions. A standard sample geometry was used with a constant heat flux or constant temperature on one boundary and insulated sides. The impact of aluminum foam was investigated as a function of PCM viscosity, heat flux magnitude, and aluminum pore density. The influence of graphite foam was considered by varying the heat flux magnitude and graphite bulk density. These experiments addressed the impact of surface area and natural convection on the thermal charging response. Following thermal charging experiments for aluminum and CENG foams, these systems were compared in terms of measured composite thermal conductivity and latent heat as well as experimentally determined junction temperature and time to end of melt. Non-dimensional parameters were developed to compare the energy storage rate and density to the junction temperature. It was shown that the thermal charging enhancement of CENG foams is superior to that of aluminum foams based on thermal charging rate, junction temperature, mass, and cost due to high thermal conductivity, low density, and small pore size.

In the second task, numerical models for PCM enhanced by aluminum foams and CENG were developed and validated with experimental data. The impact of pore size and surface area was discussed. Modeling the performance of open-cell metal foams saturated by phase change material is complicated by the nonlinear nature of the phase change process as well as the non-homogeneity of the system. While the discrete nature of the system must be known in order to predict the actual temperature distribution, it is possible to use effective medium theory in order to predict the thermal rate of charging and discharging in the system. To demonstrate this concept, an effective energy storage model

was used to represent the 3D non-linear heat transfer problem with effective properties, which converted it to a 1D linear heat transfer problem. First, an accurate Kelvin structure foam model was developed and incorporated into COMSOL to determine the effective properties of the composite. Next, effective thermophysical properties were defined to calculate the amount of energy being stored over time and compared to 3D phase change simulations with the foam model. The phase change process was accounted for through an effective heat capacity of the effective medium, while also adding thermal resistance to the heat transfer through a temperature dependent thermal conductivity. The results show satisfactory agreement with the full 3D model of the Kelvin foam in terms of the ability to predict the time to charge the composite system. This method can be adapted for multiple phase changes or non-isothermal phase change because it is based on the amount of energy absorbed over time instead of the discrete nature of the temperature distribution within the system.

While open-cell aluminum foams require a geometric aluminum foam model combined with 3D phase change simulations to determine the effective thermal conductivity, a homogeneous one-temperature model can be used to study the thermal charging response of CENG composites with volume averaged properties for density and specific heat and experimentally determined thermal conductivity and latent heat. Due to the addition of graphite, the thermal conductivity increases while the latent heat decreases. This trade-off was studied by calculating the energy storage performance, which is the amount of energy stored as latent heat divided by the time to end of melt as a function of the material bulk density. The impact of CENG bulk density, height, and applied boundary condition on the thermal charging of CENG foams was explored parametrically with the

validated model. While the optimum bulk density was a function of the size and boundary condition, it was shown that an optimum CENG bulk density will always exist that maximizes both the thermal charging rate and energy storage.

The validated CENG model was used to optimize a thermal battery for a space conditioning application. The objectives of minimizing size and refrigerant charge while maximizing heat capacity and thermal charging rate were studied as a function of the graphite bulk density, thermal battery dimensions, and refrigerant tube configuration. The optimized thermal battery was designed to store 170W over 2 hours. Through the addition of graphite, the thermal conductivity of the PCM was increased by 20x, PCM mass was reduced by 33%, and refrigerant charge was reduced by 60% as compared to a non-enhanced system. Component-level experimental thermal battery testing and model validation were discussed as well as system-level battery production and integration in a vapor compression system. The impact of thermal contact resistance and reducing lead-time and cost through innovation in production techniques were reviewed. The proposed in-situ manufacturing procedure enables integration of thermal batteries into the thermal comfort system that is different than current practice in industry. In addition to this contribution, the following invention disclosure has been filed: A. Mallow, K. Gluesenkamp, and J. Muehlbauer, “Fabrication Method for Phase Change Composite Based on Graphite", DOE S-138,406, ORNL Invention Disclosure Number: 201603759.

6.2 Future Work

While low temperature waste heat has less thermal and economic value than high temperature heat, it is ubiquitous and available in large quantities. Studies show that the

magnitude of low temperature waste heat is sufficiently large that it should not be neglected in pursuing R&D opportunities for waste heat recovery. One of the main areas of research is the development of responsive PCM composites. Since the thermal charging rate is the main limitation of phase change materials, increasing the composite thermal conductivity and understanding how this impacts the heat exchanger design is crucial to the implementation of latent heat thermal energy storage systems. Additionally, the trade-off between energy density and charging/discharging rate is important to consider in the design and optimization of thermal batteries.

As the implementation of PCM thermal batteries is highly dependent on stability, cost, and performance of the heat exchanger, future work should focus on how to deal with these constraints, while maintaining proper energy density and charging rate required of the application. For systems that require structural support, aluminum foams are a promising material, but accurate models require a better understanding of the temperature dependent effective thermal conductivity. Alternatively, CENG foam research would benefit from studies of other PCMs, long-term cycling experiments, methods to address interface resistance, and scalable manufacturing methods.

The cost driver of PCM thermal batteries is the cost of the PCM. For the work presented in this dissertation, PT37 was chosen for the optimized thermal battery design due to favorable chemical properties and availability. As reviewed in Figure 5.5, additional PCMs, such as other paraffins, fatty acids, or even salt hydrates would decrease the PCM cost. However, hurdles such as higher melting temperature or unfavorable chemical properties (salt hydrates) would have to be addressed. A promising composite that has yet

to be investigated is a fatty acid combined with CENG. Are these materials compatible and how would the system performance in long-term cycling experiments?

A design aspect that needs to be further investigated is how to reduce contact resistance between the heat transfer fluid tube and the PCM composite through advanced compression techniques. For example, is it possible to compress the graphite locally around the heat transfer fluid tube to decrease contact resistance during fabrication? Another part of fabrication that needs to be better understood is how PCM liquid viscosity and temperature impact the saturation rate. Minimizing the time to saturate the composites results in production lead-time and cost reduction. Additionally, methods of minimizing closed pores of the graphite during compression would increase the energy density of the composite. Is it possible to compress graphite within liquid PCM to maximize PCM loading? Finally, methods to minimize this additional cost beyond required materials through reduced post-processing during fabrication (such as the in-situ compression method) need to be further investigated.

Scaling the production of CENG thermal batteries requires manufacturing methods that are able to handle the large volumes required of the expanded graphite prior to compression. For large-scale systems, exploring this space requirement is significant. For example, is it possible to pre-compress and pre-saturate layers of compressed graphite and then insert into the heat exchanger? If so, studying how the additional time and post-processing cost compares to reduced compression force or space requirements is important.

REFERENCES

[1] LLNL, "Estimated US Energy Use in 2011: ~97.3 Quads," ed, 2012.

[2] I. Johnson, W. T. Choate, and A. Davidson, "Waste Heat Recovery. Technology and Opportunities in US Industry," BCS, Inc., Laurel, MD (United States)2008.

[3] C. C. S. Reddy, S. V. Naidu, and G. P. Rangaiah, "Waste Heat Recovery Methods And Technologies," *Chemical Engineering*, vol. 120, pp. 28-38, 2013.

[4] G. Shu, Y. Liang, H. Wei, H. Tian, J. Zhao, and L. Liu, "A review of waste heat recovery on two-stroke IC engine aboard ships," *Renewable and Sustainable Energy Reviews*, vol. 19, pp. 385-401, 2013.

[5] R. Kumar, A. Sonthalia, and R. Goel, "Experimental study on waste heat recovery from an IC engine using thermoelectric technology," *Thermal Science*, vol. 15, pp. 1011-1022, 2011.

[6] (2013). *Hybrid Power Generation Systems*. Available: http://www.mpoweruk.com/hybrid_power.htm

[7] (2016). *Drain-Water Heat Recovery*. Available: http://energy.gov/energysaver/drain-water-heat-recovery

[8] I. Dincer and M. Rosen, *Thermal Energy Storage: Systems and Applications*, 2 ed.: Wiley, 2011.

[9] S. D. Sharma and K. Sagara, "Latent heat storage materials and systems: a review," *International Journal of Green Energy*, vol. 2, pp. 1-56, 2005.

[10] A. Shukla, D. Buddhi, and R. L. Sawhney, "Solar water heaters with phase change material thermal energy storage medium: A review," *Renewable and Sustainable Energy Reviews*, vol. 13, pp. 2119-2125, 2009.

[11] B. Zalba, J. M. Marín, L. F. Cabeza, and H. Mehling, "Review on thermal energy storage with phase change: materials, heat transfer analysis and applications," *Applied Thermal Engineering*, vol. 23, pp. 251-283, 2003.

[12] A. Sharma, V. V. Tyagi, C. R. Chen, and D. Buddhi, "Review on thermal energy storage with phase change materials and applications," *Renewable and Sustainable Energy Reviews*, vol. 13, pp. 318-345, 2009.

[13] IRENA-IEA-ETSAP, "Technology Brief 4: Thermal Storage," I. a. IEA-ETSAP, Ed., ed, 2013.

[14] M. M. Farid, A. M. Khudhair, S. A. K. Razack, and S. Al-Hallaj, "A review on phase change energy storage: materials and applications," *Energy Conversion and Management,* vol. 45, pp. 1597-1615, 2004.

[15] S. M. Hasnain, "Review on sustainable thermal energy storage technologies, Part I: heat storage materials and techniques," *Energy Conversion and Management,* vol. 39, 1998.

[16] T. Nomura, M. Tsubota, A. Sagara, N. Okinaka, and T. Akiyama, "Performance analysis of heat storage of direct-contact heat exchanger with phase-change material," *Applied Thermal Engineering,* vol. 58, pp. 108-113, 2013.

[17] M. J. Hosseini, A. A. Ranjbar, K. Sedighi, and M. Rahimi, "A combined experimental and computational study on the melting behavior of a medium temperature phase change storage material inside shell and tube heat exchanger," *International Communications in Heat and Mass Transfer,* vol. 39, pp. 1416-1424, 11// 2012.

[18] B. Dechesne, S. Gendebien, J. Martens, and V. Lemort, "Designing and testing an air-PCM heat exchanger for building ventilation application coupled to energy storage," in *International Refrigeration and Air Conditioning Conference,* 2014.

[19] L. Hao and Y. Qichang, "Development of a Wall Collector Unit and Phase Change Material (PCM), Air Heat Exchanger for Heating Application in Greenhouses," *Energy and Environment Research,* vol. 3, p. 24, 2013.

[20] NASA. (2016). *Phase Change Heat Exchanger Project (Phase Change HX) - 07.20.16.* Available: http://www.nasa.gov/mission_pages/station/research/experiments/2077.html

[21] X. Py, R. Olives, and S. Mauran, "Paraffin/porous-graphite-matrix composite as a high and constant power thermal storage material," *International Journal of Heat and Mass Transfer,* vol. 44, pp. 2727-2737, 2001.

[22] A. Mallow, O. Abdelaziz, and S. Graham, "Thermal charging study of compressed expanded natural graphite/phase change material composites," *Carbon,* vol. 109, pp. 495-504, 2016.

[23] F. Agyenim and N. Hewitt, "The development of a finned phase change material (PCM) storage system to take advantage of off-peak electricity tariff for improvement in cost of heat pump operation," *Energy and Buildings,* vol. 42, pp. 1552-1560, 2010.

[24] T. Kim, D. M. France, W. Yu, W. Zhao, and D. Singh, "Heat transfer analysis of a latent heat thermal energy storage system using graphite foam for concentrated solar power," *Solar Energy,* vol. 103, pp. 438-447, 2014.

[25] S. Jegadheeswaran and S. D. Pohekar, "Performance enhancement in latent heat thermal storage system: A review," *Renewable and Sustainable Energy Reviews,* vol. 13, pp. 2225-2244, 2009.

[26] M. Lacroix, "Study of the heat transfer behavior of a latent heat thermal energy storage unit with a finned tube," *International Journal of Heat and Mass Transfer,* vol. 36, pp. 2083-2092, 1993.

[27] M. Gharebaghi and I. Sezai, "Enhancement of heat transfer in latent heat storage modules with internal fins," *Numerical Heat Transfer, Part A: Applications,* vol. 53, pp. 749-765, 2007.

[28] Y. Zhang, Z. Chen, Q. Wang, and Q. Wu, "Melting in an enclosure with discrete heating at a constant rate," *Experimental Thermal and Fluid Science,* vol. 6, pp. 196-201, 1993.

[29] B. J. Jones, D. Sun, S. Krishnan, and S. V. Garimella, "Experimental and numerical study of melting in a cylinder," *International Journal of Heat and Mass Transfer,* vol. 49, pp. 2724-2738, 2006.

[30] K. Ng, Z. Gong, and A. Mujumdar, "Heat transfer in free convection-dominated melting of a phase change material in a horizontal annulus," *International Communications in Heat and Mass Transfer,* vol. 25, pp. 631-640, 1998.

[31] F. Tan, "Constrained and unconstrained melting inside a sphere," *International Communications in Heat and Mass Transfer,* vol. 35, pp. 466-475, 2008.

[32] C. Liu and D. Groulx, "Numerical Study of the Effect of Fins on the Natural Convection Driven Melting of Phase Change Material," in *COMSOL Conference 2011*, 2011.

[33] M. Lacroix and M. Benmadda, "Analysis of natural convection melting from a heated wall with vertically oriented fins," *International Journal of Numerical Methods for Heat and Fluid Flow,* vol. 8, pp. 465-478, 1998.

[34] H. Ettouney, H. El-Dessouky, and E. Al-Kandari, "Heat transfer characteristics during melting and solidification of phase change energy storage process," *Industrial and Engineering Chemistry Research,* vol. 43, pp. 5350-5357, 2004.

[35] R. Akhilesh, A. Narasimhan, and C. Balaji, "Method to improve geometry for heat transfer enhancement in PCM composite heat sinks," *International Journal of Heat and Mass Transfer,* vol. 48, pp. 2759-2770, 2005.

[36] M. Lacroix and M. Benmadda, "Numerical simulation of natural convection-dominated melting and solidification from a finned vertical wall," *Numerical Heat Transfer, Part A Applications,* vol. 31, pp. 71-86, 1997.

[37] V. Shatikian, G. Ziskind, and R. Letan, "Numerical investigation of a PCM-based heat sink with internal fins," *International Journal of Heat and Mass Transfer,* vol. 48, pp. 3689-3706, 2005.

[38] K. C. Nayak, S. K. Saha, K. Srinivasan, and P. Dutta, "A numerical model for heat sinks with phase change materials and thermal conductivity enhancers," *International Journal of Heat and Mass Transfer,* vol. 49, pp. 1833-1844, 2006.

[39] S. Krishnan, S. V. Garimella, and S. S. Kang, "A novel hybrid heat sink using phase change materials for transient thermal management of electronics," *Components and Packaging Technologies, IEEE Transactions on,* vol. 28, pp. 281-289, 2005.

[40] F. Agyenim, P. Eames, and M. Smyth, "A comparison of heat transfer enhancement in a medium temperature thermal energy storage heat exchanger using fins," *Solar Energy,* vol. 83, pp. 1509-1520, 2009.

[41] A. Caron-Soupart, J.-F. Fourmigué, P. Marty, and R. Couturier, "Performance analysis of thermal energy storage systems using phase change material," *Applied Thermal Engineering,* vol. 98, pp. 1286-1296, 2016.

[42] S. Mahmoud, A. Tang, C. Toh, A.-D. Raya, and S. L. Soo, "Experimental investigation of inserts configurations and PCM type on the thermal performance of PCM based heat sinks," *Applied Energy,* vol. 112, pp. 1349-1356, 2013.

[43] J. C. Kurnia, A. P. Sasmito, S. V. Jangam, and A. S. Mujumdar, "Improved design for heat transfer performance of a novel phase change material (PCM) thermal energy storage (TES)," *Applied Thermal Engineering,* 2012.

[44] L. Tan, Y. Kwok, A. Date, and A. Akbarzadeh, "Numerical Study of Natural Convection Effects in Latent Heat Storage using Aluminum Fins and Spiral Fillers," *Int J Mech Aerosp Eng,* vol. 68, pp. 512-525, 2012.

[45] F. Agyenim, N. Hewitt, P. Eames, and M. Smyth, "A review of materials, heat transfer and phase change problem formulation for latent heat thermal energy storage systems (LHTESS)," *Renewable and Sustainable Energy Reviews,* vol. 14, pp. 615-628, 2010.

[46] Z. Chen, L. Cao, G. Fang, and F. Shan, "Synthesis and Characterization of Microencapsulated Paraffin Microcapsules as Shape-Stabilized Thermal Energy Storage Materials," *Nanoscale and Microscale Thermophysical Engineering,* vol. 17, pp. 112-123, 2013.

[47] B. Li, T. Liu, L. Hu, Y. Wang, and L. Gao, "Fabrication and Properties of Microencapsulated Paraffin-SiO2 Phase Change Composite for Thermal Energy Storage," *ACS Sustainable Chemistry and Engineering,* vol. 1, pp. 374-380, 2013.

[48] M. Zhang, X.-M. Tong, H. Zhang, and J.-H. Qiu, "Preparation and characterization of Poly (MMA-co-AA)/Paraffin microencapsulated phase change material for

thermal energy storage," *Energy Sources, Part A: Recovery, Utilization, and Environmental Effects*, vol. 34, pp. 396-403, 2012.

[49] Y. Wang, H. Shi, T. D. Xia, T. Zhang, and H. X. Feng, "Fabrication and performances of microencapsulated paraffin composites with polymethylmethacrylate shell based on ultraviolet irradiation-initiated," *Materials Chemistry and Physics*, vol. 135, pp. 181-187, 2012.

[50] L. Fan and J. M. Khodadadi, "Thermal conductivity enhancement of phase change materials for thermal energy storage: A review," *Renewable and Sustainable Energy Reviews*, vol. 15, pp. 24-46, 2011.

[51] A. Mills, S. Al-Hallaj, M. Farid, and J. R. Selman, "Thermal conductivity enhancement of phase change materials using a graphite matrix," *Applied Thermal Engineering*, vol. 26, pp. 1652-1661, 2006.

[52] E.-B. S. Mettawee and G. M. R. Assassa, "Thermal conductivity enhancement in a latent heat storage system," *Solar Energy*, vol. 81, pp. 839-845, 2007.

[53] J. Y. Long, "Study on Phase-change Temperature and Latent Heat of Organic Phase-change Nano-fluid," *Advanced Materials Research*, vol. 152-153, pp. 1591-1594, 2010.

[54] J. Y. Long, "Study on Thermal Conductivity of Organic Phase-Change Nano-Fluid," *Advanced Materials Research*, vol. 152-153, pp. 1579-1582, 2010.

[55] S.-T. Hong and D. R. Herling, "Effects of surface area density of aluminum foams on thermal conductivity of aluminum foam-phase change material composites," *Advanced Engineering Materials*, vol. 9, pp. 554-557, 2007.

[56] J. A. Molefi, A. S. Luyt, and I. Krupa, "Investigation of thermally conducting phase-change materials based on polyethylene/wax blends filled with copper particles," *Journal of Applied Polymer Science*, vol. 116, pp. 1766-1774, 2010.

[57] W. Yu, H. Xie, and X. Wang, "Enhanced Thermal Conductivity of Liquid Paraffin Based Nanofluids Containing Copper Nanoparticles," *Journal of Dispersion Science and Technology*, vol. 32, pp. 948-951, 2011.

[58] C. Y. Zhao, W. Lu, and Y. Tian, "Heat transfer enhancement for thermal energy storage using metal foams embedded within phase change materials (PCMs)," *Solar Energy*, vol. 84, pp. 1402-1412, 2010.

[59] A. Siahpush, J. O'Brien, and J. Crepeau, "Phase Change Heat Transfer Enhancement Using Copper Porous Foam," *Journal of Heat Transfer*, vol. 130, p. 082301, 2008.

[60] Y. Zhong, S. Li, X. Wei, Z. Liu, Q. Guo, J. Shi, *et al.*, "Heat transfer enhancement of paraffin wax using compressed expanded natural graphite for thermal energy storage," *Carbon,* vol. 48, pp. 300-304, 2010.

[61] P. Zhang, X. Xiao, and Z. Ma, "A review of the composite phase change materials: Fabrication, characterization, mathematical modeling and application to performance enhancement," *Applied Energy,* vol. 165, pp. 472-510, 2016.

[62] J. Long, "Preparation of uniform and stable organic phase-change nano-fluid of paraffin and nano-aluminum for thermal storage," in *Proceedings: 2010 International Conference on Digital Manufacturing and Automation*, 2010, pp. 110-113.

[63] W. Wang, X. Yang, Y. Fang, J. Ding, and J. Yan, "Enhanced thermal conductivity and thermal performance of form-stable composite phase change materials by using β-Aluminum nitride," *Applied Energy,* vol. 86, pp. 1196-1200, 2009.

[64] K. Chintakrinda, R. D. Weinstein, and A. S. Fleischer, "A direct comparison of three different material enhancement methods on the transient thermal response of paraffin phase change material exposed to high heat fluxes," *International Journal of Thermal Sciences,* vol. 50, pp. 1639-1647, 2011.

[65] J. Xiang and L. T. Drzal, "Investigation of exfoliated graphite nanoplatelets (xGnP) in improving thermal conductivity of paraffin wax-based phase change material," *Solar Energy Materials and Solar Cells,* vol. 95, pp. 1811-1818, 2011.

[66] W. Cheng, R.-m. Zhang, K. Xie, N. Liu, and J. Wang, "Heat conduction enhanced shape-stabilized paraffin/HDPE composite PCMs by graphite addition: Preparation and thermal properties," *Solar Energy Materials and Solar Cells,* vol. 94, pp. 1636-1642, 2010.

[67] O. Sanusi, R. Warzoha, and A. S. Fleischer, "Energy storage and solidification of paraffin phase change material embedded with graphite nanofibers," *International Journal of Heat and Mass Transfer,* vol. 54, pp. 4429-4436, 2011.

[68] J. Jeon, S.-G. Jeong, J.-H. Lee, J. Seo, and S. Kim, "High thermal performance composite PCMs loading xGnP for application to building using radiant floor heating system," *Solar Energy Materials and Solar Cells,* vol. 101, pp. 51-56, 2012.

[69] S. Kim and L. T. Drzal, "High latent heat storage and high thermal conductive phase change materials using exfoliated graphite nanoplatelets," *Solar Energy Materials and Solar Cells,* vol. 93, pp. 136-142, 2009.

[70] Z. G. Zhang and X. M. Fang, "Study on paraffin/expanded graphite composite phase change thermal energy storage material," *Energy Conversion and Management,* vol. 47, pp. 303-310, 2006.

[71] A. Elgafy and K. Lafdi, "Effect of carbon nanofiber additives on thermal behavior of phase change materials," *Carbon,* vol. 43, pp. 3067-3074, 2005.

[72] Y. Cui, C. Liu, S. Hu, and X. Yu, "The experimental exploration of carbon nanofiber and carbon nanotube additives on thermal behavior of phase change materials," *Solar Energy Materials and Solar Cells,* vol. 95, pp. 1208-1212, 2011.

[73] A. Mallow, "Stable Paraffin Composites for Latent Heat Thermal Storage System," Masters, Mechanical Engineering, Georgia Institute of Technology, 2015.

[74] A. Mallow, O. Abdelaziz, K. Kalaitzidou, and S. Graham, "Investigation of the stability of paraffin-exfoliated graphite nanoplatelet composites for latent heat thermal storage systems," *Journal of Materials Chemistry,* vol. 22, pp. 24469-24476, 2012.

[75] E. Aerospace. (2011). *The Basics of Duocel® Foam*. Available: http://www.ergaerospace.com/Descriptors.htm

[76] C. Y. Zhao, "Review on thermal transport in high porosity cellular metal foams with open cells," *International Journal of Heat and Mass Transfer,* vol. 55, pp. 3618-3632, 2012.

[77] C. Y. Zhao and Z. G. Wu, "Heat transfer enhancement of high temperature thermal energy storage using metal foams and expanded graphite," *Solar Energy Materials and Solar Cells,* vol. 95, pp. 636-643, Feb 2011.

[78] Z. Chen, M. Gu, and D. Peng, "Heat transfer performance analysis of a solar flat-plate collector with an integrated metal foam porous structure filled with paraffin," *Applied Thermal Engineering,* vol. 30, pp. 1967-1973, 2010.

[79] K. Lafdi, O. Mesalhy, and S. Shaikh, "Experimental study on the influence of foam porosity and pore size on the melting of phase change materials," *Journal of Applied Physics,* vol. 102, pp. 083549-083549-6, 2007.

[80] W. Li, Z. Qu, Y. He, and W. Tao, "Experimental and numerical studies on melting phase change heat transfer in open-cell metallic foams filled with paraffin," *Applied Thermal Engineering,* vol. 37, pp. 1-9, 2012.

[81] Y. Tian and C. Y. Zhao, "A numerical investigation of heat transfer in phase change materials (PCMs) embedded in porous metals," *Energy,* vol. 36, pp. 5539-5546, Sep 2011.

[82] J. M. Marín, B. Zalba, L. F. Cabeza, and H. Mehling, "Improvement of a thermal energy storage using plates with paraffin–graphite composite," *International Journal of Heat and Mass Transfer,* vol. 48, pp. 2561-2570, 2005.

[83] R. Pokhrel, J. Gonzalez, T. Hight, and T. Adalsteinsson, "Analysis and Design of a Paraffin/Graphite Composite PCM Integrated in a Thermal Storage Unit," *Journal of Solar Energy Engineering,* vol. 132, p. 041006, 2010.

[84] D. Haillot, X. Py, V. Goetz, and M. Benabdelkarim, "Storage composites for the optimisation of solar water heating systems," *Chemical Engineering Research and Design,* vol. 86, pp. 612-617, 2008.

[85] J. Klett, A. McMillan, N. Gallego, and C. Walls, "The role of structure on the thermal properties of graphitic foams," *Journal of Materials Science,* vol. 39, pp. 3659-3676, 2004.

[86] R. Warzoha, O. Sanusi, B. McManus, and A. S. Fleischer, "Development of methods to fully saturate carbon foam with paraffin wax phase change material for energy storage," *Journal of Solar Energy Engineering,* vol. 135, p. 021006, 2013.

[87] O. Mesalhy, K. Lafdi, and A. Elgafy, "Carbon foam matrices saturated with PCM for thermal protection purposes," *Carbon,* vol. 44, pp. 2080-2088, 2006.

[88] N. C. Gallego and J. W. Klett, "Carbon foams for thermal management," *Carbon,* vol. 41, pp. 1461-1466, 2003.

[89] J.-l. Song, Q.-g. Guo, Y.-j. Zhong, X.-q. Gao, Z.-h. Feng, F. Zhen, *et al.*, "Thermophysical properties of high-density graphite foams and their paraffin composites," *New Carbon Materials,* vol. 27, pp. 27-34, 2012.

[90] S. Pincemin, R. Olives, X. Py, and M. Christ, "Highly conductive composites made of phase change materials and graphite for thermal storage," *Solar Energy Materials and Solar Cells,* vol. 92, pp. 603-613, 2008.

[91] A. Sari and A. Karaipekli, "Thermal conductivity and latent heat thermal energy storage characteristics of paraffin/expanded graphite composite as phase change material," *Applied Thermal Engineering,* vol. 27, pp. 1271-1277, 2007.

[92] H. Yin, X. Gao, J. Ding, and Z. Zhang, "Experimental research on heat transfer mechanism of heat sink with composite phase change materials," *Energy Conversion and Management,* vol. 49, pp. 1740-1746, 2008.

[93] L. Xia, P. Zhang, and R. Z. Wang, "Preparation and thermal characterization of expanded graphite/paraffin composite phase change material," *Carbon,* vol. 48, pp. 2538-2548, Aug 2010.

[94] D. Haillot, V. Goetz, X. Py, and M. Benabdelkarim, "High performance storage composite for the enhancement of solar domestic hot water systems: Part 1: Storage material investigation," *Solar Energy,* vol. 85, pp. 1021-1027, 2011.

[95] K. Lafdi, O. Mesalhy, and A. Elgafy, "Merits of employing foam encapsulated phase change materials for pulsed power electronics cooling applications," *Journal of Electronic Packaging*, vol. 130, p. 021004, 2008.

[96] Z. Chen, D. Gao, and J. Shi, "Experimental and numerical study on melting of phase change materials in metal foams at pore scale," *International Journal of Heat and Mass Transfer*, vol. 72, pp. 646-655, 2014.

[97] S. Mancin, A. Diani, L. Doretti, K. Hooman, and L. Rossetto, "Experimental analysis of phase change phenomenon of paraffin waxes embedded in copper foams," *International Journal of Thermal Sciences*, vol. 90, pp. 79-89, 2015.

[98] J. P. Trelles and J. J. Dufly, "Numerical simulation of porous latent heat thermal energy storage for thermoelectric cooling," *Applied Thermal Engineering*, vol. 23, pp. 1647-1664, 2003.

[99] S. A. Khateeb, M. M. Farid, J. R. Selman, and S. Al-Hallaj, "Design and simulation of a lithium-ion battery with a phase change material thermal management system for an electric scooter," *Journal of Power Sources*, vol. 128, pp. 292-307, 2004.

[100] S.-T. Hong and D. R. Herling, "Open-cell aluminum foams filled with phase change materials as compact heat sinks," *Scripta materialia*, vol. 55, pp. 887-890, 2006.

[101] D. Zhou and C.-Y. Zhao, "Experimental investigations on heat transfer in phase change materials (PCMs) embedded in porous materials," *Applied Thermal Engineering*, vol. 31, pp. 970-977, 2011.

[102] F. Balima, V. Pischedda, S. Le Floch, A. Brûlet, P. Lindner, L. Duclaux, *et al.*, "An in situ small angle neutron scattering study of expanded graphite under a uniaxial stress," *Carbon*, vol. 57, pp. 460-469, 6// 2013.

[103] D. Haillot, F. Nepveu, V. Goetz, X. Py, and M. Benabdelkarim, "High performance storage composite for the enhancement of solar domestic hot water systems: Part 2: Numerical system analysis," *Solar Energy*, vol. 86, pp. 64-77, 2012.

[104] M. Martinelli, F. Bentivoglio, A. Caron-Soupart, R. Couturier, J.-F. Fourmigue, and P. Marty, "Experimental study of a phase change thermal energy storage with copper foam," *Applied Thermal Engineering*, 2016.

[105] G. R. Jackson and T. S. Fisher, "Response of Phase-Change-Material-Filled Porous Foams Under Transient Heating Conditions," *Journal of Thermophysics and Heat Transfer*, pp. 1-10, 2016.

[106] Y. Zhao, C. Zhao, Z. Xu, and H. Xu, "Modeling metal foam enhanced phase change heat transfer in thermal energy storage by using phase field method," *International Journal of Heat and Mass Transfer*, vol. 99, pp. 170-181, 2016.

[107] R. Baby and C. Balaji, "Thermal optimization of PCM based pin fin heat sinks: an experimental study," *Applied Thermal Engineering,* vol. 54, pp. 65-77, 2013.

[108] M. Iten and S. Liu, "A work procedure of utilising PCMs as thermal storage systems based on air-TES systems," *Energy Conversion and Management,* vol. 77, pp. 608-627, 2014.

[109] P. Lamberg, R. Lehtiniemi, and A.-M. Henell, "Numerical and experimental investigation of melting and freezing processes in phase change material storage," *International Journal of Thermal Sciences,* vol. 43, pp. 277-287, 2004.

[110] V. Alexiades, *Mathematical modeling of melting and freezing processes*: CRC Press, 1992.

[111] P. Lamberg and K. Siren, "Analytical model for melting in a semi-infinite PCM storage with an internal fin," *Heat and Mass Transfer,* vol. 39, pp. 167-176, 2003.

[112] Y. Dutil, D. R. Rousse, N. B. Salah, S. Lassue, and L. Zalewski, "A review on phase-change materials: mathematical modeling and simulations," *Renewable and Sustainable Energy Reviews,* vol. 15, pp. 112-130, 2011.

[113] W.-B. Ye, D.-S. Zhu, and N. Wang, "Fluid flow and heat transfer in a latent thermal energy unit with different phase change material (PCM) cavity volume fractions," *Applied Thermal Engineering,* vol. 42, pp. 49-57, 2012.

[114] P. Dolado, A. Lázaro, B. Zalba, and J. Marín, "Numerical simulation of the thermal behaviour of an energy storage unit with phase change materials for air conditioning applications between 17 C and 40 C," in *Proceedings of the Tenth International Conference on Thermal Energy Storage, Ecostock 2006*, 2006.

[115] V. Antony Aroul Raj and R. Velraj, "Heat transfer and pressure drop studies on a PCM-heat exchanger module for free cooling applications," *International Journal of Thermal Sciences,* vol. 50, pp. 1573-1582, 2011.

[116] R. E. Murray and D. Groulx, "Modeling Convection during Melting of a Phase Change Material," in *Proceedings of the COMSOL Conference*, 2011.

[117] X. Hu and S. S. Patnaik, "Modeling phase change material in micro-foam under constant temperature condition," *International Journal of Heat and Mass Transfer,* vol. 68, pp. 677-682, 2014.

[118] S. Feng, M. Shi, Y. Li, and T. J. Lu, "Pore-scale and volume-averaged numerical simulations of melting phase change heat transfer in finned metal foam," *International Journal of Heat and Mass Transfer,* vol. 90, pp. 838-847, 2015.

[119] Y. Du and Y. Ding, "Towards improving charge/discharge rate of latent heat thermal energy storage (LHTES) by embedding metal foams in phase change

materials (PCMs)," *Chemical Engineering and Processing: Process Intensification*, vol. 108, pp. 181-188, 2016.

[120] K. Kota, L. Chow, and Q. Leland, "Laminar film condensation driven latent thermal energy storage in rectangular containers," *International Journal of Heat and Mass Transfer*, vol. 55, pp. 1208-1217, 2012.

[121] A. Inayat, H. Freund, T. Zeiser, and W. Schwieger, "Determining the specific surface area of ceramic foams: The tetrakaidecahedra model revisited," *Chemical Engineering Science*, vol. 66, pp. 1179-1188, 2011.

[122] B. Dietrich, G. I. Garrido, P. Habisreuther, N. Zarzalis, H. Martin, M. Kind, *et al.*, "Morphological characterization of ceramic sponges for applications in chemical engineering," *Industrial and Engineering Chemistry Research*, vol. 48, pp. 10395-10401, 2009.

[123] P. Zhang, Z. Meng, H. Zhu, Y. Wang, and S. Peng, "Melting heat transfer characteristics of a composite phase change material fabricated by paraffin and metal foam," *Applied Energy*, 2015.

[124] Z. Yang and S. V. Garimella, "Melting of Phase Change Materials With Volume Change in Metal Foams," *Journal of Heat Transfer*, vol. 132, pp. 062301-062301, 2010.

[125] J. Yang, L. Yang, C. Xu, and X. Du, "Numerical analysis on thermal behavior of solid–liquid phase change within copper foam with varying porosity," *International Journal of Heat and Mass Transfer*, vol. 84, pp. 1008-1018, 2015.

[126] Y. Li, Y. He, H. Song, C. Xu, and W. Wang, "Numerical analysis and parameters optimization of shell-and-tube heat storage unit using three phase change materials," *Renewable Energy*, vol. 59, pp. 92-99, 2013.

[127] W. Ogoh and D. Groulx, "Effects of the heat transfer fluid velocity on the storage characteristics of a cylindrical latent heat energy storage system: a numerical study," *Heat and Mass Transfer*, vol. 48, pp. 439-449, 2012.

[128] K. Merlin, D. Delaunay, J. Soto, and L. Traonvouez, "Heat transfer enhancement in latent heat thermal storage systems: Comparative study of different solutions and thermal contact investigation between the exchanger and the PCM," *Applied Energy*, vol. 166, pp. 107-116, 2016.

[129] A. Greco, X. Jiang, and D. Cao, "An investigation of lithium-ion battery thermal management using paraffin/porous-graphite-matrix composite," *Journal of Power Sources*, vol. 278, pp. 50-68, 2015.

[130] W. Zhao, D. M. France, W. Yu, T. Kim, and D. Singh, "Phase change material with graphite foam for applications in high-temperature latent heat storage systems of concentrated solar power plants," *Renewable Energy*, vol. 69, pp. 134-146, 2014.

[131] X. Wang, Q. Guo, Y. Zhong, X. Wei, and L. Liu, "Heat transfer enhancement of neopentyl glycol using compressed expanded natural graphite for thermal energy storage," *Renewable Energy*, vol. 51, pp. 241-246, 2013.

[132] J.-F. Luo, H.-W. Yin, W.-Y. Li, Z.-J. Xu, Z.-Z. Shao, X.-J. Xu, *et al.*, "Numerical and experimental study on the heat transfer properties of the composite paraffin/expanded graphite phase change material," *International Journal of Heat and Mass Transfer*, vol. 84, pp. 237-244, 2015.

[133] M. M. Sedeh and J. Khodadadi, "Thermal conductivity improvement of phase change materials/graphite foam composites," *Carbon*, vol. 60, pp. 117-128, 2013.

[134] T. Oya, T. Nomura, N. Okinaka, and T. Akiyama, "Phase change composite based on porous nickel and erythritol," *Applied Thermal Engineering*, vol. 40, pp. 373-377, 2012.

[135] T. Zhang, J. Yu, and H. Gao, "Measurement of Thermal Parameters of Copper-Foam/Paraffins Composite PCM Using Transient Plane Source Method," *Acta Energ. Solar. Sin*, vol. 31, pp. 604-609, 2010.

[136] W.-q. Xu, X.-g. Yuan, and Z. Li, "Study on effective thermal conductivity of metal foam matrix composite phase change materials," *Journal of Functional Materials*, vol. 8, p. 025, 2009.

[137] X. Xiao, P. Zhang, and M. Li, "Effective thermal conductivity of open-cell metal foams impregnated with pure paraffin for latent heat storage," *International Journal of Thermal Sciences*, vol. 81, pp. 94-105, 2014.

[138] M. Almajali, K. Lafdi, and P. Prodhomme, "Effect of copper coating on infiltrated PCM/foam," *Energy Conversion and Management*, vol. 66, pp. 336-342, 2013.

[139] Y. Yao, H. Wu, and Z. Liu, "A new prediction model for the effective thermal conductivity of high porosity open-cell metal foams," *International Journal of Thermal Sciences*, vol. 97, pp. 56-67, 2015.

[140] X. H. Yang, J. X. Bai, H. B. Yan, J. J. Kuang, T. J. Lu, and T. Kim, "An analytical unit cell model for the effective thermal conductivity of high porosity open-cell metal foams," *Transport in Porous Media*, vol. 102, pp. 403-426, 2014.

[141] X. Xiao, P. Zhang, and M. Li, "Preparation and thermal characterization of paraffin/metal foam composite phase change material," *Applied Energy*, vol. 112, pp. 1357-1366, 2013.

[142] V. Calmidi and R. Mahajan, "The effective thermal conductivity of high porosity fibrous metal foams," *Journal of Heat Transfer*, vol. 121, pp. 466-471, 1999.

[143] X. Han, Y. Tian, and C. Zhao, "An effectiveness study of enhanced heat transfer in phase change materials (PCMs)," *International Journal of Heat and Mass Transfer,* vol. 60, pp. 459-468, 2013.

[144] A. Bhattacharya, V. Calmidi, and R. Mahajan, "Thermophysical properties of high porosity metal foams," *International Journal of Heat and Mass Transfer,* vol. 45, pp. 1017-1031, 2002.

[145] K. Boomsma and D. Poulikakos, "On the effective thermal conductivity of a three-dimensionally structured fluid-saturated metal foam," *International Journal of Heat and Mass Transfer,* vol. 44, pp. 827-836, 2001.

[146] F. Zhu, C. Zhang, and X. Gong, "Numerical analysis and comparison of the thermal performance enhancement methods for metal foam/phase change material composite," *Applied Thermal Engineering,* vol. 109, pp. 373-383, 2016.

[147] C. Zhao, T. Kim, T. Lu, and H. Hodson, "Thermal transport in high porosity cellular metal foams," *Journal of Thermophysics and Heat Transfer,* vol. 18, pp. 309-317, 2004.

[148] Z. Dai, K. Nawaz, Y. Park, J. Bock, and A. Jacobi, "Correcting and extending the Boomsma–Poulikakos effective thermal conductivity model for three-dimensional, fluid-saturated metal foams," *International Communications in Heat and Mass Transfer,* vol. 37, pp. 575-580, 2010.

[149] X. Yang, J. Kuang, T. Lu, F. Han, and T. Kim, "A simplistic analytical unit cell based model for the effective thermal conductivity of high porosity open-cell metal foams," *Journal of Physics D: Applied Physics,* vol. 46, p. 255302, 2013.

[150] Y. Tian and C. Zhao, "Thermal and exergetic analysis of metal foam-enhanced cascaded thermal energy storage (MF-CTES)," *International Journal of Heat and Mass Transfer,* vol. 58, pp. 86-96, 2013.

[151] E. Fleming, S. Wen, L. Shi, and A. K. da Silva, "Experimental and theoretical analysis of an aluminum foam enhanced phase change thermal storage unit," *International Journal of Heat and Mass Transfer,* vol. 82, pp. 273-281, 2015.

[152] C.-W. Nan, R. Birringer, D. R. Clarke, and H. Gleiter, "Effective thermal conductivity of particulate composites with interfacial thermal resistance," *Journal of Applied Physics,* vol. 81, pp. 6692-6699, 1997.

[153] D. Hasselman and L. F. Johnson, "Effective thermal conductivity of composites with interfacial thermal barrier resistance," *Journal of Composite Materials,* vol. 21, pp. 508-515, 1987.

[154] S. Krishnan, J. Y. Murthy, and S. V. Garimella, "Direct simulation of transport in open-cell metal foam," *Journal of Heat Transfer,* vol. 128, pp. 793-799, 2006.

[155] S. Lingamneni, M. Asheghi, and K. E. Goodson, "A parametric study of microporous metal matrix-phase change material composite heat spreaders for transient thermal applications," in *Thermal and Thermomechanical Phenomena in Electronic Systems (ITherm), 2014 IEEE Intersociety Conference on*, 2014, pp. 870-875.

[156] S. S. Sundarram and W. Li, "The effect of pore size and porosity on thermal management performance of phase change material infiltrated microcellular metal foams," *Applied Thermal Engineering*, vol. 64, pp. 147-154, 2014.

[157] N. Bianco, S. Cunsolo, W. Chiu, V. Naso, A. Migliozzi, and M. Oliviero, "Analysis of Heat Transfer and Pressure Drop Through Idealized Open Cell Ceramic Foams: Comparison Between Kelvin and Weaire-Phelan Cell Structures," in *ASME 2013 Heat Transfer Summer Conference collocated with the ASME 2013 7th International Conference on Energy Sustainability and the ASME 2013 11th International Conference on Fuel Cell Science, Engineering and Technology*, 2013, pp. V004T14A010-V004T14A010.

[158] A. Kopanidis, A. Theodorakakos, E. Gavaises, and D. Bouris, "3D numerical simulation of flow and conjugate heat transfer through a pore scale model of high porosity open cell metal foam," *International Journal of Heat and Mass Transfer*, vol. 53, pp. 2539-2550, 2010.

[159] T. T. Huu, M. Lacroix, C. Pham Huu, D. Schweich, and D. Edouard, "Towards a more realistic modeling of solid foam: Use of the pentagonal dodecahedron geometry," *Chemical Engineering Science*, vol. 64, pp. 5131-5142, 2009.

[160] G. Jiang, J. Huang, Y. Fu, M. Cao, and M. Liu, "Thermal optimization of composite phase change material/expanded graphite for Li-ion battery thermal management," *Applied Thermal Engineering*, vol. 108, pp. 1119-1125, 2016.

[161] J. Leland and G. Recktenwald, "Optimization of a phase change heat sink for extreme environments," in *Semiconductor Thermal Measurement and Management Symposium, 2003. Ninteenth Annual IEEE*, 2003, pp. 351-356.

[162] N. Zheng and R. Wirtz, "A hybrid thermal energy storage device, part 1: design methodology," *Journal of Electronic Packaging*, vol. 126, pp. 1-7, 2004.

[163] M. Raju and S. Kumar, "Optimization of heat exchanger designs in metal hydride based hydrogen storage systems," *International Journal of Hydrogen Energy*, vol. 37, pp. 2767-2778, 2012.

[164] M. Kabbara, D. Groulx, and A. Joseph, "Experimental investigations of a latent heat energy storage unit using finned tubes," *Applied Thermal Engineering*, 2016.

[165] M. Medrano, M. Yilmaz, M. Nogués, I. Martorell, J. Roca, and L. F. Cabeza, "Experimental evaluation of commercial heat exchangers for use as PCM thermal storage systems," *Applied Energy*, vol. 86, pp. 2047-2055, 2009.

[166] L. F. Cabeza, M. Ibáñez, C. Sole, J. Roca, and M. Nogués, "Experimentation with a water tank including a PCM module," *Solar Energy Materials and Solar Cells*, vol. 90, pp. 1273-1282, 2006.

[167] S. Jegadheeswaran, S. D. Pohekar, and T. Kousksou, "Performance enhancement of solar latent heat thermal storage system with particle dispersion—an exergy approach," *Clean–Soil, Air, Water*, vol. 39, pp. 964-971, 2011.

[168] J. Shon, H. Kim, and K. Lee, "Improved heat storage rate for an automobile coolant waste heat recovery system using phase-change material in a fin–tube heat exchanger," *Applied Energy*, vol. 113, pp. 680-689, 2014.

[169] A. I. N. Korti and F. Z. Tlemsani, "Experimental investigation of latent heat storage in a coil in PCM storage unit," *Journal of Energy Storage*, vol. 5, pp. 177-186, 2016.

[170] M. M. Joybari, F. Haghighat, J. Moffat, and P. Sra, "Heat and cold storage using phase change materials in domestic refrigeration systems: The state-of-the-art review," *Energy and Buildings*, vol. 106, pp. 111-124, 2015.

[171] R. Parameshwaran and S. Kalaiselvam, "Energy efficient hybrid nanocomposite-based cool thermal storage air conditioning system for sustainable buildings," *Energy*, vol. 59, pp. 194-214, 9/15/ 2013.

[172] K. Merlin, J. Soto, D. Delaunay, and L. Traonvouez, "Industrial waste heat recovery using an enhanced conductivity latent heat thermal energy storage," *Applied Energy*, vol. 183, pp. 491-503, 2016.